

# AGARD

ADVISORY GROUP FOR AEROSPACE RESEARCH & DEVELOPMENT

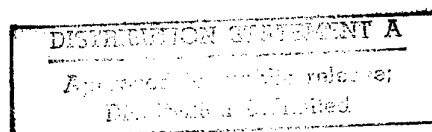
7 RUE ANCELLE, 92200 NEUILLY-SUR-SEINE, FRANCE

---

## AGARD REPORT 823

### Thermal Barrier Coatings

(les Revêtements anti-mur de chaleur)



Papers presented at the 85th Meeting of the AGARD Structures and Materials Panel, held in Aalborg, Denmark 15-16 October 1997.

19980520 102



North Atlantic Treaty Organization  
*Organisation du Traité de l'Atlantique Nord*

# The Mission of AGARD\*

According to its Charter, the mission of AGARD is to bring together the leading personalities of the NATO nations in the fields of science and technology relating to aerospace for the following purposes:

- Recommending effective ways for the member nations to use their research and development capabilities for the common benefit of the NATO community;
- Providing scientific and technical advice and assistance to the Military Committee in the field of aerospace research and development (with particular regard to its military application);
- Continuously stimulating advances in the aerospace sciences relevant to strengthening the common defence posture;
- Improving the co-operation among member nations in aerospace research and development;
- Exchange of scientific and technical information;
- Providing assistance to member nations for the purpose of increasing their scientific and technical potential;
- Rendering scientific and technical assistance, as requested, to other NATO bodies and to member nations in connection with research and development problems in the aerospace field.

The highest authority within AGARD is the National Delegates Board consisting of officially appointed senior representatives from each member nation. The mission of AGARD is carried out through the Panels which are composed of experts appointed by the National Delegates, the Consultant and Exchange Programme and the Aerospace Applications Studies Programme. The results of AGARD work are reported to the member nations and the NATO Authorities through the AGARD series of publications of which this is one.

Participation in AGARD activities is by invitation only and is normally limited to citizens of the NATO nations.

\* AGARD merged with the Defence Research Group of NATO (DRG) on 1 January 1998 to form the Research and Technology Organization (RTO) of NATO. However, both AGARD and DRG will continue to issue publications under their own names in respect of work performed in 1997.

The content of this publication has been reproduced  
directly from material supplied by AGARD or the authors.



*Printed on recycled paper*

Published April 1998

Copyright © AGARD 1998  
All Rights Reserved

ISBN 92-836-1073-3



*Printed by Canada Communication Group Inc.  
(A St. Joseph Corporation Company)  
45 Sacré-Cœur Blvd., Hull (Québec), Canada K1A 0S7*

# **Thermal Barrier Coatings**

## **(AGARD-R-823)**

### **Executive Summary**

Thermal barrier coatings are an emerging technology which will allow either increasing the inlet turbine temperatures or on the other hand decreasing the working temperature of the metal of the blades and consequently increasing their life-time.

The Workshop allowed a survey of the state of the art, a description of the existing technologies or of the technologies under development, a review of the present knowledge of damage mechanisms, including microstructural, mechanical and thermal aspects, and an account of the advantages and drawbacks of the various families as perceived by engine manufacturers and users. A final discussion was held to identify the needs for further R & D.

# **Les revêtements anti-mur de chaleur**

## **(AGARD-R-823)**

### **Synthèse**

Les barrières thermiques sont une technologie émergente qui permettra soit d'augmenter les températures d'entrée des turbines, soit de réduire la température à laquelle est soumis le métal des aubes et par conséquent d'en accroître la durée de vie.

L'atelier a eu pour objet de présenter l'état de l'art, de donner une description des technologies existantes ou en cours de développement, de donner une revue des connaissances actuelles sur les mécanismes d'endommagement incluant les aspects microstructuraux, mécaniques et thermiques, de rendre compte des avantages et des inconvénients des diverses familles tels que les perçoivent les fabricants et les utilisateurs de moteurs.

Une discussion finale a permis d'identifier les besoins futurs en R & D.



# Contents

	<b>Page</b>
<b>Executive Summary</b>	<b>iii</b>
<b>Synthèse</b>	<b>iv</b>
<b>Preface</b>	<b>vii</b>
<b>Préface</b>	<b>viii</b>
<b>Structures and Materials Panel</b>	<b>ix</b>

## Reference

### SESSION I: INTRODUCTION

<b>Thermal Barrier Coatings: the Thermal Conductivity Challenge</b>	<b>1</b>
by S. Alperine, M. Derrien, Y. Jaslier and R. Mévrel	

### SESSION II: TBC TECHNIQUES

#### Paper 2 Withdrawn

<b>Recent Developments in Plasma Sprayed Thermal Barrier Coatings</b>	<b>3</b>
by P. Fauchais, A. Vardelle and M. Vardelle	
<b>In-flight Particle Diagnostics for On-line Process Control during Deposition of Plasma-Sprayed TBCs</b>	<b>4</b>
by C. Moreau, P. Gougeon, M. Prystay and L. Leblanc	
<b>On Thick Thermal Barriers for Combustor Application</b>	<b>5</b>
by T. Haubold, H. Gans, D. Schwingel and R. Taylor	
<b>Advanced Processing of TBC's for Reduced Thermal Conductivity</b>	<b>6</b>
by J.R. Nicholls, K.J. Lawson, D.S. Rickerby and P. Morrell	
<b>TBCs on Free-Standing Multilayer Components</b>	<b>7</b>
by P.G. Tsantrizos, G.E. Kim and T.A. Brzezinski	
<b>Electron Beam Physical Vapour Deposition Thermal Barrier Coatings: A Comparative Evaluation of Competing Deposition Technologies</b>	<b>8</b>
by Y. Jaslier and S. Alperine	
<b>Processing, Characterisation and Testing of EB-PVD Thermal Barrier Coatings</b>	<b>9</b>
by W.A. Kaysser, M. Peters, K. Fritscher and U. Schulz	

**Electron Beam, PVD TBCs: Coating Industrial Blades at an Industrial Scale** 10†  
by G. Marijnissen

**Plasma Assisted CVD of Thick Yttria Partially Stabilized Zirconia Coatings** 11  
by S. Chevillard, S. Drawin and M.H. Vidal-Sétif

### **SESSION III: TBC PROPERTIES AND DESIGN**

**Thermal Sprayed Nanostructured Thermal Barrier Coatings** 12  
by L.T. Kabacoff

**Modelling the Thermal Conductivity of Thermal Barrier Coatings** 13  
by J.-M. Dorvaux, O. Lavigne, R. Mévrel, M. Poulain, Y. Renollet, C. Rio

**Microstructure and Thermal Conductivity of Layered Thermal Barrier Coatings Processed by Plasma Spray and Physical Vapor Deposition Techniques** 14  
by K.S. Ravichandran, K. An, R.E. Dutton and S.L. Semiatin

**Evaluation of Thermal Barrier Coatings from Burner Rig Tests** 15  
by J-P. Immarigeon, V.R. Parameswaran, D. Chow, D.D. Morphy, P. Gougeon, M. Prystay and C. Moreau

**Graded Design of EB-PVD Thermal Barrier Coating Systems** 16  
by U. Schulz, T. Krell, U. Leushake and M. Peters

**Bond Coat Considerations for Thermal Barrier Coatings** 17  
by A.M. Freborg, B.L. Ferguson, W.J. Brindley and G.J. Petrus

**The Effect of TBC Utilization in the Design of Robust Aircraft Combustors** 18  
by C.A. Arana

**Paper 19 Withdrawn**

**Advantages/Disadvantages of Various TBC Systems as Perceived by the Engine Manufacturer** 20  
by P. Morrell and D.S. Rickerby

**Report on the Final Discussion** D  
by S. Drawin

†Paper not available at time of printing

# Preface

Thermal barrier coatings are a technology used to protect the metal of combustion chambers, turbines blades or veins. Since these parts are air-cooled low-thickness elements, it is possible to reduce the actual temperature of the metal introducing a large temperature gradient through the ceramic coating. This technology has been used for several decades in the combustion chambers, and more recently on modern highly-cooled blades.

Since it can allow an increase of the temperature difference between the metal part and the gas flow, up to 100°C, it can be considered as one of the bottle-neck technologies giving access to higher temperatures in aeronautical engines. Alternatively, it can allow also, for the same turbine inlet temperature, a reduction of the working temperature of the metal of the blades, leading to longer lifetimes of the parts, or a reduction of the cooling air flow, with an increase in engine efficiency.

Up to now zirconia-base ceramics in particular yttria-zirconia have been used; they are compatible with metal temperatures up to 900°C for combustion chambers and 1050°C for blades, under fairly low thicknesses.

Two deposition processes are presently in use: plasma spray, which gives relatively thick, low cost, low conductivity coatings, well adapted to combustion chambers, and for blades Physical Vapour Deposition techniques which give columnar microstructure which lead to more acceptable damage and to a surface of limited rugosity, which does not perturb the aerodynamic qualities of the blades but which unfortunately lead to lower deposition rates, and also higher conductivities.

Research is in progress in several directions: improved or new deposition techniques, new composition of the ceramics.

The Workshop in this context has been dedicated to:

1. The presentation of families and technologies under development with reference to new ideas and limits.
2. The description of the advantages and drawbacks of the various families of thermal coatings as perceived by engine manufacturers or users.
3. Understanding damage mechanisms in connexion with properties and microstructure.
4. Modeling the behaviour and the lifetime of the coatings with special reference to the underlying bond coat.

P. COSTA  
Chairman of the Subcommittee

# Préface

Les barrières thermiques sont une technologie qui est utilisée pour protéger le métal des chambres de combustion, des aubes de turbine mobiles et fixes. Comme ces pièces sont des éléments de faible épaisseur fortement refroidies par un courant d'air arrière, il est possible de réduire la température effective du métal du fait d'une importante chute de température au travers du revêtement céramique. Cette technologie est utilisée depuis plusieurs décennies pour les chambres de combustion, et depuis plus récemment pour des aubes mobiles fortement refroidies.

Dans la mesure où elle permet d'accroître la différence entre la pièce métallique et le flux gazeux de près de 100°C, elle peut être considérée comme une technologie goulet pour qui veut accroître les températures dans les moteurs aéronautiques. En parallèle, elle permet aussi, pour une même température d'entrée de turbine, de réduire la température du métal des pièces travaillantes, et d'en accroître ainsi la durée de vie, ou encore de réduire les flux de refroidissement, avec un accroissement du rendement des moteurs.

Jusqu'ici, ce sont des céramiques à base de zircone qui ont été utilisées, en particulier la zircone-yttriée. Elles sont compatibles avec des températures atteignant 900°C pour le métal des chambres de combustion, de 1050°C pour les aubes mobiles, et ceci pour des épaisseurs de revêtement relativement faibles.

Deux procédés de dépôt sont actuellement utilisés, la pulvérisation plasma qui permet d'obtenir des revêtements relativement épais, de coût modéré et de faible conductibilité thermique, bien adaptés au problème des chambres de combustion, et pour les aubes des dépôts en phase vapeur, qui donnent des structures colonnaires qui sont faiblement endommageables, et un état de surface de bonne qualité ne perturbant pas l'aérodynamique de l'aube, avec toutefois des vitesses de dépôt, donc des coûts plus élevés, et également une conductibilité plus élevée. Les recherches se poursuivent dans plusieurs directions: méthodes de dépôts améliorées ou nouvelles, nouvelles compositions de la céramique.

Dans ce contexte, l'atelier a été consacré à:

1. La description des familles et des technologies existantes.
2. La présentation des familles et des technologies en cours de développement, avec une référence particulière aux idées nouvelles et à leurs limites.
3. La description des avantages et des inconvénients des diverses familles de barrières thermiques tels que les perçoivent fabricants de moteurs et utilisateurs.
4. La compréhension des mécanismes d'endommagement en corrélation avec les propriétés des barrières et leur microstructure.
5. La modélisation du comportement et de la durée de vie des revêtements, avec une référence particulière pour le revêtement intermédiaire.

P. COSTA  
Président du Sous-Comité

# Structures and Materials Panel

Chairman: Prof. R. Potter  
Business Manager  
Structural Materials Center  
Griffith Building (A7) Room 1014  
DERA Farnborough  
United Kingdom

Deputy Chairman: Ir. H.H. Ottens  
Head of Structures Department  
National Aerospace Laboratory  
(NLR)  
P.O. Box 153  
8300 AD Emmeloord  
Netherlands

## SUB-COMMITTEE MEMBERS

Chairman: Dr. Paul Costa  
Directeur Scientifique des  
Matériaux  
ONERA  
29, Av. de la Division Leclerc  
92322 Châtillon/Bagneux Cedex  
France

Members:	T. Akyurek -	TU	A. Lasalmonie	-	FR
	E. Campo -	IT	C. Moura Branco	-	PO
	H. Goncalo -	PO	R. Potter	-	UK
	P. Heuler -	GE	T. Ronald	-	US
	W. Van der Hoeven -	NE	R. Servent	-	SP
	J.P. Immarigeon -	CA	E. Starke	-	US
	R. Kochendörfer -	GE	D. Viechnicki	-	US
	L. Kompotiatis -	GR	J. Waldman	-	US

## PANEL EXECUTIVE

Dr. J.M. CARBALLAL, SP

**Mail from Europe:**  
AGARD-OTAN  
92200 Neuilly-sur-Seine  
France

**Mail from US and Canada:**  
AGARD-NATO/SMP  
PSC 116  
APO AE 09777

Tel: 33 (0) 1 55 61 22 90 & 92  
Telefax: 33 (0) 1 55 61 22 99 & 98  
Telex: 610175F

## Thermal Barrier Coatings : the Thermal Conductivity challenge

S. Alpérine<sup>1</sup>, M. Derrien<sup>2</sup>, Y. Jaslier<sup>1</sup>, R. Mévrel<sup>3</sup>

<sup>1</sup>SNECMA Materials and Process Department, Villaroche, France

<sup>2</sup>SNECMA Component Design Department Villaroche France

<sup>3</sup>ONERA Materials Science Division BP72 92322 Châtillon Cedex France

**ABSTRACT.** In this paper, the importance of the challenge associated with the control of the thermal conductivity of thermal barrier coatings for turbine engines hot stages is being reviewed (yttria stabilised zirconia mostly). It is firstly illustrated by the description of a practical aeronautic coated and uncoated turbine blade design exercise. The various contributions to TBC thermal conductivity are then reviewed. Their low conductivity finds its source not only in the nature of the ceramic layer (highly disordered material), but also in the morphology of the insulating layer, closely linked to its fabrication process parameters. The influence of various factors (such as yttria content, temperature, porosity content and distribution, etc.) on the thermal conductivity is examined, largely based on a literature review. In this field of investigation, the modelling tool should allow to predict, to a certain extent, which morphology would lead to the lowest values of thermal conductivity. Eventually attempts are made to identify research domains where further understanding is needed, and to formulate several suggestions concerning possible ways to lower the thermal conductivity.

### 1. INTRODUCTION

Yttria stabilised zirconia based thermal barrier coatings are viewed today as the new generation of protective coatings that will allow to take the next quantum step forward to increase turbine engine efficiency, without having to pay the price of replacing nickel-base superalloys by some other more refractory material [1]. They are also considered by diesel engine manufacturers to increase the efficiency of their engines. These coatings have been studied and developed for more than 20 years in the western countries and even longer in former USSR.

It can be said that one of the first concern of materials scientists in the TBC field was to optimise the coatings from a materials science standpoint. In the early days, important studies have been carried out to determine for instance which was the most adequate stabilising agent of zirconia for a given application, and in what amount [1-3]. As far as very high temperatures applications are concerned (mostly driven by the aero industry), there was a rapid and general move towards 6-8 wt. % yttria partially stabilised zirconia (Y-PSZ) because these coatings showed the highest degree of resistance to spallation in thermal fatigue solicitations [3] and an excellent thermal stability. Later, explanations of the phenomenon appeared through the identification of

the well-known  $t'$  phase [5] and its toughening mechanisms [6]. Important materials studies have also been devoted to finding an optimal metallic bond coating to support the ceramic topcoat [7,8]. The development of TBC has also been closely linked to that of the corresponding deposition processes: plasma spraying and electron beam physical vapour deposition (EBPVD). A number of studies [4, 9, 10] have thus been devoted to optimise the deposition process parameters to obtain favourable structures in order to achieve longer life cycles. The general idea there, was to try to relate coatings microstructure to their thermomechanical resistance.

This necessity to address in the very first place the feasibility and reliability problems for such coatings has somewhat hindered, until recently, the extent of research activities directly dealing with their thermal conductivity (K). The implicit notion there, was that by using stabilised zirconia as TBC would lead to a value of K for the coating not significantly different from one coating to the other, lower in any case than that of the dense material having the same composition. The scope of this paper is to emphasise the importance of the challenge associated with the control of coating thermal conductivity. It is first illustrated through a practical aeronautic turbine blade design. The various contributions to thermal barrier coating thermal conductivity are then reviewed. The low conductivity of thermal barriers comes on the one hand from the nature of the yttria stabilised zirconia ceramic layer, a highly disordered material indeed, and on the other, from the morphology of this layer, closely linked to coating processes: pores, cracks, etc. The influence of various factors (such as yttria content, temperature, porosity distribution, etc.) on the thermal conductivity is examined, largely based upon a literature review. In this field of investigation, the modelling tool should allow to predict, to a certain extent, which type of morphology would lead to the lowest values of conductivity. Eventually, attempts are made to identify research domains where further understanding is needed and to formulate several suggestions concerning possible ways to lower the thermal conductivity.

### 2. A REAL CASE DESIGN STUDY

In this case we consider a high pressure turbine vane airfoil of an aero-engine. The component is meshed for 2D finite element calculation ; for one airfoil, about 350 elements and 1200 nodes are being generated. The thermal barrier coating is represented as a single element in the foil thickness.

A mission profile is defined for the component, as the variation with time of relevant engine parameters such as altitude and thrust. Aerothermal Navier-Stokes codes are used to calculate thermal exchanges in the internal cooling passages ; thermal exchanges with hot gases are also computed, taking into account film cooling (cold gas from the cooling circuit reemitted in flow path). The result of these computations is an array of boundary conditions at the external and internal walls of the airfoil : hot and cold gas temperatures within the boundary layer, values of the wall exchange coefficients. The next step of the calculation consists in solving the Fourier equation across the airfoil walls using the above given limit conditions. The calculation ends up with a mesh of computed temperatures for each node, for every point of the mission profile :  $T = f(\text{node \#}, t)$ .

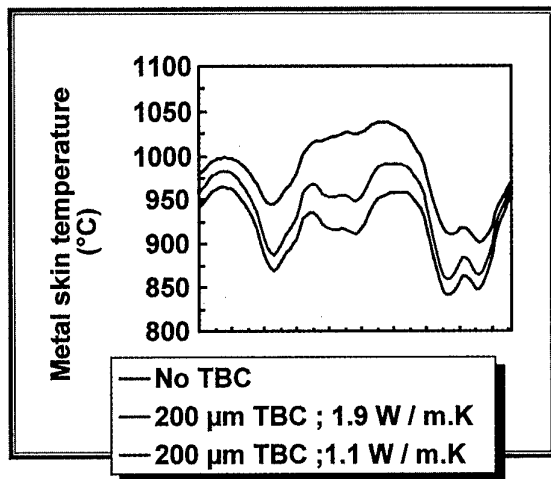


**Figure 1 :** Metal skin temperature distribution experienced by a vane during typical flight mission (leading edge profile).

In order to visualise the effect of thermal barrier conductivity, such calculations have been made for an airfoil without thermal barrier and with a coating of thickness  $200\mu\text{m}$ . In the latter case two values of the thermal conductivity of the ceramic have been taken into consideration : 1.1 and 1.9 W/m.K, typical of existing plasma sprayed and EBPVD coatings respectively.

Examination of the leading edge metal temperature profile (figure 1) shows that the application of a TBC (1.9W/m.K) reduces the maximum temperature ( $1090^\circ\text{C}$ ) of the metal by  $50^\circ\text{C}$ . Decreasing the thermal conductivity down to 1.1 W/m.K permits to gain a further  $32^\circ\text{C}$ . Considering the whole leading edge profile, the maximum gain even reaches  $113^\circ\text{C}$ .

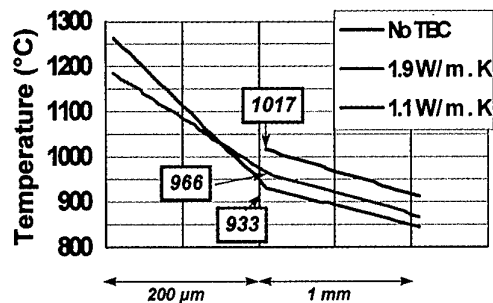


**Figure 2 :** Temperature profile across the vane wall (leading edge).

The temperature distribution across the airfoil leading edge is represented on figure 2. At the point considered, the metal temperature decreases from  $1017^\circ\text{C}$  for an uncoated airfoil down to  $966^\circ\text{C}$  with a TBC having a thermal conductivity of 1.9 W/m.K and  $933^\circ\text{C}$  with a low thermal conductivity coating. It is interesting to note that the ceramic coating external surface temperature increases correlatively (from  $1190^\circ\text{C}$  to  $1260^\circ\text{C}$ ), this being explained in part by the fact that the heat flux is kept constant. Excessive temperatures may provoke an evolution of the ceramic microstructure : transformation  $t' \rightarrow c + \text{transformable } t$ , sintering of the external layer associated with an increase of the thermal conductivity.

In terms of component life duration (taking into account creep and fatigue phenomena), and considering the leading edge, the application of a TBC with  $K = 1.1$  W/m.K permits to gain more than an order of magnitude on the number of cycles. For less stressed regions (pressure side, trailing edge), the benefit is of course less.

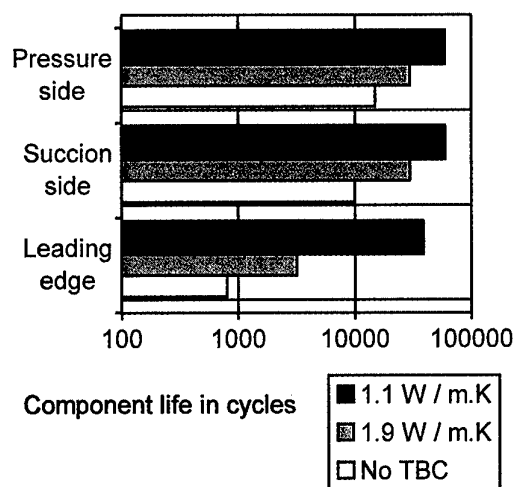


**Figure 3 :** Component life duration (creep and fatigue)  
If we consider now that the engine is run so that the components keep the same life duration, but the gain is concentrated entirely on reducing the cooling rate and by way of consequence decreasing the fuel

consumption, table 1 shows that up to 0.7% specific consumption can be saved in the cases envisaged.

Thermal conductivity (W/m.K)	Cooling rate	Specific consumption
1.9	- 15%	- 0.4%
1.1	- 25%	- 0.7%

**Table 1 :** Reduction in cooling rate and specific consumption owing to the application of a TBC of thermal conductivity  $K$  on a vane airfoil (for a given lifetime).

These few results clearly demonstrate the importance of lowering the thermal conductivity in terms of economy and performance. Moreover, a decrease in the thermal conductivity permits to lower the thickness of the coating. Given the fact that a TBC represents an added stress on a rotating blade of 10% (for a 125  $\mu\text{m}$  thick ceramic layer), lowering its thickness (provided the density is kept constant) will result in a significant gain on the stress applied on the rotating parts, blades and disks.

Of course, a rigorous computation would have to take into account the radiation contribution to the conductivity within the coating. This is an effect which depends on the actual environment seen by the airfoils within the turbine stage [11] and difficult to assess at present as the optical properties of zirconia-based plasma-sprayed and EBPVD coatings are poorly known.

### 3. THERMAL CONDUCTIVITY OF ZIRCONIA-BASED COATINGS

Although the thermal conductivity of thermal barrier coatings has not been a major research and development topic compared to work on thermomechanical behaviour for instance, a number of characterisations have been published, in particular to provide designers with data for lifetime prediction models. Looking through some of the data available and reported in table 2, several points are worth noticing :

- Thermal conductivity values for zirconia based coatings are relatively low (within the range 0.5 to 2 W/m.K). This is significantly lower than values determined on bulk zirconia [18, 19], typically in the 2 to 4 W/m.K range, depending on the composition and crystallographic structure. These values lie in the lower range of thermal conductivity for oxides.

- Thermal conductivities of EBPVD coatings are significantly higher than values measured for plasma sprayed coatings having the same composition. This can be explained by the structure of the coatings. Plasma sprayed coatings exhibit a microcrack network, with basically two crack populations : one oriented perpendicular to the coating surface and originating from cracking of individual splats during

cooling, as a result of the limited elastoplastic deformation capability of the ceramic. The other is mainly oriented parallel to the surface and corresponds to poor contacts between different splats. The latter, being perpendicular to the heat flux are particularly effective in reducing the thermal conductivity of the coating. In addition, a dispersed, spheroidal porosity contributes to lowering the conductivity.

In the case of EBPVD coatings, the reduction in thermal conductivity comes mainly from the intracolumnar fine porosity, the intercolumnar porosity being much less effective as it is arranged perpendicular to the surface. Schematically, the columnar coating can be considered, in an electrical analogy, more as a set of parallel resistances than a series set which gives a closer image of the (microcracked) sprayed coating.

System	Thermal conductivity		Comment Reference
	300K	1300 K	
ZrO <sub>2</sub> -7%Y <sub>2</sub> O <sub>3</sub> EBPVD	1.7	2	[4]
ZrO <sub>2</sub> -7%Y <sub>2</sub> O <sub>3</sub> APS	0.9		[12]
ZrO <sub>2</sub> -7-9%Y <sub>2</sub> O <sub>3</sub> APS	0.9 to 1.1		[13] Various porosity levels
ZrO <sub>2</sub> -20%Y <sub>2</sub> O <sub>3</sub> APS	0.4	0.55	As sprayed, 7% porosity [14]
ZrO <sub>2</sub> -20%Y <sub>2</sub> O <sub>3</sub> APS	1.5	1.7	100h, 1480°C, 7% porosity [14]
ZrO <sub>2</sub> -6%Y <sub>2</sub> O <sub>3</sub> APS	1.1		[15]
ZrO <sub>2</sub> -8%Y <sub>2</sub> O <sub>3</sub> APS	1.		[15]
ZrO <sub>2</sub> -12%Y <sub>2</sub> O <sub>3</sub> APS	0.6		[15]
ZrO <sub>2</sub> -7%Y <sub>2</sub> O <sub>3</sub> EBPVD	1.3	1.3	[16]
ZrO <sub>2</sub> -7%Y <sub>2</sub> O <sub>3</sub> APS	0.8	0.8	[16]
ZrO <sub>2</sub> -7%Y <sub>2</sub> O <sub>3</sub> APS	0.8	0.8	[16]
ZrO <sub>2</sub> -8%Y <sub>2</sub> O <sub>3</sub> EBPVD as coated	1.5	1.3	[17]
ZrO <sub>2</sub> -8%Y <sub>2</sub> O <sub>3</sub> EBPVD	1.9	1.5	[17]
ZrO <sub>2</sub> -7%Y <sub>2</sub> O <sub>3</sub> bulk	2.9	2.7	[16]

**Table 2 :** Typical values of the thermal conductivity of zirconia-based coatings (EBPVD : electron beam physical vapour deposition, APS : air plasma spray) Composition percentages in wt%.



System	ZrO <sub>2</sub> -Y <sub>2</sub> O <sub>3</sub>	ZrO <sub>2</sub> -MgO
Phase	K, W/m.K	K, W/m.K
Cubic	2.3	1.8
Tetragonal	3.5	4.8
Monoclinic	4.2	5.2

**Table 3 :** Thermal conductivity for zirconia polymorphs calculated from experimental data on partially or fully stabilised zirconia bulk materials [18]. The different phases correspond to various stabiliser contents.

- Thermal conductivity of EBPVD coatings remains approximately constant as a function of temperature up to about 1100°C, as illustrated in figure 4. This is in contradiction with a  $T^{-1}$  dependence predicted by the theory (cf. below) for ceramic materials. At higher temperature, though, an evolution of the structure involving sintering or phase transformation may result in an increase of the thermal conductivity. The same trend is observed for plasma sprayed coatings, in general with a transition at lower temperature.

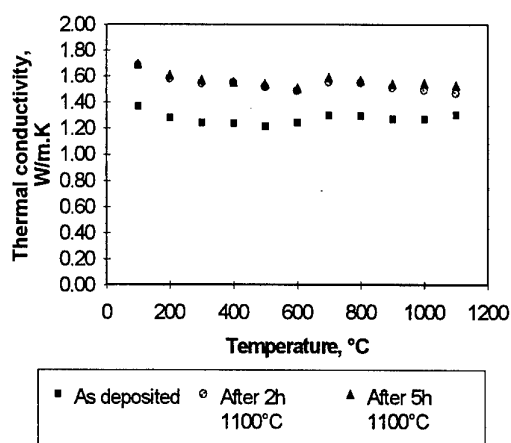


**Figure 4 :** Thermal conductivity, as a function of temperature, of an EBPVD ZrO<sub>2</sub>-7%Y<sub>2</sub>O<sub>3</sub> thermal barrier coating in as-deposited and heat treated conditions [17].

Given the fact that zirconia is translucent in the infrared, a radiation contribution to the thermal conductivity measured (which is actually an effective thermal conductivity) would result in a rise at high temperature. Such an effect has been reported by Youngblood et al. [19] in the case of single crystal ZrO<sub>2</sub>-20wt.%Y<sub>2</sub>O<sub>3</sub> (the thermal diffusivity increases rapidly as a function of  $T$  above 600°C). However, in the case of polycrystals, the same authors observe an opposite trend and it is likely that in the case of coatings (for which the dependence in temperature is much less important than the  $T^3$  predicted by theory), as well as in the polycrystals mentioned, the numerous interfaces present (gas/solid interfaces, grain boundaries) scatter the penetrating photons and thereby lower this radiation contribution to the heat flow. Yet, a thorough study would certainly be of

interest to correctly evaluate this effect with coatings, especially at very high temperature.

- A heat treatment affect the thermal conductivity of the coatings (increase). After a heat treatment, the thermal conductivity of TBCs increases, both for EBPVD [14] and plasma sprayed coatings [14, 20]. This effect is attributed to the evolution, through a sintering effect, of the porosity (cracks included) during heat treatment. For example, in plasma sprayed coatings, the poor contacts between lamellas in the as-sprayed coatings, with possible nanocrystalline (amorphous) zones corresponding to rapidly solidified regions, are likely to evolve towards equilibrium structures, assisted by atom diffusion processes at high temperature. One consequence is that thermal conductivity should be determined after a heat treatment conducting to a structure corresponding to the one that will be in service if representative values are to be used, in particular for the coated blade design. Another consequence, is that as surface temperatures are likely to increase (see preceding part) as a result of lowering the thermal conductivity, this effect has to be taken into account if the benefit of a low  $K$  thermal conductivity is to be retained in service.

- Values reported cover a surprisingly wide range and it is important to keep in mind that they may be difficult to compare, even for coatings having the same nominal composition and porosity, as experimental set ups can be different, as well as interpretation procedures from diffusivity determinations. Scattering inherent to the fact that thermal conductivity is indirectly measured (via thermal diffusivity, density, specific heat) and that diffusivity itself is a somewhat difficult property to determine. Even with high thermal conductivity material such as tungsten, data reported in the literature are spectacularly scattered, as illustrated by Taylor [21]. Moreover, thermal conductivity values most often are derived from thermal diffusivity measurements (laser flash in general) and this implies that the porosity is accurately known. It would be interesting for several laboratories to gather their efforts and, on identical specimens conduct a Round Robin test on TBCs, and compare with absolute, but more lengthy and costly methods.

#### 4. LOWERING THERMAL CONDUCTIVITY

##### 4.1. Intrinsic conductivity and chemistry:

It has been noticed in the preceding part that zirconia is already a low thermal conductivity material. One can wonder whether other materials would not present a lower thermal conductivity and could be envisaged as TBC. In fact, experimental thermal conductivity of pure zirconia, i.e. with no stabiliser, does not seem to have been reported. This is most certainly due to the difficulty of obtaining bulky specimens of pure zirconia, zirconia presenting three allotropic forms : monoclinic up to 1170°C, tetragonal in the range 1170°C- 2370°C and cubic up to the melting point

(2680°C), and the tetragonal to monoclinic transformation being accompanied by a large volume variation. The only available data seem to have been derived by Hasselman et al. [18] from experimental determination on various bulk zirconia-based system, knowing the relative proportion of the different crystallographic forms and assuming that the thermal conductivity of a mixture can be expressed simply as a function of the individual thermal conductivity. As reported in table 3, the monoclinic form would present a conductivity in the range 4 to 5 W/m.K.

Another approach, based on purely theoretical considerations, has been proposed by Klemens [22] for calculating an « intrinsic thermal conductivity » of cubic zirconia, supposed to contain no stabiliser (and therefore no associated vacancies). In a most general way, the thermal conductivity  $K$  can be expressed as :

$$K = (1/3) \int C'(\omega) \cdot v \cdot l(\omega) d\omega$$

where  $C'(\omega) d\omega$  is the contribution of the specific heat in the frequency range  $\omega$ ,  $\omega+d\omega$ ,  $v$  is the transverse phonon velocity and  $l(\omega)$  is the phonon mean free path.

In the high temperature limit and in the case of no defect present, the mean free path of phonons is limited by three phonon interactions, owing to the cubic anharmonicities of the lattice forces, and this expression leads to the following expression of the intrinsic thermal conductivity [23] :

$$K = (3/2)\gamma^2 \cdot (\mu v^2/\omega_D) T^{-1} \cdot N^{-2/3}$$

where  $\gamma$  is the Grüneisen constant,  $\mu$  is the shear modulus,  $v$  is the transverse sound velocity,  $\omega_D$  the Debye frequency,  $T$  the temperature and  $N$  the number of atoms per primitive unit cell. Recently, Klemens [22] applied such an approach to zirconia and derived for the intrinsic thermal conductivity of zirconia (i.e. that of an hypothetical « pure cubic zirconia ») :

$$K \text{ (W/m.K)} = 1700 / T \text{ (K)}$$

According to this expression, the intrinsic thermal conductivity of zirconia :

- would amount to 5.7 W/m.K at room temperature, a value surprisingly close to the values derived by [18] for pure monoclinic zirconia,
- decreases with a classical  $T^{-1}$  variation, classical for non-metallic materials [24], down to 1.3 W/m.K at 1300K. This last value appears excessively low, considering that dense PSZ polycrystals have a thermal conductivity higher than 2 W/m.K [18] and this represents a strict lower limit of pure zirconia.

Even if absolute values cannot be derived from such simplified theoretical approaches, it is possible to infer trends concerning the effect of different parameters on the thermal conductivity. This is

actually easier starting from an expression proposed by Slack [25] for non-metallic crystals and for temperatures higher than the Debye temperature  $\theta_D$  and derived from the same principles as the one followed by [22] :

$$K = B \cdot \langle M \rangle \cdot \delta \cdot \theta_D^3 / T \cdot N^{2/3} \cdot \gamma^2$$

where  $B$  is a constant,  $\langle M \rangle$  is the average atomic mass in the crystal,  $\delta^3$  is the average volume occupied by an atom and  $\gamma$  is the Grüneisen's constant ( $\gamma = \alpha/C_v \cdot \chi$  with  $\alpha$  the thermal expansion coefficient,  $\chi$  the compressibility and  $C_v$  the specific heat). Bearing in mind that  $\theta_D$  is inversely proportional to  $\langle M \rangle^{1/2}$ , it is clear that low conductivity crystals correspond to :

- high atomic mass and weak interatomic bonding (low  $\theta_D$ , which is a dominant term),
- complex crystal structure (large  $N$ ),
- high anharmonicity (large  $\gamma$ ).

According to these considerations, other ceramic materials could then be envisaged as a basis for thermal barrier coatings, keeping in mind that other criterias have to be fulfilled (thermal expansion coefficient, thermal stability, etc.). Among the parameters which can have a large influence on  $K$ ,  $\langle M \rangle$  is certainly a privileged one, and to a lesser extent  $N$ . The Grüneisen's constant ( $\gamma$ ) does not vary much from one material to another. An interesting candidate, for example, is  $\text{CeO}_2$  (the atomic mass of  $\text{CeO}_2$  is 40% higher than that of zirconia) a material which has been tested recently by Schulz et al. [26] and Maloney et al. [27]. However, if EBPVD  $\text{CeO}_2$ -9wt.% $\text{Y}_2\text{O}_3$  coatings present a low thermal conductivity (around half that of standard EBPVD  $\text{ZrO}_2$ -8wt.% $\text{Y}_2\text{O}_3$  coating [27]), they seem to exhibit a poor erosion resistance, a shortcoming which might be alleviated though, if a multilayer architecture is adopted, with a more erosion resistant external layer added on top of the coating.

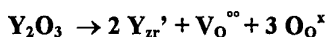
As far as compositions for the basis are concerned, other ways are explored. Observing that only the thermal conductivity at high temperature is relevant, and that for most ceramics, the thermal conductivity is a decreasing function of temperature (in principle  $T^{-1}$  law above), Padture and Klemens [28] are considering ceramic materials with complex lattice cells. An additional idea in this case is to try to develop an oxygen-impermeable dense ceramic layer to avoid or to minimise the oxidation of the bondcoat with formation of a thermally grown alumina at the ceramic/bondcoat interface (locus of the final failure in the most advanced systems). It is far from certain however, that such a ceramic material can be deposited as a reliable and dense coating and stay there in service. (thermomechanical cycles). Moreover, the garnet compositions these authors propose still have a relatively high thermal conductivity, even at 1000°C (typically above 2.5 W/m.K).

In conclusion, possibilities exist to change the chemistry of the basis material to decrease thermal conductivity. A balance has, of course, to be carefully evaluated between the expected gains and the consequences on other properties (density, thermal stability, thermomechanical resistance, erosion resistance, etc.) to evaluate the final interest of these potential new candidates.

#### 4.2. Defects :

An efficient way to decrease the thermal conductivity of an insulator is to introduce structural defects which constitute obstacles to the propagation of phonons. Several types of defect may be envisaged : vacancies, substitution ions, dislocations, interfaces (grain boundaries), etc.

The role of vacancies is particularly important in this respect for zirconia-based materials. In fact, as pure zirconia cannot be of practical use, due to its undesirable transformation at around 1100°C, it is stabilised (partially or completely) by adding heteroelements (most often Y, Mg, Ca) which stabilise the cubic (or the tetragonal phase). Thus the addition of 20wt%  $Y_2O_3$  fully stabilises the cubic form. Addition of 6 to 8wt. %  $Y_2O_3$  permits to obtain the so-called metastable  $t'$  phase (nontransformable up to around 1200°C). The incorporation of heteroelements is accompanied by the introduction of vacancies to maintain the electrical neutrality of the ionic lattice. Thus, introducing two yttrium ions is accompanied by the introduction of one vacancy according to the following reaction, using the nomenclature by Kröger and Vink :



where  $Y_{Zr}'$  is an yttrium ion on a zirconium site (single negative charge),  $V_O^{\bullet\bullet}$  is an oxygen vacancy twice positively charged and  $O_O^x$  is an oxygen ion on an oxygen site (no charge).

Effectively, incorporating heteroelements such as Ca, Mg or Y in zirconia lowers its thermal conductivity and a comparison of diffusivity measurements on zirconias with different stabilisers indicates that similar defect populations result in comparable thermal diffusivity [19]. It is to be noted though that this effect is observed only for stabiliser contents less than a critical value [29]. For high vacancy contents, they cannot be considered as independent defects and ordering may appear (as demonstrated by [30] in the case of cubic zirconia stabilised with yttria and magnesia). It is therefore likely that phonons interact less strongly with a population of ordered vacancies than with a population of randomly distributed defects.

Another source of efficient point defects acting as phonon scatter centres is substitution ions. This acts essentially through two factors :  $\Delta M / \langle M \rangle$ , the ratio of the mass difference between solute and solvent to the

average atomic mass, and relative difference in ionic size between solute and solvent. Diverse expressions have been proposed to describe their influence on the thermal conductivity [see for example 31, 32] and a critical study would be necessary to clarify the case of zirconia-based materials.

In the case of  $ZrO_2$ - $Y_2O_3$ , the replacement of zirconium ions ( $M = 91.22$ ,  $r = 0.080$  nm) by yttrium ions ( $M = 88.90$ ,  $r = 0.093$  nm) should have a minor effect, their atomic mass in particular being relatively close. However, a significant effect may be expected from other substituents, in particular heavy rare earth elements (at the expense though of the density, an important drawback for mobile components). Very few elements lighter than zirconium would satisfy these criteria, with the exception though of (expensive) scandium. As far as divalent ions are concerned, the choice is much more limited. Calcium or magnesium cannot be envisaged in high temperature applications due to structural stability problems.

Grain boundaries and interfaces can also scatter phonons and reduce the thermal conductivity. These processes are most effective at low temperature for ceramics in general [33], and only slightly at high temperature. It is to be noted that in TBCs, the grain size is much larger (typically 0.1 to 1  $\mu m$ ) than the mean free path calculated according to :

$$K \sim (1/3) C \cdot v \cdot l \sim 0.5 \text{ nm}$$

and it is doubtful that, in these conditions, conventional grain boundaries may have a significant effect.

As a conclusion, it can be said that the most efficient ways to decrease the thermal conductivity are to introduce point defects :

- vacancies associated with stabilising dopants. In zirconia-based coatings, up to 12 mol.%  $RO_{1.5}$  for a trivalent dopant R, corresponding to the stabilised cubic form, seem possible. However a fully stabilised plasma sprayed material may not present a satisfactory thermomechanical behaviour.
- for a maximum effect, the dopant should have a very different atomic mass than zirconium, provided that elastic factor does not counterbalance the mass one.

Finally, one could wonder what the minimal thermal conductivity would be with completely disordered materials, in other words what the minimal thermal conductivity for a refractory material could be. Two attempts have been proposed to calculate this minimal thermal conductivity.

Slack [25] derives the theoretical minimum conductivity assuming that the minimum mean free path for a phonon cannot be less than one phonon wavelength. For pure zirconia, the value calculated is 2.1 W/m.K. In a more recent approach, based on an adaptation of the Einstein model for highly disordered

materials, Cahill et al. [34], calculate a minimum thermal conductivity of 1.3 for dense zirconia-yttria systems. These values show that a gain may be obtained by increasing the atomic disorder, but this gain will remain limited if the base material (in occurrence zirconia) remains the same.

#### 4.3. Optimising coating architecture :

##### a. Pores, crack network.

The fact that the thermal conductivity of EBPVD, and in particular plasma sprayed coatings is much lower than for bulk materials of the same composition is explained by the presence of pores and microcracks originating from the coating deposition process, as described above. It is important to remark that up to now, only few studies have been devoted to optimise the porosity distribution and crack network with respect to thermal conductivity. In fact, most of the effort in this field has been devoted instead to the influence of these features on the thermomechanical resistance of the systems, with mainly empirical approaches.

As a first step, it is necessary to understand and describe the relationship between thermal conductivity and morphological features (pores, cracks,...). McPherson [35] was probably the first to propose a model for the microstructure of plasma sprayed coatings involving regions of good and poor contact between lamellae to explain the low thermal conductivity of coatings with respect to bulk materials. The regions of poor contact act as thermal resistances. Considering an electrical analogy, and assuming a very schematic geometry for the coating, the ratio of thermal conductivity of the coating ( $K_c$ ) to that of solid material ( $K_0$ ) can be expressed as :

$$K_c/K_0 = 2 \cdot f \cdot \delta / \pi \cdot a$$

where  $f$  is the fraction of « true contact »,  $\delta$  is the lamellae thickness and  $a$  is the radius of the individual contact areas. With a value of 0.2 for  $f$  and assimilating  $a$  with  $\delta/2$ , this relation gives  $K_c/K_0$  approximately 1/4, a right order of magnitude. It is to be noted however that the predictive capacity of such an approach is extremely limited due to the simplicity of the geometry assumed and the experimental difficulty to determine the parameters involved. This approach has been employed by Moreau et al. [36] to describe the thermal diffusivity of plasma-sprayed tungsten based coatings, the geometrical quantities being determined from image analysis.

As described in Dorvaux et al. [37], the most promising approach for developing a tool to describe the thermal conductivity in relation with microstructure seems to be via a finite difference calculation carried out on digitised images of real coatings. This type of approach presents the advantage of taking into account the complexity of the geometry involved (interconnected porosity for

example) while keeping the computations tractable on microcomputers.

This type of approach should offer guidelines for designers and coaters, provided the relationship between process parameters and coating morphology is known.

##### b. Thin films.

It has been reported by several authors [38-42] that ceramic thin films may exhibit a lower thermal conductivity than the corresponding bulk materials. Some examples are reported in table 4.

Material	Thermal conductivity of thin films (W/m.K)	Thermal conductivity of bulk material (W/m.K)	Ref.
PECVD SiO <sub>2</sub>	0.05 (100 nm) 0.4 (1.4 $\mu$ m)		[38]
Glassy SiO <sub>2</sub>	0.12	1.3 (amorphous)	[39]
TiO <sub>2</sub>	1.5-5 (depending on deposition method)	7	[40]
TiO <sub>2</sub>	0.6 (evaporated) 0.5 (sputtered)	5.5 - 7.6 (rutile)	[41]
ZrO <sub>2</sub> (evaporated, annealed 1h, 730°C)	0.8	2-5	[42]
AlN	16	70-220 (polycrystalline)	[42]

**Table 4 :** Examples of thermal conductivity of thin films compared with bulk values.

Although this effect is clear, the values reported have to be taken with care as measurements of thermal conductivity of submicronic films are very delicate and the error margins reported may be important.

Different explanations have been proposed for this effect. Most likely, this effect is due to a combination of grain-boundary scattering (the grains are particularly small) and of atomic disorder during growth of thin films. Non equilibrium structures may be obtained by PVD or PECVD, in particular for relatively low substrate temperatures (the diffusion of species on the surface of the growing coating, and bulk diffusion within the coating being too slow to reach an equilibrium state). In this respect, it is to be noted that the diffusion of cations within zirconia is quite slow. With the diffusion data ( $D = D_0 \cdot \exp(-Q/RT)$  with  $D_0 = 0.031 \text{ cm}^2/\text{s}$  and  $Q = 391 \text{ kJ/mol}$ ) published by [43], one can estimate that it takes about 8 years for a cation to travel 1  $\mu$ m at 1100°C by solid state diffusion .

To fully exploit this thin film effect, one could imagine thermal barrier coatings constituted of multiple nanolayers of different materials, such as zirconia and alumina as in [44], with the added advantage of incorporating boundary thermal resistances. The materials of each layer and the process parameters should have to be selected so that prolonged exposure at service temperature would not result in structural transformations towards equilibrium structures .

(crystallisation of amorphous material for example), activated by solid state diffusion and accompanied by an undesirable increase in thermal conductivity. In this respect, it is interesting to note that, as reported by Lee et al. [40], annealing a  $\text{HfO}_2$  thin film at  $900^\circ\text{C}$  enhances its thermal conductivity by only 20%. It is to be noted also that the fabrication of such coatings would certainly require serious modifications of techniques employed at present in production, or adapting new techniques to this application (sputtering with multiple targets for instance).

#### 4.4. Concluding remarks

Several possibilities exist, in principle to lower the thermal conductivity of TBCs : incorporation of point defects (vacancies, substitution cations), optimising the microcrack network and, to a lesser extent, porosity distribution, and introducing structural disorder via the deposition process. It must be kept in mind though that, as exposed in the introduction, TBCs must fulfil a set of requirements, and thermal conductivity is only one of them. In particular, it would be highly questionable to develop TBCs that could not be deposited with processes such as plasma spraying or EBPVD (or alternative processes currently under development). And the design of low thermal conductivity coatings must take into account the requirements associated with the processes. For instance, depositing materials having complex compositions, in particular with elements having widely differing vapour pressures, may prove to be too difficult to control in production with EBPVD processes ; similarly, a stack of numerous very thin layers presenting a highly disordered structure may be possible to fabricate by a PVD (or a CVD) process, but not by plasma spraying. Additional work is needed however to study the thermal (meta)stability of these defective structures.

## 5. CONCLUSION

Lowering the thermal conductivity of the ceramic coating of a TBC applied on airfoils in the hot stages of a turbine represents an important challenge for designing improved performance systems. This paper has modestly indicated and listed a few paths to tackle this topic, some of which have already been explored :

- changing the chemistry of the ceramic material in order to incorporate point defects (vacancies, substitution cations) by playing both on the base element (zirconia at the moment) and on the stabiliser, the main difficulty being to obtain sufficiently stable phase structures and staying within composition ranges such that the disorder is maximum as far as phonon scattering is concerned.
- optimising the coating morphological features (porosity, crack network) so that the heat transfer perpendicular to the external surface is minimised. This requires the development of modelling tools such as in the approach described in [36] and a good knowledge of the relationship between processes parameters and coating structures.

- designing new coating architectures (nanolayers).

It is felt that, up to now, several points have received little attention and would be worth exploring in more details :

- characterising the optical properties of the real coatings, in order to evaluate the possible influence of radiation to the heat transfer through the ceramic coating, and develop ways to decrease this contribution.
- assessing the thermal stability of the new systems ; with TBCs having low thermal conductivity, the surface temperatures of the ceramic coating are likely to rise, compared to the temperatures reached with present systems, and provoke a microstructural evolution of the outmost region of this ceramic layer, through sintering, or phase transformations, which in turn will increase the thermal conductivity.

Finally, it is important to insist on the fact that designing TBCs for engine airfoils requires a multidisciplinary approach taking into account various aspects : materials (ceramic behaviour, oxidation of bondcoat, thermal conductivity, etc.), processes (ceramic morphology), life prediction modelling, blade design, quality control, commercial (patents)... Thermal conductivity is only one aspect of the design and changing the ceramic composition to lower the intrinsic conductivity, for example, is likely to have important repercussions on the other properties. The design of the final coating may have to fully exploit the flexibility and capabilities offered by present coating processes, by developing multilayer coatings, each layer (corresponding to a temperature range and a particular environment in service) having a specific function .

**Acknowledgements :** Particularly fruitful discussions with Odile Lavigne, during the preparation of this paper, are gratefully acknowledged.

## References

1. Miller R.A., « Thermal barrier coatings - History and directions », in « Thermal Barrier Coating Workshop, NASA CP3312, 1995, pp 17-34.
2. Stecura S., « Optimisation of  $\text{NiCrAl/ZrO}_2\text{-Y}_2\text{O}_3$  Thermal barrier system, NASA TM 86905, 1985.
3. Bose S., DeMasi-Marcin J., « Thermal barrier coating experience in the gas turbine engine at Pratt & Whitney », in NASA CP 3312, 1995, pp 63-78.
4. Meier S.M., Nissley D.M., Sheffler K.D., Cruse T.A., « TBC life prediction model development - phase II » - PWA Final report, NASA CR 189111, 1991.
5. Miller R.A., Garlick R.G., Smialek J.L., « Phase stability in plasma-sprayed zirconia-yttria », Am. Ceram. Soc. Bull., 62, 1983, pp 1355-1358.
6. Lelait L. (1991) : Etude microstructurale fine de revêtements céramiques de type barrière thermique

- ; incidence sur la résistance thermomécanique de ces revêtements. Thèse de l'Université, de Paris Sud (Orsay).
7. Alpérine S., Lelait L., « Microstructural investigations of plasma-sprayed yttria partially stabilized zirconia TBC, in relation with thermomechanical resistance and high temperature oxidation mechanisms », in Proc. 37th ASME international Gas Turbine & Aeroengine Congress (Köln) 92-GT-317 (1992).
  8. Brindley W.J., « Properties of plasma sprayed bond coats », in TBC Workshop, March 27-29, 1995, NASA CP3312, pp 189-202.
  9. Pint B.A., Wright I.G., Lee Y.J., Zhang Y., Pruzner K., Alexander K.B., « Substrate and bond coat compositions : factors affecting alumina scale adhesion », to be published in Materials Science and Engineering.
  10. Schulz U., Fritscher K., Ratzer-Scheibe H.J., Kaysser W.A., Peters M., in Proc. 4th Internat. Symp. on High temp. Corrosion & Protection (Les Embiez, France, 20-24 May 1996), to be published.
  11. Siegel R., Spuckler C.M., « Analysis of thermal radiation effects on temperatures in turbine engine thermal barrier coatings », in Proc. TBC Workshop 97, Cincinnati, OH, 19-21 May 1997, pp 17-26.
  12. DeMasi J.T., Ortiz M., Sheffler K.D., « Thermal barrier coating life prediction model development. Phase 1 », NASA CR 182230, 1989.
  13. Miller R.A., Leissler G.W., Jobe J.M. (1993) : Characterization and durability testing of plasma-sprayed zirconia-yttria and hafnia-yttria thermal barrier coatings. Part I. NASA TP 3295.
  14. H.E. Eaton, J.R. Linsey, R.B. Dinwiddie (1994) : The effect of thermal aging on the thermal conductivity of plasma sprayed fully stabilized zirconia. Thermal Conductivity 22, 289-300. 14b. Dinwiddie R.B., Beecher S.C., Porter W.D., Nagaraj B.A., « The effect of thermal aging on the thermal conductivity of plasma-sprayed and EBPVD thermal barrier coatings », ASME 96-GT-982, pp 1-7.
  15. Morrell P., Taylor R., « Thermal diffusivity of thermal barrier coatings of  $ZrO_2$  stabilized with  $Y_2O_3$  », High Temp. High Press. 17, 1985, pp 79-88.
  16. Staniek G., Marci G., in Proc. Werkstoff-Kolloquium DLR, 10 dec. 1996, eds M. Peters et al., pp 50-53.
  17. Portal R., Etude de la conductivité thermique de couches minces de  $ZrO_2$ - $Y_2O_3$  déposées par EBPVD », Rapport de stage SNECMA, 1997.
  18. Hasselman D.P.H., Johnson L.F., Bentsen L.D., Syed R., Lee H.L., Swain M.V., « Thermal diffusivity and conductivity of dense polycrystalline  $ZrO_2$  ceramics : a survey », Am. Ceram. Soc. bull. 66(5), 1987, 799-806.
  19. Youngblood G.E., Rice R.W., Ingel R.P., « Thermal diffusivity of partially and fully stabilised (yttria) zirconia single crystals », J. Am. Ceram. Soc. 71(4), 1988, 255-260.
  20. Pawlowski L., Lombard D., Mahlia A., Martin C., Fauchais P., « Thermal diffusivity of arc plasma sprayed zirconia coatings », High Temp. High Press. 16, 1984, pp 347-359.
  21. Taylor R.E., « An overview of the measurements of thermophysical properties and some results of molten superalloys and semiconductors », in NASA CP10121, 1993, pp129-142.
  22. Klemens P.G., « Thermal conductivity of zirconia », in « Thermal conductivity 23 », Technomics, Lancaster PA (1996), pp 209-220.
  23. Klemens P.G., « Theory of the thermal conductivity of solids », in « Thermal conductivity », vol.1, Acad. Press, 1969, 1-68.
  24. Kittel C., « Introduction to solid state physics », 1986, Wiley.
  25. Slack G.A., « The thermal conductivity of nonmetallic crystals », Solid State Physics 34, 1979, pp 1 - 71.
  26. Schulz U., Fritscher, Peters M., « EBPVD  $Y_2O_3$ - and  $CeO_2/Y_2O_3$ -stabilized zirconia thermal barrier coatings - crystal habit and phase composition », Surf. Coat. Technol. 82, 1996, pp 259-269.
  27. Maloney M.J., Achter H.S., Barkalow B.K., « Development of low thermal conductivity thermal barrier coatings ». Communication presented in Thermal Barrier Coating Workshop (Cincinnati, may 1997).
  28. Padture N.P., Klemens P.G., « Low thermal conductivity in garnets », J. Am. Ceram. Soc. 80(4), 1997, pp 1018-1020.
  29. Fournier D. et al., to be published (1997).
  30. Z.R. Dai, Z.L. Wang, Y.R. Chen, H.Z. Wu, W.X. Lu (1996) : Local ordering of oxygen vacancies in cubic zirconia stabilized with yttria and magnesia. I. Electron diffuse scattering study. Phil. Mag. 73(2) 415-430. 29b. Z.R. Dai, Z.L. Wang, W.X. Lu (1996) : Local ordering of oxygen vacancies in cubic zirconia stabilized with yttria and magnesia. II. Determination of local ordering parameters of oxygen vacancies. Phil. Mag. 73(6) 1685-1698.
  31. Klemens P.G., « Theory of heat conduction in nonstoichiometric oxides and carbides », High Temp. High Press., 17, 1995, pp 41-45.
  32. Fukushima S., Ohmichi T., Handa M., « The effect of rare earths on thermal conductivity of uranium, plutonium and their mixed oxide fuels », J. Less-Common Metals, 121, 1986, pp 631-636.
  33. Klemens P.G., « Phonon scattering and thermal resistance due to grain boundaries », Internat. Journal of Thermophysics 15(6), 1994, pp1345-1351.
  34. Cahill D.G., Watson S.K., R.O. Pohl R.O., « Lower limit to the thermal conductivity of disordered crystals », Phys. Rev. B 46(10), 1992, pp 6131-6140.
  35. McPherson R., « A model for the thermal conductivity of plasma-sprayed ceramic coatings », Thin Solid Films, 112, 1984, 89-95.

36. Moreau C., Boire-lavigne S., Saint-Jacques R.G., « The relationship between the microstructure and thermal diffusivity of plasma-sprayed tungsten coatings », in Proc. 7<sup>th</sup> National Thermal Spray Conf., 20-24 June 1994, Boston, ASM, pp 621-626.
37. Dorvaux J.-M., Lavigne O., Poulain M., Renollet Y. Rio C., Mévrel R., « Modelling the thermal conductivity of TBCs », this conference, paper 12.
38. Brotzen F.R., Loos P.J., Brady D.P., « Thermal conductivity of thin SiO<sub>2</sub> films », Thin Solid Films 207, 1992, pp 197-201.
39. Henager C.H., W.T. Pawlewicz, « Thermal conductivities of thin sputtered optical films », Applied Optics 32(1), 1993, pp 91-101.
40. Lee S.-M., D.G. Cahill, T.H. Allen, « Thermal conductivity of sputtered oxide films », Phys. Rev. B 52(1), 1995, pp 253-257.
41. Lambropoulos J.C., M.R. Jolly, C.A. Amsden, S.E. Gilman, M.J. Sinicropi, D. Diakomihalis, S.D. Jacobs, « Thermal conductivity of dielectric thin films », J. Appl. Phys. 66(9), 1989, pp 4230-4242.
42. Shaw-Klein L.J., « Microstructural effect on thermal conductivity of thin films », Ph. D. thesis. University of Rochester (USA) 1992.
43. Oishi Y., Ken Ando, Sakka Y., « Lattice and grain-boundary diffusion coefficients of cations in stabilized zirconias », Adv. Ceramics, 7, 1984, pp 208-219.
44. Mullen R., Allen W.P., Gell M., Barkalow R.H., Noetzel A.A., Appleby J.W., Khan A.A., « Multiple nanolayer coating system » PCT WO 96/11288, 1996.

# RECENT DEVELOPMENTS IN PLASMA SPRAYED THERMAL BARRIER COATINGS

Drs. P. FAUCHAIS, A. VARDELLE and M. VARDELLE

L.M.C.T.S. - Equipe Plasma, Laser, Matériaux  
Université de Limoges - UPRES A 6015 - Faculté des Sciences  
123, Avenue Albert Thomas - 87060 LIMOGES Cedex - FRANCE

## Abstract

This paper presents a review of our present knowledge in the formation of plasma sprayed Thermal Barrier Coatings (TBCs). The following points are examined for TBCs made of zirconia partially stabilized with 8 wt % of yttria :

- characteristic times for particle flattening, splat cooling and solidification with the corresponding cooling rates and microstructure.
- critical preheating temperature of substrates or previously deposited layers to achieve a good contact with splats. An explanation of the effect of this critical temperature is proposed.
- times between two impact events at the same location and two successive passes. The consequences on the mean temperature within coating in conjunction are underlined for various substrate and coating cooling devices.
- the effect of substrate critical temperature and substrate oxidation stage on coating adhesion/cohesion.
- splat layering and temperature conditions at which a columnar structure can grow through the whole coating. The consequences on stresses development during and after spraying and coating Young's modulus, are discussed.

- at last, the parameters which have to be controlled during spraying to achieve a much better reproducibility of coatings. A special emphasize is given to torch voltage fluctuations related to electrodes erosion, powder injection conditions and finally substrate and coating temperature before (preheating) during and after (cooling) spraying.

## 1. INTRODUCTION

Thermal barrier coatings (TBCs) are now included as part of the initial engine of turbine-powered aircrafts. They make them possible to achieve an average reduction in the metal temperature for turbine blades of 50 to 80°C and reduction of blade hot-spot temperature of up to 139°C. The latter are only a fraction of the capability of TBCs, estimated at 170°C or more [1]. TBCs have also been used in land-based turbine combustors for 10 years, and in diesel engines where graded coatings are highly effective. In all cases, the purpose is to enhance component durability while running the engine operating temperature. In this paper TBCs for diesel engines will not be considered. The difference between nominal requirements for aircraft and power generation turbine applications are summarized in table 1 [2].

Requirement	Commercial aircraft	Power generation
Number of cycles	8000	2,400
Total hours	8000	24,000
Hours at peak conditions	300	24,000
Peak surface temperature	>1204°C (2200°F)	<1204°C (2200°F)
Peak bond coat temperature	1093°C (2000°F)	954°C (1750°F)
Relative size	1x	5x

Table 1 : Comparison of nominal TBC requirements for aircraft and power generation turbine applications [2].



The main criteria for power generation use of TBCs are the time and temperature effects on bond coat and substrate, coating densification and changes in thermal or mechanical properties of the coatings.

As underlined in reference [3] for advanced land-based gas turbines, the goals that are to be achieved together with issues and challenges are summarized in fig. 1.

For a long period (more than 20 years) TBCs were essentially plasma-sprayed in air (APS) [4-7] or controlled atmosphere [8]. Since a few years Physical Vapor Deposition assisted by Electron Beam (EB-PVD) TBCs, have been available on the market [9,10] especially for aircraft engines. The advantages claimed relatively to APS TBCs are the following :

- a columnar structure under certain conditions of evaporation,
- a fast tapering at the opening of cooling holes while plasma sprayed coatings have a greater tendency to built up coating at that location,
- possibility to achieve much more smoother surfaces,
- high adhesion/cohesion values ( $\sim 70$  MPa),
- low residual stress at room temperature ( $\sim 70$  MPa),
- reduction of temperature of 38-66°C in stage of High Pressure Turbine Blade,
- high number of cycles in engine testing : 180 for blades and 20000 for engine nozzle.

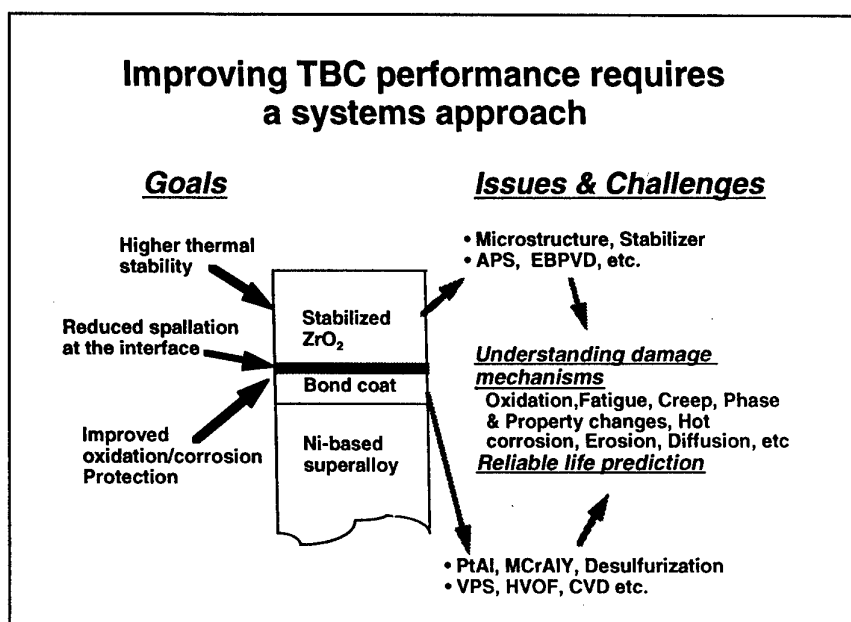


Fig. 1 : Approach for improving TBC performances [3].

However, it does not mean necessarily that APS TBCs have no future. For example they have a significant advantage in being able to accommodate the large size components found in modern large power generation machines. Each component application of a TBC requires careful study and review to determine whether APS or EB-PVD has to be used [3]. Moreover, a better understanding of the APS coating formation could result in coatings with similar properties as those obtained by EB-PVD. The aim of this paper is first to review what is our knowledge in plasma sprayed coating formation. We will first discuss the splat formation, their layering and the resulting coating adhesion/cohesion as well as residual stresses. We will second underline which parameters have to be controlled during

spraying to achieve a much better reproducibility of the plasma spray process.

## 2. PLASMA SPRAYED COATING FORMATION

All the results presented in this paper concerned fused and crushed powders with 8 wt%  $Y_2O_3$ . They are called in the following YSZ.

### 2.1. Characteristic times and cooling rates

Table 2 summarizes characteristic time values for particles in the size range 22-70  $\mu m$  sprayed with d.c. torches and impacting at velocities between 80 and 260 m/s on smooth surfaces ( $R_a < 0.1 \mu m$ ) [11-14].

Flattening time $t_f$ ( $\mu$ s)	Starting of nucleation $t_n$ ( $\mu$ s)	Solidification time $t_s$ ( $\mu$ s)	Time between two impact events at the same location $t_i$ ( $\mu$ s)	Time between two successive passes $t_r$ ( $\mu$ s)
1-3	0.3-2.5	< 10	500-5000	$10^6$ - $10^7$

Table 2 : Characteristic times in d.c. plasma spraying.

These various times show clearly that the impacting particles and resulting splats will experience very different temperature histories :

#### 2.1.1. Single splat

Many theoretical studies have been devoted to the impact and flattening of the particles on the substrate (see their description in [14]). All of them, except one, concern impacts on smooth surfaces.

##### a) Smooth surfaces

Phenomena at impact can be characterized by the particle Weber's number ( $We = \rho_p \cdot d \cdot v_p^2 / \sigma_p$  where  $\rho_p$ ,  $v_p$ ,  $d$  are the particle specific mass, impact velocity and diameter respectively and  $\sigma_p$  its surface tension), and Reynolds' number ( $Re = \rho_p \cdot v_p \cdot d / \mu_p$  where  $\mu_p$  is the particle viscosity at impact). When flattening starts,  $We$  can be rather high (up to 10000) and the flattening process is independent of particle surface tension which has importance only when flattening is almost completed. These theories end up in relationships giving the particle flattening degree  $\xi$  and flattening time  $t_f$  as functions of the Reynolds number.  $\xi$  is defined as the ratio of the splat diameter  $D$  (assumed to have a disk shape) to that of the impacting particle  $d$ .

$$\xi = \kappa \cdot Re^\alpha \quad (1)$$

$$t_f = 2 \cdot d_p \cdot Re^{0.2} / (3 \cdot v_p) \quad (2)$$

$\kappa$  varies between 0.8 and 1.2941 while  $\alpha$  is either 0.2 or 0.125 or 0.167.

Typical values for a zirconia particle 30- $\mu$ m in diameter, impacting at  $v_p = 200$  m/s at a temperature  $T_p = T_m \times 1.3$ , where  $T_m$  is zirconia melting temperature, are for example  $\xi = 4.8$  which corresponds to a splat thickness  $e_s \sim 1.1 \mu$ m and  $t_f \sim 1 \mu$ s. If the impacting particle velocity increases,  $\xi$  increases while  $t_f$  and  $e_s$  decrease and it is the reverse if  $v_p$  decreases. The most recent theories have shown that solidification can start before flattening is completed [15]. Solidification depends mainly on [14,15] the wettability of the molten material, the thermal contact resistance  $R_{th}$  with the substrate, the splat thickness  $e_s$  and the thermal properties of the substrate material. The interfacial contact resistance characterizes the real contact with the substrate or the previously deposited layers. It can vary between  $10^{-6}$  and  $10^{-8}$  m<sup>2</sup>.K/W, the last value corresponding to a perfect contact. Fig. 2 represents the time-temperature evolution of a zirconia splat 1- $\mu$ m thick for two values of  $R_{th}$ . For values below  $10^{-7}$  m<sup>2</sup>.K/W (see fig. 2.a), the temperature  $T_b$  of the lower surface of the splat decreases very fast while the substrate surface temperature  $T_i$  increases very fast. Over  $R_{th} = 10^{-7}$  m<sup>2</sup>.K/W, there is nearly no temperature gradient within the splat (see fig. 2.b) while  $T_i$  is much lower.

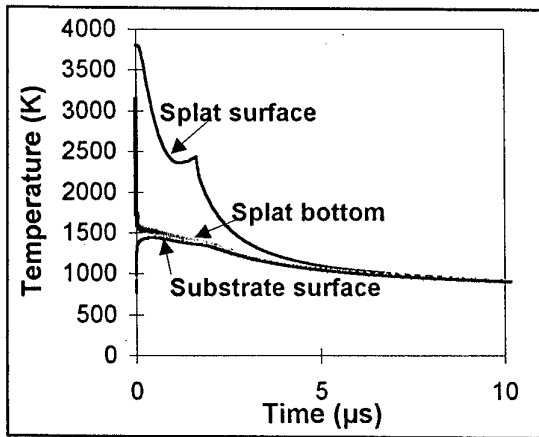
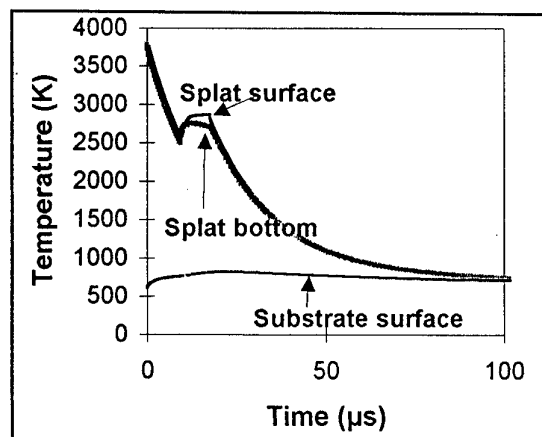
a)  $R_{th} = 10^{-8}$  K.m<sup>2</sup>/Wb)  $R_{th} = 5.10^{-6}$  K.m<sup>2</sup>/W

Fig. 2 : Splat surface and bottom as well as interface temperature evolutions for two values of  $R_{th}$  (1- $\mu$ m thick Zirconia splat on a smooth stainless steel substrate at 600 K).

In both cases the increase in splat surface temperature is due to the recalescence phenomenon. However, these results, which have been obtained by assuming a constant nucleation temperature of 2500 K and an instantaneous full contact of the whole splat, can be deeply modified if nucleation process is included in the model and the evolution of the contact surface during flattening is accounted for.

The corresponding cooling rates during the first  $\mu\text{s}$  are between  $10^6$  and  $10^9$  K/s. For  $R_{th} < 10^{-7}$   $\text{m}^2\text{K/W}$  the heat transfer rate from droplet to substrate is very high and the liquid can be cooled well below the melting point in one microsecond or less. It is therefore quite plausible that in this very short time interval, the liquid does become undercooled and nucleation of crystals is delayed until after the droplet has almost completely spread out.

As shown in fig. 2, if during flattening and just after, the cooling rate is very high, it slows down drastically for times longer than 10 to 50  $\mu\text{s}$ . The splat temperature tends then slowly to the mean substrate and previously deposited layer temperature  $T_d$  imposed by torch heating, previously deposited pass thickness and cooling devices.

#### b) Rough surfaces

Only one model accounting for the substrate roughness has been proposed [16] up to now. The roughness was schemed by cones. This model gives for the flattening degree a relationship similar to (1) but multiplied by a function depending on the cone height and the valley volume. It results, of course, in thicker splats which shape is not that of a disk. Assuming the same value of  $R_{th}$  than for smooth substrates, the cooling rate will be lower due to the higher value of  $e_s$ .

#### 2.1.2. Layering splats

As powder loading is rather low in plasma spraying [14], statistically a new particle impacts on a previously deposited splat in times  $t_i$  of the order of 500-5000  $\mu\text{s}$  i.e. on already solidified splats. The surface temperature of the first splat due to the impact of successive layering splats will depend strongly on  $R_{th}$  and the mean temperature of substrate and coating  $T_d$ . This leads, as schemed in fig. 3, in impulse reheatings with the first splat surface peak temperature decreasing progressively due to the insulation by the successively deposited splats.

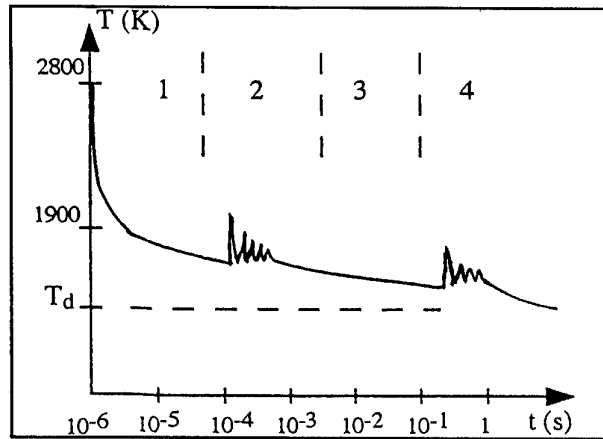


Fig. 3 : Impulse reheating of the first splat surface by the layering splats.

The temperature  $T_d$  is linked to :

- substrate preheating temperature  $T_{ph}$  ;
- substrate dimension, thickness and thermal properties (controlling the heat sink) ;
- relative movement torch to substrate. This movement determines the pass thickness  $e_p$  (the heat content of layered splats increases with  $e_p$  which can vary from a few layered splats to a few hundreds) and the time  $t_i$  for the torch to come back at the same location (heating by plasma plume flux) ;
- cooling devices used : air jets blowing at the substrate and coating surface, and air barrier blowing orthogonally to the plasma jet to reduce in a ratio up to six the plasma plume heat flux [18], but also cooling down the droplets traversing it [19].

#### 2.2. Splat formation

Experimental set-ups were developed to determine the velocity  $v_p$ , surface temperature  $T_p$  and diameter  $d$  of a single particle prior to its impact and then its temperature and surface evolutions during flattening as well as the surface temperature evolution of the resulting splat during its cooling. The interested reader can find a presentation of these set-ups in [12-14].

Other techniques allow the collection of a few thousands of splats all over the spray cone on a controlled temperature substrate to determine their diameter and shape factor distributions [13].

At last, a detailed observation of the structure of the splats collected on smooth surfaces can be obtained by Atomic Force Microscopy making it possible to see the details of the columnar growth [20].

The main results are as follows :

### 2.2.1. On smooth surfaces

Experimental evidences [21] have shown that there is a substrate critical temperature  $T_c$ , below which the splats are extensively fingered while over which, they have almost a perfect disk shape as shown in fig. 4. For  $ZrO_2$  it was found that this transition temperature is between 450 and 550 K.

This phenomenon seems to be almost independent of the particle impact velocity. For example Table 3 presents results obtained with  $-45 \pm 22 \mu m$  particles which velocities range between 200 m/s along the jet axis to 110 m/s at the limit of the spray cone. The data of this table correspond to about 3000 splats processed by image analysis. On the

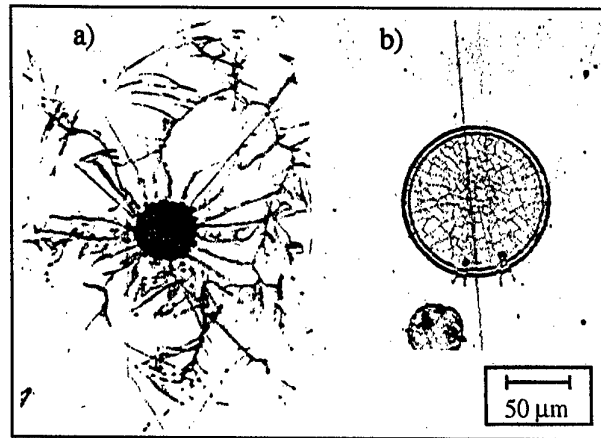


Fig. 4 : Micrographs of zirconia particles sprayed, on (a) 350 K substrate, (b) 550 K substrate (impact velocity  $\sim 200$  m/s).

Substrate temperature $T_{ph}$ (K)	350		573	
Analyzed area	center	periphery	center	periphery
D splat mean diameter ( $\mu m$ )	$67 \pm 24$	$59 \pm 20$	$107 \pm 44$	$101 \pm 36$
SF shape factor ( $\mu m$ )	$0.68 \pm 0.20$	$0.67 \pm 0.21$	$0.95 \pm 0.13$	$0.94 \pm 0.12$
CR cooling rates (K/ $\mu s$ )	100-200	--	500-800	--

Table 3 : Splat mean diameter  $D$ , shape factor  $SF$  and cooling rate  $CR$  with substrate temperature and location within the spray cone.

hot substrate, the mean Shape Factor  $SF$  is close to one, both in the spray cone central part and its periphery even if the mean splat diameter  $D$  is slightly smaller in the spray cone periphery, as it could be expected.  $SF$  is defined as  $4 \pi S/P^2$  where  $P$  is the splat perimeter and  $S$  its surface area ( $SF = 1$  for a disk). For cold substrates  $D$  is by far smaller due to material splashing and  $SF \sim 0.67$  against 0.94. The dispersion is also higher. However, if the substrate is oxidized (due to a too long preheating) splats are again extensively fingered. The oxidation stage depends strongly on the preheating time with the plasma jet and the substrate material [20,22]. Splat cooling rates, measured by fast pyrometry [12-14], are 3-6 times higher with the hot substrate. For the disk shape splats obtained at 573 K, the splat cooling theoretical curve [23] of a 1-D model has been adjusted to the experimental curve by varying the thermal contact resistance. Values of  $R_{th} \sim 10^{-7} - 10^{-8} m^2 K/W$  were obtained corresponding to an almost perfect contact as confirmed by the crack network due to quenching stress relaxation observed in fig. 4.b. On cold substrates, the contact resistance  $R_{th}$  calculated assuming that the splats have a disk-shape, were found to be of the order of  $10^{-6} m^2 K/W$ . This poor contact resistance is confirmed by the pulling off of splats by the tip of a perthometer. This does not occur when splats are collected on hot substrates.

The latter exhibit on their whole surface, a homogeneous microstructure with a columnar growth perpendicular to the surface [20] (see fig. 5.a) except in the splat rim (see fig. 5.b) where the columnar structure is parallel to the substrate. Indeed, due to splat curling [24] the rim is not in contact with the hot substrate and cooling occurs through the already solidified columnar structure of the central part of the splat resulting in a columnar structure parallel to the substrate. As the cooling is much slower, the size of the columns is bigger. On cold substrates ( $T_{ph} < T_c$ ) only a very few AFM measurements could be done, the splats being pulled off very easily. In this case, the central part of the splat consists of a few islands where the contact is good (columnar structure), however with bigger columns than on hot substrates, surrounded by rims where the crystal growth is parallel to the substrate [20]. The "fingers" exhibit the same morphology as that of the rims. As a general rule, the size of the columns depends very strongly on the cooling rate as illustrated in Table 4 for two different substrate materials and spraying equipments. With the RF plasma torch, the particle impact velocities are lower than 80 m/s resulting in splat thicknesses  $e_s$  in the range  $2-2.5 \mu m$  against  $0.9-1.2 \mu m$  with d.c. plasma torches. These thicker splats cool down slower (in a ratio 6-10) than the thinner splats.

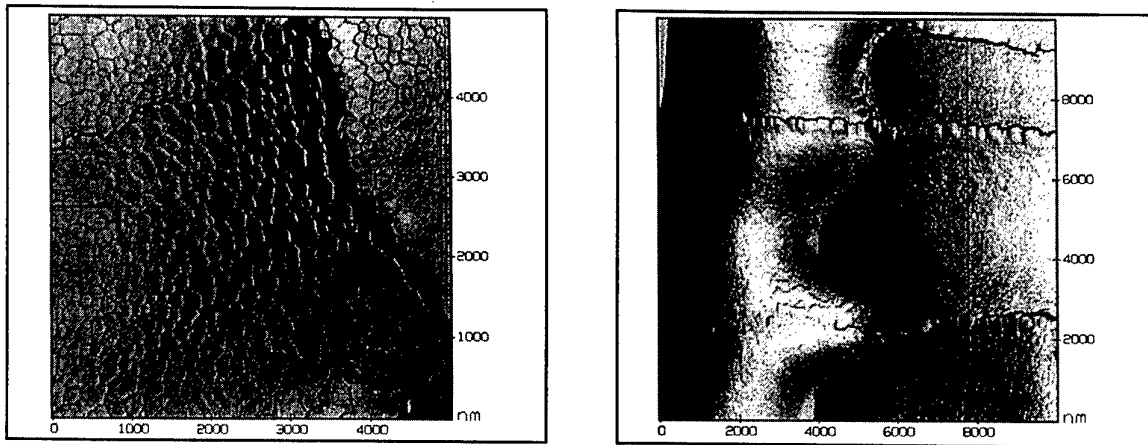


Fig. 5 : AFM view of an YSZ plasma sprayed with a d.c. torch ( $v_p = 210$  m/s,  $T_p = 3400$  K)  
(a) splat central part (note the cracks) (b) splat rim.

Plasma torch	d.c. torch with a 7 mm i.d. nozzle		r.f. torch with a 50 mm i.d.	
substrate material	stainless steel 304	YSZ	stainless steel 304L	YSZ
splat thickness $e_s$ ( $\mu\text{m}$ )	0.95		2.2	
CR cooling rate ( $\text{K}/\mu\text{s}$ )	645	115	105	16
$t_s$ solidification time ( $\mu\text{s}$ )	0.74	1.23	4.54	7.6
column width (nm)	125	250	320	>400

Table 4 : YSZ column width with respect to cooling conditions [19].

To explain the occurrence of the critical temperature, Vardelle et al. [11,14] have proposed to compare the time  $t_{ft}$  at which flattening is almost completed ( $t_{ft} \sim 0.3-0.4 \times t_f$ ) to the time  $t_n$  corresponding to the onset of nucleation (see fig. 6). If  $t_n > t_{ft}$ , nucleation starts only when flattening is almost completed and it covers the whole splat surface allowing it to keep its disk shape. This is confirmed by the observation of splats collected on tilted substrates : these splats exhibit an elliptical shape with a larger thickness in the direction of the inclined substrate. If  $t_n < t_{ft}$  nucleation starts at a few points which impede the liquid flow, resulting in splashing, which seems to be confirmed by the AFM splat study.  $t_n$  depends strongly on the maximum value of the interface temperature  $T_i$  which, in turn, is linked to the preheating temperature  $T_{ph}$ .

### 2.2.2. On rough surfaces

Fig. 7 shows SEM pictures (back scattered electrons) of zirconia splats collected on rough 304L substrate ( $R_a \sim 6 \mu\text{m}$ ) [13]. It can be seen that, compared to smooth substrates, the particles are by far more extensively fingered but here again the contact is much better with the hot substrate as shown by the microcrack network exhibited by splat surface. The splats collected on rough substrates are thicker. This

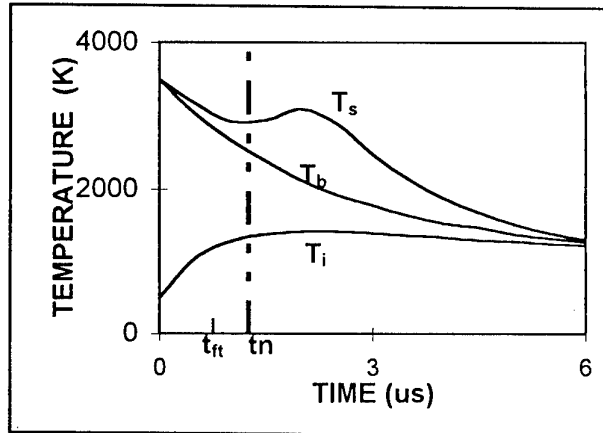


Fig. 6 : Characteristic times and temperatures  $T_s$ ,  $T_b$  and  $T_i$  at splat surface, splat bottom and interface respectively ;  $T_{ph}$  is the substrate preheating temperature.

results in a drop of the splat cooling rate. On the 304L stainless steel substrates CR was found to be about  $650 \text{ K}/\mu\text{s}$  for smooth hot substrates and  $120 \text{ K}/\mu\text{s}$  for cold substrates. With the rough substrates, the drop in CR is lower.

## 2.3. Coating formation

### 2.3.1. Thin passes

Coatings were sprayed [13,25] on a rotating substrate holder 110 mm in diameter in front of which

the torch was moved parallel to the holder axis. The substrates were either buttons ( $\varnothing = 25$  mm,  $e = 6$  mm) or beams ( $2 \times 100 \times 15$  mm<sup>3</sup>) made of cast iron FT25 (only bottom type), ordinary steel XC38, stainless steel 304L and Inconel 100.

The adhesion/cohesion (A/C) of coatings is closely linked to residual stresses [26,27]. Beside those resulting from grit blasting which play a role in A/C [28], the two most important are the quenching stress  $\sigma_q$  which is rather low for YSZ coatings [29] ( $\sigma_q < 20$  MPa) and the expansion mismatch stress  $\sigma_{\Delta\alpha}$  which depends strongly on the temperature difference between the constant spraying temperature  $T_d$  and room temperature. In order to reduce as much as possible residual stresses, YSZ coating thickness was limited to 300  $\mu$ m and the pass thickness was 3  $\mu$ m thanks to a fast relative movement torch/ substrate. In such conditions as measured  $\sigma_q \sim 8$  MPa [25] and  $\sigma_{\Delta\alpha} \sim -15$  MPa at 300°C and -36 MPa at 500°C on 304L stainless steel. Thus the stress difference at the interface substrate coating is rather low and the coating adhesion/cohesion A/C, measured using the test DIN 50150 is mainly pure A/C. Table 5 presents typical A/C values obtained on 304L stainless steel, each result corresponding to the mean value of 5 measurements. It can be seen, that A/C values increase with substrate temperature but decrease with preheating time. This result is in good agreement with the previous observations on splat formation.

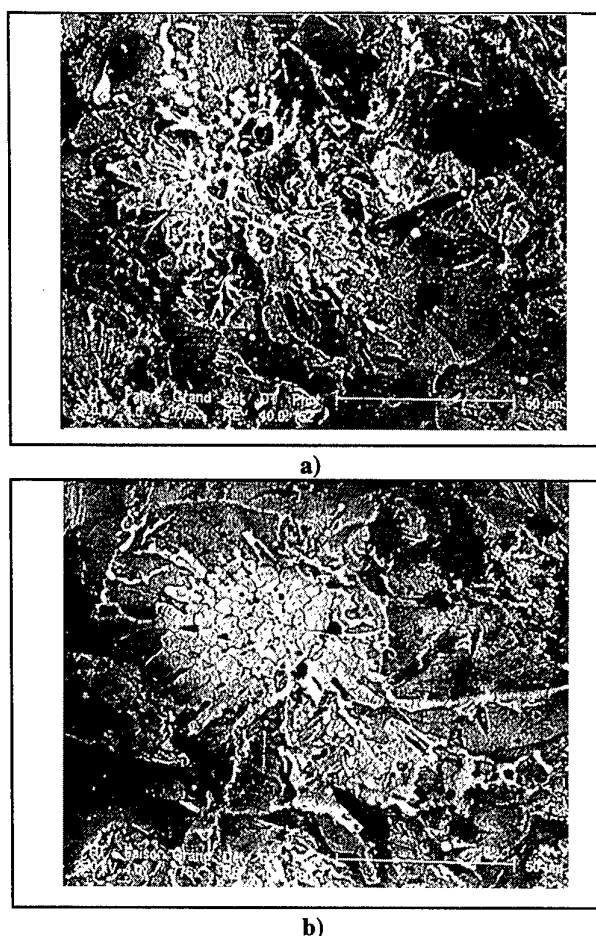


Fig. 7 : Splats collected on rough substrates ( $R_a \sim 5-6$   $\mu$ m). a)  $T_{sub} = 350$  K, b)  $T_{sub} = 573$  K.

Preheating temperature (K)	573 K				773 K			
Preheating time (s)	0	60	300	900	0	120	300	900
Coating adhesion/cohesion A/C (MPa)	20 $\pm$ 2	50 $\pm$ 2	40 $\pm$ 2	31 $\pm$ 4	20 $\pm$ 2	64 $\pm$ 5	49 $\pm$ 2	45 $\pm$ 2

Table 5 : Coating adhesion/cohesion (A/C) values on 304 stainless steel substrates preheated by the plasma jet at two different temperatures for different times.

The decreasing in A/C values when the preheating time increases is explained by the time-growth and time-composition change of the oxide layer at the 304L surface, as shown by recent studies [22] : the plasma plume contains atomic oxygen and oxidation is somewhat different from that obtained by preheating substrates in a furnace. Similar results are obtained on FT25, XC38 and In 100 substrates for different temperatures and preheating times. The coating Young's moduli obtained by comparing the deflections of XC38 beams measured during spraying [25,28] with values calculated using a 1-D code based on the equations proposed by Tsui and Clyne [30], are in the range 20-30 GPa. However, the precision is poor ( $\pm 30\%$ ) with such low values.

### 2.3.2. Thick passes

In order to limit oxidation problems 300  $\mu$ m thick coatings sprayed on In 100 substrates were preheated to different temperatures and the pass thickness was varied from 25 to 300  $\mu$ m/pass. With 25  $\mu$ m passes for preheating temperature  $T_{ph}$  over 873 K,  $\sigma_q$  is more than doubled : 20 MPa against 8 MPa. For  $T_p \sim 973$  K, the fractured cross section of coatings exhibits a columnar structure growing through the whole coating (see fig. 8.a). The Vickers hardness with a 5N load is increased to  $1200 \pm 80$  MPa against  $800 \pm 70$  MPa with the 3- $\mu$ m thick pass (with  $T_p = 773$  K). Unfortunately when spraying on In 100 substrates preheated at 973 K, the coating detached upon cooling probably due to oxidation problems.



a)



b)

Fig. 8 : Fractured cross section of an YSZ coating :

a) at  $x = 0.4$  mm from substrate and sprayed on an already deposited YSZ coating ( $300\text{ }\mu\text{m}$  on In 100) preheated at  $973\text{ K}$   $e_p = 25\text{ }\mu\text{m}$ , b) sprayed on In 100 preheated at  $973\text{ K}$ ,  $x = 0.005\text{ mm}$ .

When spraying on In 100 at  $873\text{ K}$  with  $e_p = 80\text{ }\mu\text{m}$ , the first  $25\text{--}30\text{ }\mu\text{m}$  exhibit no columnar growth except for 2-3 layered splats and afterwards a columnar growth through the whole coating. When measuring continuously the beam deflection, a slope change occurs after the time corresponding to the first  $25\text{--}30\text{ }\mu\text{m}$  corresponding successively to  $\sigma_q = 8$  and  $22\text{ MPa}$ . The Young's modulus of this last part is  $100\text{--}120\text{ GPa}$  against  $50\text{ GPa}$  for the first  $25\text{--}30\text{ }\mu\text{m}$ . During A/C tests, debonding takes place in the first  $25\text{ }\mu\text{m}$  and the maximum A/C value reaches  $40\text{ MPa}$  which could be explained by the tougher layer after  $25\text{ }\mu\text{m}$  [27]. However, it must be underlined that with hot surfaces the sticking of the small ( $< 1\text{ }\mu\text{m}$ ) droplets resulting from YSZ particles evaporation and recondensation [31] has to be carefully avoided between successive passes because it reduces the A/C values by a factor at least of 2. The columnar growth through layered splats and successive passes can be explained on the basis of the temperature diagram shown in Fig. 2. Calculations with thick passes ( $e_p > 25\text{ }\mu\text{m}$ ) and  $T_p \sim 973\text{ K}$  show that nucleation of the impacting splat is delayed almost to the end of particle flattening ( $t_n \sim t_f$ ) which could promote the columnar growth with the columns of the underlying solidified splat as nucleation sites.

### 3. REPRODUCIBILITY OF THE PLASMA SPRAY PROCESS

In industrial conditions the reproducibility of coatings is by far the most important problem and many parameters have to be controlled either before spraying or on-line during spraying, and assessed by coating analysis.

#### 3.1. Powders

##### 3.1.1. Characteristics

The main parameters are the YSZ particles chemistry and distribution of stabilizer within each particle, shape, density and size distribution. The first three parameters are closely linked to powder manufacturing process [32] and the last one to sieving. The density of the starting particles is one of the key parameter, the best results for coating thermomechanical properties being obtained with dense particles such as fused and crushed ones [33] or agglomerated and densified ones [34]. The stabilizer distribution within each particle has also a great influence which is enhanced by the faster evaporation of the  $\text{Y}_2\text{O}_3$  stabilizer compared to  $\text{ZrO}_2$ . That is probably why particles made by sol-gel process, and then plasma densified, allow to increase the thermal shock resistance of the corresponding coatings by about  $100^\circ\text{C}$  compared to fused and crushed particles [35]. In the sol-gel technique  $\text{Y}_2\text{O}_3$  grains, in the  $0.1\text{ }\mu\text{m}$  size range, are uniformly distributed within each particle. Moreover, it has been shown that after plasma treatment, fused and crushed powders present a better homogeneity than agglomerated ones, sintered or not [36].

Another important questions is which particle size range has to be used : rather narrow such as  $- 45 + 22\text{ }\mu\text{m}$  or large  $- 106 + 10\text{ }\mu\text{m}$  ? and which lower limit  $22, 10$  or  $5\text{ }\mu\text{m}$  ? The answers depend on the desired properties. As a general rule, YSZ particles which diameter is over  $50\text{--}60\text{ }\mu\text{m}$  are not fully molten with d.c. plasma torches because of the heat propagation phenomenon in the particles [37]. Thus, powders with a large particle size range may result in coatings with higher porosity but lower mechanical

resistance. For the lower limit of the particle distribution the injection problems are critical. Most of small particles, especially those below 10  $\mu\text{m}$ , hardly penetrate within the plasma jet, travel in its periphery and are sucked down farther downstream resulting in defects in the coating when they stick to it, which is especially the case when the coating surface is kept over 773 K during spraying.

### 3.1.2. Powder injection in the plasma-jet

Internal injection allows a better penetration of the particles within the plasma jet compared to external injection [37]. However with small particles, requesting a higher carrier gas flow rate, the plasma flow perturbation is more important with internal injection [38]. The position of the injection port and its distance  $z$  from the torch axis is very critical. A variation of  $z$  of a few tenths of mm modifies deeply the particles mean trajectory. Thus, any change in the injector port location and its wear have to be checked very carefully and regularly. It is also the case of the internal wear of the injector, a rough internal surface modifying deeply the powder distribution at the injector exit compared to that obtained with a new injector with a smooth internal surface. More precisely (see section 3.2.2) the trajectory distribution of particles within the plasma jet has to be followed continuously because it controls acceleration and heating of the particles.

## 3.2. Plasma spray process

### 3.2.1. Wear of the electrodes

The arc behavior at the anode and cathode is quite different. Thoriated tungsten cathode tip wear is rather fast ( $\sim 1$  h). It is due to the fast diffusion of thoria which increases drastically the cathode tip temperature (by about 1000 K) and induces a neck erosion below the tip which is blown up after a while [39,40]. The transition of a sharp cathode tip to a rounded one, which extremity becomes slowly and progressively wider, induces, within the first working hour, a reduction of the flow velocity of about 20% and a reduction of the arc voltage of 4 to 6% [41]. The widening of the cathode tip reduces progressively the voltage by 5-8% after 20 h, and the jet velocity by about 10%.

The arc root fluctuations (restrike mode) [41,42] which condition the arc root life time and thus the anode erosion, evolve with operation time and number of torch ignitions. This erosion is distributed in an area which length is about  $1.5 \times d$  ( $d$  being the internal diameter of the anode). The depth of the eroded area as well as the life time of the arc root increase with the operation time. Anode erosion

results in an increase of the jet instability and a decrease in jet length coupled with a decrease in coating quality. When a tungsten insert is used this erosion problem may become even more critical when tungsten particles are ejected and imbedded within coatings. Therefore, it is important to monitor the anode erosion by the statistical analysis of the voltage signal [43] or its power spectrum [44], and determine when this wear will induce poor quality coating, long before its failure.

This type of monitoring makes it possible to check rapidly a defective gun assembly resulting for example in a poor electrode centering ; a non symmetrical arc attachment influencing deeply the restrike mode frequency and the voltage signal evolution.

### 3.2.2. Real time control

The outputs that have to be set and maintained are the particles mean temperature, velocity, trajectory and the substrate and then coating surface temperature before (preheating), during and after (cooling down) spraying. Among these parameters the most important, at least to our opinion, are the two last ones.

Substrate and coating temperature control depends strongly on the size, shape and thickness of the parts to be coated, the relative movements between the torch and the substrate and powder feed rate, linked to the pass thickness, and cooling means. If the surface temperature can be followed by IR pyrometry, the close-loop controller has to be designed according to substrate and coating heating and cooling, if possible by using simplified 1-D or 2-D computer codes easily adaptable to different geometries and pass thicknesses.

The mean trajectory of the particles within the plasma jet is very sensitive to the powder injection conditions which have to be adapted to the spraying conditions [37]. With a 1-D photodiode array, it is possible to follow continuously the hot particles distribution and, when coupling it to a laser sheet, to have simultaneously the trajectory distribution of the cold particles. The hot particles distribution is very sensitive to any variation of the injection parameters [46]. For example with  $\text{ZrO}_2$  particles ( $-45 + 22 \mu\text{m}$ ) a variation of the powder feed rate of 50 g can be seen and the signal intensity is multiplied by 1.9 when the powder flow rate is doubled (from 1 kg/h to 2 kg/h). Only 1.9 and not 2 due to the starting of the load effect. Any change of the optimum carrier gas flow rate  $m_{cg}^\circ$  modifying the trajectory is immediately detected. For example a change of 10% relatively to



its optimum value induces a 10% change of the signal amplitude and position.

Of course, it is also possible to control on line the surface temperature of the particles prior to their impact [47] or together the temperatures, velocities and trajectories of the particles [48]. These robust easy-to-use optical sensors, now commercialized, allow us, after positioning the torch in front of the sensor head for 1 minute, to check in industrial conditions the optimization of the spray parameters and their time evolution. For this last point after a certain spraying time the torch has to be positioned again in front of the sensor head. Such devices make them possible to determine when the load effect becomes important, measure the time necessary before reaching the stability of particle spraying conditions, increase the reproducibility of the spraying process.

### Conclusion

Plasma sprayed TBCs thermomechanical properties depend strongly upon the contacts between splats and substrate and layered splats.

A better understanding of yttria partially stabilized (YSZ) splat formation made it possible to find a critical substrate preheating temperature  $T_c$ , in the 400-500 K range over which these contacts are strongly improved whatever may be the metallic substrate or the YSZ previously deposited layers. It seems that preheating over  $T_c$  increases the splat-substrate interface temperature allowing delay the time  $t_n$  at which nucleation starts to a value higher than the time to achieve an almost completed flattening. The adhesion/cohesion (A/C) of coatings increases with preheating temperature  $T_{ph}$  provided the substrate oxidation is limited. With 304 L stainless steel or In 100 substrates which oxidation resistance is good. A/C values can reach 70 MPa with  $T_{ph} = 773$  K and a preheating time with the plasma torch below 120 s.

To compete with EB-PVD coatings, conditions have been searched to have a columnar structure through the whole coating (up to 1 mm thick). This structure is obtained when substrate or coating temperature reaches about 973 K. According to oxidation problems, when spraying in air, the substrate temperature has to be kept below this temperature and thus the first 20  $\mu\text{m}$  of the coating do not exhibit this columnar structure but works are in progress to solve this problem. When spraying under such conditions the quenching stress increases drastically (from 8 to 25 MPa) with a corresponding increase of the coating Young's modulus (from 50 to 150 GPa). Therefore, to

control the induced residual stresses, temperature of substrate and coating have to be monitored continuously by adjusting the pass thickness and the cooling devices to the coated part dimensions with the help of simplified 1-D or 2-D computer codes.

At last, to improve coatings reproducibility, strongly linked to the molten state and velocity of impacting particles, a rather simple set-up has been developed giving in real time the trajectory distribution of hot particles within the plasma jet and allowing to check any change in powder flow rate, carrier gas injection flow rate, injector wear... Compared to commercial set-ups following particle velocity, surface temperature and flux density it is by far much simpler and seems to be as efficient. The erosion of the torch nozzle has also to be followed by analyzing the voltage fluctuations which vary drastically when conditions are reached where coating quality is affected and allows also the detection of defective gun assembly.

### Nomenclature

A/C	adhesion/cohesion (MPa)
APS	Atmospheric Plasma Spraying
CR	cooling rate (K/ $\mu\text{s}$ )
D	splat mean diameter ( $\mu\text{m}$ )
d	particle diameter ( $\mu\text{m}$ )
$e_p$	pass thickness ( $\mu\text{m}$ )
$e_s$	splat thickness ( $\mu\text{m}$ )
$R_e$	Reynold's number (dimensionless)
$R_{th}$	thermal contact resistance ( $\text{m}^2\cdot\text{K}/\text{W}$ )
SF	splat shape factor (dimensionless)
$T_b$	temperature of the lower surface of the splat (K)
$T_d$	equilibrium temperature reached by coating upon spraying (K)
$T_i$	interfacial contact between splat and substrate (K)
$T_m$	particle melting temperature (K)
$T_p$	particle impact temperature (K)
$T_{ph}$	substrate preheating temperature (K)
$t_f$	flattening time ( $\mu\text{s}$ )
$t_{ft}$	time at which flattening is almost completed ( $\mu\text{s}$ )
$t_i$	time between two successive impacts ( $\mu\text{s}$ )
$t_n$	time at which nucleation starts ( $\mu\text{s}$ )
$t_s$	time at which solidification is completed ( $\mu\text{s}$ )
$t_t$	time between two successive passes ( $\mu\text{s}$ )
$v_p$	particle velocity at impact (m/s)
$W_e$	Weber's number (dimensionless)
$\mu_p$	molten particle viscosity (kg/m.s)
$\rho_p$	particle specific mass ( $\text{kg}/\text{m}^3$ )
$\sigma_p$	molten particle surface tension (N/m)
$\xi$	flattening degree ( $\xi = D/d$ )

## References

- [1] W.J. Brindley, *Journal of Thermal Spray Technology* **5** (4) (1996) 379-380.
- [2] W.A. Nelson and R.M. Orenstein, *Journal of Thermal Spray Technology* **6** (2) (1997) 176-180.
- [3] W.P. Parks, E.E. Hoffman, W.Y. Lee and I.G. Wright, *Journal of Thermal Spray Technology* **6** (2) (1997) 187-198.
- [4] D.W. Wortman, B.A. Nagaraj and E.L. Duderstadt, *Mater. Sci. Eng.* **A121** (1989) 443-440.
- [5] R.A. Miller, *Surf. Coat. Technol.* **30** (1987) 1-11.
- [6] B.C. Wu and E. Chang, *Thin Solid Films* **172** (1989) 185-196.
- [7] M. Yoshida, K. Abe, T. Aranami and Y. Harada, *Journal of Thermal Spray Technology* **5** (3) (1996) 259-268.
- [8] S. Sodevka, M. Sazaki and K. Ueno, *Journal of Thermal Spray Technology* **5** (3) (1996) 277-282.
- [9] D.V. Rigney, R. Vignie, D.J. Wortman and D.W. Skelly, *Journal of Thermal Spray Technology* **6** (2) (1997) 167-175.
- [10] A. Maricocchi, A. Bartz and D. Wortman, *Journal of Thermal Spray Technology* **6** (2) (1997) 193-198.
- [11] A. Vardelle, N.J. Themelis, B. Dussoubs, M. Vardelle and P. Fauchais, *Transport and chemical rate phenomena in plasma sprays*, *J. of High Temp. Material Processes* **4** (1997), to be published.
- [12] P. Fauchais, M. Vardelle, A. Vardelle, L. Bianchi and A.C. Léger, *Plasma Chemistry Plasma Processing* **16** (1) (1996) 99S-126S.
- [13] L. Bianchi, A.C. Léger, M. Vardelle, A. Vardelle and P. Fauchais, *Plasma Sprayed zirconia splat formation and cooling*, accepted in *Thin Solid Films* (1997).
- [14] P. Fauchais, A.C. Léger, M. Vardelle and A. Vardelle, *Formation of plasma-sprayed oxide coatings*, in *Proc. of J. Szekely Memorial Symp. on Materials Processing* (Pub.) TMS (1997).
- [15] M. Pasandideh-Fard, Y.M. Quiav, S. Chander and J. Mostaghimi, *Physics of Fluids* **8** (1996) 650-659.
- [16] H. Fukanama, in *Thermal Spray : Practical Solutions for Engineering Problems* (ed.) C.C. Berndt and H. Herman, (Pub.) ASM Int. OH, USA (1996) 647-656.
- [17] S. Kuroda, T. Dendo and S. Kitahara, *Journal of Thermal Spray Technology*, **4** (1) (1995) 75-84.
- [18] F. Monerie-Moulin, F. Gitzhofer, P. Fauchais, M. Boulos and A. Vardelle, *J. of High Temp. Chem. Processes* **1** (3) (1992) 249-257.
- [19] A. Haddadi, F. Nardou, A. Grimaud and P. Fauchais, in *Advances in Thermal Spray Science and Technology* (eds.) C.C. Berndt and S. Sampath (Pub.) ASM Int. OH, USA (1995) 249-254.
- [20] L. Bianchi, A. Denoirjean, F. Blein and P. Fauchais, *Thin Solid Films* **299** (1997) 125-135.
- [21] M. Fukumoto, S. Katoh and I. Okane, *Proc. of 14<sup>th</sup> ITSC* (Ed.) A. Ohmori (Pub.) High Temp. Soc. of Japan, Osaka, Japan (1995) 353-358.
- [22] A. Denoirjean, A. Grimaud, P. Fauchais, J. Pech and B. Hannoyer, *Influence of substrate oxidation on alumina splats in plasma spraying*, *Proc. of United Thermal Spray Conf., Indianapolis 15-18 Sept. (1997)*, (Pub.) ASM Int. OH, USA.
- [23] A. Vardelle, M. Vardelle, P. Fauchais and D. Gobin, *NATO Series E : Applied Science* **282** (1995) 95-121.
- [24] M. Bertagnoli, M. Marchese and G. Jaccuci, *J. of Thermal Spray Technology* **4** (1) (1995) 41-49.
- [25] A.C. Léger, PhD Thesis (in French), Univ. of Limoges, France, March 12<sup>th</sup> (1997).
- [26] T.W. Clyne and S.C. Gill, *J. of Thermal Spray Technology* **5** (4) (1996) 401-418.
- [27] Y.C. Tsui and T.W. Clyne, see [16], (1996) 275-284.
- [28] M. Mellali, P. Fauchais and A. Grimaud, *Surf. and Coatings Technol.* **81** (1996) 275-286.
- [29] A.C. Léger, A. Grimaud, P. Fauchais and C. Catteau, see [16] (1996) 891-896.
- [30] Y.C. Tsui and T.W. Clyne, *An analytical model for predicting residual stresses in progressively deposited coatings. Part 1 : Plasma geometry*, submitted to *Thin Solid Films* Dec. (1996).
- [31] K.A. Gross, J. Tikkanen, J. Keskinen, P. Fauchais, M. Vardelle and A. Grimaud, *Vaporization and ultrafine particle generation during the plasma spraying process*, to be published in *United Thermal Spray Conference, Indianapolis Sept. (1997)* (Pub.) ASM Int. OH, USA.
- [32] H. Eschnauer, *Thin Solid Films*, **73** (1980) 1-17.
- [33] F. Gitzhofer, A. Vardelle, M. Vardelle and P. Fauchais, *Materials Science and Eng.* **A147** (1991) 107-120.
- [34] A. Denoirjean, A. Vardelle, C. Martin, P. Fauchais, T. Cosack, E. Lugscheier, I. Rass, P. Chandler, R. McIntyre and H.L. Heijen, in *Thermal Spray : Int. Advances in Coatings*

- Technology (Pub.) ASM Int. OH, USA, (1992) 967-982.
- [35] D. Bernard, PhD's thesis, Univ. of Limoges, June 25 (1990).
  - [36] B. Kolman, J. Forman, J. Dubsky and P. Chraska, *Mikrochim. Acta* **114/115** (1994) 335-342.
  - [37] M. Vardelle, A. Vardelle and P. Fauchais, *J. of Thermal Spray Technology* **1** (2) (1992) 117-128.
  - [38] B. Dussoubs, A. Vardelle, M. Vardelle, P. Fauchais and N.J. Themelis, *13<sup>th</sup> Int. Symp. on Plasma Chem.* **5** (1997) 2056-2061 (ed.) Prof. C.K. WU, Institute of Mechanics, Chinese Academy of Sciences, Beijing 100080, China.
  - [39] X. Zhou and J. Heberlein, *Plasma Chem. Plasma Proc.* **16** (1) (1996) 299S-244S.
  - [40] X. Zhou, B. Ding and J. Heberlein, *IEEE Trans. Components Pkg. and Mfg. Tech.* **19** (3) (1996) 320-328.
  - [41] P. Fauchais, J.F. Coudert and M. Vardelle, Transient phenomena in plasma torches and for plasma sprayed coating generation, accepted in *J. de Physique III*.
  - [42] J.F. Coudert, M.P. Planche and P. Fauchais, *Plasma Chem. Plasma Proc.* **16** (1) (1996) 211S-228S.
  - [43] M.P. Planche, PhD's thesis (in French), Univ. of Limoges, France (1995).
  - [44] Z. Duan, L. Beall, M.P. Planche, J. Heberlein and E. Pfender, Arc voltage fluctuations as an indication of spray torch anode condition, to be published in *proc. of UTSC 97*, (Pub.) ASM Int. OH, USA.
  - [45] K.I. Li, M. Vardelle and P. Fauchais, see [19] (1995) 59-66.
  - [46] M. Vardelle, A.C. Léger, A. Vardelle and P. Fauchais, Influence of the variation of plasma torch parameters on particle melting and solidification, to be published in *Proc. of UTSC 97*, (Pub.) ASM Int. OH, USA.
  - [47] W.D. Swank, J.R. Fincke and D.C. Haggard, see [19] (1995) 111-116.
  - [48] C. Moreau, P. Gougeon, A. Burgess and D. Ross, see [19] (1995) 141-147.

# In-flight Particle Diagnostics for On-line Process Control during Deposition of Plasma-Sprayed TBCs

C. Moreau, P. Gougeon, M. Prystay and L. Leblanc

National Research Council Canada

Industrial Materials Institute

75 de Mortagne

Boucherville (Québec)

CANADA, J4B 6Y4

## 1. SUMMARY

Plasma-sprayed TBCs are built by the successive addition of molten or partially-molten particles spreading upon impact on the substrate surface. Consequently, the temperature and velocity of the sprayed particles are among the most important parameters influencing the microstructure and properties of the deposited coatings. On-line measurement of these parameters, as well as the particle trajectories, is thus an efficient way to monitor the state of the spray process. This approach should permit to minimize the influence of uncontrolled parameters such as the electrode wear or changes in particle injection conditions.

A rugged and easy-to-use optical sensor system has been developed to perform on-line particle diagnosis during spraying in a production environment. In this system, the thermal radiation emitted by the in-flight particles is collected by a compact sensing head and transmitted through an optical fiber bundle to a detection cabinet located away from the dusty environment around the plasma torch.

In this paper, a review of some applications of this diagnosis system used to determine the influence of the spray parameters on the particle temperature, velocity and trajectory and to control the spray process during deposition of TBCs are presented. The system was used in production at Pratt & Whitney Canada (PWC) for two months giving information about the stability and reproducibility of the plasma spray process.

## 2. INTRODUCTION

Plasma spraying is a powerful technique that has been extensively used for the last twenty years to produce protective coatings on a large variety of substrates. During this period, the technique progressed mostly in an empirical manner, attention being focused on the effect of input spray parameters on the resulting coating properties [1,2]. Consequently, the spraying process control was implemented by monitoring and regulating the spray parameters to keep them at a predetermined optimum value. Arc current and power, arc gas flow rates, powder feed rate, powder carrier gas flow rate, net plasma energy are the main parameters usually monitored and automatically controlled during plasma spraying. This control approach has important drawbacks. Indeed, it is complex because a large number of input parameters must be monitored and controlled. It is also incomplete because some variables, such as the electrode wear state, cannot be monitored at all. Moreover, due to the huge temperature and velocity gradients in the plasma plume, a very small change in the

plasma shape or in the injection geometry may have a significant effect on the particle trajectories and thus on their thermal histories and velocities. Significant variations in the coating properties may result from these uncontrolled perturbations.

Plasma-sprayed coatings are built by the successive addition of molten or partially-molten particles spreading upon impact on the substrate surface. Thus, the temperature and velocity of the sprayed particles immediately prior to their impact are among the most important parameters influencing the microstructure and properties of the deposited coatings [3]. On-line measurement of these parameters, as well as the particle trajectories, is thus an efficient diagnostic tool for characterizing the spray process. Since this approach permits to minimize the influence of uncontrollable parameters, one should expect a closer control of the spraying process leading to a better reproducibility of the coating properties.

Different techniques have been already developed to carry out both temperature and velocity measurements of plasma-sprayed particles [4-10]. However, the required equipment is difficult to transfer to an industrial environment due to its complexity and the use of large optical components and fragile laser devices. Other approaches have been also used to provide information on the plasma spray process by monitoring only the particle velocity [11,12] or the thermal radiation from the hot particles [13-16].

Over the last 20 years, the aerospace industry has acquired a large experience in controlling plasma spraying process. Furthermore, the quality standards have led to the development of numerous recipes to control the process. These controls have shown their efficiency as the different coatings succeed in passing the corresponding standard tests required by the industry. Using particle monitoring systems in the aerospace industry can however be useful to evaluate the process stability and then the efficiency of the existing process control. Moreover, more efficient control approaches such as the one based on the measurement of the temperature and velocity of in-flight particles may be the only way to achieve higher quality coatings required in future applications.

This paper first describes the particle monitoring system developed at NRC. This system is dedicated to monitoring of in-flight particles in the laboratory and in production. In a second time, a review of a few applications of the monitoring system is presented. A focus is made on the influence of the temperature and velocity of yttria-stabilized zirconia (YSZ) particles on the coating structure and on the

effect of the wear of the electrodes during deposition of TBCs. The presented results include those collected over a period of 2 months at Pratt & Whitney Canada during the production of plasma-deposited coatings.

### 3. PARTICLE MONITORING SYSTEM

The monitoring system, the DPV2000, is based on the detection and analysis of the thermal radiation emitted by the hot sprayed particles [17,18]. This system, commercialized by Tecnar Automation Ltée [19], consists of a sensor head located near the spray gun, a detection box linked to the sensor head by an optical fiber bundle and a computer (PC) for analysis and statistical computation (Fig. 1). The dimensions of the sensor head are 9 cm long and 3 cm diameter. When a hot particle passes in the measurement volume defined by optics, its image is formed on a two-slit optical mask fixed on the end of an optical fiber inside the sensor head. This event gives rise to a two-peak signal at the output of the photodetectors receiving the radiation through the optical fiber. Fig. 2 shows a schema of the sensor head and the corresponding fields of view of the detection optics. The distance between the slits as well as the magnification of the detection optics being known, the particle velocity can be computed from the time of flight of the particle image between the two slits. The particle temperature is obtained from two-color pyrometry by analyzing the signals from the two photodetectors receiving the radiation in two separate spectral ranges. Finally the particle diameter is computed from the absolute radiation intensity at one wavelength and the temperature of the particle.

Simultaneously to the measurements on the individual particles, the monitoring system measures also parameters of the particle jet considered as a whole. This information is useful to detect problems with the injection of the particles in the plasma jet. For that purpose, the radiation of the

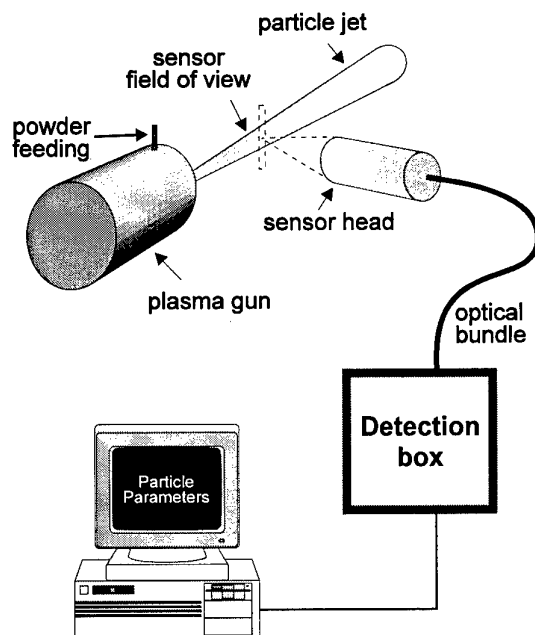


**Figure 1** Schema of the optical system. The thermal radiation from the particles is received by the sensor head and the corresponding signals analyzed by the personal computer.

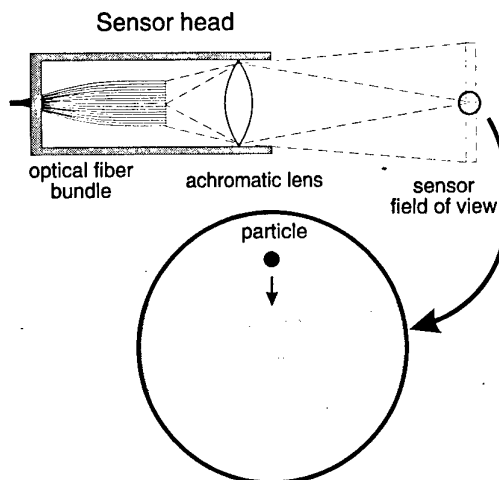


**Figure 2** Schema of the sensor head and fields of view of the linear array and two-slit mask on the center fiber.

particle jet is collected and imaged on a row of optical fibers located in the sensor head near the fiber used for the measurement of the individual particle parameters. The height of the field of view seen by the optical fiber row is 4 cm. The optical fibers are coupled to a CCD linear camera located in the detection box. The parameters of the particle jet are computed from the analysis of the video signal of this CCD camera which is a representation of the spatial distribution of radiation in the particle jet. Three different parameters are obtained from this analysis: the position of the particle jet relative to the axis of the sensor head, the width of the particle jet and its total radiative intensity. This last parameter is very useful to detect variations in the powder feeding rate which are detected as time variations of the intensity. Measurements of individual particle parameters and particle jet parameters are made simultaneously and give complementary information on the spraying conditions.

### 4. RESULTS AND DISCUSSION

#### 4.1 Monitoring of particle properties during coating production

The objective of this study was to follow, during a relatively long period of production, the evolution of the particle characteristics as measured with the DPV2000 monitoring system [20]. For that purpose, the procedure to produce coatings has been slightly modified. Usually, at beginning of spraying, the operator waits until the process is stable before moving the torch in front of the part to be coated. For this study, when the process became stable, the torch stayed in place near the sensor head to allow the measurement of particle parameters for one minute with the monitoring system. In the same way, once the part was coated, the process was not stopped immediately and the torch came back in front of the sensor head for another one-minute measurement. All the measurements were carried out at 63 mm from the torch which is the usual spray distance.

An example of results obtained in this way is illustrated in Figs. 3a and 3b. These figures show the evolution of the

particle temperature just before and after spraying a YSZ coating on a specific part. In Fig. 3a, the spraying process starts at 50 seconds and, before reaching the stability criteria at 150 seconds, a large increase of temperature is noted. After the one-minute stability period, around 210 seconds, the torch moves in front of the part for coating deposition and there are no more particles measured by the monitoring system. In the example of Fig. 3, the spraying process lasts about one hour, and then the torch comes back in front of the sensor head for one minute during which the process is stable. After this minute, at around 4300 seconds on Fig. 3b, the process is stopped according to the normal procedure of PWC. Results similar to those of Fig. 3 have been obtained for all the parts sprayed with YSZ powders. These results show that the temperature of the sprayed particles is stable when the PWC criteria of stability are reached.

From these results, the average values on the 60 seconds of stability can be computed for each measured parameter, i.e. the particle temperature, velocity and diameter. The average temperature of the YSZ powder sprayed with 3 guns used in production is shown in Fig. 4. These results are obtained during production of coatings with three sets of identical electrodes using the same spraying conditions. The abscissa of Fig. 4 is the number of hours of operation for each set. Measurements before (down triangles) and after (up triangles) coating deposition are represented at the same abscissa if they correspond to deposition on the same part.

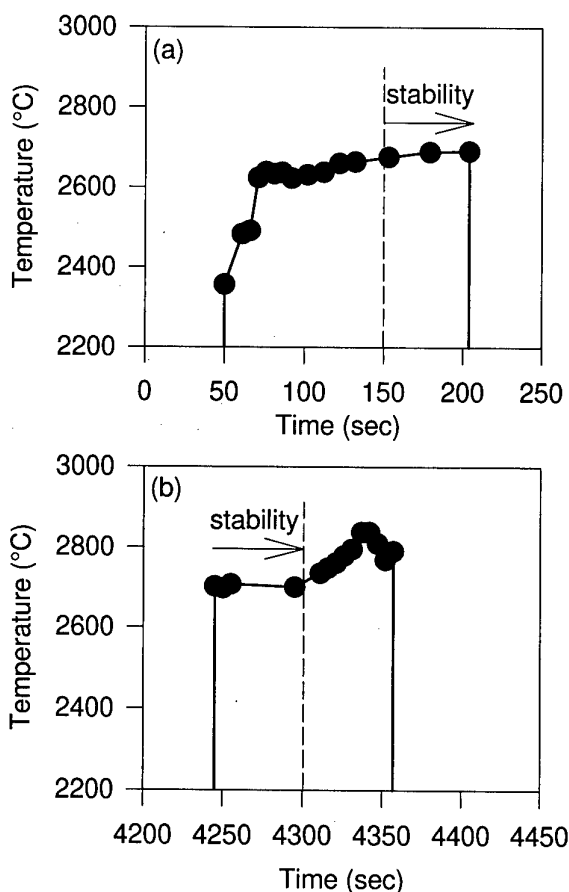


**Figure 3** Example of particle temperature evolution during coating production with YSZ particles. (a) before deposition, (b) after deposition.

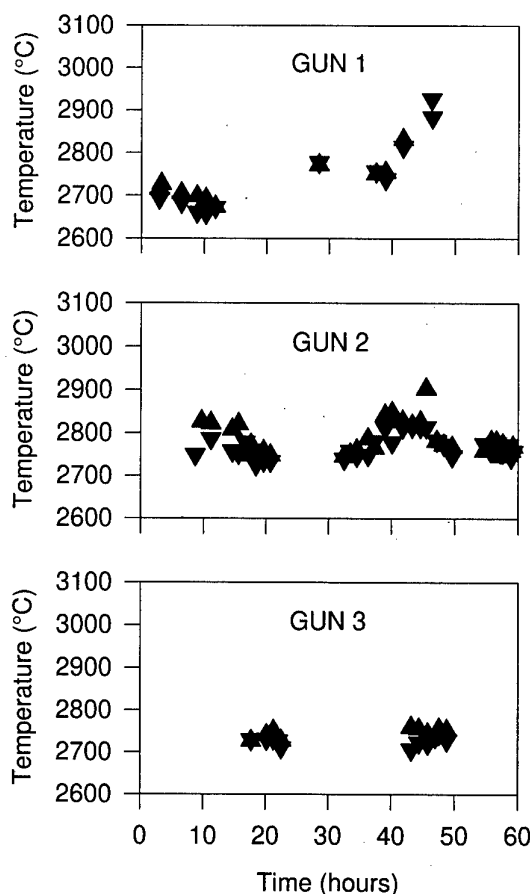


**Figure 4** Time evolution of YSZ particle temperature for 3 guns used in production : (▼) before and (▲) deposition on different parts.

The number of points differs for each gun as the guns were used for spraying different powders and only the measurements on YSZ particles are shown. It is worth noting that there is a difference of typically 20°C between temperature measured before and after deposition on each part. Even if this difference is small, it is significant, indicating that the conditions of the particles have slightly changed during spraying.

The guns 1,2,3 have been changed after 46, 58 and 48 hours of spraying, respectively. For gun 3, the reason of change is not imposed by consideration of stability of the process but is due to a problem of waterproofness in the torch. With this gun, the process was considered stable according to the PWC criteria and also according to the measurements on the particles (Fig. 4). The situation is different for guns 1 and 2 as the temperature and also velocity of the particles (not shown) vary significantly during the use of these guns in production. It appears that these variations are often related to variations of voltage between electrodes which is one of the parameters recorded by the operators. In fact, when the voltage variations are too large, the usual procedure is to stop spraying as it is the case for gun 1 after 46 hours of operation. Consequently, the two triangles at 46 hours correspond to a beginning of spraying but no deposition was made as the voltage variation was too large. Even if gun 1 was used for coating deposition during 46 hours, Fig. 4

shows that the spraying conditions of the particles have constantly and significantly changed after 35 hours of operation. It is worth noting that the process was controlled by keeping the input power constant. So, as the electrodes become worn, the voltage tends to decrease and the controller reacts by increasing the current in the gun. In the case of gun 1, it clearly appears that such a correction was too large leading to a significant increase of the temperature of the sprayed particles. A corresponding increase in the velocity of the particles was also noted.

The gun 2 was changed because it reached 60 hours of spraying time. In such a case, changing the gun prevents eventual problems which can appear during production of coatings. After the 58 hours of operation of gun 2, no significant change was noted for the particle temperature. However, an increase of the particle temperature has been observed between 40 and 46 hours of gun operation but after 46 hours the conditions become again similar to what they were before 40 hours. This variation of temperature between 40 and 46 hours is correlated with a variation of the voltage between the electrodes but this change was considered too small to stop the process. It should be noted that during production with guns 1 and 2 particle temperatures have varied by 180°C and velocities by 30 m/s. This means that, in spite of the process control used to produce coatings, the particle spraying conditions can vary significantly.

The values for the average particle parameters for each gun are given in Table 1. The values for each parameter are average values obtained during the first hours of use of each gun, that means during the period of time they give relatively stable conditions for the particles. From Table 1, it appears that the different particle parameters are very similar for guns 1 and 3 except the difference of 50°C in temperature. The differences with gun 2 are larger as the temperature difference reaches 82°C. From Table 1, it is clear that in spite of the control established on the process, there are still significant differences in the particle characteristics. These differences can be explained by a variation in the way the particles are injected in the plasma jet. This is especially important if the plasma characteristics change as we can expect if the plasma gun is changed. Consequently, a control of the particle state appears more sensitive to variations in the process conditions than the current approach based on the control of plasma power.

It was observed that, in the case of YSZ particles, the spraying conditions are relatively stable during the stability periods (Fig. 3) even if the temperature can slightly vary during deposition. This is not true in the case of finer

metallic (NiCoCrW) powders, 27  $\mu\text{m}$  average diameter. Figure 5 shows the evolution of the particle jet intensity before and after deposition. In this case, the process didn't reach a stable operation point even after 3 minutes of spraying when the torch normally moves to spray the part to be coated. Such a long time to obtain stable spray conditions is likely related to the feeding conditions of the fine powder into the plasma.

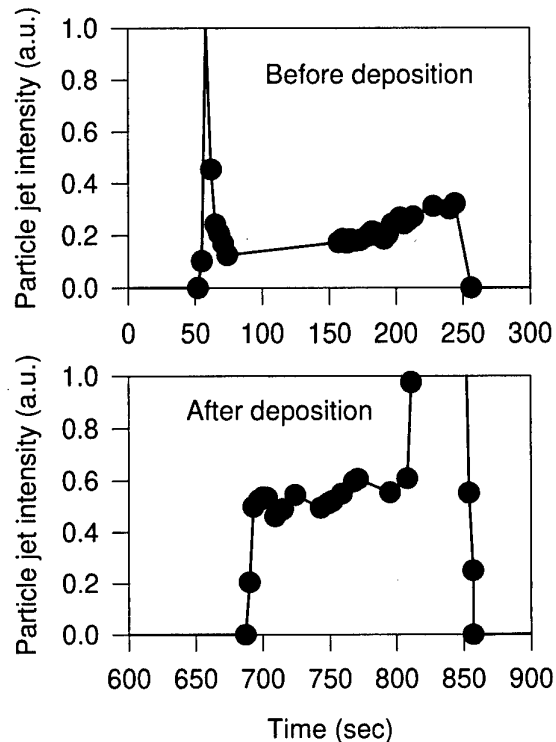


**Figure 5** Time evolution of the particle jet intensity collected by the CCD camera.

#### 4.2 Effect of the wear of the electrodes

In order to better understand the effect of the wear of the electrodes during spraying, a series of measurements of the particle characteristics was carried out in the laboratory [21]. A torch was mounted with a new set of electrodes and the state of the particles was monitored as a function of the spraying time. At regular intervals, YSZ coatings about 500  $\mu\text{m}$  thick were sprayed.

##### 4.2.1 Two-Dimensional Profiles

Four 2-D profiles were measured after 1, 8, 22 and 37 hours of spraying. Mean temperature, velocity and diameter of the sprayed particles were monitored during the scans. These profiles were collected by moving the sensor head with a X-Y unit, scanning in this way the measurement volume of the DPV2000 across the particle jet at 65 mm from the gun. The number of detected events which is related to the particle flux at the measurement volume location was also counted for a fixed period of time (25 ms). This number can't be taken as the true particle flux but is qualitatively related to it in the sense that both follow the same trends.

**Table 1** Particle parameters measured during the first hours of operation for 3 guns used in production.

	GUN 1	GUN 2	GUN 3
Temperature (°C)	2687	2769	2734
Velocity (m/s)	156	161	152
Diameter ( $\mu\text{m}$ )	55	67	60
Flux (part./min.)	1065	1290	1123
Jet position (mm)	-0.9	0.0	-0.5
Jet width (mm)	4.7	4.6	4.7
Jet intensity (a.u.)	1.0	1.3	1.1

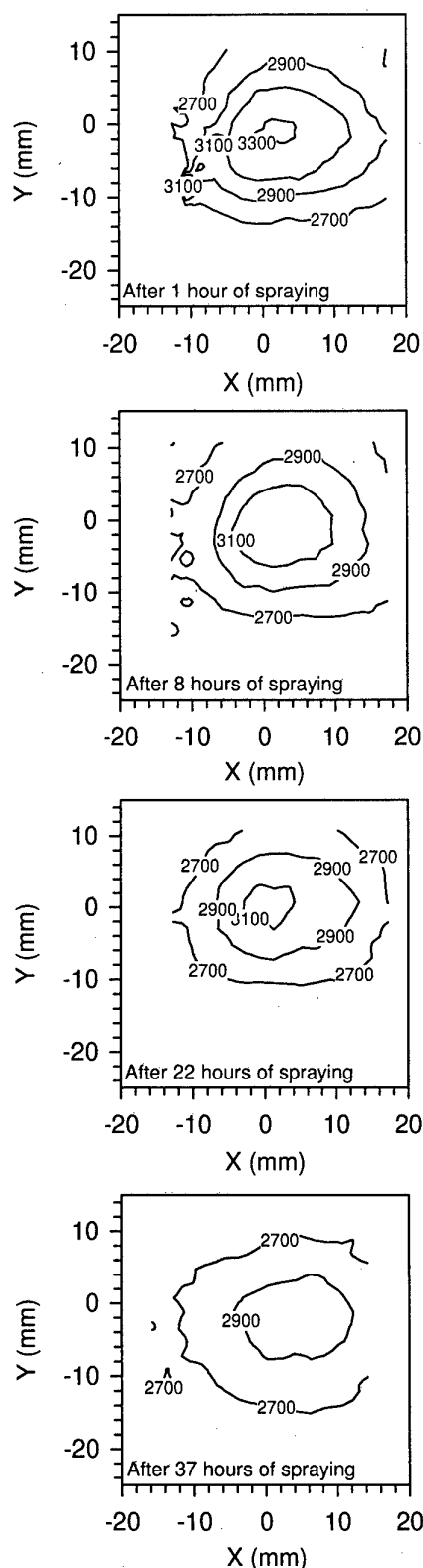
Figure 6 represents the evolution of the mean particle temperature with the spraying time. The temperature distribution as well as the velocity distribution (not illustrated here) followed the same behavior during the experiment starting with their highest values at the beginning of the experiment (one hour of spraying) and decreasing continually until the end of the experiment (37 hours of spraying). A variation of more than 200 °C is observed between the temperature distributions measured at the beginning and at the end of the forty-hour experiment. During this time, the velocity distribution has varied by more than 30 m/s. It is worth noting that, in this series of measurements, the plasma current was kept constant at 800 A. The results show that even though the input spray parameters stayed the same, the particle state has significantly changed. Such temperature variations may lead to important coating microstructure and thermal property changes [22].

Figure 7 shows the evolution of the distribution of the number of detected events which is related to the particle flux. At the beginning of the experiment the distribution was not symmetric, being nearly 50% wider in the horizontal direction. However, the distribution tended to get more symmetric with increasing spraying time. It is also observed in Fig. 7 that the maximum number of events decreased with increasing spraying time suggesting that the more the plasma gun was used the more the hot particles were lost from the spray jet. This has also been observed recently with alumina [23].

#### 4.2.2 Coatings and Deposition Efficiency

Coatings were sprayed after 3, 10, 22 and 37 hours of spraying in order to evaluate the effects of the sprayed particle state on the microstructure of the deposited material through the long-term experiment. Image analysis showed that the total porosity was the same for all coatings, at about 16%.

After three hours of spraying, the deposition efficiency was 55% while at the end of the experiment (37 hours of spraying) it fell to 41% reflecting important changes in the state of the sprayed particles. Figure 8 shows the microstructure of the coatings deposited after 3, 10 and 37 hours of spraying. As seen in the figure, a clear evolution of the coating microstructure took place with increasing spraying time. At the beginning, after 3 hours of spraying, the deposited coating contained a relatively large amount of cracking. The cracking pattern, though still present, is not so apparent in the coating sprayed after 10 hours. The mean particle temperature was nearly the same for these two coatings whereas the particle velocity differed by nearly 30 m/s. Coatings sprayed after 22 (not shown in Figure 8) and 37 hours were very similar in their microstructure. However, in these coatings cracking patterns like those observed after 3 and 10 hours of spraying did not form. These microstructure differences can be attributed to the different particle state before their impact on the substrate. Indeed, in a previous communication [22] it has been demonstrated with a similar ceramic powder that a mean particle temperature variation of 200°C, such as the one measured in the present experiment between 3 and 37 hours of spraying, can result in a more than 10% thermal diffusivity variation as well as significant microstructure changes. It should be reminded that between 3 and 37 hours of spraying the gun power



**Figure 6** Temperature distribution (°C) of the sprayed particles after different spraying times. The gun axis corresponds to  $X = 0$  mm and  $Y = 0$  mm.



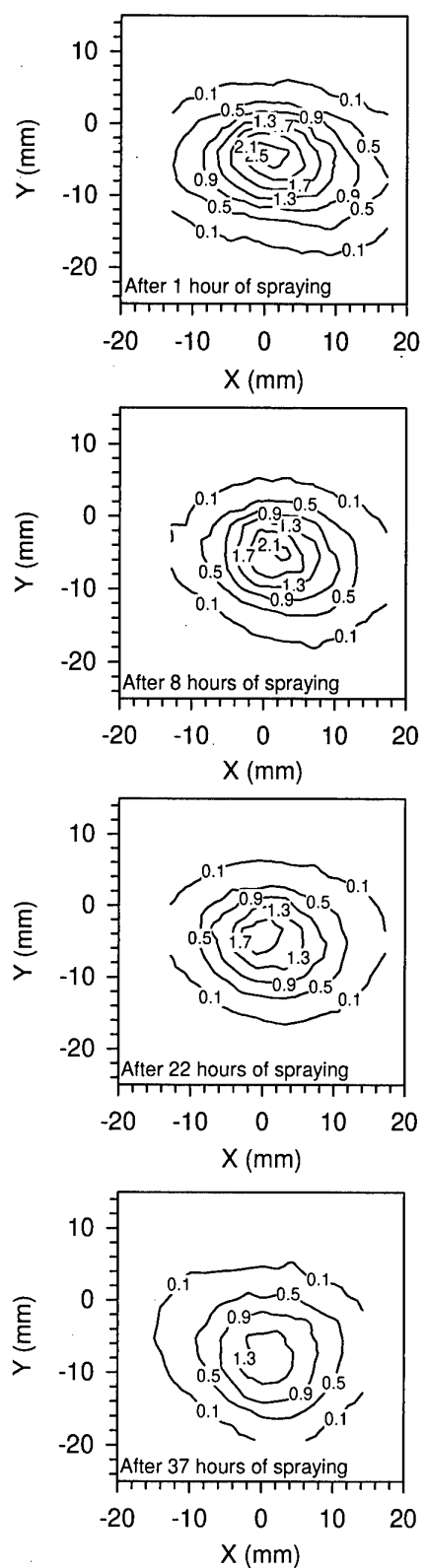


**Figure 7** Number of detected events (thousands) after different spraying times. The gun axis corresponds to  $X = 0$  mm and  $Y = 0$  mm.

*after 3 hours of spraying*



*after 10 hours of spraying*



*after 37 hours of spraying*

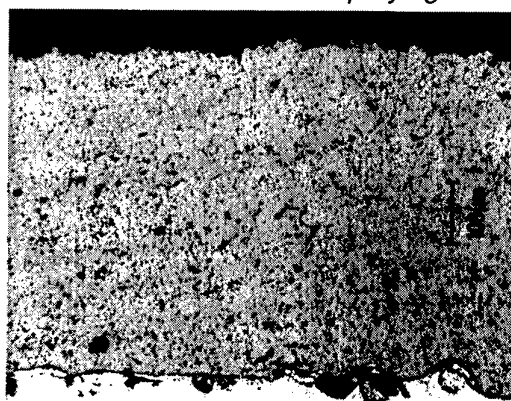


**Figure 8** Pictures of coatings deposited after 3, 10 and 37 hours of spraying. The coatings are about 580, 480 and 520  $\mu\text{m}$  thick, respectively. The number of vertical cracks decreases with the spraying time as electrode wear becomes significant.

varied by only 1 kW. It would have been difficult, if not impossible, to predict any microstructure changes from this power variation. Present results show that coatings prepared after different spraying times with the same input spray parameters can result in materials having significant differences in their microstructures and properties.

#### 4.2.3 Attempts to Recover Initial Particle State

After the forty-hour experiment, the electrodes were disassembled from the plasma gun. They were mounted again several months later when attempts were made to try to recover the initial particle parameters. In a first attempt, the gun current was set to 900 A. However, no significant changes in the mean particle temperature and velocity were observed neither when gun current was increased from 800 A to 900 A and to 1000 A, nor when the powder carrier gas flow rate was changed. Nevertheless, when hydrogen proportion was changed to 5% (as compared to 3.9% vol. during the forty-hour experiment) the mean particle temperature increased by about 150°C (from 3000°C to 3150°C) whereas the mean particle velocity increased by more than 15% (from 148 m/s to 175 m/s). Moreover when the total gas flow rate was increased from 52.0 l/min to 60.6 l/min, keeping the hydrogen proportion to 5% vol., the mean particle temperature increased from 3150°C to 3200°C while the mean particle velocity increased from 175 m/s to 190 m/s. These velocity and temperature are similar to those measured after two hours of spraying. The measured gun power was 35 kW, which is about 5 kW higher than its value after two hours of spraying.

Using these spraying conditions, 2-D profiles of the particle jet were measured. They are rather similar to those measured after eight hours of spraying (see Figs. 6 and 7). The numbers of detected events are similar to those observed after 8 hours of spraying (Fig. 7). A coating as well as a deposition efficiency test were performed using the new input parameters. The deposition efficiency was measured to be 53% which is essentially the same as what had been measured after three hours of spraying (55%) and much higher than the 41% value measured after 37 hours of spraying. The microstructure of the coating prepared

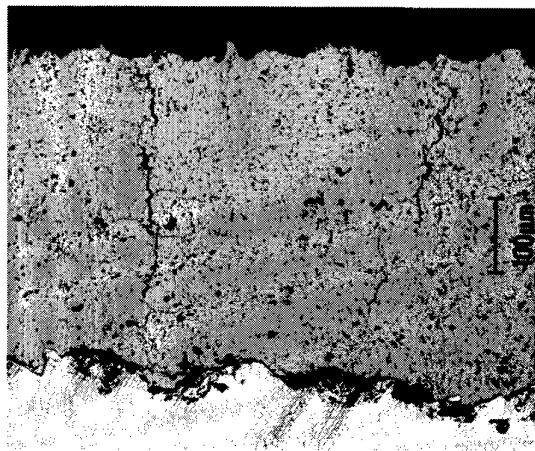


**Figure 9** Picture of a coating deposited with higher hydrogen proportion and gas flow rate. The coating is about 450  $\mu\text{m}$  thick.

with higher hydrogen proportion and gas flow rate is shown in Fig. 9. It can be seen from this figure that the cracking pattern is rather similar to that of the coating sprayed after 3 hours, as seen in Fig. 8.

So after a long spraying time (about 40 hours) by changing some input parameters it was possible to recover the sprayed particle parameters obtained after three hours of spraying and to recover the same type of coating structure observed before significant electrode wear took place.

#### 4.3 Controlling the particle state and coating structure

In order to implement a feedback loop to control the state of the in-flight particles, it is necessary to know how the input spray conditions influence the state of the particles. It is also necessary to know how the temperature and velocity of the impinging particles affect the coating structure. For TBCs coatings, one key characteristic is the crack network within the coating. Indeed, it seems advantageous to maximize the number of cracks perpendicular to the substrate while minimizing the number of parallel cracks [24].

An example of how the arc current and total gas flow rate influence the state of YSZ particles is shown in Fig. 10 [22]. The powder used in this study was a fused and crushed YSZ powder ( $-45 +11 \mu\text{m}$ ). After setting the plasma current and total gas flow rate, the powder carrier gas flow rate was adjusted to position the spray jet axis at a constant angle of about 3 degrees below the torch axis. As shown in the process control plot of Fig. 10, an increase in plasma current increases both the temperature and velocity of the particles whereas an increase in the gas flow rate increases their velocity but decreases their temperature. Subsequently, conditions for spraying particles at an exact temperature and velocity may be obtained by carefully regulating both the arc current and gas flow rates. In this way it is possible to regulate the spray process in order to spray coatings in a reproducible manner.

After having established the data shown in Fig. 10, it is possible to optimize the coating structure by varying independently the temperature and velocity of the sprayed

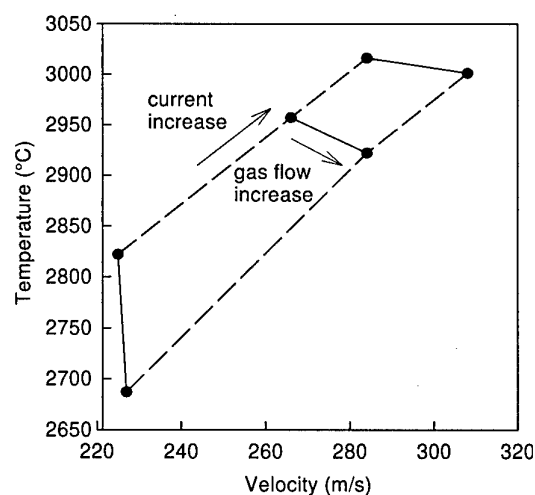


**Figure 10** Process control plot showing the effect of the arc current and arc gas flow rates on the particle temperature and velocity. The arc gas is Ar with 33% He and the powder is YSZ ( $-44 +11 \mu\text{m}$ ).

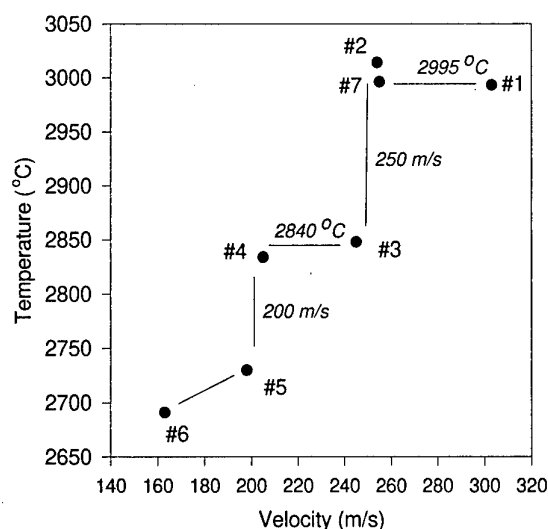


**Figure 11** Average temperature and velocity of the sprayed particles for coatings sprayed in the study of *Prystay et al.*

particles instead of varying the input spray parameters. For example, in the work of *Prystay et al.* [22], the coatings were sprayed in the 7 conditions shown in Fig. 11. The velocity and temperature effects were decoupled by selecting operating parameters to generate data points that fall along a staircase pattern. For example, the influence of particle velocity at about 2995 °C is seen by comparing coatings 1 and 7. (The average temperature between the particle temperatures of samples 1 and 7 is used. Other values shown on the graph were determined in the same manner.) The effect of velocity at particle temperatures of 2840 °C is seen by comparing samples 3 and 4. The results of changing particle temperature for fixed particle velocities are obtained by comparing sample 4 with 5 (200 m/s) and sample 3 with 2 (250 m/s).

In this work the angular crack distribution was characterized by image analysis using a dedicated algorithm developed in our laboratory. This algorithm treats each pore or crack as an individual feature of equal weighting and no results regarding their width are included. The orientation of each feature is determined and the total length of the features (in pixels) as a function of their orientation is calculated.

An example of results is given in Fig. 12 where the crack distribution of coatings 4 and 5 are compared. Both coatings were sprayed at particle velocity of 250 m/s but with different particle temperatures. In this case, the increase in temperature has the effect of sharply decreasing the number of horizontal cracks (0 degree) and increasing the vertical cracking (at 90 degrees). In fact, coating sprayed with particles at 250 m/s and 3014 °C exhibits only a weak preferred angular crack orientation. In addition, although this coating is not the densest in this study, it is the coating with the highest thermal diffusivity [22]. This suggests that the significant reduction in horizontal cracking decreased the thermal insulating properties of the coating.

## 5. CONCLUSION

Plasma-sprayed coatings are used in a wide range of new and demanding applications. As the quality requirements of

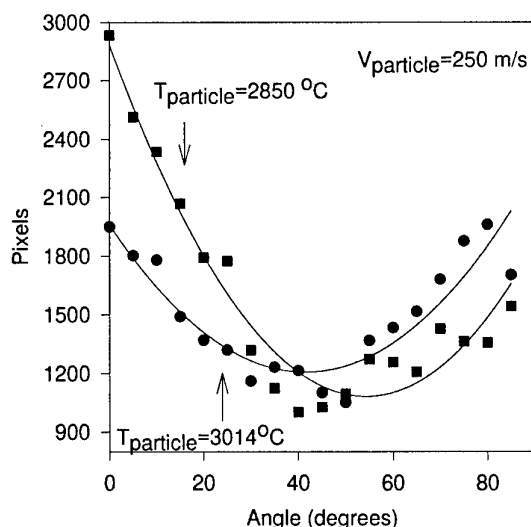


**Figure 12** Angular crack distribution in coatings 4 and 5 sprayed with particles at 250 m/s and (●) 3014 °C and (■) 2850 °C, respectively.

the sprayed coatings increase, the process control becomes a key issue in order to produce, day after day, high quality coatings in a reproducible manner. Monitoring the temperature, velocity and trajectory of in-flight particles before their impact on the substrate appears as an efficient way to characterize the process and to perform feedback on the input spray parameters. Moreover, it is also an efficient tool to optimize the spraying conditions by varying parameters that have the most crucial effects on the coating properties.

## 5. ACKNOWLEDGEMENTS

The authors are grateful to many people that contributed in this work. In particular, we would like to thank M. Lamontagne and S. Bélanger from NRC Canada for their help in spraying coatings and developing the optical diagnosis system. Moreover, we are grateful to F. Richard for taking charge of the project at Pratt & Whitney Canada.

## 6. REFERENCES

1. Smith, R.W., "Plasma Spray Deposition: A Need for Direct Process Control", in "Review of progress in quantitative nondestructive evaluation," Vol 8B, D. O. Thomson and D. E. Chimenti (Eds), Plenum Press, New York, 1989, pp 1169-1183.
2. Fincke, J.R., "Diagnostics and Sensor Development for Thermal Spray Technologies", in "Thermal Spray: International Advances in Coatings Technology," Proc. Inter. Thermal Spray Conference, Orlando, ASM International, Materials Park, OH (1992) pp 1-9.
3. McPherson, R., "The Relationship Between the Mechanism of Formation, Microstructure and Properties of Plasma-Sprayed Coatings", *Thin Solid Films*, 83, 1981, pp 297-310.
4. Mishin, J., Vardelle, M., Lesinski, J. and Fauchais, P., "Two-colour Pyrometer for the Statistical Measurement of the Surface Temperature of Particles under Thermal Plasma Conditions", *J. Phys. E:Sci. Instrum.*, 20, 1987, pp 620-625.

5. Vardelle, M., Vardelle, A., Fauchais, P., Boulos, M.I., "Plasma-Particle Momentum and Heat Transfer: Modelling and Measurements", *AIChE Journal*, 29, 1983, pp. 236-243.
6. Sakuta, T., Ohtsuchi, T., Sakai, K., and Takashima, T., "Measurement of In-Flight Particle Parameters in Thermal Plasma Spraying Process by the Light Pulse Analysis Method", in "Proc. Jpn. Symp. Plasma Chem.", Vol. 4, 1991, pp. 175-180.
7. Fincke, J.R., Swank, W.D., Jeffery, C.L. and Mancuso, C.A., "Simultaneous Measurement of Particle Size, Velocity and Temperature", *Meas. Sci. Technol.* 4, 1993, pp 559-565.
8. Guselnikov, S.M., Zavargin, A.G., Lyagushkin, V.P., Mikhhalchenko, A.A. and Solonenko, O.P., "Laser Optical Diagnostics Complex For Investigation of High-Temperature Heterogeneous Jets", in "Plasma Jets", Solonenko and Fedorchenko (Eds.), VSP, 1990, pp 163-170.
9. Coulombe, S., Boulos, M.I. and Sakuta, T., "Simultaneous Particle Surface Temperature and Velocity Measurements under Plasma Conditions", *Meas. Sci. Technol.*, 6, 1995, pp. 383-390.
10. Kudora, S., Fujimori, H., Fukushima, T. and Kitahara, S., "Measurement of Temperature and Velocity of Thermally Sprayed Particles using Thermal Radiation", *Trans. Jpn. Welding Soc.*, 22, 2, 1991, pp. 10-17.
11. Frind, G., Goody, C.P. and Prescott, L.E., "Measurement of Particle Velocity in Two Low-Pressure Plasma Jets", in "6th Inter. Symposium on Plasma Chemistry (ISPC-8)", Montreal, 1983, pp 120-125.
12. Mayr, W. and Henne, R., "Investigation of a VPS Burner with Laval Nozzle using an Automated Laser Doppler Measuring System", in "First Plasma-Technik Symposium", Vol. 1, 1988, pp 87-97.
13. Sölter, H.-J., Müller, U. and Lugscheider, E., "High-Speed Temperature Measurement for On-line Process Control and Quality Assurance during Plasma Spraying" *Powder Metal. International*, 24, 1992, pp. 169-174.
14. Hencken, K.R., Tichenor, D.A. and Wang, C.F., "Optical Double-Slit Particle Measuring System", U.S. Patent 4,441,816, 1984.
15. Swank, W.D., Fincke, J.R. and Haggard, D.C., "A Particle Temperature Sensor for Monitoring and Control of the Thermal Spray Process", in "Advances in Thermal Spray Science and Technology", Proc. 8<sup>th</sup> National Thermal Spray Conf., ASM International, 1995, pp. 111-116.
16. Li, K.-I., Vardelle, M. and Fauchais, P., "Comparison Between Single and Double Flow Injectors in the Plasma Spraying Process", in "Advances in Thermal Spray Science and Technology", Proc. 8<sup>th</sup> National Thermal Spray Conf., ASM International, 1995, pp. 45-50.
17. Moreau, C., Gougeon, P., Lamontagne, M., Lacasse, V., Vaudreuil, G. and Cielo, P., "On-line Control of the Plasma Spraying Process by Monitoring the Temperature, Velocity, and Trajectory of In-flight Particles", in "Thermal Spray Industrial Applications", C. C. Berndt and S. Sampath (Eds.), Proc. National Thermal Spray Conference, Boston, ASM Intern., Boston, 1994, pp 431-437.
18. Gougeon, P., Moreau, C., Lacasse, V., Lamontagne, M., Powell I., and Bewsher, A., "A New Sensor for On-line Diagnostics of Particles under Thermal Spraying Conditions", in "Advances in Powder Metallurgy & Particulate Materials", Vol.6, Advanced Processing Techniques, C. Lall and A. J. Neupaver (Eds.), Proc. Inter. Conf. on Powder Metallurgy and Particle Materials, Toronto, Canada, Metal Powder Industries Federation, 1994, pp 199-210.
19. Tecnar Automation Ltée, 3502, First Street, St-Hubert, Quebec, Canada, J3Y 5K2.
20. Gougeon, P., Moreau, C. and Richard, F., "On-line Control of Plasma Sprayed Particles in the Aerospace Industry", in "Advances in Thermal Spray Science and Technology", C. C. Berndt and S. Sampath (Eds.), Proc. National Thermal Spray Conference, Houston, Texas, ASM International, 1995, pp 149-155.
21. Leblanc, L., Gougeon, P. and Moreau, C., "Investigation of the Long-Term Stability of Plasma Spraying by Monitoring Characteristics of the Sprayed Particles", in "Proc. United Thermal Spray Conf., Indianapolis, Indiana, ASM Inter., Sept. 1997, to be published.
22. Prystay, M., Gougeon, P. and Moreau, C., "Correlation Between Particle Temperature and Velocity and the Structure of Plasma Sprayed Zirconia Coatings", in "Thermal Spray: Practical Solutions for Engineering Problems", C.C. Berndt (Ed.), Proc. National Thermal Spray Conf., Cincinnati, Ohio, ASM Inter., 1996, pp 517-523.
23. Lethinen, T., Knuuttila, J., Vattulainen, J., Mäntylä, T. and Hernberg, R., "Correlations Between In-flight Particle Concentrations and Coating Properties in Atmospheric Plasma Spraying on Alumina", in "Thermal Spray: Practical Solutions for Engineering Problems", C.C. Berndt (Ed.), Proc. National Thermal Spray Conf., Cincinnati, Ohio, ASM Inter., 1996, pp 525-530.
24. Bengtsson, P., Jonannesson, T. and Wigren, J., "Crack Structures in Plasma Sprayed Thermal Barrier Coatings as a Function of Deposition Temperature", in "Thermal Spraying - Current Status and Future Trends", Proc. Inter. Thermal Spray Conf., Kobe, Japan, A. Ohmori (Ed.), 1995, pp 347-351.

## ON THICK THERMAL BARRIERS FOR COMBUSTOR APPLICATION

**T. Haubold**

**H. Gans**

BMW Rolls-Royce GmbH  
Material Technology  
Hohemarkstr. 60-70  
D-61440 Oberursel, Germany

**D. Schwingel,**

**R. Taylor**

University of Manchester  
Materials Science Institute(UMIST)  
Grosvenor Street  
Manchester, M1 7HS, UK

### SUMMARY

Basic features for future advanced gas turbines will be low emission rates and increased efficiency. To fulfil these requirements a reduction of cooling air in the combustor chamber demanding more efficient cooling technology and/or an increasing inner wall temperature is needed. The development of thicker thermal barrier coatings for combustor tile applications is one concept followed to enable a reduction in cooling air.

Thermal barrier coatings with a thickness up to 2mm and improved thermal cycling life have been developed as well as mechanical and thermophysical data determined.

Combustor segment rig testing demonstrated a potential of 25% cooling air reduction by the use of thick thermal barriers for the tile design investigated.

### 1. INTRODUCTION

A basic feature for the development of advanced gas turbines will be low emission rates of Nitrogen Oxides (NO<sub>x</sub>), Carbon monoxides (CO) and Hydrocarbons (HC) to suit expected lower limits for pollution in the future. One way to fulfil these requirements is a reduction of cooling air in the combustor chamber demanding more efficient cooling technology and/or increasing inner wall temperatures.

Beside the development of more efficient cooling technologies there are several materials technology concepts that are followed at BMW Rolls-Royce to reduce cooling air requirements in the combustor:

- i) a development of improved superalloys for combustor application with higher temperature capability,
- ii) investigation of the potential of ceramic matrix composite materials for combustor tiles and
- iii) development of thicker thermal barrier coatings (TBCs) for combustor tile applications.

This paper will focus on the latter.

Typical current applications of TBCs are thin coatings on guide vanes, blades and combustors of gas turbines often introduced during overhaul in order to extend lifetime of parts. Current technology is the use of plasma sprayed bond coat (BC) such as CoNiCrAlY mainly for adhesion and oxidation protection and partially stabilised  $\text{ZrO}_2$  (about 8wt%  $\text{Y}_2\text{O}_3$ ) with a thickness below 0.5mm. The benefit is a component temperature reduction up to 150°C resulting in reduced cooling airflow requirements and/or component durability improvement (1, 2, 3). Thickness and lifetime of the barriers are limited by mechanical and thermal stresses in the coatings due to the mismatch of thermal expansion coefficients of the ceramic and the metals and/or oxidation of the bond coat.

In a current Brite Euram project (BE7287)<sup>1</sup> plasma sprayed thermal barrier coatings up to 2mm in thickness have been developed to meet the requirements of improved thermal insulation (4). Different microstructures of coatings has been addressed from different partners. Volvo Aero Corporation has investigated segmented TBCs (4), BMW Rolls-Royce 'conventional' highly porous TBCs and ANSALDO Richerche has developed a process route to spray highly porous TBCs using a mixed ceramic-polymer powder (5).

This paper will report on the development of the highly porous coatings, the investigation of thermophysical and mechanical properties and thermal cycling experiments as well as combustor sector rig tests performed to determine the potential for cooling air reduction of thicker TBCs applied on combustor tiles. The sector rig test has been performed in the course of a national research programme.

## 2. EXPERIMENTAL

### Spraying

In general TBC development within the above mentioned Brite Euram Project has had the objective to reduce Young's modulus as one method to reduce thermal mismatch stress. Mechanisms chosen have been segmentation (vertical cracking) or production of highly porous coatings.

Spraying of porous 7% $\text{Y}_2\text{O}_3$  stabilised  $\text{ZrO}_2$  TBCs

has been performed at the BMW Rolls-Royce APS spray facility (Sulzer Metco A3000S, 9MB gun) using different spray parameters. During spraying temperature has been measured by means of a pyrometer at the coating surface and by means of thermocouples at the backside of the substrate. Substrates have been 2mm thick flat plates of Hastalloy X.

Microstructural investigations are performed at BRR to determine typical coating features such as thickness, porosity and crack density.

### Thermophysical and mechanical Properties

Four point bend testing has been performed at UMIST at room temperature and elevated temperature to determine the nominal strength, the failure strain and Young's modulus. For testing free standing TBCs have been used by dissolving away the substrate. This has been possible due to the thickness of the coating.

For the measurement at elevated temperatures, a high temperature rig has been designed in accordance with European standards. All parts of the rig within the hot zone of the furnace are made out of Alsint 99,7 which can theoretically withstand a temperature of 1700 °C. The capacity of the furnace enables temperatures up to 1500 °C. Figure 1 shows the design of the apparatus. The sample is supported by two rollers 20 mm apart. In order to minimise the torsional loading, one of these rollers can also rotate about an axis parallel to the length of the sample. The specimen is loaded by a second set of rollers which are isocentric to the first ones. They are 10 mm apart and both of them allow a rotation about their own axis as well as about the axis of the sample.

The Young's modulus is strongly affected by the ratio of the sample length  $l$  and its thickness  $h$  and turns out to be too low in comparison with results from adequate tensile tests. In order to come to an understanding of the influence of the  $l/h$  ratio of the samples on the calculation of the Young's modulus, a coating was measured by an ultrasonic pulse method at 'Fraunhofer Institut Werkstoffphysik und Schichttechnologie' in Dresden resulting in a compensation factor for the  $l/h$  ratio of the 4 point bend test specimen.

<sup>1</sup>Partners of the Brite Euram Project BE7287 are: BMW Rolls-Royce GmbH, Volvo Aero Corporation, ANSALDO Richerche, CTAS Air Liquide, Fraunhofer Gesellschaft Institut für Betriebsfestigkeit, University of Lund, UMIST, Kvernes Technology, IceTec, RWTH Aachen, Rolls-Royce plc.

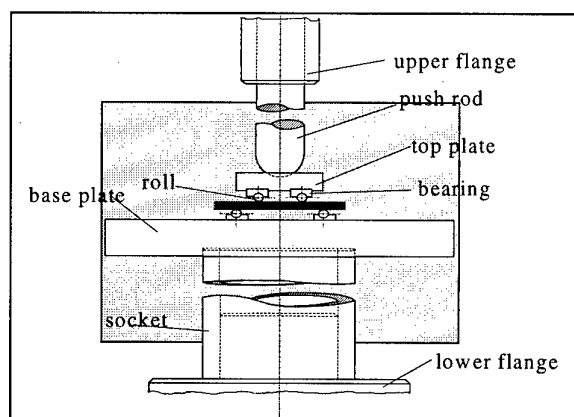


Fig. 1: design of the four-point bending rig, the hot furnace area is marked by the grey background

For the measurement of the thermal diffusivity  $\alpha$ , the laser flash method was used. The samples examined had a dimension of 10 mm \* 10 mm with a thickness of about 2 mm. In this experiment, a heat flux through the sample is caused by an energy pulse from a Nd glass laser which is incident on the front face of the specimen. The heat flux causes a temperature rise at the sample rear side, which is monitored as a function of time using an InSb detector. From this trace, the thermal diffusivity can be calculated. For the samples investigated, the measurements of the thermal diffusivity were performed under vacuum. The experiments were done in a temperature range from 80 °C to 1200 °C(6).

Thermal expansion measurements were performed in a conventional  $\text{Al}_2\text{O}_3$  pushrod dilatometer, over a temperature range from 30 °C to 1000 °C. The heating rate was 60° h<sup>-1</sup>. After reaching the maximum temperature, the sample was cooled at -250 °C h<sup>-1</sup>. Since the push rod and the guiding tube it is surrounded by also expand, this effect had to be compensated mathematically. The temperature gradient across the pushrod-guiding tube arrangement is taken into account by a compensation measurement. The latter one was performed following the same heating and cooling programme as for the actual measurement (6). The samples tested were about 15 mm long and 4 mm wide. Their thickness was about 2 mm, but varied slightly due to the sprayed coating thickness not being constant.

### Thermal Cycling

Thermal cycling experiments are one typical test performed to rank TBCs for gas turbine applications. Tests should simulate heating up and cooling down of the specimen to create failure such as spallation by thermal mismatch stresses resulting from cycling.

Thermal cycling tests have been performed at the University Karlsruhe (IKM). The cycling time is about 60 sec for heating up ( $T_{\text{TBC}} = 1250^\circ\text{C}$ ,  $T_{\text{substrate}} = 800^\circ\text{C}$ ) and cooling down to 60°C. Temperature measurements are performed using a pyrometer at the TBC surface and thermocouples on the substrate. Specimen geometry is a flat plate of 10x50mm, substrate thickness has been 2mm. Cycles are controlled by temperatures of the substrate, i.e. heating is restarted at a substrate temperature below 60°C. Maximum temperature at the TBC of 1250°C is settled for different specimens by varying distance from torch to specimen. By this the same temperature gradient of TBC surface to substrate back side is guaranteed and temperatures at the interface bond coat to TBC will be comparable. Additionally bending of the specimen can be measured using an inductive measurement device from the backside of the specimen. Fig. 2 exhibit an example of the temperature cycle obtained and the bending of the specimen measured.

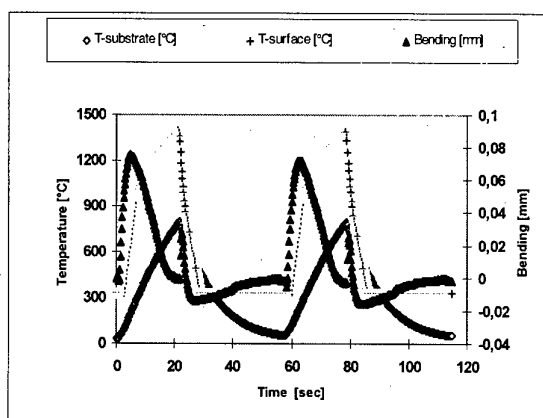


Fig. 2: Thermal cycles performed at IKM

### Combustor Sector Rig Test

In the course of a German national research programme combustion liner tiles with 7% $\text{Y}_2\text{O}_3$  stabilised  $\text{ZrO}_2$  were tested in the BR700 High Pressure 90°-sector rig. For the investigations on liner cooling a rig combustor was made and segments of outer and inner liner were cut out. The free space allows mounting of liner panels with various cooling designs. Hence, it is possible to test new cooling concepts using relative cheap panel specimen in a representative annular combustor. The objective of a test run is to demonstrate the thermal integrity and the temperature distribution of specimen close to engine take off conditions as well as to evaluate the potential for cooling air reduction. After ignition

the conditions are raised to take off rating with an inlet air pressure of 20 bar and inlet temperature of 885K. The facility limits the inlet pressure to 20 bar.

### 3. RESULTS

#### Spraying

Several parameter settings have been investigated to spray highly porous coatings. Typical temperature spectra measured during spraying are shown in Fig. 3 a and b.

Porosity values obtained for the different specimen are in the range of 8.5 to 20% (see fig. 4). For a number of specimen segmentation cracking has been found, which has been related to porosity values in the range of 8.5 - 12.5%.

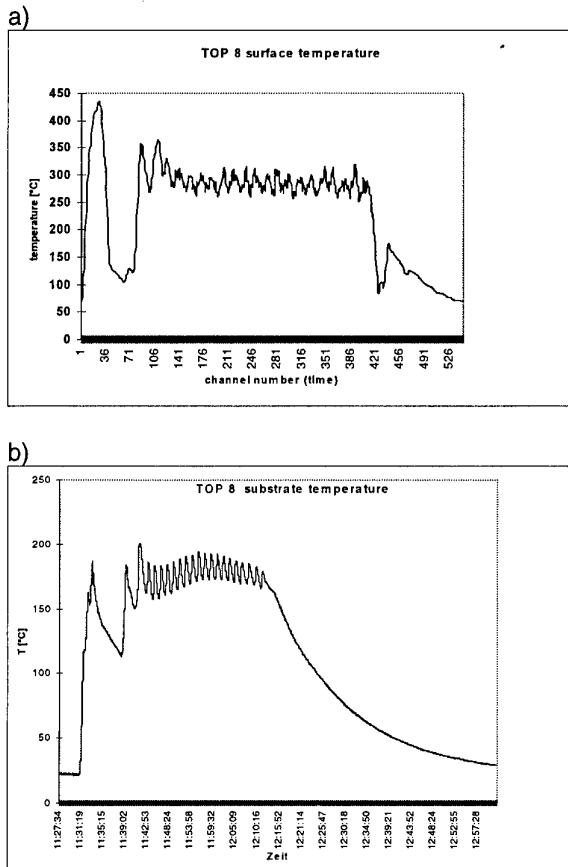


Fig. 3: Temperature readings during spraying from the coating surface (a) and substrate backside (b).

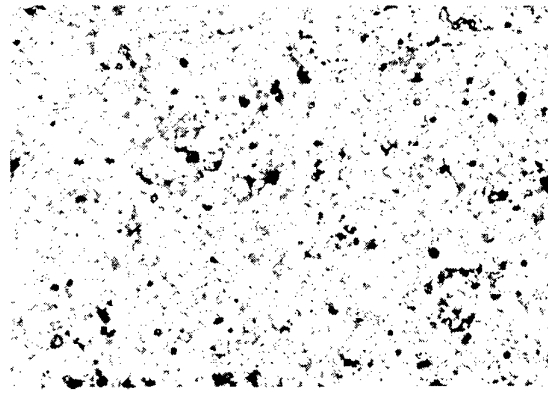


Fig. 4: micrograph of TOP 7, 15%porosity, x 150

#### Thermophysical and mechanical properties

Since the structure of the coatings is expected to vary through thickness two different loading types have been considered; where the top is either in the state of compression or of tension.

Mechanical properties determined are listed in table 1. Numbers given there are mean values out of the two loading types. Values from the experiments, where the surface of the TBC is under compression were found to be slightly higher in most cases. Youngs moduli found are lower than typical values reported on plasma sprayed TBCs, which lies in the range of 10 - 50 GPa (see for example ref. 8, 9, 10) .

Specimen	Youngs modulus [GPa]	failure strength [MPa]	failure strain [%]
Top 7	5.7	15.9	0.29
Top 8	6.9	13.6	0.22
Top 11	3.3	7.4	0.26
Top 12	8.8	30.4	0.37
Top 13	7.8	25.1	0.35

Table 1: Mechanical properties of thick TBCs

No significant change in these properties was observed in the experiments carried out up to 1000°C.

The failure strength and stress is found to be correlated to the Youngs Modulus determined (Fig. 5).



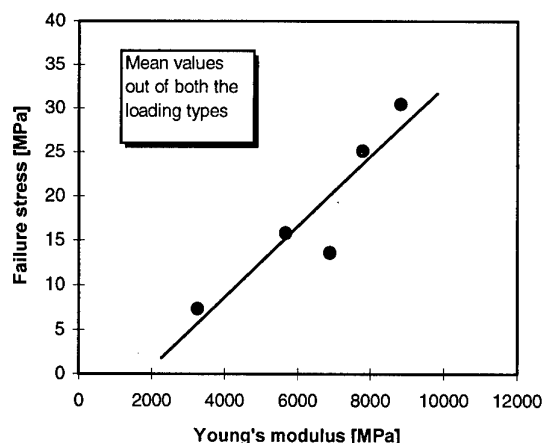


Fig. 5: Failure stress versus Young's modulus

The expansion coefficient of the samples tested seems to have a rather constant value of  $10.7 \cdot 10^{-6} \text{ K}^{-1}$ , which is typically for plasma sprayed 7% $\text{Y}_2\text{O}_3$  stabilised  $\text{ZrO}_2$  (8, 11). Obviously, the porosity has rather little influence. Over the whole temperature range, the thermal expansion coefficient is almost constant and differences during heating and cooling, a typical indicator of phase changes, cannot be determined.

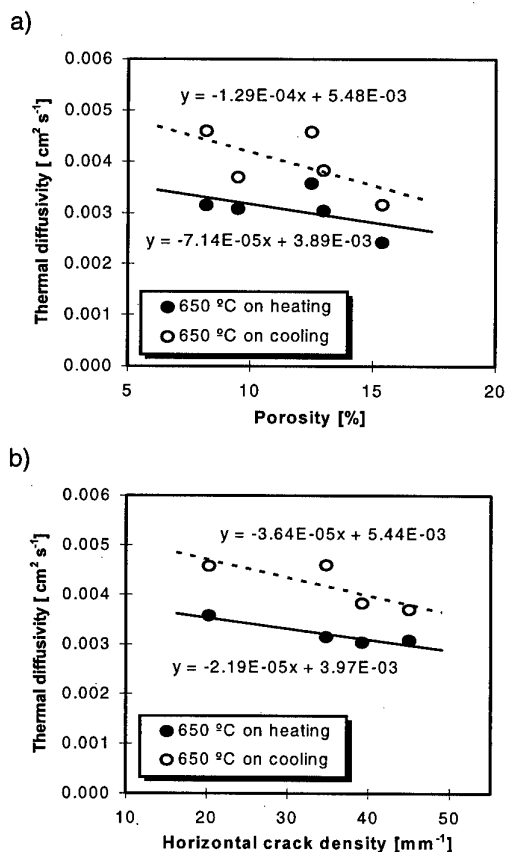


Fig. 6: thermal diffusivity versus porosity (a) and horizontal crack density (b)

For all specimen measured the thermal diffusivity obtained on cooling was higher than that observed during heating, showing that some irreversible change had occurred during first cycle only. The values obtained ranged from  $0.0029 \text{ cm}^2\text{s}^{-1}$  (Top 7) up to  $0.0057 \text{ cm}^2\text{s}^{-1}$  (Top 8). There is a general trend for the diffusivity to decrease with increasing porosity (Fig. 6a), but the effect is more pronounced when diffusivity is plotted against horizontal crack density (Fig. 6b).

From the diffusivity  $\alpha$ , the thermal conductivity  $\lambda$  can be calculated as:

$$\lambda = \alpha \cdot \rho \cdot c_p$$

with  $\rho$  and  $c_p$  being the density and the specific heat capacity respectively (6). Values ranged from  $0.8 \text{ W/mK}$  to  $1.5 \text{ W/mK}$  for the TBCs investigated here.

### Thermal cycling

Thermalshock test at BRR (performed at University Karlsruhe, IKM) used a cycling time of 60 sec for heating up ( $T_{\text{TBC}} = 1250^\circ\text{C}$ ,  $T_{\text{substrate}} = 800^\circ\text{C}$ ) and cooling down to room temperature and has been performed for several specimen up to 2000 cycles yet in comparison to a cycling life below 10 cycles for the first tests. Some specimen tested to 2000 cycles did not fail at all. Fig 7 was an overview about number of cycles obtained.

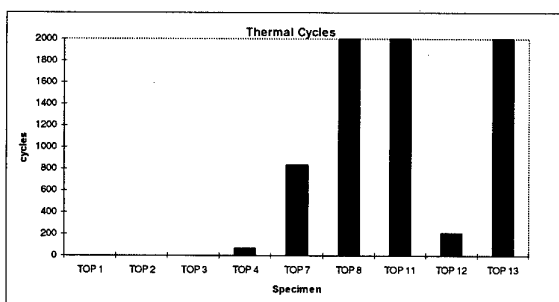


Fig 7: mean number of cycles reached for several specimen

The main influence on thermal cycling life is determined to be the temperature during spraying. A correlation from porosity to thermal cycling life could not be found (Fig. 8 and 9). Specimens exhibiting segmentation cracks instead of high porosity tend to show higher life times in the tests performed.

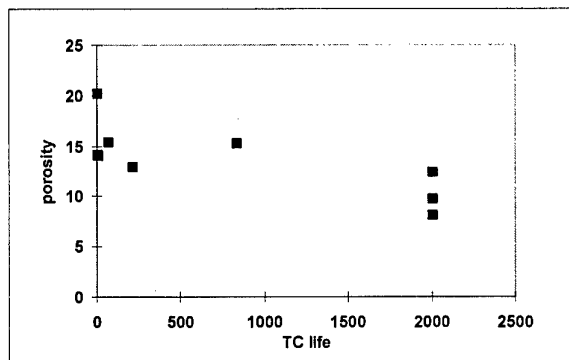


Fig. 8: porosity versus thermal cycling life

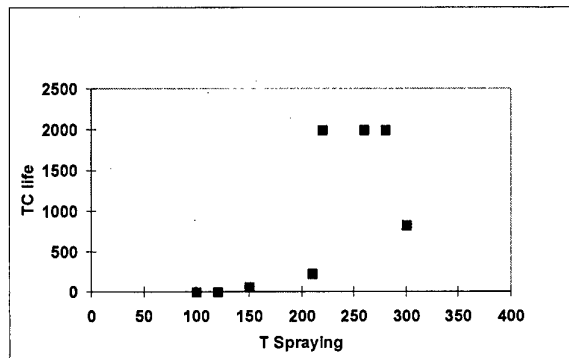


Fig. 9: Spray temperature versus thermal cycling life

FEM simulations have been performed using thermophysical and mechanical data described above to compare calculated and measured bending of the specimen during cycling. The bending behaviour (see Fig. 2) could be described qualitatively, quantitative deviations are expected to be related mainly to the quality of temperature data recorded during cycling.

#### Combustor Sector Rig Test

Two panels with different coating thicknesses (0.40 mm and 1.35 mm TBC thickness) were tested. The panel have been cooled by an array of impingement holes on the carrier. At the end of each tile the cooling air is used as a film for the hot side of the following tile. The tiles has been painted with thermal paint to investigate temperatures and temperature distributions. For the tiles with thick TBCs on the amount of cooling air used was reduced compared to the thin TBC tiles.

The specimens were not tested under identical conditions. The fuel to air ratio of the test with thin TBCs was approx. 5% lower than for the test with the thick coated specimen. This means that the

specimen with a thick TBC was exposed to slightly more severe conditions.

The coating surface of the specimen with the 0.4mm TBC thickness shows only small spots with temperatures above the 1160°C limit of the thermal paint, whereas the 1,35mm thick TBC specimen has approximately 50% of the surface hotter than 1160°C. It should be noted however that the amount of cooling air has been reduced for the thick TBC specimen.

The metal temperature on the cold side of the 0,4mm coated tile was around 830°C with peaks at approximately 900°C. The thick insulated tile had approx. 50°C lower temperatures on the inner side.

A cooling film on the hot side is still necessary for thick coated tiles to keep the maximum temperature of the top coating below 1250°C. With the current design temperatures of top - and bond coating a thickness of the ceramic layer of approx. 1,3 mm should provide the desired temperature drop of 350 to 400°C between the hot surface and the critical layer where the ceramic adheres to the bond coating.

With a thick coated tile approximately 25% of the cooling air required for a standard coated tile could be saved.

#### **4. CONCLUSIONS**

TBCs with a thickness up to 2mm and improved thermal cycling life have been developed as well as mechanical and thermophysical data determined.

Thermal cycling life is mainly influenced by spray temperature. Porosity has not found to be of high importance, but segmentation seems to be beneficial in the test performed.

Youngs Moduli in the range of 3 - 9 GPA has been determined. Failure strengths range from 7 to 30 MPA, failure strains from 0.2 - 0.4%.

Successful simulation of the bending of the specimen during cycling indicates that the materials data obtained are of reasonable quality.

Combustor segment rig testing demonstrated a potential of 25% cooling air reduction for the tile design investigated.

## ACKNOWLEDGEMENT

The authors thank all partners of the Brite Euram project BR7287, especially J. Wigren (VOLVO Aero Corporation) and Dr. C. Gualco (ANSALDO) for helpful discussions. The support from Dr. M. Alaya ( University of Karlsruhe, IKM) during thermal cycling experiment is gratefully acknowledged.

Part of the work has been performed within the Brite Euram Project BE 7287 funded by the CEC under the contract BRE2-CT94-0936.

The combustor sector rig testing has been funded by the German BMBF under HTGT Turbotherm contract 0326760B.

## REFERENCES

1. R. A. Miller, Journal of Thermal Spray Technology, Vol 6 (1), 35-42 (1997)
2. A. Bennett, Materials Science and Technology 2, 257 (1986)
3. F.C. Toriz, A.B. Thakker, S.K. Gupta, ASME 88-GT-279, 1988
4. J. Wigren, J. Dahlin, M.-O. Hansson, submitted to ASME '98
5. C. Gualco, A. Campora, S. Corcorato, R. Taylor, D. Schwingel, S. Oswald, Proceedings of the UTSC 1997.
6. D. Schwingel, C. Persson, R. Taylor, T. Johannesson, J. Wigren, High Temperature High Pressure 1995/1966, Vol 27/28, p. 273-281.
7. M. Alaya, PhD Thesis 1997.
8. R. McPherson, Surface and Coatings. Technology, 39/40 (1989) 173-181
9. W. Mannsmann, PhD Thesis 1995.
10. T.A. Cruise, B.P. Johnson and A. Nagy, Journal of Thermal Spray Technology, Vol 6 (1), 57- 66 (1997).
11. L. Pawlowski and P. Fauchais, Int. Materials Review Vol. 37 No. 6 (1992) p. 271-289.

## Advanced Processing of TBC's for Reduced Thermal Conductivity

J. R. Nicholls<sup>x</sup>, J. K. J. Lawson<sup>x</sup>, D. S. Rickerby<sup>\*</sup> and P. Morrell<sup>\*</sup>

<sup>x</sup> Cranfield University, Cranfield, Bedford UK

<sup>\*</sup> Rolls Royce plc, Derby, UK

### ABSTRACT

Zirconia-8wt% yttria thermal barrier coatings (TBC's) provide the potential to increase the operating temperatures within the modern aeroengine gas turbine.

Of particular interest are the columnar, strain tolerant thermal barriers produced by electron beam physical vapour deposition which can be applied to rotating components and can reduce the metal surface temperature by up to 150°C. Measured thermal conductivities for this columnar microstructure are typically 1.8-2.0 W/m.K. Should it be possible to reduce this value to that observed for plasma sprayed ceramics (0.9-1.0 W/m.K) then further benefits from the use of such a ceramic layer could ensue including either a further increase in operating temperature or a reduction in cooling air requirements.

This paper examines the advanced processing of TBC's with the aim of reducing thermal conductivity. The role of coating thickness is reviewed, where it is shown that for thin coatings, circa 100µm thermal conductivities of 1.0 W/m.K can be achieved. This is thought to be due to increased scattering of thermal waves close to the early confused growth region. The possibility of further reducing thermal conductivity by using layered structures is examined. These structures have been manufactured by control of rotation, controlled dwell and through the use of plasma assistance during the deposition process. The benefits of such layers in scattering thermal waves is discussed.

### LIST OF SYMBOLS

x total coating thickness  
 $x_1$  thickness of inner "nucleate" zone  
 k thermal conductivity for the complete TBC.  
 $k_1$  thermal conductivity of the inner "nucleate" zone  
 $k_2$  thermal conductivity of the outer columnar structure  
 $k_p$  is the phonon thermal conductivity,  
 $k_r$  is the contribution to thermal conductivity due to radiation,  
 $C_v$  is the specific heat capacity at constant volume,  
 $\rho$  is the density of the material,  
 $\bar{v}$  is the mean velocity of phonons in the material (speed of sound)

$l_p$  is the phonon mean free path.

$\sigma$  is Stefan Boltzmann's constant =  $5.67 \times 10^{-8}$  W/(m<sup>2</sup>.K),

T is the thermodynamic temperature (K),

n is the refractive index of the material,

$l_r$  is the photon mean free path

$l_i$  is the intrinsic mean free path of phonons due to the lattice and differing ion masses,

$l_{vac}$  is the mean free path of phonons due to vacancies in the lattice,

$l_{gb}$  is the mean free path of phonons due to grain boundaries,

$l_{strain}$  is the mean path of phonons due to local strain centres within the lattice.

### 1. INTRODUCTION

The drive to improve engine performance and fuel efficiency, while reducing emissions, has meant that the operating temperatures of the turbine section of aero-engines has increased significantly over the last 20 years. This has been achieved by novel material design, improved cooling technologies and better manufacturing methods [1]. The latest development in this drive for improved performance is to apply thermal barrier coatings to turbine aerofoil surfaces. Thermal barrier coatings offer the potential of increasing turbine operating temperatures by up to 150°C, without any increase in metal operating temperatures (Figure 1), or alternatively permits a reduction in the mass of cooling air required while maintaining the turbines operating temperature giving improved specific fuel consumption.

Thermal barrier coatings (TBC's) have been used in the gas turbine engine since the 1970's [2-4] to lower mean metal temperatures. These coatings, based on partially stabilised zirconias, are deposited using thermal spray processing and have performed well in service, extending the lives of combustion chambers and annular platforms of high pressure nozzle guide vanes within the turbine section of the engine [5]. However, the use of thermal sprayed TBC systems have not generally been

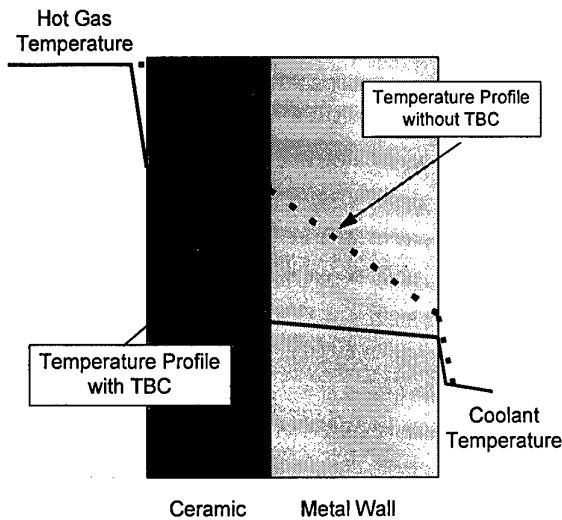


Figure 1 Schematic of thermal barrier coating systems showing thermal gradient subtended across the ceramic layer

extended to high-pressure turbine aerofoils, due to their poor surface finish, high heat transfer coefficient, low erosion resistance and poor mechanical compliance. Success in coating turbine aerofoils has been achieved by adopting electron beam physical vapour deposition (EB-PVD) technology to coat these parts. Thermal barrier coatings deposited by EB-PVD processes have a good surface finish [5], columnar microstructures with high strain compliance [5,6] and good resistance to erosion [5,7] and foreign object damage [7]. EB-PVD thermal barrier coatings have been used in production since 1989 [8].

Unfortunately, the microstructure which gives the EB-PVD TBC system its high strain compliance and good erosion resistance leads to a relative high thermal conductivity when compared to thermally sprayed coatings (Figure 2). Table 1 compares the properties and performance of commercially produced thermally sprayed and EB-PVD deposited PTSZ thermal barrier coatings. Previous work in the development of ceramic alloy compositions indicated that there is opportunity to reduce the thermal conductivity of the zirconia-based

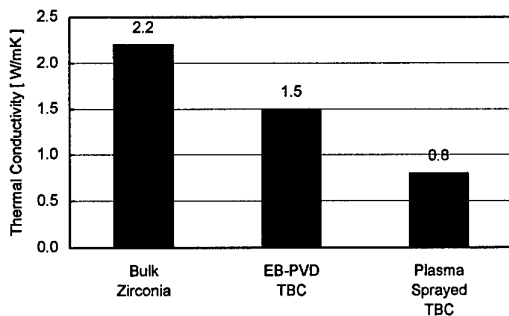


Figure 2 Thermal conductivities of bulk, EB-PVD and thermally sprayed zirconia-yttria materials at room temperature.

systems by alloying with ceria and yttria [9]. This paper discusses the theoretical models of heat transfer in solids with regard to the reduction of the thermal conductivity, and reviews these against the measured values on TBC coatings engineered for low conductivity.

Table 1 Properties of TBC's at Room Temperature

Property/Characteristic	EB-PVD	Plasma Sprayed
Thermal Conductivity (W/mK)	1.5	0.8
Surface Roughness ( $\mu\text{m}$ )	1.0	10.0
Adhesive Strength (MPa)	400	20-40
Young's Modulus (GPa)	90	200
Erosion Rate (Normalised to PVD)	1	7

## 2. THEORY OF CONDUCTION

The theory of thermal conductivity in solids is fully described elsewhere and will only be briefly reviewed here [10-12]. In crystalline solids heat is transferred by three mechanisms, (i) electrons, (ii) lattice vibrations and (iii) radiation. As zirconia and its alloys are electronic insulators (electrical conductivity occurring at high-temperatures by oxygen ion diffusion), electrons play no part in the total thermal conductivity of the system.

The contribution to thermal conductivity from lattice vibrations (the quanta of which are known as phonons) is given by:

$$k_p = \frac{1}{3} \int C_v \rho \bar{v} l_p \quad [1]$$

Whilst equation [1] describes the phonon conductivity, the total thermal conductivity of the material is higher than this figure due to the contribution to the thermal conductivity by radiation. Zirconia is susceptible to radiation transport (photon transport) at high-temperatures (Figure 3). The contribution to the total thermal conductivity due to radiation can be written;

$$k_r = \frac{16}{3} \sigma n^2 T^3 l_r \quad [2]$$

Therefore the total theoretical thermal conductivity of zirconia-based systems is merely the sum of the two terms :

$$k = k_p + k_r \quad [3]$$

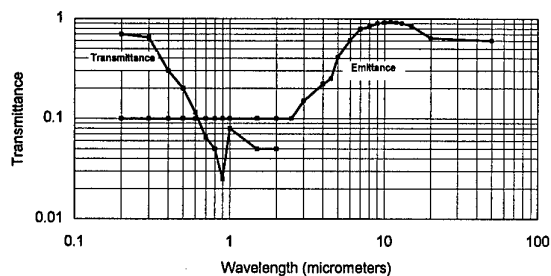


Figure 3 Emittance and transmittance of zirconia as a function of wavelength.

If the mean free path for radiative transport is assumed to be the thickness of the coating then, for an application where the surface of the TBC is operating at 1473K and the interface operates at 1323K the contribution to total thermal conductivity due to radiation could be as high as 1 W/m.K. In this case the heat flux which could arise through radiation is of the order of 80-90 kW/m<sup>2</sup> out of typical total values of 800 kW/m<sup>2</sup> seen in high heat flux regions in engines. Clearly the mean free path of photons is not the thickness of the coating and therefore radiation is attenuated within the TBC structure reducing the contribution to the total conductivity from the value listed above. However, as the operating temperature increases the contribution to thermal conductivity from radiation becomes more important.

Therefore to lower the intrinsic thermal conductivity of a system, reductions in the specific heat capacity, phonon velocity and mean free path, density or refractive index are needed. The specific heat capacity at constant volume for any system is constant at a value of  $3.kbN \approx 25 \text{ J/(K.mol)}$  [13] above the Debye temperature (380K [13] for zirconia). Therefore to engineer a lower thermal conductivity in zirconia-based ceramics, the only options are to lower the mean free paths of the heat carriers, to lower the velocity of the heat carriers, or to lower the density of the material.

In real crystal structures scattering of phonons occurs when they interact with lattice imperfections in the ideal lattice. Such imperfections include vacancies, dislocations, grain boundaries, atoms of different masses and other phonons. Ions and atoms of differing ionic radius also scatter phonons by locally distorting the bond length and thus introducing elastic strain fields into the lattice. The effects such imperfections cause can be quantified through their influence on the phonon mean free path. This approach has been used by several workers, for which the phonon mean free path ( $l_p$ ) is defined by:-

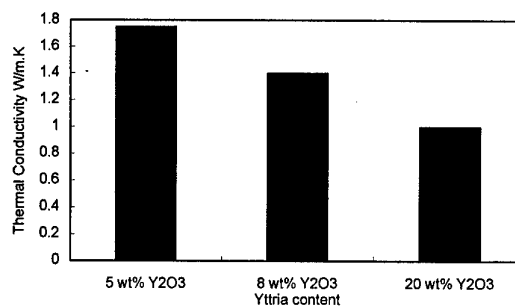


Figure 4 Theoretical conductivity of EB-PVD zirconia ceramics as a function of yttria content.

$$\frac{1}{l_p} = \frac{1}{l_i} + \frac{1}{l_{vac}} + \frac{1}{l_{gb}} + \frac{1}{l_{strain}} \quad [4]$$

Of these the grain boundary term has the least effect on the phonon mean free path, whilst the intrinsic lattice structure and strain fields have the most significant effect. For example, the addition of NiO has a marked effect on the intrinsic mean free path in MgO, reducing the mean free path by a factor of 10 [14]. However, the addition of alloying oxides has the largest effect on simple systems, the zirconia-yttria crystal system is more complex than MgO and the effect of alloying additions is less. For zirconia based systems, workers in the field have demonstrated that increasing the level of yttria in the alloy, decreases the thermal conductivity [15,16] which is commensurate with shorter intrinsic mean free paths with increasing yttria content (Figure 4).

Further to the reduction in the intrinsic mean free path due to alloying, local strain fields and vacancies can be generated in the lattice. These strain fields and vacancies act to scatter phonons directly increasing phonon dispersion in the lattice. With increased dispersion, there is a high probability that phonon-phonon interactions will occur whereby the mean free path will be further reduced. The benefit of a 20-30% lower thermal conductivity by adding divalent transition metal dopants, as reported by Tamarin et al [17] is attributed to this effect and in part to the dopants ability to attenuate radiation within the ceramic layer.

For thermally sprayed TBC's the typical grain size is of the order of 1  $\mu\text{m}$  and for EB-PVD TBC's the grain size varies from c.a.  $<<1 \mu\text{m}$  at the interface whilst the column length is 100-250  $\mu\text{m}$  in the bulk of the coating. These dimensions have little effect on the mean free path of phonons. However, these dimensions can have an effect on the radiative transport in the ceramic, where a reduction in the mean free path for photons from 250  $\mu\text{m}$  to 1  $\mu\text{m}$  would cause a reduction in the radiation contribution to total thermal conductivity from 1 to

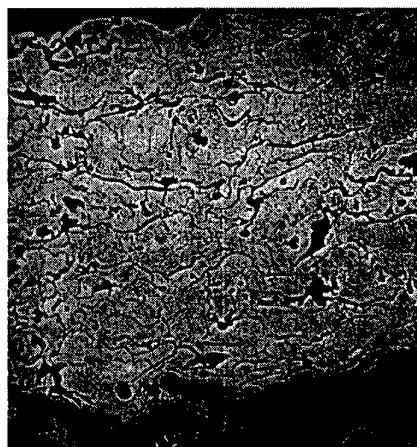


Figure 5 photomicrographs of thermally sprayed (top) and EB-PVD TBC's (bottom), showing the differences in microstructure.

0.005 W/m.K from equation [2].

In real coating systems grain boundaries are associated with air-gaps (inter-splat boundary porosity and inter-column porosity in thermally sprayed and EB-PVD TBC's respectively - Figure 5) and these have a significant effect on the thermal conductivity. The alignment of the inter-splat boundaries in the case of the thermally sprayed coatings has by far the larger effect reducing the conductivity of zirconia-yttria TBC materials from theoretical values of 2.2-2.6 W/m.K to values in the range 0.7-0.9 W/m.K (refer to Table 1). This behaviour is well documented and is due to the reduction of mean free paths of photons (radiative heat transfer) by scattering at the splat boundaries, but more importantly, by the reduction in the composite thermal conductivity due to the air-gaps [18].

### 3. THERMAL CONDUCTIVITY IN EB-PVD TBC's

Whilst the thermal conductivity of air plasma sprayed

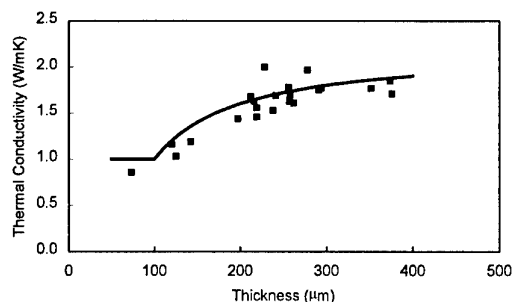


Figure 6 Effect of coating thickness on thermal conductivity of EB-PVD at room temperature.

PYSZ ceramic and bulk zirconia are essentially insensitive to coating thickness this is not the case for EB-PVD ceramics [19]. This behaviour is illustrated in Figure 6.

The explanation for this increase in thermal conductivity with thickness relates to the unique columnar microstructure which characterise PVD ceramics when grown from the vapour phase. During deposition, competitive growth occurs, as illustrated in Figures 7 and 8. This results in a decrease in the number of oblique columnar boundaries in the outer part of the coating as grains with "less favoured" growth directions are eliminated from the coating structure. The number

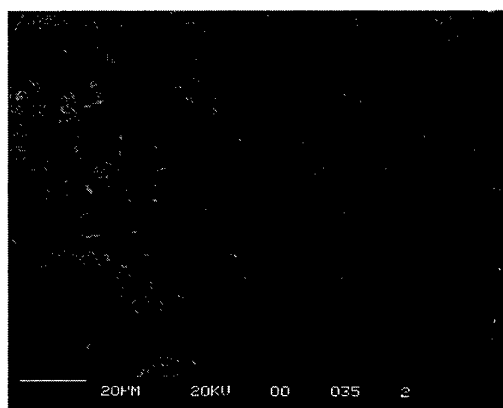
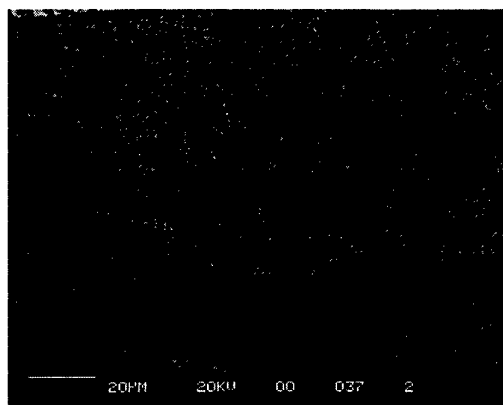


Figure 7 Differences in the column density for the nucleate zone (top) and the steady state region (bottom)

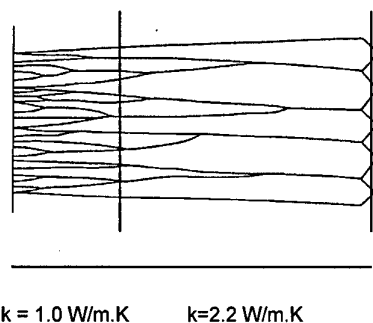


Figure 8 Schematic of an EB-PVD TBC and the associated variation of thermal conductivity for the two-layer model

and distribution of columnar boundaries is responsible for the reduction in thermal conductivity. More boundaries mean additional centres capable of scattering thermal waves. Thus the thermal conductivity of an EB-PVD TBC can be modelled successfully using a two-layer model, shown schematically in Figure 8 [19]. The inner "nucleate" zone is dominated by defect/grain boundary scattering and this results in a lower conductivity of around 1.0 W/m.K. With increasing thickness, the structure is characterised by a dominant crystallographic texture and the thermal conductivity increases as the outer part of the coating becomes more perfect. In this outer zone the thermal conductivity approaches that of bulk zirconia at circa 2.2 W/m.K. The overall coating thermal conductivity results from the combined effect of these two layers and can be predicted using a rule of mixtures. For coating thicknesses ( $x$ ) less than  $x_1$  (100  $\mu\text{m}$  for the schematic illustrated in Figure 8) then

$$k = k_1 \quad [5a]$$

while for coating thickness ( $x$ ) greater than  $x_1$

$$k = \frac{x_1 k_1}{x} + \frac{(x - x_1)}{x} k_2 \quad [5b]$$

Figure 9 provides a comparison between predicted and measured thermal conductivities for EB-PVD zirconia thermal barrier coatings, illustrating the good agreement to experiment of this two layer thermal conductivity model.

It should be expected that the thermal conductivity of chemical vapour deposited (CVD) ceramic should show a similar thickness dependence to EB-PVD zirconia as both coating morphologies are grown from the vapour phase. A study on the thermal conductivity of CVD deposited synthetic diamond confirms this hypothesis [19,20].

From the foregoing, it is evident that the manufacturing

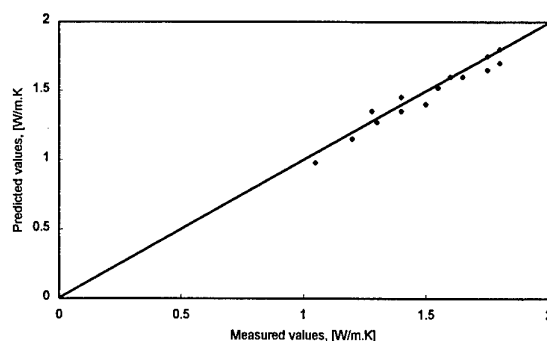


Figure 9 Comparison between predicted and measured thermal conductivities of EB-PVD TBC's of varying thickness.

process used to produce the thermal barrier coating strongly affects the coatings resultant thermal conductivity. Lamellar interfaces, parallel to the coating/substrate interface as produced in plasma sprayed ceramic, act to strongly scatter thermal waves reducing the coatings thermal conductivity. This behaviour is observed to a lesser extent in the inner growth zone of EB-PVD deposited coatings due to the inclined nature of many of these inner boundaries. Defect scattering must also play a role in this early deposition zone of EB-PVD ceramics. However, due to the competitive nature of coating growth for vapour deposited coatings a dominant growth texture is developed. This vertically aligned microstructure of the outer layer of an EB-PVD coating results in thermal conductivities close to that for the bulk ceramic.

These observations would suggest that to further reduce the thermal conductivity of EB-PVD TBC's one should introduce layers and/or additional phonon scattering centres into the coating.

#### 4. REDUCTION OF THERMAL CONDUCTIVITY IN EB PVD COATINGS BY LAYERING

The former section discussing heat transfer into and through the ceramic has highlighted a number of methods capable of reducing the thermal conductivity of the zirconia ceramic. To reduce radiative transport 'colouring' and 'layering' are possibilities, while introducing 'atom dimension defects', 'local changes in ceramic density' and 'local variation in ceramic elastic modulus' may be effective in reducing phonon conduction.

As indicated earlier the plasma sprayed TBC structure is such that the contribution to total thermal conductivity by radiation is minimised by the lamellar splat boundaries at a typical spacing of 1  $\mu\text{m}$ . If this attenuation of the radiative transport mechanism could be applied to EB-PVD it could make a significant contribution to the reduction of the thermal conductivity,



especially at high temperatures. Thus layering of the ceramic appears a most promising route to lower the ceramics thermal conductivity, especially if it can be coupled with changing the local density or elastic modulus of the material. A suitable periodicity of the layers should be  $0.2\text{--}2.0\mu\text{m}$  (between  $\lambda$  and  $\lambda/4$  for an incident radiation of  $0.5\text{--}5.0\mu\text{m}$ ), which is able to scatter photons and thus reduce radiative transport. This concept of layering within each column of an EB-PVD coating is illustrated schematically in Figure 10.

To reduce phonon conduction layer periods would have to be of near atomic dimensions ( $0.3\text{--}2.0\text{nm}$ ) and this is not considered feasible, although it should be possible to locally change either the elastic modulus or density of the ceramic by introducing atomic level defects into the lattice.

The PVD process offers a number of ways to tailor coating microstructures and thereby introduce multi-layers, since both the column angle and morphology may be influenced by variations in the flux density and the direction this flux subtends to the substrate surface [21].

Three alternative EB-PVD processing routes could be used to generate layering within the columns.

- Route 1 varying the speed of rotation of the parts during coating
- Route 2 rocking the substrate between two fixed tilt angles.
- Route 3 varying the degree of ion bombardment to change the density of the ceramic.

The principle behind each of these routes is to introduce interfaces into each of the column structures which are essentially parallel to the ceramic/bond coat interface, but without disrupting the overall columnar structure that provides the coating with its good strain tolerance and erosion resistance. Thus, these layered structures should offer the best of the properties currently available from commercial EB-PVD coatings and thermally sprayed ceramic coatings, namely low thermal conductivity, good strain tolerance and good erosion

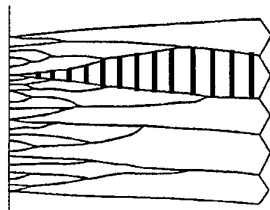


Figure 10 Schematic of layering within an EB-PVD column to reduce radiative heat transfer within the coating.

resistance. The concept is the subject of a European patent [22].

This paper focuses on the use of ion bombardment to create layers in the EB-PVD structure with varying density.

#### 4.1 Layering by Plasma Assisted Deposition

This method uses a glow discharge plasma to vary the density of the ceramic during deposition. Figure 11 illustrates a typical micrograph of the morphological changes that can be introduced.

The layers were produced by switching the D.C. bias applied to the substrate between high and low levels during deposition. This has the effect of periodically changing the degree of ion bombardment and thus altering the density of the layers produced. The micrograph illustrated in Figure 11, was produced by switching between a D.C. bias with a peak voltage of  $2500\text{V}$  and ground. The degree of bombardment that is attained depends on the applied bias and local current density, current densities typically greater than  $0.1\text{mA}/\text{cm}^2$  are required to achieve a significant density change [22].

The measured thermal conductivity for this microstructure is significantly lower than that for a coating produced without ion bombardments (Figure 12). Reductions of the order of 37-45% compared to state-of-the-art EB-PVD TBC's have been measured for these layered structures that are approaching the values for thermally sprayed TBC systems.

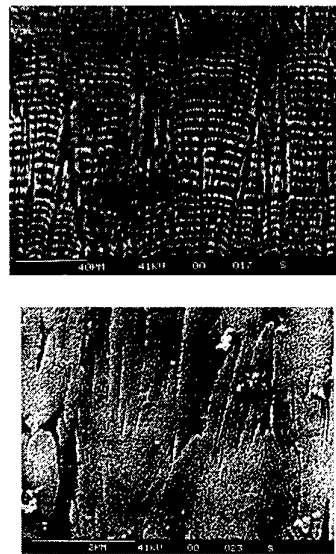


Figure 11 Layered structures introduced by PAPVD processing of the ceramic. Top general view, bottom detail of a boundary region.

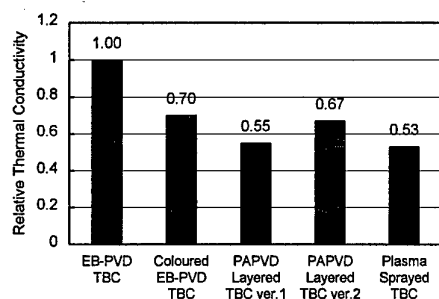


Figure 12 Relative thermal conductivity of modified EB-PVD TBC systems compared to state-of-the-art EB-PVD and thermally sprayed TBC's.

Clearly, the combination of layering at micron dimensions and the introduction of density change from layer to layer work in combination to significantly reduce the thermal conduction of the coating. As discussed earlier the layering periodicity has been selected to significantly reduce photon transport, while local changes in layer density act to scatter phonons and thus reduce thermal conduction by lattice vibrations.

Using this process route it has been possible to introduce layers into individual columns, without change the overall vertical columnar microstructure required for good strain, tolerance and good erosion resistance. For example, it can be seen from Figure 13 that layering produces no significant deterioration to the erosion performance of an EB-PVD thermal barrier coating.

Also it is possible by programming the sequencing of bias application to tailor the position of the layers in the coating. This potentially has benefits in allowing the properties of the coating to be varied from the surface to the interface. For example more erosion resistant structures could be generated at the outer surface of the coating with the application of bias in this region, whilst the inner zone of the coating is layered to lower the thermal conductivity. To demonstrate this a coating was produced where the early deposition has no bias applied,

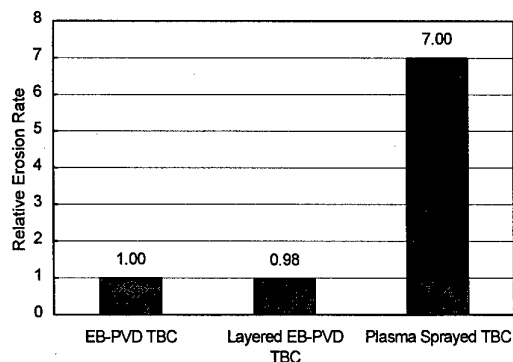


Figure 13 Erosion performance of various modified EB-PVD coatings.

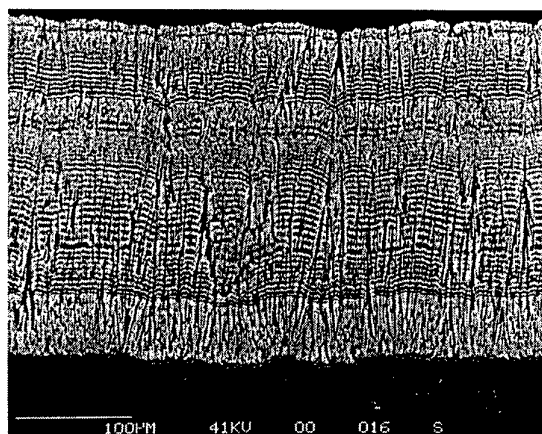


Figure 14 An example of a tailored EB-PVD layered structure.

followed by a region with bias and high ion current density to produce maximum density changes between layers. This was followed by a region of low current density giving low density differences between layers and finally a region of high current density giving a denser structure. (Figure 14).

#### 4.2 Addition of dopants to reduce thermal conductivity

Tamarin and co-workers [17] have examined the addition of divalent transition metal oxides to reduce the thermal conductivity of zirconia-yttria TBC's. As eluded to earlier this has two effects, firstly to reduce the phonon transport in the material and secondly a reduction in the radiative transport mechanism. The use of a divalent transition metal oxide introduces vacancies as well as strain centres into the lattice both of which will reduce the phonon mean free path. In addition this doping changes the colour of the TBC material to dark grey, reducing radiation transport in the visible range and by inference in the near infra-red.

Following this concept of dopant additions, further reduction in phonon thermal conductivity could be achieved by the selection of low levels of dopant which maximise lattice strain and lattice anharmonicity. This is best achieved by the addition of transition metal ions with high mass and large ionic radii.

#### 5. SUMMARY OF REMARKS AND CONCLUSIONS

This paper has examined the factors that control the thermal conductivity of thermal barrier coatings and has highlighted the significance of three factors capable of lowering the coating thermal conductivity.

1) **Colouring** of the coating by addition of dopant materials can be used to increase the opaqueness to infra-red radiation and therefore radiative transport through the coating.

2) **Atomic level defects**, such as atoms of differing mass, vacancies etc. can be introduced by adding dopants or by ion bombardment. These are effective in reducing phonon conduction, i.e. heat transfer by lattice vibrations (Figure 15). A recent patent by Strangman [23] describes a TBC system with stabilised porosity wherein the pores are coated with a noble metal (Figure 16). This stabilised porosity along with the noble metal coating is claimed to reduce the thermal conductivity and improve its sintering behaviour at high temperatures.

3) **Layering**, can be used to introduce interfaces parallel to the ceramic bond coat interface and is effective in reducing both radiative and phonon transport. The layer periodicity when set at levels between 0.5 and 2.0  $\mu\text{m}$  is effective in reducing photon transport, when coupled with a significant change in layer density from one layer to another. These local changes to the ceramic density are also believed to be effective in reducing phonon conduction. Thus layering has been shown to be a most effective method of modifying the thermal conductivity of EB-PVD thermal barriers (Figure 16).

By using a switched D.C. bias, applied to the substrate it is possible to introduce these layers during the deposition processes. The degree of ion bombardment controls the density changes achieved, thus allowing tailoring of the ceramic microstructure to engineer the most appropriate mechanical and thermal properties in the coating for the operational requirements placed on it.

## 6. ACKNOWLEDGEMENTS

The authors wish to acknowledge the sponsorship of the

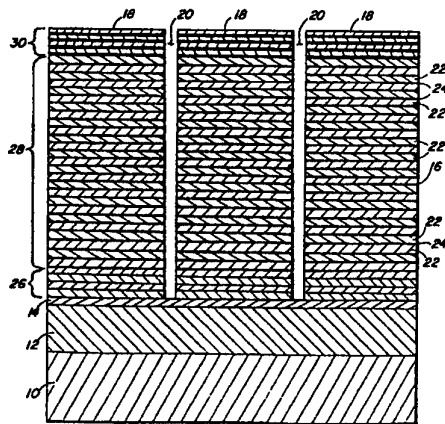


Figure 15 Schematic of EB-PVD TBC systems with stabilised porosity after Strangman

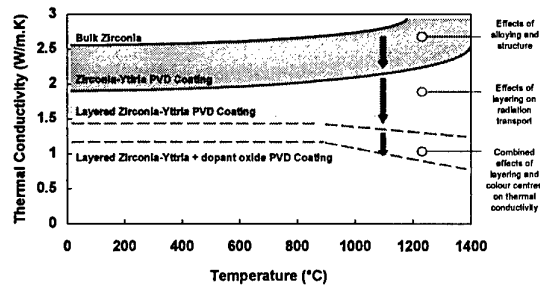


Figure 16 Summary of the reductions achievable in thermal conductivity in zirconia thermal barriers as a result of alloying and layering the structure.

following organisations during work on the development of advanced thermal barrier coating systems: Rolls Royce plc, DERA, CEC and the EPSRC.

## 7. REFERENCES

1. Brandon J. R., Taylor R. and Morrell P. "Microstructure, composition property, relationships in plasma-sprayed thermal barrier coatings", *Surface and Coatings Technology*, **50**, (1992) 141.
2. Liebert C. H. et al, "Durability of zirconia thermal barrier coatings on air cooled turbine blades in cyclic jet engine operation", NASA TMX-3410 (1976).
3. Grisaffe S. J., "Thermal barrier coatings" NASA TMX-78848 (1978).
4. Driver D., Hall D. W. and Meetham G. W., in "The development of the gas turbine engines", Applied Science Publishers (London), 1981.
5. Rickerby D. S. and Morrell P., "Design and development of EB-PVD thermal barrier coatings for gas turbines" in "High Temperature Engineering" Institute of Materials, London UK (1997) to be published.
6. Strangman T. E. "Tailoring zirconia coatings for performance in a marine gas turbine environment" *Journal of Engineering for Gas Turbines and Power*, Vol. 112.
7. Nicholls J.R., Yaslier Y. and Rickerby D. S., "Erosion and foreign object damage of thermal barrier coatings" in 4<sup>th</sup> Int. Symp. on High Temperature Corrosion, Les Embiez, France, May 1996
8. Meier S. M. and Gupta D. K., "The evolution of thermal barrier coatings in gas turbine engines applications", *Trans. ASME*, **116**, (1994), 250.
9. Ragaswami S. European Patent, EP0166 097 (1988)
10. Klemens P. G., "Thermal conductivity of solids", Ed. R. P. Tye, Volume 1, Publ. Academic Press London (1969).
11. Parrott J. E. and Stuckes A. D. "Thermal

- conductivity in solids", Publ. Pion Limited, (1975).
12. Peterson R. B., "Direct simulation of phonon mediated heat transfer in a Debye crystal", Trans ASME J. Heat Transfer 116, 815, (1994).
  13. Slack G.A., "Thermal conductivity of nonmetallic solids", in Solid State Physics; Advances in research Applications, 34, pp1-74, Academic Press (1979)
  14. Kingery W.D., "Introduction to Ceramics", 2nd Edition, J.Wiley (1976).
  15. Morrell P. and Taylor R., "Thermal diffusivity of thermal barrier coatings or ZrO<sub>2</sub> with Y<sub>2</sub>O<sub>3</sub>", High Temperatures-High Pressures, 17, (1985) 79.
  16. Klemens P. and Gell M., "Thermal conductivity of TBC's", in the proceeding of the TBC Workshop, Cincinnati Ohio, May (1997).
  17. Tamarin Y. A., Kachanov E. B. and Zherzdev S. V., "Thermophysical properties of ceramic layers in EB-TBC" in 4<sup>th</sup> Int. Symp. on High Temperature Corrosion, Les Embiez, France, May 1996
  18. Hassleman D.P.H and Singh J.P, "Effects of cracks on thermal conductivity", J. Compos. Mater., 12, 403, (1978).
  19. Lawson K. J., Nicholls J. R. and Rickerby D. S., "The effect of coating thickness on the thermal conductivity of CVD and PVD coatings", 4<sup>th</sup> Int. Conf. on "Advanced in Surface Engineering", Newcastle, UK, 1996.
  20. Graebner J. E., Jin S., Kammlott G. W., Bacon B., Seibles L. and Banholzer W., J. Appl. Phys. 71, (1992) 5353.
  21. Lawson K. J., Nicholls J. R. and Rickerby D. S., "Thermal conductivity and ceramic microstructure" in High Temperature Engineering" Institute of Materials, London UK (1997) to be published.
  22. Rickerby D. S., European Patent EP 0628090 B1 (1993).
  23. Strangman, T.E., US Patent, 5,512,382, (1995).

## TBCs ON FREE-STANDING MULTILAYER COMPONENTS

P. G. Tsantrizos  
G. E. Kim  
T. A. Brzezinski  
PyroGenesis Inc.  
1744 William, Montreal  
Quebec, Canada H3J 1R4

### **ABSTRACT**

PyroGenesis Inc. has developed a unique process for the production of components designed to operate in the hot section of gas turbines. The new process involves spray forming multilayer components by Vacuum Plasma Spraying (VPS) onto molds and subsequently separating the mold from the near net-shape free-standing component. Advanced TBCs have been developed and incorporated into the multilayer structure in an effort to extend the component's high temperature performance capabilities. The spray formed components are heat treated to improve the mechanical properties of the superalloys. PyroGenesis has used the VPS near net-shape forming process to fabricate closed components with a TBC inner layer, consisting of calcia silica ( $\text{Ca}_2\text{SiO}_4$ ) and zirconia partially stabilized with yttria (PSZ), a CoNiCrAlY bond coat, and an IN-738LC outer layer. Preliminary results indicate that the spray formed components have excellent mechanical properties, can operate at much higher temperatures than similar conventionally fabricated components and require less cooling. The TBCs showed uniform thickness and microstructure with a smooth surface finish. The bond coat and structural superalloy layers were very dense with no signs of oxidation at the interface.

After heat treatment, the mechanical properties of the IN-738LC compare favourably to cast materials. Finally, the cost of spray forming multilayer components is lower than the cost of conventional fabricating options.

### **INTRODUCTION**

Combustion system components of gas turbine engines are constructed from high service temperature materials, such as ceramics and superalloys. For complex hot gas containment components, such as combustor liners and transition ducts, the current fabrication process consists of: (i) mechanically forming several sections of the component; (ii) thermal spraying the inner surface of each section to form the thermal barrier coating (TBC); (iii) welding the sections; (iv) thermal spraying the protective TBC coating on the welds, whenever possible; and (v) laser drilling thousands of small holes into the structure through which cooling air is passed, to provide for additional film cooling. Several significant problems exist with components which have been fabricated in this fashion. One problem is the inhomogeneity at the welds. Weld regions act as weak sites from which failure may initiate due to poor quality finish of both the ceramic top coat

and metallic bond coat of the TBC. The rough surface of the TBC, inherent to this approach and particularly of the weld regions, leads to an undesirable change in flow pattern of the hot gas. Moreover, because the current fabricating process consists of mechanically forming sections of the component, there is a limitation on the choice of applicable superalloys (only superalloys with relatively high elongation can be used). Finally, the cost of drilling the thousands of small holes required for cooling is exorbitant and the use of cooling air significantly adds to the size of the compressor.

There have been numerous studies on spray forming of metals and ceramics via VPS [1, 2, 3, 4]. However, to the authors' knowledge, there has not been any published work on spray forming complex shape components with a ceramic inner layer, followed by multiple metallic layers. A closed component with an inner ceramic layer has potential applications for thermal barrier or wear protection components. In the absence of film cooling, the use of a conventional thermal barrier coating does not provide adequate insulation to protect the component. The temperature drop across conventional TBCs is approximately 120°C. In order to protect the combustion liners and transition ducts of an advanced turbine operating without film cooling, a temperature drop across the barrier of approximately 350°C is required. Thus, both a new fabrication technique and a dramatically improved TBC is needed for the proposed application.

PyroGenesis' experience in VPS-applied zirconia based TBC systems (both top and bond coats) for gas turbine engine applications has revealed superior thermal cycling performance at a lower cost over the commonly used TBC's, where the bond

coat is deposited by VPS and the top coat by APS. NASA's Marshall Space Flight Center [5] has reported a five fold increase in thermal cycling over the conventional TBC, when both the bond and top coats are applied via VPS. Furthermore, PyroGenesis has experimented with advanced TBC's which can be much thicker than conventional zirconia and offer significantly improved thermal protection.

PyroGenesis has committed itself to addressing the problems associated to current combustion system components and their fabrication method, by combining the advantages of spray forming and advanced TBCs with those of the VPS technology.

## **PROCESS DESCRIPTION**

A suitable mold material was selected and surface machined to the inner geometry of the desired component. The mold was then cleaned and placed inside the VPS chamber, ready for service. The following unit operations were then used to fabricate multilayered combustion system components by VPS spray forming: (i) mold preconditioning; (ii) preheating the mold to a suitable temperature and depositing the TBC layer; (iii) preheating the mold to a higher temperature and depositing the bond coat and the structural superalloy; and (iv) removing the mold from the near net-shape component. Figure 1 illustrates the process.

The design of the mold is of particular importance in the VPS spray forming process. The mold is used both to define the shape of the component and to control the energy balance of the process, a critical issue in controlling the stresses within the spray formed structure.

The mold surface was preconditioned using the plasma jet; this was a critical step which ensured proper bonding between the mold and the deposit during spray forming, yet allowed for proper detachment at the same interface upon cooling. The deposition onto the mold started with the TBC layer (up to 1.5 mm thick), followed by a CoNiCrAlY bond coat layer (150  $\mu\text{m}$ ), and finally reinforced with a thick IN-738LC structural layer (5 mm). Between layers the mold was preheated in an effort to minimize stresses within the deposited structure. Upon completion of the deposition step, the coated mold was cooled to room temperature in an inert atmosphere. The difference in the coefficient of thermal expansion between the mold and the deposited layers provides natural debonding to occur at this interface. Upon the removal of the mold, a near net-shape component was obtained with a uniform TBC incorporated into the inner surface.

The component was then heat treated to transform the lamellar grain structure which is typically produced by spray forming to a fine equiaxed grain structure with significantly improved mechanical properties. Finally, the heat treated component was machined to the desired shape and tolerances.

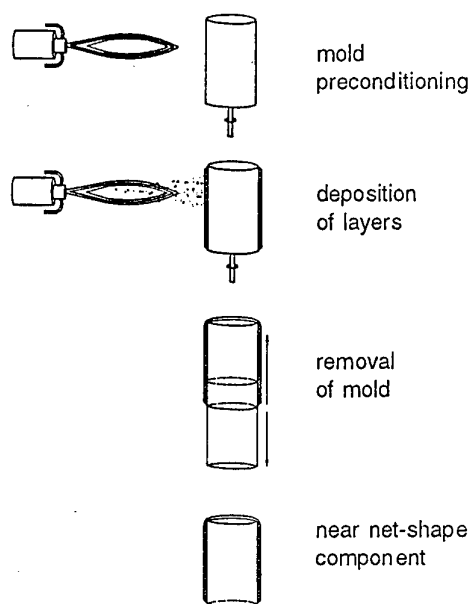


**Figure 1. Schematic of VPS near net-shape forming process.**

## **RESULTS AND DISCUSSION**

**Macroscopic Features.** Several macroscopic features were evident on the near net-shape component. The inside surface of the component, or the top coat surface of the TBC, had a very smooth ( $R_z < 20 \mu\text{m}$ ) surface finish which mirrored the surface finish of the mold. The component's inner geometry was slightly larger (0.6%) than the machined mold due to the slight thermal expansion experienced during processing. If required, the mold could be easily machined under final tolerance to compensate for the expansion.

**Microscopic Features.** The microstructure of the component cross-section is presented in Figure 2. The porosity level of the TBC top coat could be controlled, between less than 1% up to 20%, to maximize its thermal barrier characteristics and thermal shock resistance. The porosity level of the

TBC presented in Figure 2 is approximately 7%. The CoNiCrAlY bond coat and IN-738LC structural layers were applied in dense form; porosity levels were below 1% for both layers. Typical to VPS-applied metals, both of the metal layers reveal an absence of oxidation.

Figure 3 is a micrograph of IN-738LC after etching. The sprayed microstructure reveals the typical features found in as-sprayed coatings: lamellar and dendritic structures. After heat treatment the microstructure is more homogeneous, with fine grains and lower in porosity (Figure 4). The average grain size, after heat treatment, is approximately  $1\mu\text{m}$ .

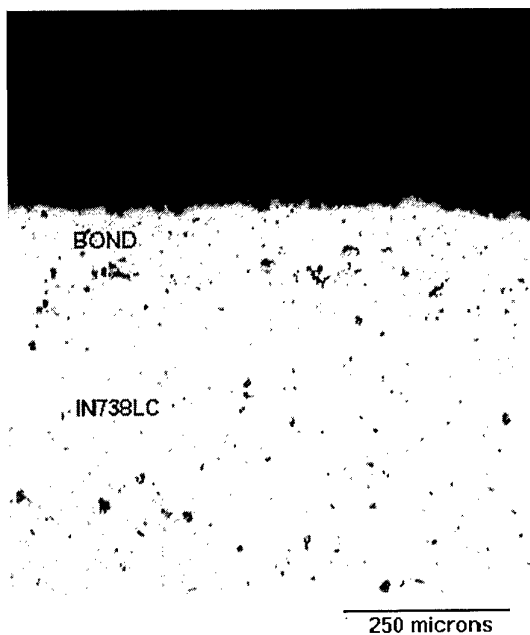


**Figure 2. Micrograph of component cross-section (unetched).**

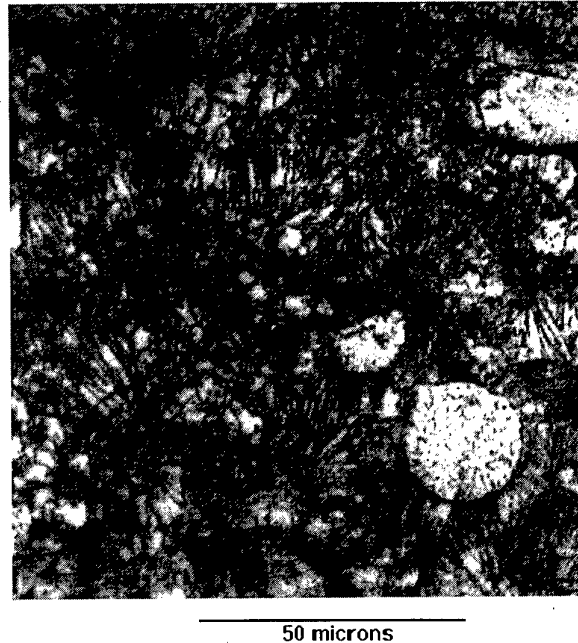


**Figure 3. Micrograph of as-sprayed IN-738LC (etched).**

**Mechanical Properties.** The mechanical properties of the VPS-applied IN-738LC were measured and compared to cast IN-738LC (Table 1). The as-sprayed properties of the superalloy show higher tensile strength and lower ductility, characteristic of thermally sprayed metals. After heat treatment, however, the elongation increases dramatically while maintaining high strength. In fact, the mechanical properties of the sprayed and heat treated IN-738LC are superior to those of cast IN-738LC. The tensile strength of the sprayed and heat treated superalloy remains relatively high at elevated temperatures.





50 microns

**Figure 4. Micrograph of VPS-applied and heat treated IN-738LC (etched).**

<b>Table 1. Mechanical properties of VPS-applied and Cast IN-738LC.</b>				
	Cast* @RT	VPS @RT	VPS+H T @RT	VPS+HT @800°C
YS (MPa)	896	-	960±10	666
UTS (MPa)	1034	1195±1 2	1161±13	752
Elong (%)	9	0.6±0.2	9.5±0.5	-
Hard (HV)	-	338±72	352±12	-

\* from technical data published by INCO Inc.

**TBC Development.** A number of TBC options were considered for the envisioned application. The target was to create a TBC thick enough to offer a  $\Delta T$  of 350°C. The thickness of the TBC depends on the thermal conductivity, and therefore, composition and morphology, of the TBC. Table 2 shows the theoretical thickness required for three TBC options.

<b>Table 2. TBC Options for 350°C <math>\Delta T</math></b>		
Material	k (W/m K)	Thickness
PSZ	0.8	0.7 mm
Al <sub>2</sub> O <sub>3</sub>	6	4.9 mm
Ca <sub>2</sub> SiO <sub>4</sub>	1.7	1.4 mm

While PSZ offers the lowest thermal conductivity, a durable 700  $\mu\text{m}$  monolithic PSZ layer is unlikely. Our experience suggests that PSZ layers thicker than 300  $\mu\text{m}$  are susceptible to cracking and delamination either during spraying or upon thermal cycling. Pure alumina is also not suitable due to its relatively high thermal conductivity.

Following a preliminary screening of 12 TBC options, two compositions were identified for further testing: (i) a MCrAlY/PSZ graded and laminated structure; and (ii) a PSZ/Ca<sub>2</sub>SiO<sub>4</sub> graded structure. The two selected TBC options were sprayed onto flat coupons and tested for thermal shock resistance, thermal cycling, and oxidation at 1100°C.

A microstructure of the as sprayed MCrAlY/PSZ TBC is shown in Figure 5. The MCrAlY used in this study is AMDRY

995 (CoNiCrAlY). While the thermal shock test (heating to 1,100°C and rapidly quenching in water) showed satisfactory results for this TBC option, the oxidation tests proved that graded MCrAlY layers oxidize very rapidly above 900°C. A microstructure of the TBC after 25 hrs in air at 1,100°C is shown in Figure 6. Under these conditions the coating expands in volume and delaminates. Based on this catastrophic failure, no thermal cycling tests were performed for this option.

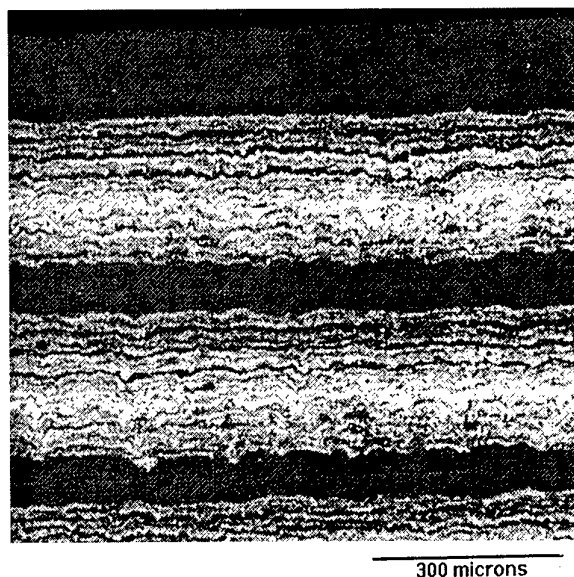


**Figure 5. Micrograph of as-sprayed graded and laminated MCrAlY/PSZ TBC.**

The PSZ/Ca<sub>2</sub>SiO<sub>4</sub> TBC consisted of a 200-300 μm layer of PSZ followed by a 300-650 μm PSZ/Ca<sub>2</sub>SiO<sub>4</sub> graded layer and a 300-1,000 μm layer of Ca<sub>2</sub>SiO<sub>4</sub>. A typical micrograph of this TBC option is shown in Figure 7. This option showed excellent resistance to thermal shock and minimal weight gain due to oxidation at temperatures as high as 1,300°C.

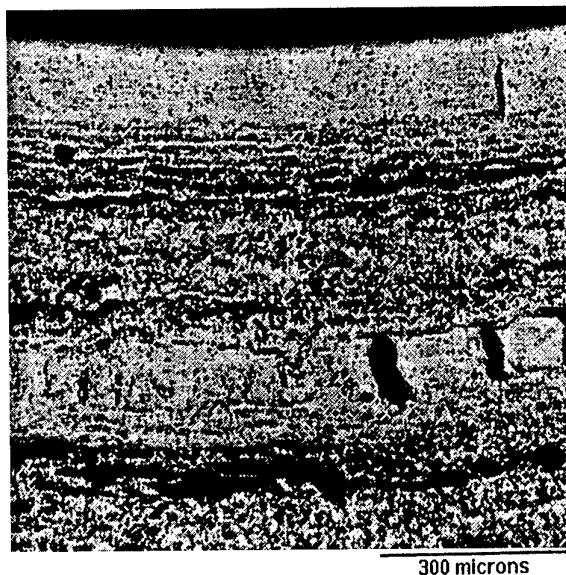


**Figure 6. Micrograph of MCrAlY/PSZ TBC after 25 hrs oxidation at 1,100°C.**

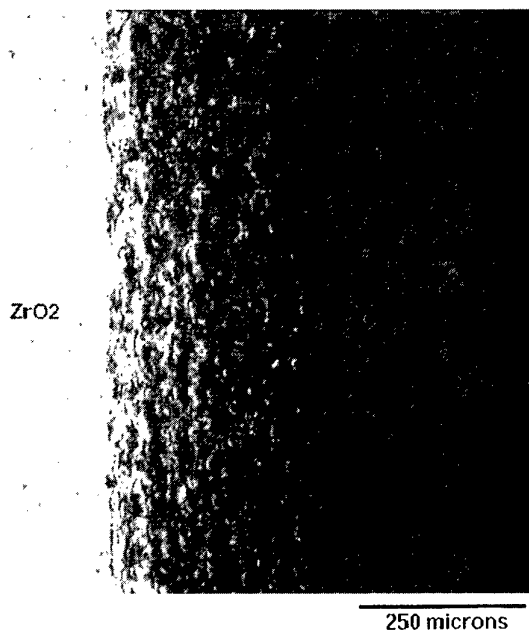


**Figure 7. Micrograph of as sprayed PSZ/Ca<sub>2</sub>SiO<sub>4</sub> TBC.**

Thermal cycling was performed on the PSZ/Ca<sub>2</sub>SiO<sub>4</sub> TBC by heating flat coupons to 1,100°C with an oxyacetylene torch and cooling rapidly with compressed air. Following 300 cycles no delamination was observed.

A number of PSZ/Ca<sub>2</sub>SiO<sub>4</sub> TBCs were produced on flat stainless steel substrates and tested for their thermal barrier properties. The test was performed by heating the TBC face with two high intensity infrared lamps and measuring the temperature of both the hot TBC surface and the cooler stainless steel surface. A list of the samples evaluated in this study is shown in Table 3.

**Table 3. PSZ/Ca<sub>2</sub>SiO<sub>4</sub> Samples Tested for Thermal Conductivity.**

Sample	Average Thickness (μm)		
	PSZ	Graded	Ca <sub>2</sub> SiO <sub>4</sub>
Z-10	245		
C-4			559
ZC-7	238	303	317
ZC-3	308	330	650
ZC-10	210	424	455
ZC-6A	225	584	303
ZC-9	248	655	921

Sample Z-10 represents a conventional PSZ TBC sprayed by VPS. Sample ZC-9 represents a TBC which theoretically should provide a ΔT in excess of 350°C and thus meet the performance requirements for advanced combustion liners and transition ducts without film cooling.

The results from the thermal conductivity study are presented in Figure 8. Figure 8 shows that the ΔT between the hot and cold faces of a uncoated stainless steel coupon is approximately 200°C when the hot phase reaches 1,000°C. By comparison, a conventional PSZ TBC structure offers a ΔT of 275°C (Sample Z-10). Under the same operating condition an advanced 1.8 mm thick PSZ/Ca<sub>2</sub>SiO<sub>4</sub> TBC offers a ΔT of approximately 420°C (Sample ZC-9). Thus, the thermal barrier properties of the PSZ/Ca<sub>2</sub>SiO<sub>4</sub> developed in this study can be almost 3x better than a conventional TBC, which should be sufficient to meet the requirements of the proposed application.

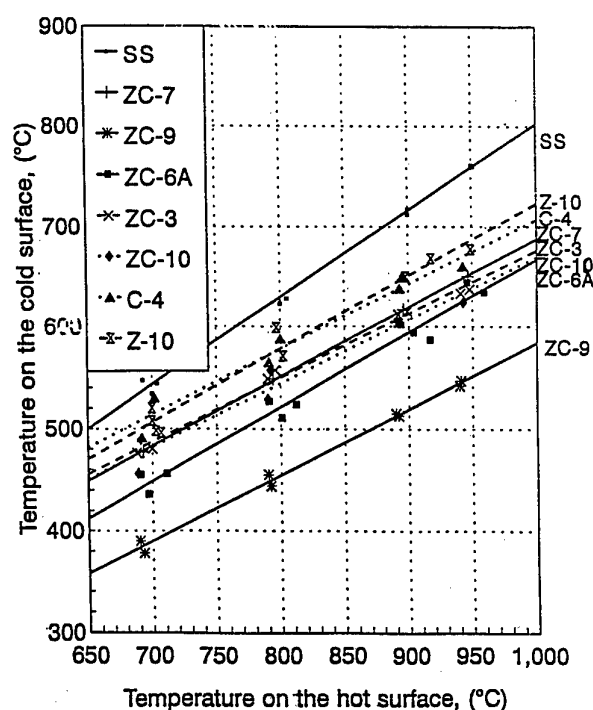


**Figure 8. Thermal properties of PSZ/Ca<sub>2</sub>SiO<sub>4</sub> advanced TBCs.**

## **SUMMARY**

The feasibility of VPS near net-shape forming multilayered free-standing components has been demonstrated. This innovative fabrication process was used to produce a combustion system component of a gas turbine engine. The improved qualities of VPS near net-shape formed combustion system component include: (i) an advanced TBC capable of offering  $\Delta T$  in the order of  $350^{\circ}\text{C}$ ; (ii) a superior high-temperature structural superalloy; (iii) smoother inner TBC surface; (iv) no irregularities (welds) within the component; (v) excellent mechanical properties; and (vi) consistent reproducibility. The cost of fabricating the components using the VPS net-shape forming technology is significantly lower than conventional methods. Furthermore, it is hoped that the need for film cooling can be eliminated.

## **REFERENCES**

1. M.R. Kim, R.W. Smith, and D. Kapoor, Thermal Spray: Practical Solutions for Engineering Problems, 7-11 (1996).
2. G. Montavon, E. Roussel, C. Coddet, E. Fauvet, J.P. Huchin, D. Cornu, J.M. De Monicault, J.C. Garcia, and F. Pellerin, Proceedings of the 7th National Thermal Spray Conference, 485-489 (1994).
3. T. McKechnie, P. Krotz, and Y. Liaw, Proceedings of the 7th National Thermal Spray Conference, 457-461 (1994).
4. H.-D. Steffens, M. Dvorak, and K. Nassenstein, Proceedings of the International Thermal Spray Conference & Exposition, 369-374 (1992).
5. NASA Tech Briefs MFS-30081.

# ELECTRON BEAM PHYSICAL VAPOUR DEPOSITION THERMAL BARRIER COATINGS: A COMPARATIVE EVALUATION OF COMPETING DEPOSITION TECHNOLOGIES

Y.Jaslier, S.Alpérine  
SNECMA - Materials and Processes Department  
Site de Villaroche - Bâtiment 41  
77550 Moissy-Cramayel  
France

## ABSTRACT

The need for improving the performance and maintenance costs of gas turbine engines has led to the development of advanced thermal protection systems for critical components such as high pressure turbine (HPT) blades and vanes. This led to the concomitant development of advanced coating deposition techniques. Electron beam physical vapour deposition (EB-PVD) first made possible the application of corrosion resistant overlay coatings on turbine blades. The EB-PVD technology has since been gaining ever more interest world-wide as it stands as the best industrial technique for the deposition of thermal barrier coatings on first stage HPT aerofoils. The strategic nature of the EB-PVD process means that it has been developing somewhat independently on both sides of the *iron curtain* during the cold war years. Today, both American and ex-USSR technologies are open to the market. This is the object of this paper to compare the two state-of-the-arts both from a deposition process standpoint and from a laboratory evaluation on samples. This evaluation covers structural studies as well as thermal cycling testing. The relationship between the deposition process and the coating functional behaviour is discussed.

## INTRODUCTION

In the Western countries, the electron beam physical vapour deposition process was originally developed in the late sixties by Airco Temescal jointly with Pratt & Whitney for the application of overlay type oxidation resistant coatings onto high temperature blades and vanes of jet engines<sup>1</sup>. The so-called MCrAlY's, where M is nickel, cobalt, iron or a mixture thereof, offered then superior environmental resistance compared to diffusion aluminides. In parallel with the development of advanced oxidation resistant coatings, emerged a new class of high temperature coatings designated as thermal barrier coatings. A thermal barrier coating (TBC) is a duplex system consisting of a heat insulating ceramic layer deposited on a bond coat underlayer providing adhesion to the ceramic as well as corrosion resistance to the underlying base alloy. The ceramic coating is commonly yttria-stabilised-zirconia for its low thermal conductivity and high thermal expansion coefficient.

The early application of TBC's was the protection of combustor parts. This application involved applying the ceramic coat on top of an MCrAlY coating used as a bond coat, both deposited by air plasma spraying. One advantage of the air plasma spraying technique is to provide the MCrAlY coating with a rough surface onto which the ceramic coating can mechanically bond. Another advantage of air plasma spraying lies in the heavily microcracked ceramic microstructure it produces which is beneficial in terms of strain tolerance and thermal shock resistance.

Since the potential benefits of thermal barrier coatings were additive to the gains in high temperature strength capability of superalloys and in internal and film cooling technologies,

there has been a strong drive to extend the application of TBC's to protecting the aerofoil of high pressure turbine blades and vanes. Unfortunately, the plasma spray process proved inadequate for depositing ceramic coatings onto high pressure turbine (HPT) aerofoils due to the poor coating surface finish retention and cooling hole obstruction problems. It has been alleged that ceramic plasma sprayed coatings had 'insufficient' spallation resistance for this application<sup>2</sup>.

In the late seventies/early eighties, the EB-PVD technique was found to be a very interesting potential alternative to plasma spraying for depositing TBC's onto aerofoils. Refractory materials deposited by EB-PVD typically exhibit a unique columnar morphology, which has been vehicled as a key feature to accommodate the thermal expansion mismatch strains with the metallic substrate upon thermal cycling and to resist severe thermal shocks. A second advantage of the electron beam physical vapour deposition process is its capability to produce coatings with an acceptable surface finish as-deposited which is retained in service in spite of the erosive environment. A third and not least advantage is that the EB-PVD technique makes controllable and reproducible the obstruction of cooling holes. This is due to the deposition mechanism that takes place through the condensation of coating vapour in the EB-PVD process rather than through the impingement of large semi-molten particles in the plasma spray process.

Although the potential of EB-PVD TBC's was recognised, the know-how to reliably produce TBC's by electron beam physical vapour deposition proved to be arduous to establish because of 'infant mortality' problems as reported by the Western pioneers themselves<sup>3,4</sup>. The strategic nature of the EB-PVD applications means that the difficulties have been tackled and the process technology matured somewhat independently on both sides of the *iron curtain* during the cold war years. Companies such as Airco Temescal, Pratt and Whitney and Chromalloy made essential contributions to make the technology of EB-PVD TBC's industrially viable<sup>4</sup>. Production coatings have been flying in PWA engines since 1989<sup>2</sup>.

In the Eastern countries, the EB-PVD technology was bred in prestigious institutes such as the Paton Welding Institute in Ukraine and the VIAM in Russia, with industrial recipients such as Saturn and Nikolai Kuznetsov (NK). The first Structure Zone Model for physical vapour deposited coatings was first published in 1963 by Movchan and Demchishin<sup>5</sup> and has been universally referred to since. The design approach of Russian jet engine manufacturers was such that it was not felt there was a need for coating HP vane aerofoils with EB-PVD TBC's. As a result Russian experience in production was bound to coating blades, not vanes<sup>6</sup>. This detail bears some implications on the development of tool design and masking technology (or lack of) in the former

USSR. EB-PVD TBC's applied on single crystal blades have been flying on NK engines' since 1985.

Today, both the American and ex-USSR technologies are open to the market. This is the object of this paper to shed some light on how the two state-of-the-arts compare from the technology stand-point. Some of the commonalities and differences in the TBC concept and manufacturing technology are first highlighted. Results from a laboratory evaluation of coatings that are representatives of these technologies are then presented and discussed.

## COMMONALITIES AND DIFFERENCES

### TBC constituents

Whether they originate from the East or from the West, EB-PVD TBC's have overall much in common if one considers that they all consist of an oxidation resistant bond coat overlaid with a ceramic top coat deposited by electron beam physical vapour deposition. Typical bond coats are from the MCrAlY type. Only in the West, does it appear that diffusion aluminides have been used as bond coats beside MCrAlY's. The range of thicknesses for the MCrAlY and ceramic layers are typically 75-125 and 80-250 microns respectively. Another invariant between the two technologies is the standard ceramic composition which consists of  $ZrO_2$ -6to8wt% $Y_2O_3$  (YSZ). It is interesting to note that this composition range was originally selected from the thermal cyclic life optimisation of TBC's deposited by plasma spraying<sup>8</sup>.

### The EB-PVD manufacturing process

In generic terms, the EB-PVD process involves evaporating coating material in a vacuum chamber by means of electron beam heating. The coating vapour so generated condenses on the work piece at high temperature. The coating flux being line-of-sight, the parts are manipulated above the evaporation source to maximise coating coverage.

The design of Western EB-PVD coaters is based on the principle that the evaporating conditions must be kept as steady as possible with no interruptions, with a batch of parts being coated in the deposition chamber at any time of the campaign. This approach implies that the parts must be loaded and pre-heated externally to the deposition chamber. The architecture of Western type EB-PVD coaters is thus generally based on a central deposition chamber with separate pre-heating and unloading chambers (see Figure 1). Although the main concern in this approach is to maximise the coater's productivity and reproducibility, the machine design actually has implications on the deposition physics that govern the coating properties and this must be borne in mind when comparing the two technologies. In the deposition chamber, the parts are maintained at temperature mainly thanks to the radiative heating from the molten pool. For metallics however, where the melt pool surface temperature is not as high as for ceramics, supplementary heating of the parts is provided by a resistive radiator<sup>9,10</sup>. Depending on the coater's design, whether it be Temescal or Leybold, the parts are manipulated in the vapour cloud with various complex motion patterns involving rotation and tilting. One of the specificity of the Western technology though is the bleed, inside the coating chamber, of an oxygen containing gas when depositing ceramics<sup>9,10</sup>. The argument put forward to justify for the need of oxygen bleeding is to compensate for the dissociation of zirconia upon heating which would otherwise lead to some oxygen deficiency.

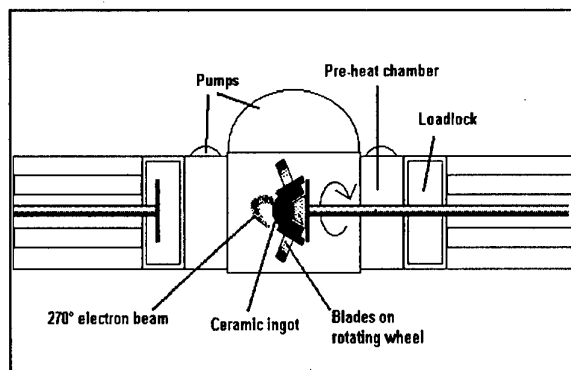


Figure 1: Top view schematic of a Western type (Temescal) production EB-PVD coater<sup>16</sup>

This deficiency is manifested in the black colour of the zirconia coating. The lack of stoichiometry of zirconia deposits is in itself not a problem since it can be restored via a simple heat treatment in air at temperatures as low as 700°C. Some people have claimed that the lack of oxygen during the coating atomic build up actually affected the coating microstructure in a detrimental manner due to the material swelling as a result of restoring its stoichiometry<sup>11</sup>. Another argument for the need of oxygen bleed inside the coating chamber, is the need to establish, prior to depositing the ceramic, a thin film of aluminium oxide at the work piece surface onto which the ceramic condensate can chemically bond<sup>12,13</sup>. The oxygen rich environment surrounding the parts in transit from the pre-heating chamber to the deposition chamber is prone to forming a thin film of alumina acting as the 'glue' of the ceramic coat to be deposited. To the authors, the *in situ* bond coat pre-oxidation prior to ceramic deposition is a stronger argument to justify for the need of oxygen bleed inside the coating chamber rather than stoichiometry or microstructure of the deposit. Yet, the Eastern technology of EB-PVD TBC's matured without identifying oxygen bleed as a key deposition parameter.

Figure 2 is a schematic of a Russian production coater. Its architecture is based on a central deposition chamber with two load locks on each side. There is no separate preheating chambers as in the Western coaters.

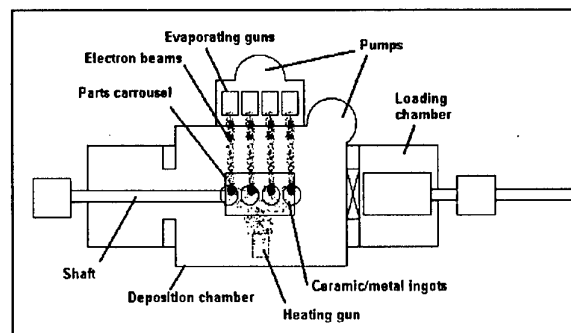


Figure 2: Top view schematic of an Eastern type production EB-PVD coater

Pre-heating of the parts is accomplished inside the deposition chamber by the means of an electron beam gun located in a separate chamber above the deposition chamber. This gun is also used as auxiliary heating of the parts during the coating process. Four stacks of ceramic or metal ingots are positioned in a row and are evaporated by four individual linear electron beam guns. The deposition process is carried out at a vacuum

level of a few  $10^{-4}$  Torr. There is no intentional bleed of a reactive gas into the chamber. A typical coating cycle consists first in mounting the carousel holding the parts on the driving shaft inside the loading chamber. After the loading chamber has been evacuated, the locking vane is opened and the carousel with the cold parts is introduced into the deposition chamber by translation of the shaft. The parts are pre-heated inside the deposition chamber by the heating electron beam gun while the evaporating guns are kept shut down. Evaporation is started after the work pieces have reached the right temperature regime. Once the deposition is completed the carousel is driven back into the loadlock where it is left to cool down before it is unloaded.

It should be noted at this point that Western coaters are generally designed to be dedicated to one type of coatings i.e. metallics or ceramics whereas, in the Eastern art, the coaters are designed and used to deposit both types of coatings. Whether the latter approach is better or worse from the production standpoint than the dedicated type coater approach is not the debate of the present discussion. The point is that the flexibility of the Eastern type coaters permits to evaporate metallics concurrently with ceramics or to deposit both in sequence in the same coating cycle and this is essential to their art<sup>14</sup>.

## SCOPE OF LABORATORY EVALUATION

### Coating systems

Two thermal barrier coating systems were evaluated in this study. The Russian coating was manufactured at the Samara plant of NK Engines under the technical supervision of the VIAM Institute in Moscow. The American thermal barrier coating is the well known RT31/RT33 system manufactured by Chromalloy in the USA. The nominal designation of these systems is given in the table below:

Bond coat/ Top coat Designation	Bond coat composition	Ceramic top coat composition
RT31/RT33	Co34Ni20Cr8Al0.5Y	ZrO <sub>2</sub> -7 wt%Y <sub>2</sub> O <sub>3</sub>
SDP2/KDP1	Ni20Cr12Al0.5Y	ZrO <sub>2</sub> -7wt%Y <sub>2</sub> O <sub>3</sub>

For each system, both bond coat and ceramic coat were applied by electron beam physical vapour deposition on disk and cylinder shaped test pieces made out of Hastelloy X. The composition of Hastelloy X is given in the table below in wt%:

Ni	Cr	Fe	Mo	Co	W
bal	22	18	9	1	0.2

### Characterization

The morphology of the ceramic layers was evaluated using a field emission gun scanning electron microscope (FEG-SEM). Energy Dispersive X-Ray analysis coupled with SEM was used to perform chemical analysis in both the as-deposited and as-tested state. Ceramic phase composition was determined using CuK $\alpha$  X-Ray diffraction.

TBC performance was evaluated using a thermal cycling test. Thermal cycling was conducted on 6 and 10mm diameter bars in a furnace with a cycle consisting of 55 minutes at 1100°C with a 5 minute heat up and 15 minute cool down to room temperature using forced air convection cooling. The probability for the ceramic to spall off after many cycles increases with dwell time at room temperature. This effect,

although poorly understood, is known to be moisture related. Other investigators have reported the effect of moisture on the spallation resistance of thermally grown oxides on bare superalloys<sup>15</sup>. In these tests, thermal cycling was interrupted every 20 cycles with the test pieces left at room temperature for a time up to 4 hours, after what the specimens were inspected and the cycling resumed. A dwell time of 4 hours at room temperature was chosen so as to let enough chance for the moisture to have an effect, if any. The failure criterion was a ceramic spalled area of at least 20% of the specimen coated surface.

## RESULTS

### Characterization of as-deposited TBC's

The overall TBC systems are presented in Figure 3. It may be seen that each ceramic coating system exhibits a specific ceramic morphology. For a same nominal YSZ composition, the RT33 process produces a coarser, more columnar shape morphology compared to the finer, feather-like, KDP1 ceramic morphology. Moreover, the KDP1 feathered columns coarsen towards the outer surface. This effect is not as dramatic in the RT33 morphology.

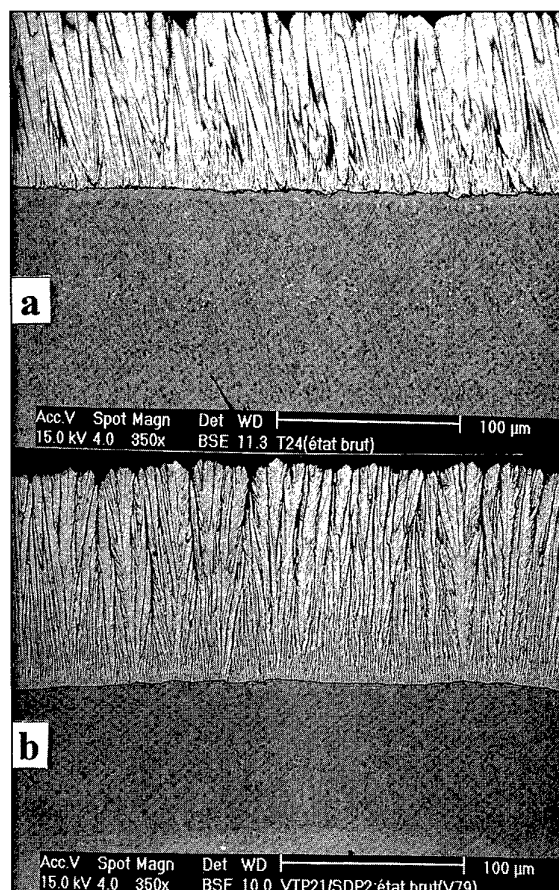


Figure 3: SEM back-scattered electron image of the as-deposited RT31/RT33 (a) and SDP2/KDP1 (b) TBC systems

High magnification examination of the ceramic layers at 50 micron height from the bond coat gives some insight into the column sub-structure (Figure 4). Back-scattered electron imaging reveals internal striation consisting of alternate dark and white layers. This effect is a lot less pronounced in the



case of the KDP1 ceramic where only minor striation may be distinguished in the core centre line of the feathered columns.

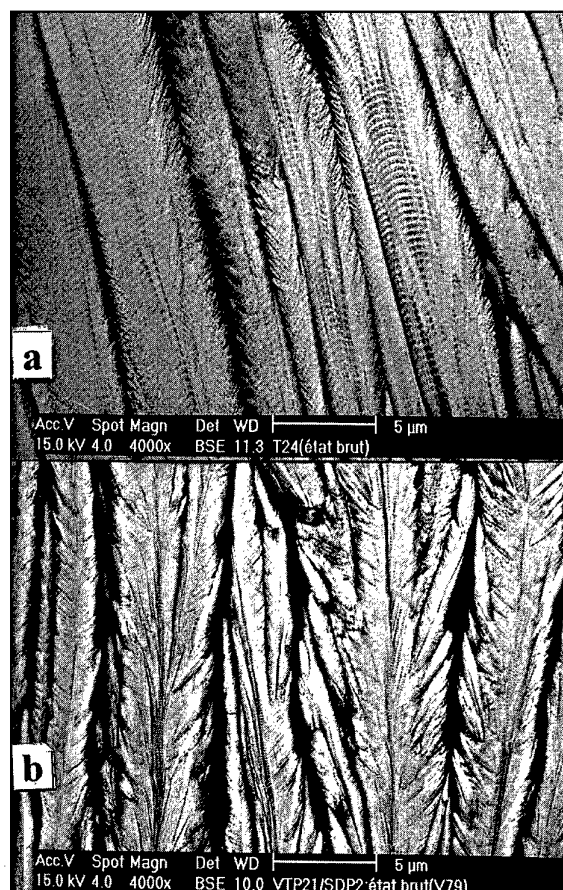


Figure 4: SEM back-scattered electron images showing details of as-deposited RT33 (a) and KDP1 (b) ceramic morphologies.

X-Ray diffraction patterns of each ceramic layer are presented in Figure 5. It was found that each ceramic system was single phased and consisted of the non-transformable tetragonal phase ( $t'$ ).

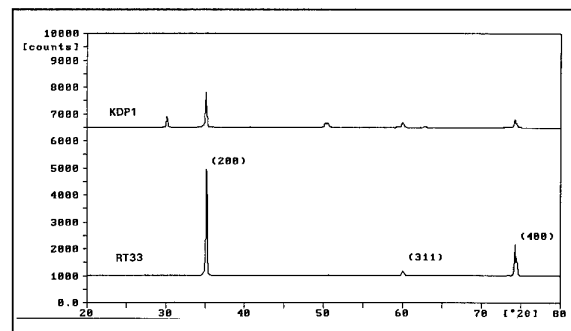


Figure 5: X-ray diffraction patterns of RT33(a) and KDP1 (b) ceramic layers.

All coatings exhibited the (200) preferential growth orientation. This texture is however less pronounced in the Russian ceramic. No peak broadening was observed indicating that the diffracting domains were larger than 0.1 micron in size.

Overall bond coat composition was determined using semi-quantitative EDS analysis over an 80x80microns window centred within the bond coat depth. The analysis results are shown in the table below:

	Co	Ni	Cr	Al	Y	Fe
RT31 wt%	bal	38	18	8.9	<1	<1
SDP2 wt%	-	bal	14	12	<1	<1
at%			14	22		

A band of white dots identified as yttrium rich precipitates was found at mid-height in the RT31 CoNiCrAlY (see Figure 3). It was observed at higher magnification that this yttrium rich phase was nucleated at the  $\gamma/\beta$  phase boundary. No yttrium rich precipitates were observed in the SDP2 NiCrAlY layer. A feature peculiar to the SDP2 MCrAlY layer was the presence of a population of chromium rich nodules of 1 micron in average diameter (see Figure 6). These constituents appeared black in back-scattered electron imaging. Examination in the secondary electron emission mode revealed a surface relief suggesting that these nodules were harder than the matrix. These observations point to the presence of chromium carbides ( $Cr_7C_3?$ ,  $Cr_{23}C_6?$ ), indication that would need to be confirmed using X-Ray diffraction.

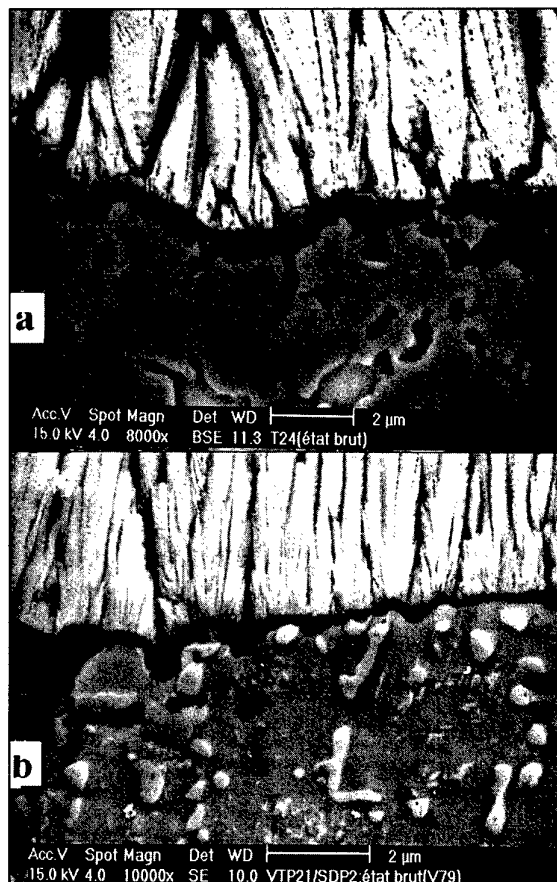


Figure 6: SEM secondary electron image of ceramic/bond coat interface for RT31/RT33 (a) and SDP2/KDP1 (b)

A close examination of the ceramic/bond coat interface reveals that the alumina film developed on the SDP2 bond coat is continuous and thinner than that developed on RT31 (see Figure 6). For the latter, alumina seems to only have formed at the interface with the  $\gamma$  phase i.e. no alumina could



be identified at the YSZ/ $\beta$ -(Ni,Co)Al phase interface using SEM.

Right underneath the alumina film formed on SDP2, there exists a thin (1.5 to 2 $\mu$ m) and very fine grained MCrAlY sub-layer separated from the bulk of the bond coat by a line of alumina inclusions (see Figure 7).

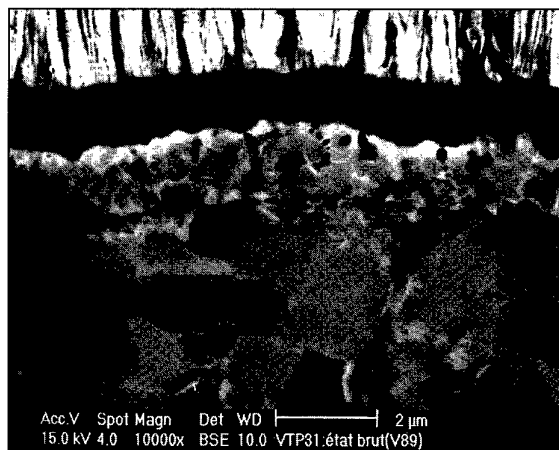


Figure 7: SEM back-scattered electron image of as-deposited ceramic/SDP2 interface region

#### Thermal cycling performance

Figure 8 is a bar chart showing thermal cycles-to-failure for the SDP2/KDP1 and RT31/RT33 coatings on 10mm diameter bars (unless otherwise stated).

Coating spallation life is found to be very scattered for both systems. There appears however that, under the specific testing conditions used in this study, the SDP2/KDP1 coating overall exhibits a superior spallation resistance compared to that of the RT31/RT33 coating. Mean, low and high thermal cyclic lives are shown in the table below for comparison.

	RT31/RT33	SDP2/KDP1
Low	19	96
Mean	260	460
High	710	1081

Ceramic spallation occurred at room temperature. In most cases, the spallation event was not progressive but abrupt, with typically 80% of the ceramic loss occurring at once from a no spall situation. One exception was the SDP2/KDP1 specimen that was stopped after 1080 cycles. This specimen failed via the occurrence of discrete spalls that were dispersed and small in size (no bigger than 2mm) but the number of which increased with test cycles.

The short life specimens typically exhibited a shiny metallic surface on the substrate surface where the ceramic had spalled. The longer the lifetime of the test pieces and the more grey and mat this surface looked. For the high life specimens, this surface appeared covered with a grey film of dust. This film could be rubbed off with the finger tip. This pattern was generally followed by both the RT31/RT33 and SDP2/KDP1 systems. In two instances with the SDP2/KDP1 coating (96 and 114 cycles), the ceramic free substrate surface and the inner side of the ceramic spalls were blue/green in colour, indicating the presence of nickel and chromium rich oxides. These visual observations were followed with SEM evaluation.

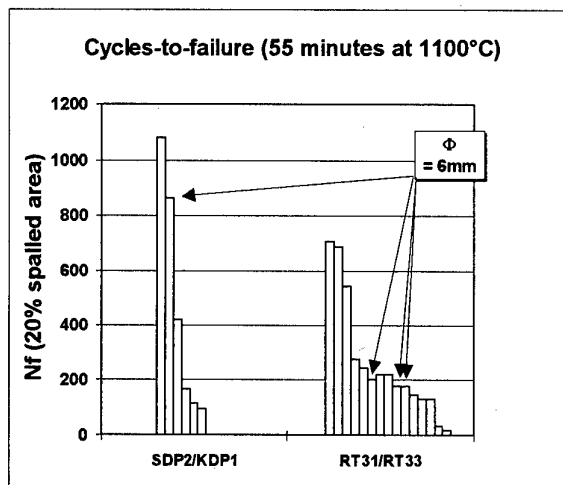


Figure 8: Thermal cyclic performance of RT31/RT33 and SDP2/KDP1 systems

#### Characterization of as-tested TBC systems

Micrographs of a typical low life (106 cycles) RT31/RT33 system are shown in Figure 9. The substrate surface was analysed and consisted of MCrAlY with small isolated alumina patches. The remnant alumina most often contained yttrium rich oxides that show up as white constituents using atomic contrast imaging. The inner side of the ceramic spall was analysed by EDS and consisted of alumina with isolated yttrium rich oxide phases. The alumina grains imprints can be recognised on the bond coat surface. These observations demonstrate that ceramic spallation occurred through the propagation of a crack running at the MCrAlY/alumina interface breaking off the yttrium rich alumina protrusions.

The failure morphology of low life SDP2/KDP1 coatings was similar to that described above, with the exception that no yttrium rich oxide phases seemed to have formed. In Figure 10 are shown micrographs of a SDP2/KDP1 coating failed after 96 cycles. This specimen was peculiar in that a continuous layer of (Ni,Cr,Al) bearing oxides, presumably spinels, had formed between the alumina scale and the ceramic. This mixed oxide layer that appears voided in cross section (Figure 10b) behaved as another site for crack propagation in addition to the MCrAlY/alumina interface.

In Figure 11 are presented micrographs of the RT31/RT33 specimen that failed after 710 cycles. EDS analysis of the inner side of the ceramic spall indicated that it consisted predominantly of YSZ ceramic. Inversely, the substrate surface side consisted mainly of aluminium oxide, implying that cracking had occurred at the ceramic/alumina interface. The respective fractured surfaces reveal a comparable topography consisting of equiaxed spherical grains less than 1 micron in size. Some isolated (Ni,Co,Cr,Al) mixed oxides were also observed at the interface between the ceramic and alumina scale although this feature remained marginal.

The most durable SDP2/KDP1 specimen (1080 cycles) was assessed on a polished cross-section. The progressive failure of this specimen into discrete ceramic spalls did not make possible to look at freshly spalled surfaces. It can be seen in Figure 12a that a crack is running predominantly within the outer region of the alumina scale with some excursions into the ceramic. It cannot be determined whether this crack is the result of metallographic preparation or whether it is a genuine defect generated from the cycling.

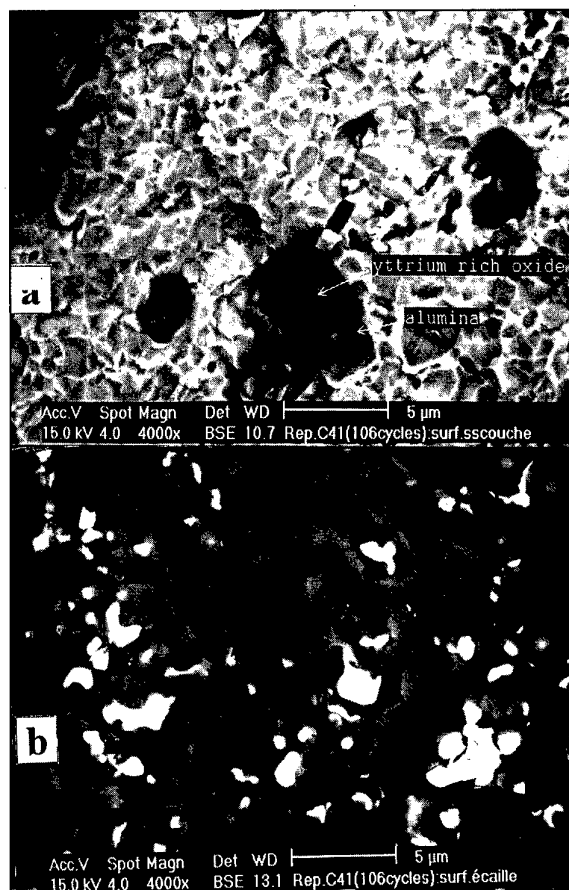


**Figure 9: SEM back-scattered electron images of bond coat surface (a) and inner side of ceramic spalls obtained from a low life RT31/RT33 system (b)**

Its location however indicates that the ceramic/alumina interface region is the weakest link. Some isolated nodules of (Ni,Cr,Al) mixed oxides were also found to have formed between the alumina scale and the zirconia, locally lifting off the ceramic coat (see Figure 12b). The formation and growth of these mixed oxide nodules may be responsible for the discrete ceramic spalls that were observed on this specimen. The alumina scale thickness on this coating after 1080 cycles was measured at 5.5 microns which is to be compared to the 7.5 microns alumina scale developed on RT31/RT33 after 710 cycles (see Figure 13).

## DISCUSSION

### As-deposited thermal barrier coating systems

#### *Ceramic considerations*

The difference in ceramic morphologies obtained from the RT33 and the KDP1 process clearly demonstrates how sensitive the morphology of EB-PVD deposits can be to specific deposition conditions. Morphology is classically affected by the substrate surface roughness<sup>16,17</sup>, substrate temperature<sup>5,17</sup>, deposition rate and part motion pattern in the vapour cloud such as rotation speed<sup>18</sup>. No major differences exist in either the deposition temperature range or the bond coat surface finish between the two processes that could account for this effect. The part motion pattern and the vapour cloud distribution inside the coating chamber, both very dependent on the coater design, are however very different. These parameters are therefore potential

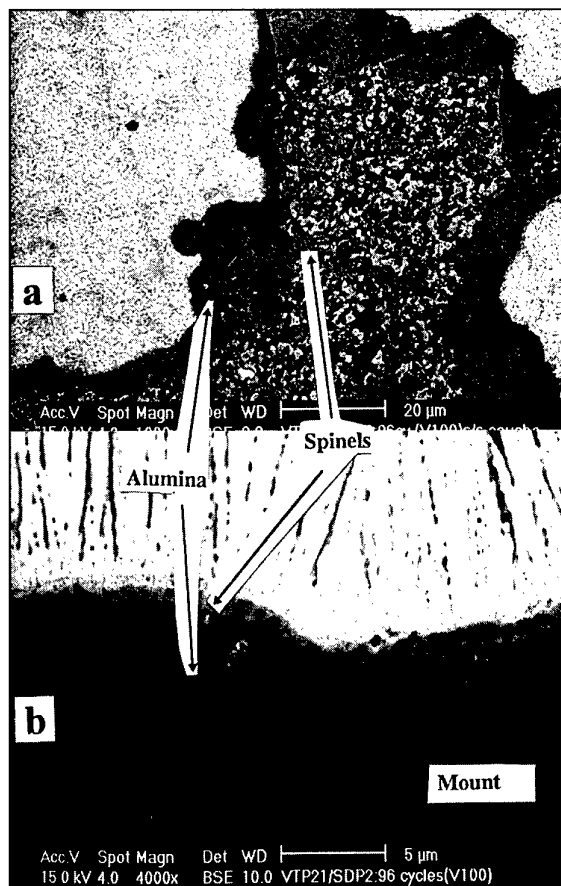


**Figure 10: SEM back-scattered electron images of bond coat surface (a) and cross section of a low life SDP2/KDP1 system (b)**

contributors to the difference in ceramic morphology that is observed. This argument must be put in perspective with the fact that Western EB-PVD TBC's deposited either from a Leybold or a Temescal machine are very similar in morphology<sup>19</sup> with yet massive differences in the coating chamber configuration. The role of chamber pressure and deposition rate (higher in the Western process) on morphology should not be ignored.

Another difference in ceramic structure was found in the column striation which is significant in RT33 but only marginal in KDP1. This well-known feature is usually related to rotation of the work piece during deposition<sup>20</sup>. As the parts are rotated in the vapour cloud, the surface to be coated sees alternate regimes of high deposition rate at high temperature when facing the source (brighter lines) to low deposition rate at lower temperature when facing away from it (darker lines). Lelait et al<sup>21</sup> have identified using transmission electron microscopy that the darker lines corresponded to aligned porosity in the ceramic columns. Later, a 'dynamic sintering' coating growth model has been proposed to account for the presence of intra-columnar porosity in EB-PVD deposits<sup>17</sup>. This model was developed on the consideration that a PVD deposit builds up as a porous atomic network and that this spontaneous defectiveness is overcome at high temperature by diffusion processes resulting in an array of micropores (coalesced vacancies). It was proposed that not only the ceramic surface temperature played a role in the rotation induced striation of the ceramic columns but also the kinetic

energies of the condensing species which were in turn affected by gas scattering effects.

It may be understood that the ceramic striation is less pronounced in the case of Russian ceramics if one considers that:

- the ceramic surface temperature does not fluctuate with rotation as much in amplitude as in the Western process since the part temperature relies to some extent on auxiliary electron beam heating.
- when the surface to be coated faces away from the source, only the thermalised fraction and back scattered molecules of the vapour cloud can possibly deposit. In the KDP1 process, where the evaporation takes place in a vacuum of a few  $10^{-4}$  Torr, the surface to be coated hardly receive any coating flux when facing away from the source.

Unlike morphology, the phase composition was found to be an invariant between the two kinds of ceramic. The finding of the ( $t'$ ) phase in 7YSZ EB-PVD deposits was first established by Lelait et al<sup>21</sup> after previous authors had concluded to the presence of the cubic phase. This phase is typically obtained from quenching the cubic phase of bulk  $ZrO_2$ -7wt% $Y_2O_3$  ceramic<sup>22</sup>. It is also found in plasma sprayed  $ZrO_2$ -7wt% $Y_2O_3$  deposits due to the rapid solidification nature of this process. The formation of the ( $t'$ ) phase in EB-PVD deposits can be explained from the fact that the yttrium and zirconium oxide molecules condense randomly at a relative temperature  $T/T_m$  of 0.4 approximately (where  $T$  and  $T_m$  are the absolute surface temperature and melting point of zirconia respectively). In this temperature regime, cation diffusion is too sluggish to allow for the yttrium to redistribute into the yttrium rich cubic phase and the low yttrium content transformable tetragonal phase. Given that the RT33 and KDP1 processes involve a same ceramic composition (zirconia alloyed with 7wt%yttria) and a low deposition temperature relatively to the melting point of zirconia, one could expect the formation of ( $t'$ ) phase in both ceramic deposits.

The RT33 ceramic deposits exhibited a preferred (200) orientation that was much more pronounced than in the case of KDP1. A zirconia condensate with a (200) texture builds up with atomic layers in the coating plane that consist exclusively of oxygen atoms. It may therefore be argued that the richer oxygen environment characteristic of the RT33 process will favour the (200) growth orientation compared to a deposition process carried out in vacuum.

#### Bond coat considerations

MCrAlY bond coats are classically described as consisting of  $\beta$ -(Ni,Co)Al precipitates in a solid solution of  $\gamma$ -(Ni,Co)CrAl. Both RT31 and SDP2 bond coats fit this pattern. Some differences were found relative to the presence of a third population of constituents identified as yttrium rich precipitates in the former and presumed chromium carbides in the latter. These differences most probably reflect different bond coat processing histories involving work hardening and heat treatment steps. Some deviation from the nominal composition was noticed in the chromium content of the SDP2 bond coat. This deficiency of a bond coat applied on an otherwise chromium rich substrate, may be partly attributed to chromium evaporation during the vacuum heat treatments at 1050°C that preceded ceramic deposition.

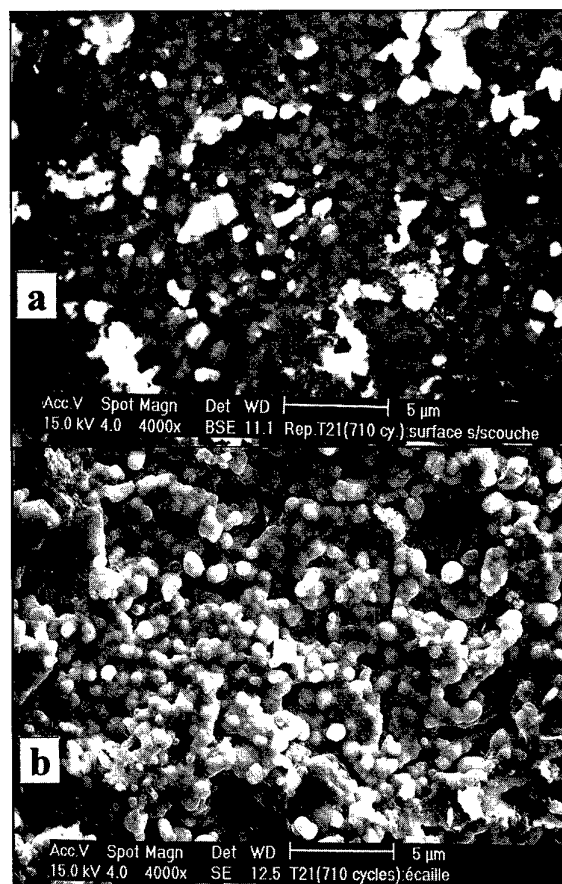


**Figure 11: SEM secondary and back-scattered electron images of bond coat surface (a) and inner side of ceramic spalls (b) obtained from a high life RT31/RT33 system**

The most peculiar feature that distinguishes the SDP2 bond coat from RT31 is the presence of a fine grained MCrAlY sublayer adjacent to the ceramic coat. This thin layer originates from the evaporation of a flash of MCrAlY on top of the already mechanically prepared and heat treated bond coat surface. The Russian art is such that, for each ceramic deposition run, the evaporation of MCrAlY for tens of seconds precedes the onset of ceramic evaporation. This philosophy probably is meant to deposit the ceramic layer on a fresh, reactive and contaminant free surface.

The nature of the bond coat metal surface is of prime importance as it controls the nucleation and growth of the oxide film that acts as the glue of the ceramic layer. Evidence was shown that this native oxide was different (in thickness and continuity at least) whether it was formed at the RT31/RT33 or SDP2/KDP1 interface.

The interfacial oxide film may form as a result of one or a combination of mechanisms such as:

1. *ex-situ* bond coat oxidation prior to the ceramic deposition step. In both the Western and Russian manufacturing processes, the bond coat metal surface is mechanically prepared in a way that is prone to removing any oxide scale formed during a prior heat treatment. It is therefore unlikely that the interfacial alumina observed originates from *ex-situ* oxidation.

2. *in-situ* bond coat oxidation during the transient pre-heat stage in vacuum.
3. *in-situ* bond coat oxidation during the transit from the pre-heat chamber to the deposition chamber in a partial pressure of oxygen, this mechanism standing for the Western type coating process.
4. *in-situ* bond coat oxidation during ceramic deposition. Bearing in mind that the ceramic is porous and that oxygen diffusivity in YSZ ceramics is significant<sup>23</sup> above 900°C, oxygen can be conducted to the aluminium bearing bond coat metal through the ceramic coating and fuel alumina growth.
5. *ex-situ* bond coat oxidation post ceramic deposition during heat treatments at 1050°-1100°C for times up to 4 hours. Beside oxidation from the residual oxygen present in a vacuum of  $10^{-4}$  Torr, it is suggested that the reservoir of oxygen contained in the YSZ ceramic participates to some degree to bond coat oxidation. This suggestion follows the observation that white zirconia deposits typically darken out after a 4 hour heat treatment at 1080°C in a partial pressure of argon, implying the loss of oxygen from the ceramic.

None of the mechanisms 2 to 5 proposed above appears to have activated the oxidation of the RT31 bond coat  $\beta$  phase. This observation is somewhat in contradiction with a previous result reported by Leyens et al<sup>24</sup> who studied the effect of various pre-oxidation treatments of NiCoCrAlY bond coats. It was found that mainly the  $\beta$  phase was covered with oxides after a 4 hour vacuum heat treatment at 1080°C.

To account for the preferential oxidation of the bond coat gamma phase in RT31/RT33, it is proposed that the chromium rich  $\gamma$  phase readily forms chromia nuclei during the transient heat up stage. These nuclei would act as nucleation sites<sup>26</sup> and subsequent growth of alumina at a working oxygen partial pressure that is insufficient to nucleate alumina on the  $\beta$  phase.

It is interesting to note that the Russian process produces a continuous film of alumina between ceramic and bond coat metal whereas the Western process fails to form a continuous film, as-deposited, in spite of the oxygen bleed inside the deposition chamber.

One could argue that, prior to ceramic deposition, the flash of evaporated MCrAlY consists mainly of the  $\gamma$  solid solution since the time at temperature is too short to allow for extensive growth of  $\beta$  precipitates. The low  $\beta$  phase content at the time bond coat oxidation is initiated could be one argument to explain why the alumina film is continuous between KDP1 and SDP2. Moreover, the fine grain size of this MCrAlY sub-layer should promote the formation of a high density of chromia nuclei. This would further help the alumina film to cover the whole metal surface. Finally, the role of electron beam irradiation on the bond coat oxidation in the KDP1 process should not be overlooked. Electron bombardment is known to activate chemical reactions which would otherwise not take place under thermodynamic equilibrium conditions.

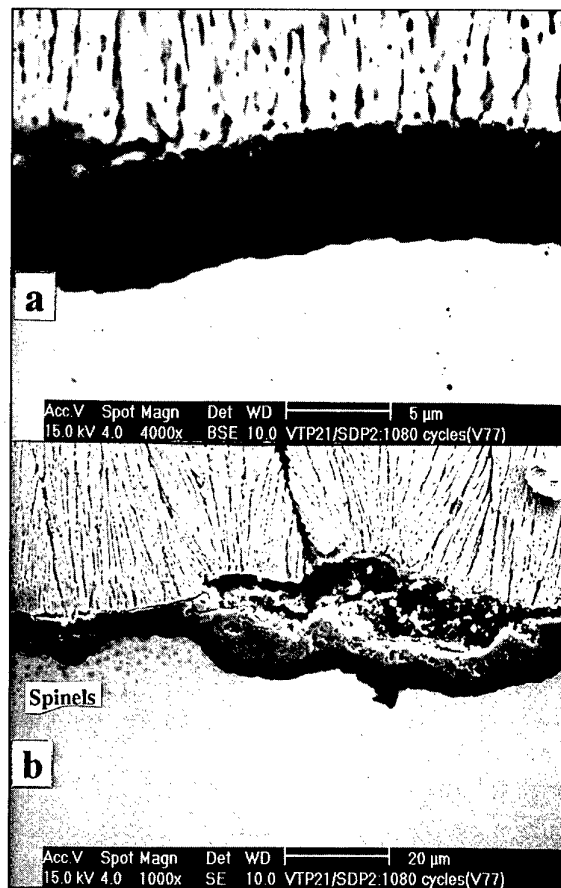


Figure 12: SEM back-scattered and secondary electron cross-section images of SDP2/KDP1 after 1080 cycles

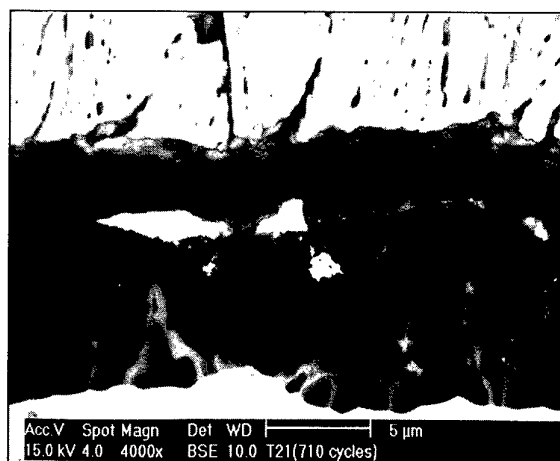


Figure 13: SEM back-scattered electron cross-section image of RT31/RT33 failed after 710 cycles.

#### Thermal cycling performance

EB-PVD TBC's have long been described as failing at the interface between the TGO (thermally grown oxide) and the bond coat metal<sup>25</sup>. It was shown in this work that a same nominal thermal barrier coating system could exhibit different spallation mechanisms ranging from a lack of adhesion at the alumina/bond coat metal to failure at the ceramic/TGO interface. Adhesive failure at the bond coat metal/TGO interface was synonymous of short cyclic lives for both the RT31/RT33 and SDP2/KDP1 systems. Whenever

the metal/oxide adhesion was good, TBC spallation life seemed to be controlled by the integrity of the ceramic/TGO interface. Failure at this interface could be the result of the formation of unprotective (Ni,Cr,Al) mixed oxides between the alumina scale and the ceramic coat as seen in the case of SDP2/KDP1. The growth of spinels at the YSZ/TGO interface implies the transport of Ni and Cr cations through the alumina scale. This could be explained by the formation of local through-cracks of the scale. No such cracks were however identified. Even in the absence of mixed oxide formation, the YSZ/alumina bond in the RT31/RT33 system seemed to deteriorate upon thermal ageing (see Figure 11). How the integrity of the YSZ/alumina interface evolves with time at temperature is an issue that may depend both on the alumina growth mechanism and ceramic sintering mechanisms.

MCrAlY coatings are known to exhibit parabolic oxidation kinetics. The scale thickness was measured on micrographs from the long life RT31/RT33 and SDP2/KDP1 systems such as those in Figures 12 and 13. Neglecting the transient oxidation on heating and cooling, estimated parabolic rate constants at 1100°C (in  $\text{g}^2/\text{cm}^4\text{s}$ ) were determined based on scale thickness considerations:

System	Number of cycles	Al <sub>2</sub> O <sub>3</sub> scale thickness ( $\mu\text{m}$ )	K <sub>P</sub> ( $\text{g}^2/\text{cm}^4\text{s}$ )
RT31/RT33	710	7,5	$8,4 \times 10^{-13}$
SDP2/KDP1	1080	5,5	$3,9 \times 10^{-13}$

These values are consistent with published data on parabolic rate constants of bare alumina forming alloys<sup>27</sup>.

In the absence of a fine microstructural characterization of the scales, it is difficult to account for this difference in oxidation kinetics. It is tempting though to try to correlate the higher oxidation kinetics of the RT31 bond coat to the presence of yttrium rich oxide phases within the alumina scale. The oxygen diffusivity of yttrium oxides is much higher than that of pure alumina. These yttrium rich oxides thus may act as fast oxygen diffusion paths through the scale to the bond coat/oxide interface and create as many fast growing oxidation fronts.

Bond coat oxidation kinetics is one argument to account for the superior spallation resistance of the SDP2/KDP1 system over RT31/RT33. The compressive stress within the oxide scale is maximum at room temperature. It results both from the thermal expansion mismatch between oxide and bond coat metal in addition to growth stresses. Both kinds of stresses increase with scale thickness. Moreover, under a given stress state, the probability for the scale to contain a critical flaw size also increases with scale thickness.

Whether the difference observed in ceramic morphology will also affect the spallation resistance of TBC's is a complicated issue. XRD patterns at room temperature suggest from the absence of peak shifts that EB-PVD ceramic layers contain negligible residual stresses (no more than a few hundred MPa). In another study<sup>28</sup>, the low residual stress level in as-deposited EB-PVD ceramics was verified within the coating depth by polishing the ceramic layer.

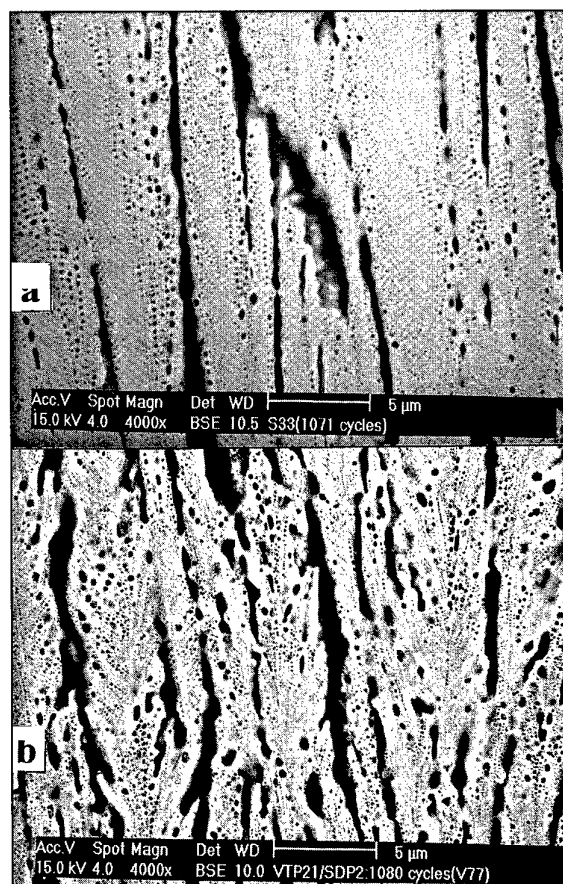


Figure 14: SEM back-scattered cross-section images of RT33 deposited on a LPPS MCrAlY bond coat after 1071 cycles (a) and KDP1 after 1080 cycles (b)

The ceramic morphology however evolves dramatically with ageing (see Figure 14 to be compared with Figure 4, both sets of pictures taken at 50 micron height from the bond coat). After more than 1000 cycles at 1100°C, sintering mechanisms have resulted in the columns branching up and microwelding together. The columnar structure is effectively partly lost. Some loss of ceramic compliance could be expected from this structural change potentially adding more stress to the TGO. This effect combined with a potential strength reduction of the ceramic/TGO interface with ageing may be responsible for the crack propagation within the region of this interface after long exposures. How the ceramic deposition process affects the integrity and stability of this interface is an open question.

## CONCLUSIONS

- Western and Eastern type TBC systems exhibit different ceramic morphologies and TGO films.
- Thermal cyclic lives were found to be very scattered for both SDP2/KDP1 and RT31/RT33.
- Short lives were synonymous of lack of adhesion between TGO and bond coat metal.
- High life specimens failed in the ceramic/TGO interface region.
- The SDP2/KDP1 exhibited overall superior spallation resistance and this could be correlated to lower bond coat oxidation kinetics than in the RT31/RT33 system.

**Acknowledgements:** The work concerning the study of Russian TBC's was supported by the SPAÉ. The authors gratefully acknowledge the contributions of E.Célrier and M.Scher for the thermal cycling work as well as J.M.Duchemin and J.M.Thubert for the SEM work at Snecma. The X-ray diffraction studies were performed by C.Diot at Onera. Fruitful contacts and discussions with Pr Y.Tamarin at the VIAM Institute in Moscow were much appreciated. Last but not least, the authors would like to thank Rémy Mévrel at Onera for returning his useful comments on the first draft of this paper.

## References

1. W.K.Halnan, D.Lee, « EB-PVD process for coating gas turbine airfoils », High temperature protective coatings 112<sup>th</sup> AIME Annual meeting, Atlanta, Georgia, March 7-8, 1983
2. S.M.Meier, D.K.Gupta, K.D.Sheffler, Ceramic TBC's for commercial gas turbine engines, JOM, March 1992
3. K.D.Sheffler, D.K.Gupta, Current status and future trends in turbine applications of TBC's, Gas Turbine Aeroengine Congress and R&P., Amsterdam, Sep. 30 1988 ASME 88-GT-286
4. Comments from W.Goward, D.Boone, W.Halnan, TBC Workshop 1997, May 19-21, Cincinnati, Oh
5. B.A.Movchan, A.V.Demchishin, « Study of the structure and properties of thick vacuum condensates of nickel, titanium, tungsten, aluminium oxide and zirconium dioxide » Fiz.metal.metalloved.28N°4, 653-660, 1969
6. Y.Tamarin, Private communication
7. A.V.Shavkunov, Private communication
8. S.Stecura, Optimisation of NiCrAl/ZrO<sub>2</sub>-Y<sub>2</sub>O<sub>3</sub> Thermal barrier system, NASA TM 86905, 1985
9. A.Feuerstein, W.Dietrich, H.Lammermann, « Advanced PVD overlay coating equipment for aircraft gas turbine engine applications », Tokyo International Gas Turbine Congress, 1987
10. H.Lammermann, A.Feuerstein, « PVD overlay coating for blades and vanes of advanced aircraft engines », 1992, Yokohama International Gas Turbine Congress
11. T.E.Strangman, « Development and performance of physical vapor deposition thermal barrier coating systems », Proceedings of the 1987 Coatings for advanced heat engine workshop III-63 to III-71, July 87
12. T.E.Strangman, US Patent 4,321,311 1982
13. N.E.Ulson, D.L.Ruckle, US Patent 4,414,249 1983
14. B.A.Movchan, « EB-PVD Technology in the gas turbine industry: present and future », JOM November 1996
15. M.A.Smith, W.E.Frazier, B.A.Pregger, « Effect of sulfur on the cyclic oxidation behavior of a single crystalline, nickel-base superalloy », Materials science and Engineering A203 (1995) 388-398
16. D.V.Rigney, R.Viguie, D.J.Wortman, D.W.Skelley, « PVD thermal barrier coating applications and process development for aircraft engines », TBC Workshop 1995, NASA Conference publication 3312
17. Yann Jaslier, « Development of EB-PVD TBC's: the role of deposition temperature and plasma assistance », PhD thesis, Cranfield University, 1995
18. U.Schulz, K.Fritscher, H.J.Ratzer-Scheibe, W.A.Kaysser, M.Peters, « 4th Int.Symp.on high Temp. Corrosion & Protection » Mat. Les Embiez, Fr.20-24/05 1996, To be published
19. Snecma unpublished work
20. Maricocchi, Rigney, US Patent 5,350,599 Sep.1994
21. L.Lelait, S.Alpérine, C.Diot « Microstructural investigations of EB-PVD TBC's », Journal de Physique IV, Colloque C9, supplément au journal de physique III, vol 3, déc 1993
22. M.G.Scott, « Phase relationships in the zirconia-yttria system », J.Mat.Sci, 10 (1975), pp.1527-1535
23. E.C.Subbarao, « Zirconia-an overview », Science and technology of zirconia, Advances in ceramics, vol.3, A.H.Leuer, L.W.Hobbs, 1981
24. C.Leyens, K.Fritscher, R.Gehrling, M.Peters, W.A.Kaysser « Oxide scale formation on an MCrAlY coating in various H<sub>2</sub>-H<sub>2</sub>O atmospheres », Surface and coatings technology 82 (1996) 133-144
25. S.M.Meier, D.M.Nissley, K.D.Sheffler, T.A.Cruse, « Thermal barrier coating life prediction model development » J.Eng.Gas.Turb.&Power, 114 (1992), 258-63
26. P.Lamesle, « Revêtements d'aluminures modifiés par le palladium: mécanismes de formation et comportement en oxydation/corrosion à haute température », Thèse de Doctorat, Université Henri Poincaré, Nancy 1, 1995
27. K.L.Luthra, C.L.Bryant, « Mechanisms of adhesion of alumina on MCrAlY alloys » Oxid.Met. 26 (5/6) 397-416 (1986)
28. Onera Rapport technique 22/3729 MY

# PROCESSING, CHARACTERISATION AND TESTING OF EB-PVD THERMAL BARRIER COATINGS

W. A. Kaysser  
M. Peters  
K. Fritscher  
U. Schulz

DLR  
German Aerospace Research Establishment  
Institute of Materials Research  
D-51170 Köln  
Germany

## Summary

Thermal barrier coatings (TBCs) are increasingly applied to hot components in gas turbines. Contrary to plasma spraying, the electron-beam physical vapour deposition (EB-PVD) process offers the opportunity to generate coatings having a unique columnar microstructure. The main advantage of this structure is its superior tolerance against straining and thermoshock, thus giving it a major edge in lifetime. Furthermore, cooling hole closure will be prevented and the aerodynamic design of the blades will be maintained.

This paper will outline the advantages of EB-PVD for the production of TBCs on rotating gas turbine components like blades and vanes. The effect of EB-PVD processing parameters on the microstructural evolution and respective lifetimes of partially yttria stabilised zirconia (PYSZ) TBCs will highlight the potential of the evaporation process. Alternative stabilisers like Ce and La are looked at in terms of increase of application temperatures as well as life extension of the blades. An extended structural zone diagram for PVD is proposed incorporating the influence of substrate rotation on microstructural evolution. Finally, the limits of evaporation processing will be stressed.

## 1. INTRODUCTION

There is no single parameter to verify the competitiveness of an aircraft. However, it is commonly accepted that direct operating cost (DOC) is a useful indication of the potential of a given type of aircraft. If a new aircraft is introduced it has to show significant DOC benefits of at least 5 to 10% compared to the aircraft currently in service to make it an attractive proposition to an airline. For an aero engine manufacturer the DOC is primarily reduced by control of fuel costs through weight savings, drag reduction and specific fuel consumption. For a new engine a realistic picture would call for a 2-3% improvement in specific fuel consumption and for about 5% in weight reductions [1].

Apart from specific fuel consumption, the thrust of an

engine is another design criterion, more precisely the specific thrust as expressed in the thrust-to-weight ratio. Both, specific fuel consumption and thrust-to-weight ratio have been significantly improved over the years accomplished through increased operating temperatures as well as improved structural efficiency [2]. It is very obvious that here advanced materials play a major role. In fact, modern aero engines represent some of the most demanding and sophisticated applications for structural materials in any engineering system manufactured today. This has been manifested by the steady increase in service temperature, product reliability and usage of lightweight materials [2].

But engines need not to be only reliable, economical on fuel and profitable, they also have to be environmentally acceptable. In terms of emission nitrogen oxides and carbon dioxide are of prime concern. NO<sub>x</sub> is particularly a problem since emission increases with increasing pressure ratio and process temperature - both are obvious ways to increase engine performance.

Blades and vanes of the high pressure turbine section of aero engines are among the most highly stressed parts in engineering components. Internally cooled aerofoils of state-of-the-art Ni-base superalloys operate at temperatures of about 1000°C with short-term peaks yielding even 1100°C which is close to 90% of the alloys' melting points. These temperatures are maintained in service due to a highly sophisticated cooling technology by which however thermal energy is withdrawn from the aerofoils in the order of 1 MW/m<sup>2</sup> thus reducing the overall fuel efficiency of the engine. The necessity of a close control of materials temperatures can be expressed by the simple rule that blade life on creep is halved for every 10 to 15°C increase in temperature [3].

But further increases in thrust-to-weight ratio of advanced aero engines will require even higher gas turbine inlet temperatures. Figure 1 shows how these temperatures have increased over the years. Today turbine inlet temperatures exceed 1400°C while 1760°C are aimed at within the next twenty years. There is no doubt that this ambitious goal can only be met by usage of uneconomically extensive cooling

techniques or by advanced high temperature materials [4] and in particular through the introduction of electron-beam physical vapour deposition (EB-PVD) thermal barrier coatings (TBCs) [5].

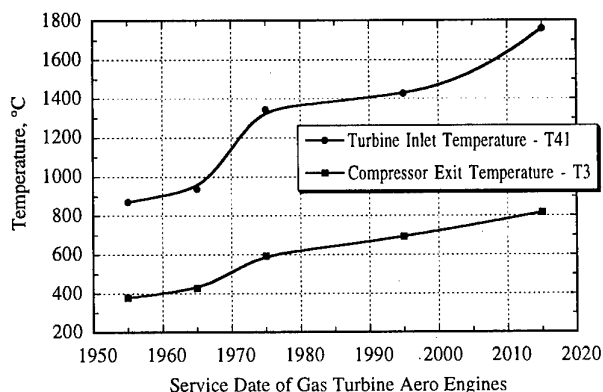


Figure 1: Increase of turbine inlet temperature of aircraft gas turbine engines [2]

## 2. THERMAL BARRIER COATINGS

TBCs consist of thin ceramic layers of low thermal conductivity - typically partially stabilised zirconia - which are applied on aerofoil surfaces that just have a metallic corrosion resistant coating. The coating imparts good adhesion of the ceramic to the substrate. Application of the TBCs enables increasing engine performance/thrust by either increasing the gas temperature or reducing the cooling air flow. Alternatively the lifetime of the turbine blades can be extended by decreasing metal temperatures as schematically outlined in Figure 2 [6, 7].

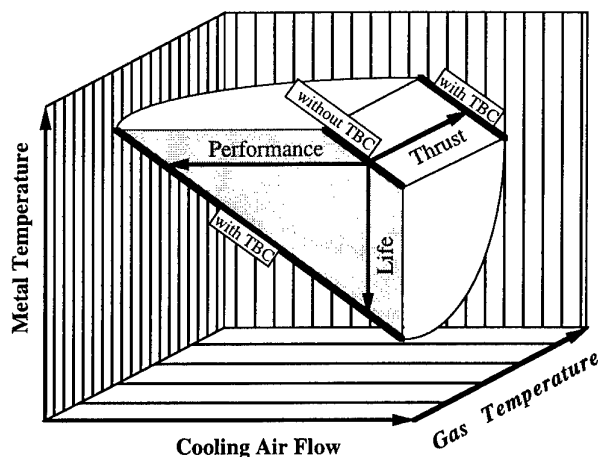


Figure 2: TBCs allow increased engine performance and/or life extension

## 3. HISTORIC DEVELOPMENTS IN TBCS

Since the early sixties PS (plasma sprayed) calcia- and magnesia-stabilised zirconia TBCs have been used extensively as ceramic top coat on combustion chamber walls and on burner cans to prolong their

lives by avoiding hot spot formation and subsequent failure by thermal fatigue. These materials were broadly accepted for 20 years until their replacement by PYSZ (partially yttria-stabilised zirconia) coatings was initiated. The APS (air-plasma sprayed) PYSZ TBCs offer outstanding mechanical, chemical and thermal properties. Two generations of high temperature ( $>1000^{\circ}\text{C}$ ) TBCs were based on these unique ceramics (generation I is APS MCrAlY / APS PYSZ and generation II is LPPS (low-pressure plasma sprayed) MCrAlY / APS PYSZ) which allowed in the early eighties to introduce TBCs on highly thermally loaded parts like vane platforms and vane airfoils. The need for higher operating temperatures in turbines, however, inspired material scientists for half a decade to search for TBCs which could also be applied on blade platforms and airfoils which are subjected to high thermal and additional mechanical loads.

Here the electron-beam physical vapour deposition (EB-PVD) technology offered the opportunity to generate TBCs with vastly superior strain tolerance. This is due to their specific coating structure which grows from the vapour phase in a columnar form with individual ceramic columns being weakly bonded to their neighbour columns as e.g. shown in Figures 8a or 13.

Coating all these high performance parts with reliable TBCs would allow to alter the initial component design and to operate the TBC bearing components with the coatings as an integral part of them. The exploitation of strain-tolerant TBCs initiated a renaissance of industrial EB-PVD technology in 1987 which until then had been utilised for deposition of metallic MCrAlY-type coatings for 20 years. The novel EB-PVD PYSZ ceramic layers with advanced LPPS MCrAlY bond coat, designated now as generation III TBC, offered a roughly 3 times improvement in blade life or a surface temperature increase on the hot sections of airfoils of approximately 150K.

## 4. PROCESSING OF TBCS

Plasma-sprayed (PS) TBCs have been widely applied to hot components like burner cans since the sixties while in recent applications to more pretentious parts like turbine blades EB-PVD technology is favoured. Contrary to plasma spraying, EB-PVD processing offers the opportunity to generate coatings having a unique columnar microstructure with 2 to 25  $\mu\text{m}$  in diameter. The main advantage of this structure is its superior tolerance against straining and thermoshock, thus giving it a major edge in lifetime [8]. Furthermore, cooling hole closure will be prevented and aerodynamic design of the blades is maintained. In Table 1 the two processing methods are compared as far as thermal barriers for turbine blades are concerned.

During EB-PVD processing a high energy electron beam melts and evaporates a ceramic source ingot in a vacuum chamber. Ingots are bottom fed into the crucibles during evaporation to ensure continuous



TBC growth. To achieve defined stoichiometry of the zirconia a controlled amount of oxygen is bled into the deposition chamber. Preheated substrates are positioned in the vapour cloud above where the vapour is deposited on substrates at deposition rates of 100 to 250 nm/s [9]. Typical columnar microstructures and aerodynamically smooth surfaces are obtained without the need for final polishing or conditioning of cooling holes. Due to the columnar microstructure the life time of the TBCs is prolonged and the damage tolerance improved. Typical characteristics and major advantages of thermally sprayed and on-evaporated TBCs are schematically outlined in Figure 3 [10]. Figure 4 shows a selection of EB-PVD TBCs on aero engine and stationary gas turbine blades produced at DLR on semi-commercial single-source 60kW Leybold and dual-source 150kW von Ardenne EB-PVD coaters.

Table 1: Plasma sprayed (PS) versus on-evaporated (EB-PVD) TBCs

	PS	EB-PVD
Surface Finish	good but extra polish	excellent
Bond Coat Roughness	grit blasted	smooth
Bonding Mechanism	mechanical	chemical
Alloy Flexibility	high	limited
Typical Thickness	0.2-3mm	0.1-0.3mm
Cooling Hole Closure	poor	excellent
Coating Source	movable	fixed
Large Parts predictable	favourable	costly
Parts per Charge	1	1-10
Investment Costs (%)	100	100-400

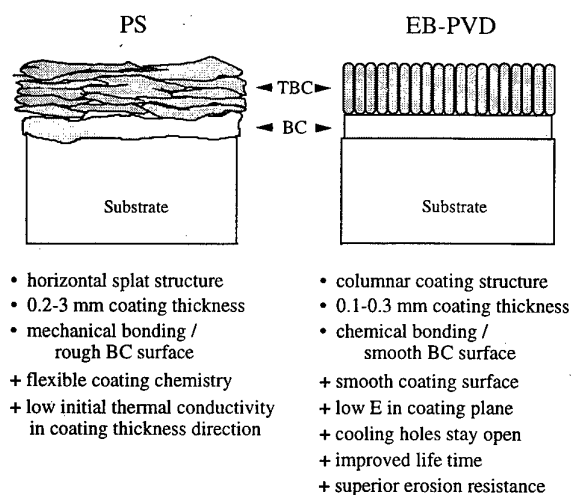


Figure 3: A simplified comparison of properties for plasma sprayed (PS) and evaporated (EB-PVD) TBCs (schematic)

## 5. FAILURE MECHANISMS AND PREVENTION

Pertinent usage of TBCs as a reliable component or future TBC applications as integral design elements of highly loaded engine parts need a more comprehensive understanding of the failure mechanisms of

the coating systems. Failure in TBC systems almost always occurs by TBC spallation due to stresses in the ceramic or in the bond coat. But failure of EB-PVD processed TBCs happens, unlike those for PS based TBCs, at the ceramic - bond coat interface. There is a thermally grown oxide (TGO) of a few  $\mu\text{m}$  in thickness which plays a key role in the adhesion of EB-PVD TBCs since it is considered to be the weak link in the system. Its strength and adhesion to the bond coat governs the true location of failure whether first cracks will propagate within or along the TGO - bond coat interface. Here spallation is initiated by accommodation of stresses surmounting a critical value.

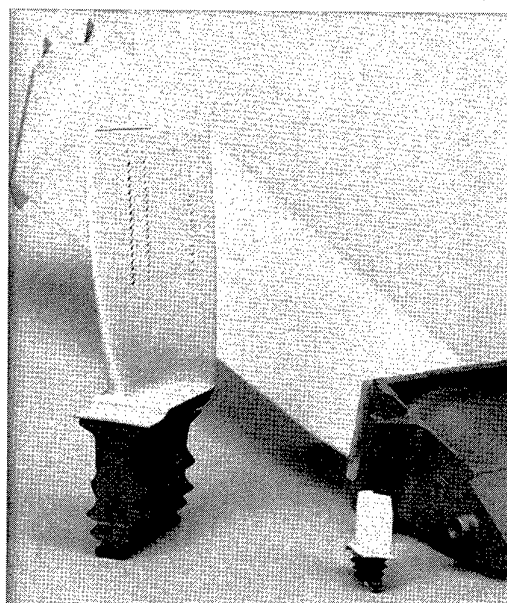


Figure 4: EB-PVD TBCs on turbine blades for use in stationary gas turbines, civil aero engines and helicopter engines (decreasing in size)

A way to minimise misfit stresses in TBC systems is to reduce the growth rate of TGOs. The early overlay bond coatings which were EB-PVD MCrAlYs were followed by PS MCrAlY families. Advanced MCrAlYs contain additional elements like Si and/or Ta, Hf for providing lower scaling rates and better hot corrosion resistance. These coatings with low vapour pressure elements (mostly refractory elements) are more easily deposited by LPPS techniques. TGOs grow more slowly and thus effectively prolong the lifetime of the TBCs on them.

Another route to minimise misfit stresses and improve spallation resistance is to make the bond coatings more creep resistant which will bring more stability to the TBC root area on thermomechanical cycling. This change in mechanical characteristics is successfully done in recent LPPS MCrAlY overlay coats by converting the former  $\gamma/\beta$  phase structure into a  $\gamma/\gamma'$  structure by appropriate alloying. Due to the introduction of a significant portion of refractory ele-

ments the modified high creep resistance phase structure offers further benefits which refer to a low diffusivity and a reduced coefficient of thermal expansion (CTE). The latter property is of uppermost importance for the amount of residual stresses accumulating in the TGO layer. They can be reduced if the differences between the CTEs of the respective ceramic and metallic partners of the whole system are minimised.

Finally the involvement of superalloy substrates in the interplay of the physical properties of the respective material components and their influence on the compositional behaviour of TBC systems has to be addressed. Ni-base superalloys have gained a high degree of technical maturity in the early nineties. They have passed a lot of development stages, e. g. hardening by precipitated  $\gamma'$  phases, extensive solid solution strengthening, directional solidification and finally single crystals to trust in more creep-resistant crystal orientations and continuous grain structures [11]. The most creep-resistant crystal orientation (001), however, provides the least Young's modulus of only 120 MPa. Obviously it is a drawback for the adhesion of TBCs as thin-walled airfoils can be bent more rigorously under same loads in service than the conventionally cast counterparts. Three generations of single crystal superalloy development, however, resulted in a reduction of the CTE which compares with the recent low expansion bond coats.

## 6. SURFACE TREATMENT/ROUGHNESS

Another key issue for utilising the full potential of TBCs is their surface finish. Increasing roughness results in higher aerodynamic losses as well as increased heat transfer to the airfoil [12]. It also has an impact on TBC adherence. So the roughness of the TBCs needs to be closely controlled.

The processing steps before TBC deposition are essential for attaining the targeted surface characteristics of the final surface. For EB-PVD TBCs the bond coats have to have a finish on mechanical surfacing better than 1 to 1.5  $\mu\text{m Ra}$ . Identical pilot sample parts are attached with thermocouples at representative locations in order to have a means to calculate in analogy the temperature distribution over time within real parts during a real deposition process as closely as possible. Optimal T-t histories for the thermal cycle during preheating and TBC deposition have to be assured. The TBC deposition must be performed within an operating window which takes care of a number of parameters, the most important of which are [13]

- component temperature during coating
- pressure in the coating chamber
- oxygen partial pressure in the coating chamber
- part rotation rate during coating.

The final coating will then have a 1 to 1.5  $\mu\text{m Ra}$  roughness [14]. Further reductions of roughness may be advantageous.

## 7. INFLUENCE OF STABILISERS ON TBC PERFORMANCE

Partially yttria-stabilised zirconia (PYSZ) is the current state-of-the-art material for TBCs. Unfortunately, the material shows insufficient phase stability and accelerated sintering at temperatures above 1200°C. Therefore, further increases of gas inlet temperature require alternative stabilisers with improved phase stability. Another argument for new stabilisers in zirconia or for completely new ceramics is the insufficient resistance of current TBCs against chemical attack by pollutants in the combustion gas. Hot corrosive decay of TBCs by  $\text{Na}_2\text{SO}_4$  and vanadates are reported which involves leaching out of stabilisers from parent zirconia. The degradation occurs by transformation of high temperature phases to monoclinic zirconia on cooling. This failure mode may be found mainly in heavy duty engines and off-shore service [15].

One alternative stabiliser for zirconia is  $\text{CeO}_2$ . The benefits of ceria-stabilized (CeSZ) TBCs are good corrosion resistance [16-17] and excellent phase stability at high temperature [18]. Furthermore, the thermal conductivity is found to be lower than for PYSZ and some benefits for lifetime and thermocyclic resistance are reported, too.  $\text{La}_2\text{O}_3$  is another candidate for replacing  $\text{Y}_2\text{O}_3$  in zirconia.

To get more insight into single-source EB-PVD processing of new compositions for TBCs a feasibility study was performed on four differently stabilised zirconias (Table 2) using identical substrate alloys and EB-PVD NiCoCrAlY bond coat compositions [19].

Table 2: Differently stabilised zirconias investigated

	$\text{ZrO}_2 +$
PYSZ	6.5 wt% $\text{Y}_2\text{O}_3$
FYSZ	20 wt% $\text{Y}_2\text{O}_3$
LaSZ	8 wt% $\text{La}_2\text{O}_3$
CeSZ	25 wt% $\text{CeO}_2$ - 2.5 wt% $\text{Y}_2\text{O}_3$

A columnar structure of the TBCs of about 250  $\mu\text{m}$  thickness was found for all four chemistries with some noticeable differences between the various ceramics. FYSZ and CeSZ possess a larger column diameter and a higher degree of ordering compared to PYSZ and LaSZ. On the other hand, LaSZ has the most nonuniform shape of the terminal section of columns. The microstructure of standard PYSZ lies between these two extremes with more irregularities than CeSZ and FYSZ but not as many as with LaSZ.

One possible explanation for the variations in morphology are the differences of the respective homologous temperatures  $T_{\text{deposition}} / T_{\text{melting}}$  which have a strong relation to diverse microstructural zones within common structural zone diagrams [20-21]. Although the deposition temperature was nearly the same for all four zirconia, their melting points differ widely, thus resulting in different microstructures according to the structure zone models mentioned

above. Other effects that affect the microstructure include variations in phase composition, ion radii, and surface energy aspects during condensation [22].

Phase analyses by X-ray diffraction (XRD) revealed that the compositions of the three binary TBCs, PYSZ, FYSZ, and LaSZ, were close to the ingot compositions. For PYSZ exclusive tetragonal (*t'*) phase was identified while FYSZ only contained cubic (*c*) phase and LaSZ exhibited a mixture of mainly tetragonal, minor cubic, and substantial amounts of monoclinic (*m*) phase. In the case of the ternary composition  $\text{ZrO}_2\text{-CeO}_2\text{-Y}_2\text{O}_3$ , however, analysis showed no constant but fluctuating compositions across the TBC thickness. Due to these variations the surface content of ceria varied among test pieces of different deposition runs between 13 and 38 wt%. For CeSZ a mixture of cubic, tetragonal, and occasionally monoclinic phases was found [22].

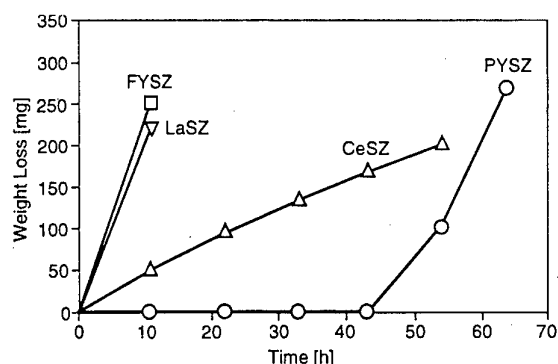


Figure 5: Weight loss of cyclically burner rig tested samples versus time

These four differently stabilised TBCs were subjected to cyclic burner rig testing at Mach 0.35 gas velocity with cyclic heating up to 1150°C for 57 minutes and forced air cooling to room temperature for 3 minutes. The results are summarised in Figure 5. Rapid spallation of FYSZ and LaSZ TBCs was observed as characterised by high weight losses after short testing times. PYSZ proved to be the most stable coating system over long times, followed by sudden spallation of TBC.

CeSZ exhibited a different behaviour. Here a quasi-continuous weight loss was observed after each inspection cycle. The different failure mode of CeSZ in comparison to "standard" failure by spallation of PYSZ is visible in Figure 6: a step-wise degradation in layers was observed instead of spallation of the whole TBC in a single event as noticed in all other cases. A thin layer of ceramic was still present on top of the bond coat after the tests.

Considering the lifetime of the TBCs a similar ranking was also found in cyclic furnace tests between 150°C and 1100°C. Here, however, for all stabilisers the main failure location was found between the thermally grown oxide (TGO) and the bond coat rather than between TGO and TBC.

Burner rig tests as well as furnace tests revealed that composition and phase structure of the variously stabilised zirconias are closely related to the cyclic lifetime of the coating system. The only phase found in PYSZ was metastable non-transformable *t'*. The equilibrium phase diagram [23] predicts a two-phase mixture consisting of *t* containing 4 %  $\text{Y}_2\text{O}_3$  and *c* containing 16 %  $\text{Y}_2\text{O}_3$  at deposition temperature.

The *c* phase, however, can only be maintained at RT under the preconditions that a very low critical grain size of *c* is established and/or the *c* particles are subjected to high compressional stresses by the surrounding *t* matrix. Both mechanisms would cause the half widths of the XRD peaks to be broadened which, however, is not observed. Therefore, formation of the *t'* phase is considered to be caused via rapid quenching on PVD processing as can similarly be assumed for solidifying TBCs during PS deposition.

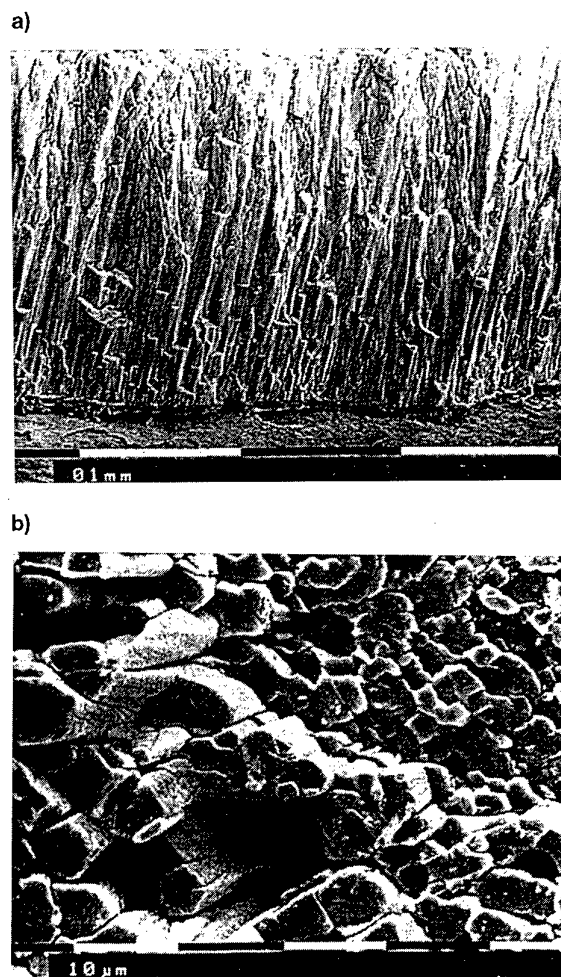


Figure 6: SEM micrographs of burner rig tested TBCs after 65hrs at 1150°C:

a) PYSZ (cross section); b) CeSZ (surface)

A major drawback of PYSZ is the lack of high temperature phase stability as supported by annealing experiments. Whereas EB-PVD TBCs are stable at

temperatures up to 1150°C, they transfer after 100 hrs annealing at 1400°C to a mixture of 48% tetragonal + 48% cubic + 4% monoclinic (mol%) phases [24]. The transformation into three phases suggests a sequential mechanism consisting of yttrium cation diffusion out of  $t'$  and destabilisation of  $t'$  into  $c$  and  $t$  with subsequent phase transformation to  $m$  during cooling. At temperatures below the stability point  $t'$  is still the most effective phase for durability in thermal barrier coatings as can be seen in Figure 5. The  $t'$  microstructure is characterised by outstanding bending strength, high crack propagation energy, high fracture toughness and highly tolerant thermoshock behaviour. Lattice distortion due to tetragonality, a domain structure and the well-described tweed microstructure inside the  $t'$  grains [25] are supposed to be responsible for the excellent performance of PYSZ.

The formation of a single cubic phase for FYSZ TBCs is in accordance with all findings on EB-PVD as well as PS TBCs known from literature. FYSZ suffers from low thermal shock resistance and poor fracture properties of the equilibrium  $c$  phase. Earlier reports on PS TBCs [26-27] have shown that FYSZ possesses poor thermocyclic behaviour. However, some inconsistency in the literature on TBCs of this composition must be recognised. The present results support findings [28] that the columnar EB-PVD structure is not able to overcome the intrinsic problems of FYSZ leading to poor integrity of such coatings after cyclic testing (Figure 5).

Monoclinic phases that undergo a phase transformation during temperature variation will cause rapid spallation of EB-PVD TBCs. The volume change associated with the phase transformation  $m \rightarrow t$  creates high stresses. Even strain tolerant structures like columnar EB-PVD ones are unable to accommodate these stresses on transformation. Early spallation of LaSZ gives clear evidence for such a failure mechanism. It has to be taken into account that high rate condensation from a vapour phase is not necessarily a process that stabilises equilibrium phases. Therefore, phase diagrams do not allow a safe prediction of the phases of real coatings.

CeSZ showed the most interesting behaviour. The condensing matter is evaporated from a ceramic ingot source material at approximately 3500°C [29]. The presence of ceria considerably lowers the melting interval of the ingot. Selective processes are facilitated which cause the preferential evaporation of high vapour pressure components and enrichment of low vapour pressure elements in the melting pool. Vapour pressures are  $8 \cdot 10^2$  Pa for  $ZrO_2$  and  $9 \cdot 10^5$  Pa for  $CeO_2$  at 3060°C [30] and thus differ more than three orders of magnitude. This difference is probably even higher at the evaporation temperature which is indeed too much for viable single-source EB-PVD processing. As a matter of fact the evaporation process becomes instationary resulting in the compositional fluctuations observed. However, burner rig results of CeSZ were promising (Figure 5). Quasi-continuous weight loss and a degradation of the CeSZ TBCs in thin layers were found but no spallation. One reason for a step-wise loss is, of course,

the fluctuation of composition across the thickness of the TBC. This may cause alternating layers of "weak" phases including monoclinic and "strong" phases like  $t'$  [24]. Apparently, the coating will first break in weaker regions. Lattice misfits between the various layers may further contribute to reduced adhesion between the layers. Higher erosion rates of CeSZ found for PS TBCs [28, 31] may also account for this failure mode. The partial loss of this TBC may act as a strain/stress relief mechanism that allows the remainder part of the coating, which is thinner due to partial spallation, to adhere longer. CeSZ apparently offers some potential in thermal barrier coatings especially if a columnar microstructure can be utilised. Multiple source evaporation is however required to bring about reproducible CeSZ TBCs of stable composition.

## 8. INFLUENCE OF MORPHOLOGY ON TBC PERFORMANCE

The microstructure of EB-PVD layers is essentially influenced by four basic processes:

shadowing,  
surface diffusion,  
volume diffusion and  
desorption.

Their evolution is roughly predicted in structural zone diagrams [20-21]. Rotation of substrates during deposition, however, is not regarded as an essential contribution to the growth process so far. Nevertheless, it causes an additional microstructural feature in zirconia-based TBCs. A beaded or "c-shaped" structure of the columns is formed due to the continuous change of vapour impact angle and amount of vapour particles that adhere on the surface during each revolution [32-33]. Elevated substrate temperatures during EB-PVD cause a higher density of the TBCs and a higher hardness as well [34]. In addition to stabiliser type and content the degree of ionisation of the vapour cloud, gas pressure, surface roughness, deposition rate and vapour impact angle are other parameters that influence the columnar microstructure of EB-PVD thermal barrier coatings [22].

EB-PVD TBC production upon 3-D coated parts like vanes and blades necessitates substrate rotation during deposition. Therefore, the influence of rotational speed on microstructural evolution of the coatings has been investigated in more detail. The differences in microstructure between TBCs deposited under two separate process parameter sets are illustrated in Figure 7. SEM pictures of the surface of TBCs display that microstructures of EB-PVD TBCs strongly depend on process parameters, particularly substrate temperature and rotation.

Aiming at customising microstructures of TBCs for specific performance it is noteworthy that substrate temperature and rotational speed are alternative process parameters that cause the same microstructural features in the TBCs within certain limits. At low temperature and low rotational speed columns

often vary in diameter from root to top or from one column to the other. Columns at the root section are much thinner than at the top and are enlarging discontinuously from root to top conically. Increasing both temperature and rotational speed improves the regularity and parallelity of the microstructure and enlarges the column diameter. After competitive selection of favoured crystal orientations in the thin root area during the first stages of coating growth, columns start immediately to grow in width to their terminal diameter. Although the coating density measured is higher for high temperature/high rotational speed TBCs than in low temperature deposited TBCs, the columns appear to be less densely packed.

a)



b)



Figure 7: Surface of YPSZ TBCs: a) 980°C; 12rpm; b) 1050°C; 30rpm

The microstructure can be varied without altering the deposition temperature by different rotational speeds. At low rotational speed the beaded structure is formed within the columns while it disappears immediately after changing to a higher speed. An increase of column diameter was also found.

This processing tool allows to manufacture microstructurally graded TBCs that can be adapted to the

need of appropriate column features in particular TBC thickness zones. Several aspects may contribute to the observed effects including surface temperature fluctuations, change of diffusion kinetics and enlarged shadowing due to rotation. For instance, measurements of actual surface temperatures on flat samples during deposition gave temperature differences of 60 to 80°C for a low rotational speed compared to 15 to 25°C for a three times higher speed.

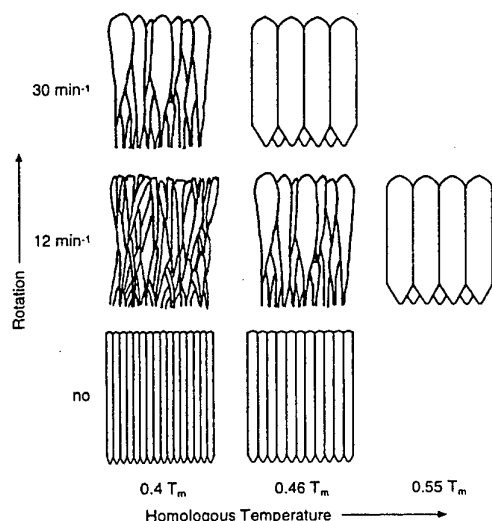


Figure 8: Schematic representation of the influence of substrate temperature and rotational speed on columnar microstructure evolution of EB-PVD TBCs

These observations suggest that structural zone diagrams should be modified when substrates are rotated during deposition. It is therefore proposed to incorporate a second axis in the models as a further degree of freedom similar to sputtered coatings where e.g. the role of argon pressure was considered. To give a first idea of a potential model extension, the observed microstructures for the interval of homologous temperature investigated are summarised in Figure 8 [35].

## 9. INFLUENCE OF DEPOSITION ANGLE ON TBC STRUCTURE

Another processing parameter of interest for EB-PVD component coating is the angle under which the vapour cloud hits the substrate. This is of particular practical importance since usually substrates like turbine vanes and blades irregularly shaped.

First it was shown that for both single source and dual source evaporation morphology and texture of PYSZ TBCs produced under a perpendicular vapour incline angle were nearly identical for [35]. In all cases a {100} plane nearly parallel to the surface was found, an example of which is given in Figure 9 [36].

The good performance of TBCs on highly loaded parts in severest environments, achieved in less than a decade of development, is a good indication for the versatility of the columnar structure concept of TBCs. The unfavourable crystallographic relations between the columns and the direction of highest straining in service, hypothetically addressed before, stand for a positive view into the future of TBCs: they still bear a potential for further improvements.

## 11. STRUCTURE PROPERTY RELATIONSHIPS

Some representative microstructures of TBCs produced by single source evaporation were chosen for cyclic furnace testing (Figure 12). All samples had the same EB-PVD NiCoCrAlY bond coat and surface treatments. Samples with a microstructure consisting of tapered and discontinuous columns due to multiple branching on growth exhibit the longest cyclic lifetime (12rpm/1020°C). TBCs with more regular columns of larger diameters appear less tolerant against thermocyclic loading. Burner rig tests confirm these results. Obviously, microstructure of TBCs and thermocyclic lifetime are closely interlinked. Figure 12 evidences the superiority of TBCs with a non-regular microstructure consisting of columns with variable diameters over TBC with large uniform column diameters and a regular microstructure.

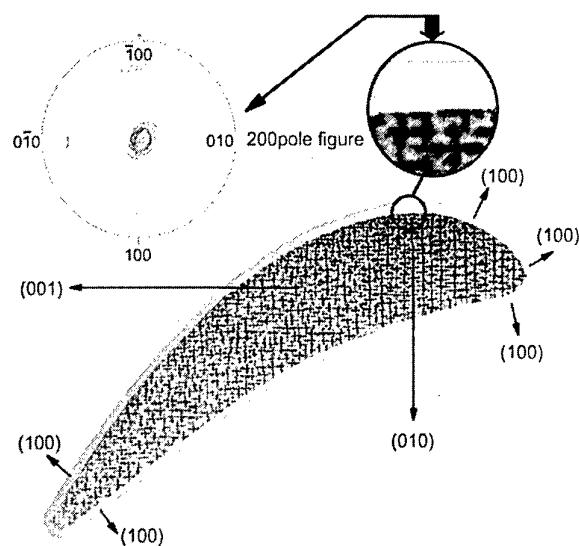


Figure 11: Crystallographic orientation of single crystal blades and EB-PVD TBC

Changes in stress state, elastic moduli, and adhesion between contacting columns that possess high numbers of protrusions may be responsible for this different behaviour. On the other hand, in the regular microstructure, crack propagation paths were provided along the parallel columns that cover the whole thickness of the TBC. Indeed early crack formation was found for these microstructures.

In hot corrosion testing of EB-PVD TBCs no evidence was found for hot corrosion of the bond coat and for a chemical reaction between the TBC and corrosion accelerators like molten salts and sulphur compounds [37, 38]. However, TBC failure can be initiated by mechanical attack of solidified salt compounds. Spallation of small areas of TBC in a funnel-shaped manner with some thinner coating still adherent on the bondcoat indicate this failure mechanism. For columns that possess larger voids between the interior column faces, salts may penetrate deeper into the coating than in denser columnar microstructures. Consequently, the weight loss is higher for a coarser microstructure deposited at higher rotational speed compared to a microstructure deposited at lower temperature and rotational speed [37].

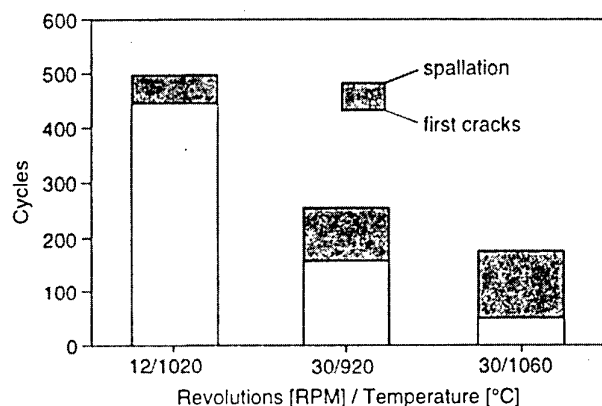


Figure 12: Cyclic lifetime in furnace test between 1100°C and 130°C

## 12. OUTLOOK AND CONCLUSION

To exploit the full potential of TBCs on highly stressed rotating turbine components further work has in particular to be directed to efforts which determine critical stresses more accurately based on detailed understanding of failure mechanisms of entire TBC systems with more confidence. The progress in the manufacture of more reliable TBC systems on single crystal materials will address the design of conveniently microstructured TBCs with superior strain tolerance on advanced bond coats with predictable TGO formation. The tailoring of respective microstructures to differing substrates with regard to optimal adaption of their "porosity" and of the thermal expansion mismatch has to be taken into account. Here the disposal of appropriate EB-PVD technologies will enable to manufacture unique microstructures for service-tolerant TBCs.

Future applications of TBCs aim at surface temperatures of 1250°C and above where aero engines as well as industrial gas turbines will operate. Today's state-of-the-art PYSZ ceramics, however, exhibit destabilisation of the tetragonal  $t'$  phase to monoclinic and cubic on extended exposure at temperatures above 1150°C, and sintering phenomena become predominant. Alternative ceramics will be needed with reduced sintering rates, improved phase stability and lower thermal conductivity. The need for ad-

In Figure 10 two EB-PVD PYSZ coatings are compared with vapour incline angles of 25-40° (Figure 10a) and < 10° (Figure 10b) deposited under constant rotating conditions. It is obvious that the columnar structure closely follows the incline angle of the vapour cloud to the substrate surface. This shows that the angle of the columns is directly related to the vapour incline angle, which is, however, different for the crystallographic orientation. Texture measurements have revealed that the deposition conditions clearly influence the type of texture of EB-PVD TBCs [36]. For rotated substrates a four-fold symmetry with {100} planes nearly parallel to the surface evolves independent of vapour incline angle, as indicated in Figure 10. The technical importance of textures in TBCs is related from the fact that the associated anisotropy in elastic moduli as well as thermal expansion within the t' phase may very well have a profound influence on the lifetime of the coating systems.

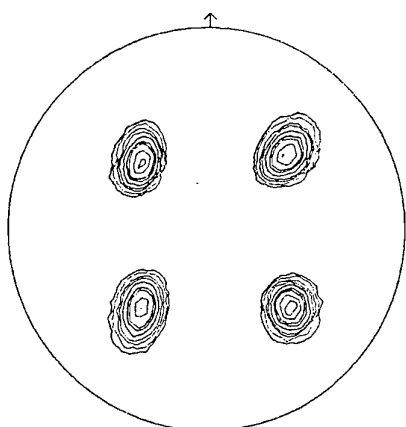


Figure 9: Characteristic texture of EB-PVD processed PYSZ TBCs indicated by {111} pole figure [36]

#### 10. SINGLE CRYSTAL SUBSTRATES

As discussed before, the columns of EB-PVD TBCs exhibit a preferred {100} texture in perpendicular direction to the substrate. How does this reflect on advanced substrate material which more and more tends to be of single crystal nature? The technical advantage may be twofold, namely a slightly higher thermal expansion (CTE) in in-plane direction for a better fitting to the bond coat and a hypothetically lower Young's modulus (note: the Young's modulus is highest in {100} orientation for zirconia monocrystals) which provides more stress relief at the interface on mechanical loading.

Some controversy may arise on the appropriate definition of the "right" Young's modulus which becomes effective as a stress depressant in in-plane direction. Is the effective Young's modulus the intrinsic physical property of an individual crystal column, or is it the - much lower - overall Young's modulus of the whole stack of TBC constituents composed of columnar and wedge shaped crystals, grain boundaries, loosely adherent interfaces and some free space e.g. at abandoned crystal positions?

This question in mind the habit morphology and orientation of a TBC will be detailed first. EB-PVD TBCs form a preferred {100} texture not only in normal but also in in-plane direction which will establish along the main axis of rotation and perpendicular to it (Figure 11). This axis usually coincides with the main axis of a turbine blade which also is most heavily subjected to mechanical stressing in service. In essence, the in-plane {100} texture orientation of TBCs is the most heavily strained one. Any other crystal orientation should be better. A look over a TBC in lateral direction (Figure 7b) clearly shows the longitudinal and often diamond-shaped cross section of crystals which spread with their elongated main diagonals in {100} direction. So less stress-depressant boundaries will accumulate in this direction compared to all others.

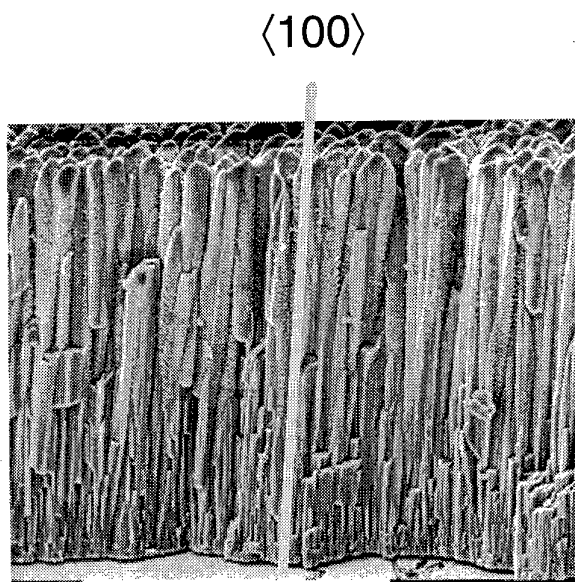
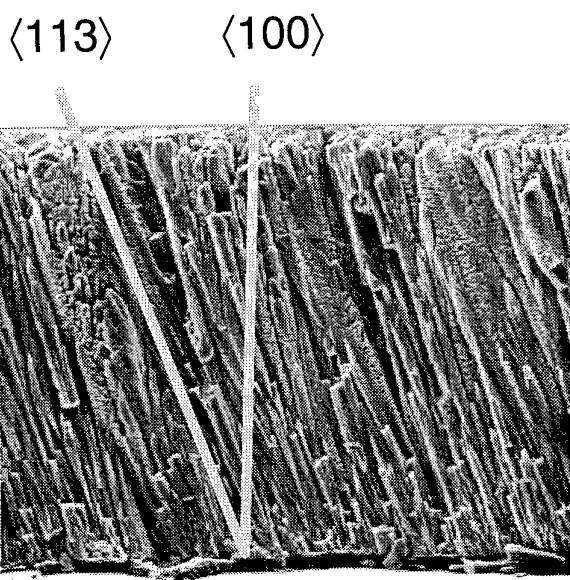


Figure 10: PYSZ EB-PVD coatings deposited under vapour incline angles of 25-40° (a) and < 10° (b)



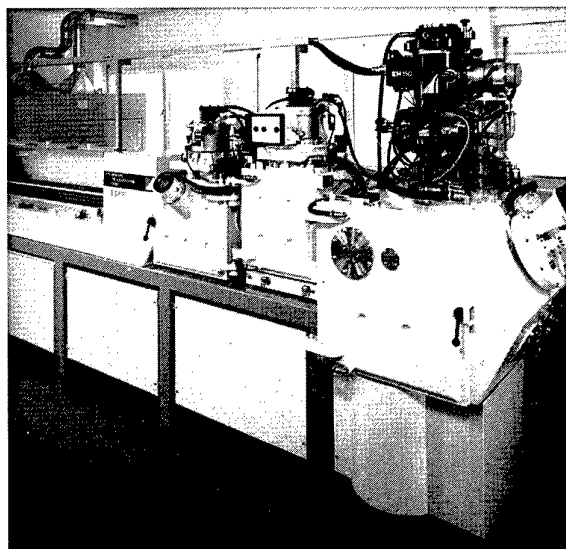


Figure 13: DLR's 150 kW dual-source EB-PVD laboratory coater (von Ardenne Anlagentechnik) for the production of novel TBCs and bond coats on aeroengine and stationary gas turbine components

vanced ceramic materials will force EB-PVD processing development to overcome pertinent materials restrictions. Multiple-source high rate coaters will be a valuable tool to enable the production of TBCs which are composed of low and high vapour pressure components (Figure 13).

Advanced electron beam gun design allows the use of only one gun in combination with jumping electron beam technology for dual source evaporation [39]. Fast to and fro movements of the electron beam from one pool to another and provides a quasi-continuous evaporation from multiple sources. Such equipment also allows to produce advanced bond coat compositions which may attribute their share to the manufacture of safer TBC systems.

New microstructures encompass compositionally graded, density graded and multilayered arrangements where, especially in the last case, a reduced heat conduction may allow the application of thinner overlays. CVD techniques can attribute their particular thin layer virtues. Basic and applied research capabilities have to focus on alternative materials and processing routes while earnestly guarding all cost requirements. Non-destructive testing and life-prediction methodologies for TBC systems have to be furnished. Finally, research and development efforts have to be combined to fully exploit the temperature potential of TBCs in aeroengine gas turbines and at the same time make TBCs mature for extensive usage for rotating components also in stationary gas turbines for energy conversion purposes [6].

### 13. ACKNOWLEDGEMENTS

The authors highly acknowledge the experimental assistance given by J. Brien, C. Kröder, H. Mangers,

H. Schurmann and W.-D. Zimmermann.

### 14. REFERENCES

- [1] S.J. Swadling, An Airframe Manufacturer's View on the Development of Aero Engines, *Proc. European Propulsion Forum*, 1-13, Royal Aeronautical Soc., London, 1993
- [2] J.C. Williams, The Development of Advanced Gas Turbines: the Technical and Economic Environment, in: D. Coutsouradis et al. (eds.), *Materials for Advanced Power Engineering*, II, 1831-1846, Kluwer Acad. Publishers, Dordrecht/Boston/London, 1994
- [3] G.F. Harrison, *Proc. European Propulsion Forum*, (London, UK: The Royal Aeronautical Society, 1993) 3.1-3.16
- [4] K. Fritscher, M. Peters, H.J. Rätzer-Scheibe, U. Schulz, Superalloys and Coatings, in: H. Buhl (Editor), *Advanced Aerospace Materials*, 84-107, Springer, Berlin/Heidelberg/New York/London/Paris/Tokyo/Hong Kong, 1992
- [5] J.T. DeMasi-Marcin and D.K. Gupta, Protective Coatings in the Gas Turbine Engine, *Surface and Coatings Technology*, 68/69 (1994) 1-9
- [6] M. Peters, K. Fritscher, G. Staniek, W.A. Kaysser, U. Schulz: "Design and Properties of Thermal Barrier Coatings for Advanced Turbine Engines", *Materialwissenschaft und Werkstofftechnik* 28 (1997) 357-362
- [7] J.T. DeMasi-Marcin and D.K. Gupta, "Protective Coatings in the Gas Turbine Engine", *Surface and Coatings Technology*, 68/69 (1994), pp.1-9
- [8] S.M. Meier, D.M. Nissley, K.D. Sheffler, T.A. Cruse: "Thermal barrier coating life prediction model development", *ASME J. Eng. Gas Turbine Power* 114 (1992) 258-263
- [9] B.A. Movchan, EB-PVD Technology in the Gas Turbine Industry: Present and Future, *JOM* 48 (11/1996) 40-45
- [10] M. Peters, G. Staniek, K. Fritscher, U. Schulz, W.A. Kaysser, "Effective Thermal Barrier Coatings for Modern Turbine Engine Design", *Proc. 1997 European Propulsion Forum*, 179-188, Berlin, 1997
- [11] G.L. Erickson, A New Third Generation Single-Crystal Casting Superalloy, *JOM* 47 (4/1995) 36-39
- [12] F. Soechting, NASA Conf. Publ. 3312(1995)1
- [13] D.V. Rigney, R. Viguie, D.J. Wortman, D.W. Skelly, "PVD Thermal Barrier Coating Applications and Process Development for Aircraft Engines", *Proc. Thermal Barrier Coating Workshop*, NASA Conf. Publ. 3312, pp.135-150, Cleveland, OH, USA, 1995
- [14] A. Maricocchi, A. Bartz, D. Wortman, "PVD TBC Experience on GE Aircraft Engines, *Proc. Thermal Barrier Coating Workshop*, NASA Conf. Publ. 3312, pp.79-89, Cleveland, OH, USA, 1995
- [15] K. Fritscher, M. Peters, H.-J. Rätzer-Scheibe, and U. Schulz: "Superalloys and Coatings", *Advanced Aerospace Materials*, ed. H. Buhl, (Berlin, Heidelberg, Germany: Springer-Verlag, 1992), pp. 84-107



- [16] B.A. Nagaraj, A.F. Maricocchi, D.J. Wortman, J.S. Patton, and R.L. Clarke, "Hot Corrosion Resistance of Thermal Barrier Coatings", *ASME paper 92-GT-44* (1992)
- [17] B.A. Nagaraj and D.J. Wortman, "Burner Rig Evaluation of Ceramic Coatings With Vanadium-Contaminated Fuels", *ASME J. Eng. Gas Turbine Power* **112** (1990) 536-542
- [18] P. Vincenzini, G. Appiano, F. Brossa, and S. Meriani, "Stability of Thermal Barrier Coatings", *Proc. 3rd Int. Symp. "Ceramic Materials and Components for Engines"*, ed. V.J. Tennery (1989), pp. 201-210
- [19] U. Schulz, K. Fritscher, M. Peters, "Thermocyclic Behavior of Various Stabilized EB-PVD Thermal Barrier Coatings", *Journal of Engineering for Gas Turbines and Power*, **119** (1997) in print
- [20] J.A. Thornton, "Influence of Substrate Temperature and Deposition Rate on Structure of Thick Sputtered Cu Coatings", *J. Vac. Sci. Technol.*, **12** (1975) pp. 830-835
- [21] B.A. Movchan and A.V. Demchishin, "Study of the Structure and Properties of Thick Vacuum Condensates of Nickel, Titanium, Tungsten, Aluminium Oxide and Zirconium Dioxide", *Fiz. Metal. Metalloved.*, **28** (1969), pp. 83-90
- [22] U. Schulz, K. Fritscher, and M. Peters, "EB-PVD  $Y_2O_3$  and  $CeO_2/Y_2O_3$  Stabilized Zirconia Thermal Barrier Coatings - Crystal Habit and Phase Composition", *Surface and Coatings Technology*, **82** (1996) 259-269
- [23] H.G. Scott, "Phase Relationships in the Zirconia-Yttria System. *J. Mat. Sci.*, **10** (1975) 1527-1535
- [24] U. Schulz, K. Fritscher, and M. Peters, "Thermocyclic Behavior of Various Stabilized EB-PVD Thermal Barrier Coatings", *ASME Turbo Expo*, 10-13.6.1996 Birmingham, *ASME paper 96-GT-488*
- [25] L. Lelait, S. Alperine, C. Diot, and R. Mevrel, "Thermal Barrier Coatings: Microstructural Investigation after Annealing", *Mater. Sci. Eng.*, **A121** (1989) 475-482
- [26] R.A. Miller and C.C. Berndt, "Performance of Thermal Barrier Coatings in High Heat Flux Environments", *Thin Solid Films*, **119** (1984) 195-202
- [27] S. Stecura, "Effects of Compositional Changes on the Performance of a Thermal Barrier Coating System", *NASA Technical Memorandum 78976* (1979)
- [28] N.P. Anderson and K.D. Sheffler, "Development of Strain Tolerant Thermal Barrier Coating Systems", *NASA Contract NAS3-22548*, Report No. NASA-CR-168251 (1983)
- [29] O. Unal, T.E. Mitchell, and A.H. Heuer, "Microstructures of  $Y_2O_3$ -Stabilized  $ZrO_2$  Electron Beam-Physical Vapor Deposition Coatings on Ni-Base Superalloys", *J. Am. Ceram. Soc.*, **77** (1994) 984-992
- [30] N.S. Jacobson, "Thermodynamic Properties of Some Metal Oxide-Zirconia Systems", *NASA TM 102351* (1989), pp. 1-63
- [31] R. Taylor, J.R. Brandon, and P. Morrell, "Microstructure, Composition and Property Relationships of Plasma-Sprayed Thermal Barrier Coatings", *Surface and Coatings Technology*, **50** (1992) 141-149
- [32] R.E. Demaray, W.K. Halnan, and S. Shen, "Development of Electron Beam Physical Vapor Deposition of Ceramic Coatings", *Proc. 2nd Conf. on Advanced Materials for Alternative Fuel-Capable Heat Engines*, (Palo Alto, CA: Electric Power Research Institute 1981), pp. 151-184
- [33] D.V. Rigney, R. Viguie, D.J. Wortman, and D.W. Skelly, "PVD Thermal Barrier Coating Applications and Process Development for Aircraft Engines", *NASA Conference 3312* (1995) pp. 135-149
- [34] K. Fritscher and U. Schulz, "Burner-Rig Performance of Density-Graded EB-PVD Processed Thermal Barrier Coatings" in *Ceramic Coatings*, ed. K. Kokini, *ASME MD-Vol.44* (1993), New York, pp. 1-8
- [35] U. Schulz, K. Fritscher, C. Leyens, M. Peters, W.A. Kaysser, "Thermocyclic Behavior of Differently Stabilized and Structured EB-PVD Thermal Barrier Coatings", *Materialwissenschaft und Werkstofftechnik* **28** (1997) 370-376
- [36] U. Schulz, H. Oettel, W. Bunk, "Texture of EB-PVD thermal barrier coatings under variable deposition conditions", *Zeitschrift für Metallkunde* **87** (1996) 488-492
- [37] U. Schulz, K. Fritscher, H.-J. Rätzer-Scheibe, M. Peters, and W.A. Kaysser, "Thermocyclic Behaviour of Microstructurally Modified EB-PVD Thermal Barrier Coatings", *Materials Science Forum*, in press
- [38] B.A. Nagaraj, A.F. Maricocchi, D.J. Wortman, J.S. Patton, R.L. Clarke, "Hot corrosion resistance of thermal barrier coatings", *ASME paper 92-GT-44* (1992)
- [39] P. Lenk, J. Senf, B.-D. Wenzel, "Von Ardenne guns and their suitability for PVD processes for thermal barrier coating", *Proc. conf. on electron beam melting and refining-state of the art, 1996*; ed. R. Bakish, Bakish Materials Corporation, Engelwood, USA, 182-190

# PLASMA ASSISTED CVD OF THICK YTTRIA PARTIALLY STABILIZED ZIRCONIA COATINGS

S. Chevillard  
S. Drawin  
M.H. Vidal-Sétif

ONERA - Materials Science Department  
BP 72  
92322 CHATILLON CEDEX  
FRANCE

## SUMMARY

Plasma-assisted chemical vapor deposition has been successfully used to deposit thick (20 - 150  $\mu\text{m}$ ) zirconia - (5-20wt%) yttria coatings on metallic and alumina substrates, with high rates (up to 150  $\mu\text{m}/\text{h}$ ) at temperatures ranging from 400 to 750°C. Tetrachloride ( $\text{ZrCl}_4$ ) and  $\text{Y}(\text{thd})_3$   $\beta$ -diketonate were used as zirconium and yttrium source materials. Vaporization conditions have been studied for both precursors. Morphology, impurity content and crystallographic structure of the coatings were investigated. At all deposition temperatures, the coatings exhibited columnar morphology and {100} crystallographic texture. At low substrate temperature (400°C), the pore volume fraction was high (ca. 50%) and the coatings incorporated some carbon and chlorine impurities, but at high temperature (750°C), the pore fraction reduced to about 25% and little carbon and no chlorine were detected. Metastable tetragonal «t'» phase was the main constituent of coatings with 7 and 10wt% yttria. Annealing for 24 and 120 hours of  $\text{ZrO}_2$  - 7wt%  $\text{Y}_2\text{O}_3$  coating deposited at 400°C showed that cubic phase with an yttria content of about 11wt% is allowed to form, at the expense of the «t'» phase whose yttria content diminishes to 4wt%. This relatively fast evolution towards thermodynamic equilibrium may be related to the high porosity level.

## 1. INTRODUCTION

The use of thermal barrier coatings (TBCs) cannot be currently by-passed for the enhancement of both aeronautical and industrial gas turbine performance and efficiency. Zirconia-based compositions, and especially 6-8wt% yttria partially stabilized zirconia, are widely used, because of an outstanding behaviour at high temperature (high chemical and structural stability, high coefficient of thermal expansion, low thermal conductivity) and a good resistance to thermal cycling [1].

Numerous deposition techniques of zirconia-based films are reported in the literature, including :

- sol-gel processing [2],
- chemical vapor deposition (CVD): conventional thermal CVD [3], metal-organic CVD (MOCVD) [4], plasma-enhanced (or assisted) CVD (PECVD or

PACVD) [5], electrochemical vapor deposition (EVD) [6], combustion CVD (CCVD) [7],

- physical vapor deposition (PVD): sputtering [8], laser PVD [9], electron beam PVD (EBPVD) [10], and
- plasma spraying [11],

for numerous applications : TBCs for gas turbine engines [12, 13], stationary gas turbines [14] and diesel engines [15], solid electrolytes for fuel cells [16], gas sensors [5], insulating layers for semiconductors, buffer layers for  $\text{YBaCuO}$  superconductors, hard coatings, optical coatings, etc. But few techniques are suited for thick (150 to 300  $\mu\text{m}$ ) coatings, which require high deposition rates, as needed for TBCs.

Plasma spraying and EBPVD are currently the only processes used in production for TBCs [17, 18]. Yet being typically line-of-sight processes, they are limited to the coating of simple-shaped airfoils, and deposition on shadowed regions of multiple airfoils may be very difficult [19]. A non-directive alternative deposition process would present definite advantages in this respect.

CVD techniques are in that sense well fitted. EVD allows deposition rates as high as 100  $\mu\text{m}/\text{h}$  [16] but requires porous substrates, and too low deposition rates (typically 1  $\mu\text{m}/\text{h}$ ) exclude thermal CVD. Plasma activation, at either radio (13.56 MHz) or microwave (2.45 GHz) frequencies, has been widely used for the deposition of various layers in microelectronics, hard coatings and oxide diffusion barriers [20]. It presents two benefits : lowering of the substrate temperature, in some cases down to less than 100°C, and enhancement of the deposition rate by up to two orders of magnitude.

Moreover, PECVD processes allow to vary the coating morphology ; in the particular case of zirconia-based coatings *columnar* morphologies can be obtained, as already shown by Cao [5] for zirconia-yttria solid solutions and Bertrand [21, 22] and Gavillet [23] for pure zirconia. Compared to the lamellar morphology of plasma-sprayed coatings, the columnar morphology is generally preferred for cycled applications at high temperature as in gas turbine engines [19]. The improved strain tolerance is due to the orientation of the intercolumnar porosity perpendicular to the

substrate/coating interface, thus allowing contraction and expansion without cracking.

This paper presents the work in progress at ONERA to develop a PECVD process for the deposition of yttria partially stabilized zirconia thermal barrier coatings. Electrodeless microwave plasma generation has been preferred to radio-frequency, because of the potentially higher electron densities involved ( $10^{17} - 10^{18} \text{ m}^{-3}$ ) and thus higher active species densities and higher deposition rates.

## 2. EXPERIMENTAL DETAILS

All deposits were performed in a home-built laboratory-scale reactor based on the apparatus used by Bertrand [21, 22]. The reactor can schematically be decomposed into four parts (Figure 1) [24]:

- the gas generation and distribution system allows the vaporization of the zirconium and yttrium solid precursors and their transport, together with argon carrier gas and oxygen, to the deposition chamber;
- the deposition chamber is a 100 mm in diameter, 280 mm long quartz tube. It is surrounded by a microwave cavity (180 mm in diameter) coupled through a waveguide to a 1200 W maximum power 2.45 GHz microwave generator;
- the substrate (20 mm in diameter, 2 mm thick) is placed on a temperature-controlled holder resistively heated by a Ni-Cr wire connected to a 600 VA power supply. The substrate temperature,  $T_s$ , can reach a maximum of 1000°C for short durations, but this has to be reduced to 750°C for longer durations due to the rapid oxidation of the Ni-Cr wire at high temperature and low pressure. The distance from the injection nozzle to the substrate can be varied. Substrates are metallic (NiCoCrAlY, preoxidized at 1100°C to allow the growth of an adherent alumina film) or ceramic (sintered  $\alpha$ -alumina); a hole is drilled on the sample side so that a thermocouple can be introduced to monitor the sample temperature;
- the gases are evacuated by a Roots blower (Alcatel,  $150 \text{ m}^3 \text{ h}^{-1}$ ) connected to a primary pump (Alcatel,  $33 \text{ m}^3 \text{ h}^{-1}$ ). Corrosive gases are condensed in a liquid nitrogen trap. The total pressure in the deposition chamber is controlled by a throttle valve and a Baratron gauge.

Airtightness is obtained using conventional Viton® O-ring seals, except for the gas generation part which is heated up to 250°C where Kalrez® seals were used. All metallic parts are made of AISI 316 L stainless steel.

Experimental conditions for the deposition of  $\text{ZrO}_2\text{-Y}_2\text{O}_3$  TBC coatings are given in Table 1.

### 2.1 Zr and Y source materials

Since neither mineral nor metal-organic zirconium and yttrium compounds are gaseous at room temperature, condensed source materials have to be used and vaporized in a specific manner (bubbler, furnace, etc).

The precursors for Zr and Y were chosen from literature data and specific investigations were conducted on some

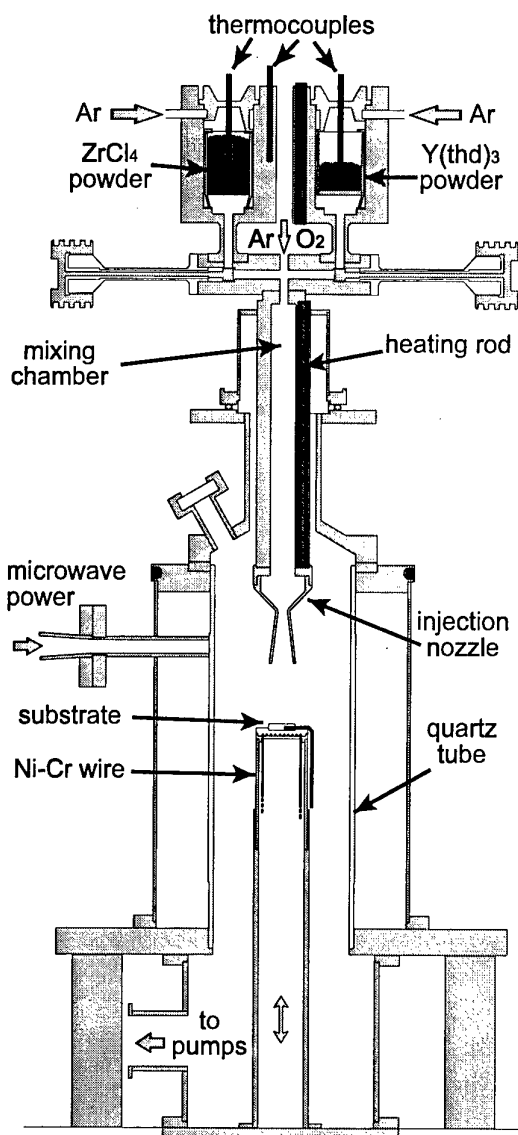


Figure 1 - Apparatus for PECVD of  $\text{ZrO}_2 - \text{Y}_2\text{O}_3$  thermal barrier coatings.

of them [24, 25]. The main selection criteria were :

- a high vapor pressure to ensure high deposition rates (this requirement is less stringent for the Y precursor, because the aimed Y:Zr atomic concentration ratio in the coatings is always less than 1:5) ;
- a good chemical and thermal stability ;
- low toxicity, low moisture sensitivity, low cost.

Zirconium tetrachloride ( $\text{ZrCl}_4$ ) and  $\text{Y}(\text{O}_2\text{C}_{11}\text{H}_{19})_3$  (tris(2,2,6,6-tetramethyl-3,5-heptanedionate)yttrium or « Y(thd)<sub>3</sub> ») have been finally selected.

$\text{ZrCl}_4$  powder is commercially available at high purity levels (more than 99.5%) and presents high vapor pressures (315 to 4000 Pa) in the range 200-250°C. This allows the design of a vaporization furnace working at relatively low temperature. In practice, a porous silica crucible is half filled with  $\text{ZrCl}_4$  and placed in the temperature-controlled furnace (70 cm<sup>3</sup> inner volume). Argon carrier gas is then forced through the powder and

the  $\text{ZrCl}_4$ -enriched gas flows to the mixing chamber. This percolation technique ensures a good solid to gas mass transfer.

The metal-organic compound  $\text{Y}(\text{thd})_3$  is available commercially at slightly lower purity levels (more than 98%). It melts at  $174^\circ\text{C}$  and presents a high enough vapor pressure at temperatures greater than *ca.*  $160^\circ\text{C}$ . A silica boat with a small amount of  $\text{Y}(\text{thd})_3$  is placed in a second temperature-controlled furnace. Argon circulates over the powder surface, which is pasty at the selected temperatures. The  $\text{Y}(\text{thd})_3 + \text{Ar}$  gas mixture is then introduced into the mixing chamber.

Oxygen and argon are added to the gas flow in the mixing chamber. Argon is used as an inert carrier gas but also to facilitate the ignition of the plasma, to improve its stability and to adjust the partial and total pressures in the deposition chamber.

Only a few grams of Zr and Y precursors are vaporized at each deposition experiment, as given by crucible mass measurements. This corresponds, in the standard conditions (see Table 1), to approximate mass loss rates of 1.4 g/h and 0.25 g/h and gaseous precursor mole fractions in the mixing chamber of about  $2 \cdot 10^{-3}$  and  $1.5 \cdot 10^{-4}$ , respectively. After deposition, the crucibles with the remaining powder are removed from the furnaces, after having cooled down to room temperature, and stored until the next utilisation. Vaporization conditions for both furnaces were investigated, and charts of precursor mass loss vs. furnace temperature and argon flow rate were drawn.

Although both precursors are moisture sensitive, they can be stored for several months in appropriate dessicators, without significant variation of their properties. To prevent corrosion of metallic parts by hydrochloric acid (produced by the reaction of moisture with chlorides), the whole apparatus is flushed with argon after each

deposition experiment and is continuously kept under vacuum. No excessive corrosion is noticed after three years operation.

The whole gas generation part, from the furnaces downwards to the injection nozzle, is heated at  $250^\circ\text{C}$  to avoid condensation of the gaseous precursors.

## 2.2 Gas injection

The injection of the precursor gases into the deposition chamber is of primary importance as coatings with homogeneous thickness are required. This is especially the case if real complex-shaped turbine blades are to be coated. But the present laboratory-scale deposition reactor has been designed for investigations on small samples, so that this requirement is less severe. Nevertheless, both to get insight in the fluid dynamics around the sample and to prepare an up-scaling of the reactor, flow simulations in the deposition chamber have been performed [24].

The small cylindrical nozzle used by Bertrand [22] has been replaced by a conical convergent-divergent nozzle as shown on Figure 2. The nozzle has been designed using one-dimensional isentropic flow relations [26] so that a shock wave is located in the divergent part. The flow at the nozzle exit remains thus subsonic in a wide range of experimental conditions. The flow properties at that location were then used as input boundary conditions for finite element calculations [27] in the deposition chamber, neglecting the presence of Zr and Y precursors (less than 1 mol%), as illustrated on Figure 3. For some calculations, the heating of the gas by the microwave plasma was taken into account, but the numerous chemical reactions induced by the plasma were up to now neglected. These simulations will be used to optimize the deposition process, with respect to both deposition efficiency and coating homogeneity on complex-shaped substrates.

Table 1 - Experimental conditions for the deposition of  $\text{ZrO}_2\text{-Y}_2\text{O}_3$  TBC coatings.

Parameter	Range	Standard conditions
$\text{O}_2$ flow rate (sccm)	25 - 500	200
Ar total flow rate (sccm)	50 - 1400	800
for Zr furnace (sccm)	20 - 700	100
for Y furnace (sccm)	10 - 140	50
Zr furnace temperature ( $^\circ\text{C}$ )	25 - 250	210
Y furnace temperature ( $^\circ\text{C}$ )	25 - 250	170
Total pressure in deposition chamber (Pa)	13 - 1330	133
Microwave input power (W)	0 - 1200	750
Substrate temperature ( $^\circ\text{C}$ )	300 - 750	400
Nozzle exit - substrate distance (mm)	25 - 90	50
Deposition duration (h)	0.25 - 3	1

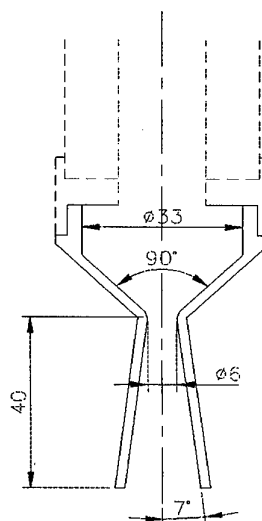


Figure 2 - Schematic view of the gas injection nozzle.

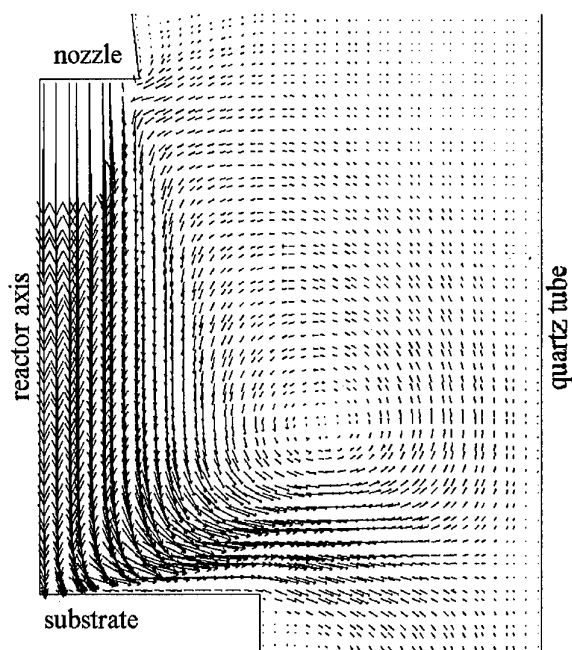


Figure 3 - Simulation of the gas flow in the deposition chamber.  $P = 130$  Pa, total flow rate : 1000 sccm (80% Ar - 20%  $O_2$ ), distance from nozzle exit to substrate : 50 mm,  $T_s = 400^\circ\text{C}$ , input gas temperature :  $220^\circ\text{C}$ , no plasma.

### 3. RESULTS AND DISCUSSION

The structure of the  $ZrO_2$  - (5-20wt%)  $Y_2O_3$  coatings has been characterized using scanning electron microscopy (SEM) and X-ray diffraction (XRD ;  $CuK\alpha$  radiation). The yttrium content in the various phases has been indirectly obtained by XRD, using the following relations obtained from Scott's measurements [28] between the  $YO_{3/2}$  mole fraction,  $X$ , and the lattice parameters  $a$  and  $c$  (in angstroms) :

for  $0.03 < X < 0.13$  (tetragonal phase) :

$$a_t = 5.08 + 0.358 X \quad (1)$$

$$c_t = 5.195 - 0.31 X \quad (2)$$

for  $0.12 < X < 0.33$  (cubic phase) :

$$a_c = 5.115 + 0.16 X \quad (3)$$

The yttria contents will be given in  $Y_2O_3$ wt%, which is approximately equal to  $YO_{3/2}$ mol%. The impurity content has been measured using nuclear reaction spectroscopy (NRS) and particle-induced X-ray emission spectroscopy (PIXE), for carbon and chlorine detection (detection limits : 0.4 and 0.1at%, respectively). These techniques were also used to check the overall Y content in some coatings.

#### 3.1 Morphology

All deposited coatings showed columnar morphology, as illustrated on Figure 4. The columns, originating from the substrate surface, exhibit conical shape, leading to domed top surface. This morphology, frequently obtained in CVD, results from the nuclei preferential growth in given directions.

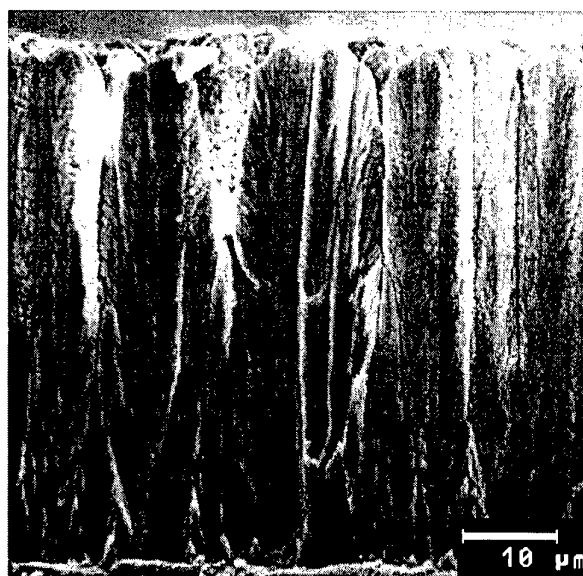


Figure 4 - SEM cross-sectional view of a  $ZrO_2$  - 5wt%  $Y_2O_3$  coating deposited in the standard conditions (deposition duration : 1 hour).

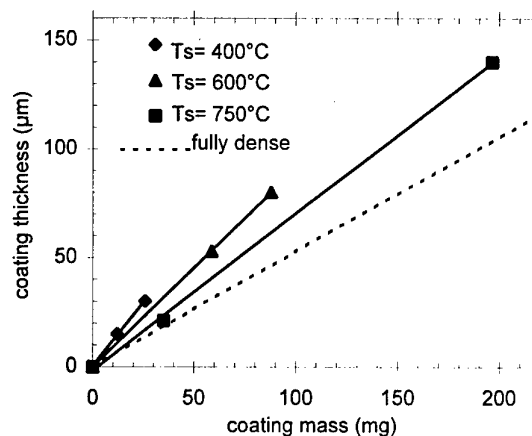


Figure 5 - Coating thickness vs. coating mass for various substrate temperatures and for a fully dense coating (with  $\rho = 6020$  kg/m<sup>3</sup>).

The pore volume fraction in the coating has been evaluated by the simple relation  $P = 1 - \rho_{exp}/\rho_{th}$ , with  $\rho_{exp}$  the experimental coating specific mass, measured as the substrate mass increase over coating volume ratio, and  $\rho_{th}$ , the specific mass of fully dense  $ZrO_2$  - 8wt%  $Y_2O_3$  ( $\rho_{th} \approx 6020$  kg/m<sup>3</sup>) ; because of the errors on the coating mass and volume measurements, these results are estimated to be accurate within  $\pm 10$  rel%. Figure 5 shows the variation of the coating thickness vs. coating mass for various substrate temperatures. The slope of the straight lines is  $1/(\rho_{exp}S)$ , with  $S$  the substrate surface area. This allows to calculate  $\rho_{exp}$  and  $P$ , as summarized in Table 2.

It is seen that the porosity level is highly dependent on the substrate temperature during deposition. This is a typical coating growth feature for high deposition rate processes (especially PVD), as a competition between ad-particle (atoms, molecules) arrival rate and thermally

Table 2 - Measured specific mass  $\rho_{exp}$  and pore volume fraction  $P$ , for various substrate temperatures.

Substrate temperature (°C)	$\rho_{exp}$ (kg/m <sup>3</sup> )	$P$
400	2760	54 %
600	3500	42 %
750	4420	26 %

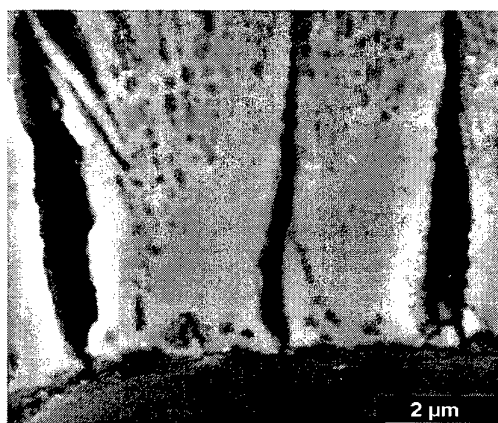
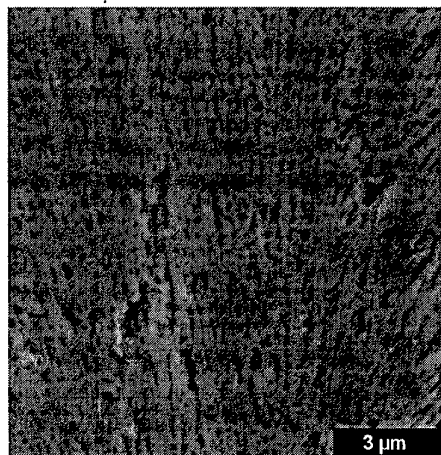


Figure 6 - SEM cross-sectional view of a coating deposited in the standard conditions ( $T_s = 400^\circ\text{C}$ ) and annealed for 24 hours at  $1100^\circ\text{C}$  in air : bulk of coating (top) and substrate-coating interface (bottom).

activated particle surface diffusion [29]. In the present case, the time interval between ad-particles arrival is about 20 ms, being defined as  $c/2R$  with  $c$  the lattice parameter ( $c \approx 5 \cdot 10^{-10}$  m) and  $R$  the deposition rate. At low deposition temperatures, the distance travelled by the adsorbed particles by surface diffusion during that time interval is too small to allow the construction of a « perfect » crystal so that many voids (vacancy clusters or pores) are incorporated into the coating. It is seen on the SEM coating cross-sections (Figure 4) that intercolumnar porosity cannot account for the whole measured 54% pore volume fraction, showing that intracolumnar porosity exists which cannot be resolved by SEM. At higher deposition temperatures, surface

diffusion becomes more important, by *ca.* one order of magnitude between  $400^\circ\text{C}$  and  $750^\circ\text{C}$  if a 1eV activation energy is assumed, so that less porous structures are allowed to grow. At high temperatures, bulk diffusion can also contribute to the elimination of porosity.

The porosity is not homogeneous throughout the coating, the first micrometers appearing to be more dense. Annealing at  $1100^\circ\text{C}$  in air for 24 hours produces the coalescence of the intergranular porosity which becomes observable by SEM. This sintering takes place throughout the coating, as seen on Figure 6 (bulk of coating and column base).

The deposition of highly porous coatings could have been interesting with respect to lowered thermal conductivities, if the obtained morphology had been thermally stable up to temperatures corresponding to gas turbine applications. This is clearly not the case here.

### 3.2 Deposition rate

The deposition rate is about  $55 \mu\text{m/h}$  ( $48 \text{ mg/h}$ ) in the standard conditions. Figure 7 shows that the deposited zirconia amount (here at  $T_s = 400^\circ\text{C}$ ) is proportional to the vaporized precursor mass and thus to the partial pressure of zirconium compounds in the gas phase. Figure 8 shows that the substrate temperature has very little effect on the deposition rate. This indicates that the process is not controlled by surface kinetics. Further experiments are necessary to determine the limiting step of the deposition process (mass transport, gas phase reactions, ...) for various deposition conditions. Note that the analysis of the deposition mechanism is more complicated than for conventional thermal CVD, as the influence of the plasma must be taken into account.

The deposition rate depends both on the gaseous precursors flow rates (at least for  $\text{ZrCl}_4$ ) and the overall deposition efficiency. The former is related to the vaporization capability of the  $\text{ZrCl}_4$  and  $\text{Y}(\text{thd})_3$  furnaces. The  $\text{ZrCl}_4$  furnace has been tested up to mass flow rates corresponding to deposition rates of  $150 \mu\text{m/h}$  (about  $200 \text{ mg/h}$   $\text{ZrO}_2 - \text{Y}_2\text{O}_3$ , deposited on the substrate, at  $T_s = 750^\circ\text{C}$ ); up-scaling of both furnaces should not present any problems. The latter is related first to the physical and chemical processes in the gas phase and at the gas/coating interface and secondly to the gas injection conditions and to the geometrical configuration of the deposition chamber, *i.e.* nozzle geometry, substrate size and shape, nozzle-substrate distance, *etc.* Hence, the deposition efficiencies, defined as the number of deposited Zr moles to the number of vaporized Zr moles ratio, that can be calculated from Figure 8, *i.e.* 8-10%, apply only to the current non-optimized deposition configuration. For instance, the deposition rate for a nozzle exit - substrate distance of 75 mm is the half of that at 50 mm : this is due to the fact that the flow undergoes a conical expansion in the nozzle and in the deposition chamber. An efficiency of at least 20% would be achievable after process optimization.

Most coatings were deposited at rates lower than about  $80 \mu\text{m/h}$ , because beyond that value thickness

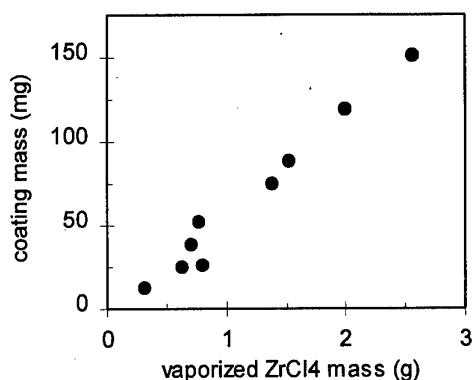


Figure 7 - Deposited zirconia mass vs. vaporized  $\text{ZrCl}_4$  precursor mass.  $T_s = 400^\circ\text{C}$ ,  $P = 133 \text{ Pa}$ , flow rates : direct Ar, 500-700 sccm, Zr-furnace carrier gas (Ar), 50-300 sccm,  $\text{O}_2$ , 200-300 sccm, microwave power : 400-900 W, nozzle-substrate distance : 50 mm.

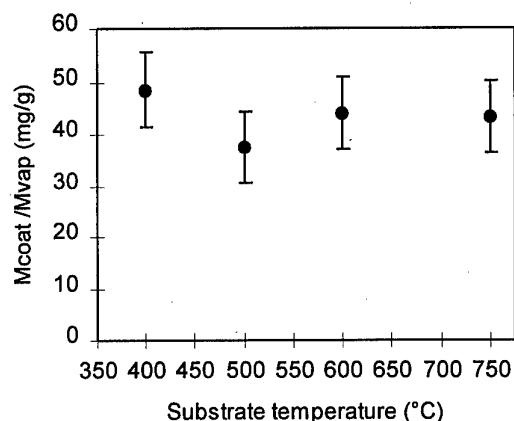


Figure 8 -  $\text{ZrO}_2$  mass deposition rate (in g/h), normalized to the vaporized  $\text{ZrCl}_4$  rate (in mg/h), as a function of substrate temperature  $T_s$ .

heterogeneity increases (the thickness ratio at substrate center and edge becoming higher than about 2, in this configuration).

### 3.3 Impurity content

Because these elements are present in the chloride and organo-metallic gaseous precursors, chlorine and carbon may be incorporated into the  $\text{ZrO}_2 - \text{Y}_2\text{O}_3$  coatings. Table 3 shows the atom contents measured at two deposition temperatures. At  $T_s = 400^\circ\text{C}$ , the C content is not negligible (even if this corresponds to only 2wt%, approximatively) and reflects the fact that the gas phase has been enriched in carbonaceous compounds, originating from the (partial) dissociation of  $\text{Y}(\text{thd})_3$  in the plasma, which was able to adsorb on the coating surface. It had not been possible to check whether the carbon is incorporated preferentially as free carbon or as a Zr compound. Nevertheless, at high deposition temperature, the C content is drastically reduced (less than 0.5wt%) probably because the kinetics of the

Table 3 - Measured C and Cl atom contents in  $\text{ZrO}_2 - \text{Y}_2\text{O}_3$  coatings at low and high deposition temperatures.

Substrate temperature ( $^\circ\text{C}$ )	C content (at%)	Cl content (at%)
400	$6.8 \pm 0.5$	2.0
750	1.5	< 0.1

oxidation by atomic or molecular oxygen leading to gaseous products ( $\text{CO}$ ,  $\text{CO}_2$ ) has become favoured.

At low deposition temperature, the coatings incorporate some chlorine. The measured content can appear to be relatively high if corrosion issues are in mind ; but it also shows how efficient the plasma decomposition and reaction processes are, by reducing the Cl:Zr atom ratio from 4:1 in the mixing chamber to about 2:30 in the coating, knowing that at  $T_s = 400^\circ\text{C}$  thermal CVD cannot take place. For  $T_s = 750^\circ\text{C}$ , no chlorine can be detected in the coatings, here also because reactions of chlorine compounds with oxygen leading to volatile products are favoured at that high temperature.

### 3.4 Crystallographic structure

Zirconia coatings, partially stabilized with yttria with mass fractions in the range 5 - 20 %, were deposited at  $T_s = 400^\circ\text{C}$ . XRD diagrams for coatings with approximately 7, 10 and 16wt%  $\text{Y}_2\text{O}_3$  are shown on Figure 9 ( $T_s = 400^\circ\text{C}$ ). All coatings exhibit crystallographic texture, the {100} planes being preferentially oriented parallel to the sample surface. The yttria content was deduced from the value of the  $a$  lattice parameter. In accordance to the phase diagram, for both  $\text{ZrO}_2 - 7\text{wt}\% \text{Y}_2\text{O}_3$  and  $\text{ZrO}_2 - 10\text{wt}\% \text{Y}_2\text{O}_3$  coatings, the main phase is the metastable non-transformable phase «  $t'$  » (with a small amount of monoclinic phase «  $m$  »), while the  $\text{ZrO}_2 - 16\text{wt}\% \text{Y}_2\text{O}_3$  coatings crystallize in the cubic phase «  $c$  ».

The  $\text{ZrO}_2 - 7\text{wt}\% \text{Y}_2\text{O}_3$  has been more specifically studied. After annealing at  $1200^\circ\text{C}$  for 24 hours in air, the texture (which is here more precisely {100}) is amplified, but from there on remains stable, as shown by further annealing for 96 hours. During this high temperature treatment, the «  $t'$  » phase is depleted in yttria while cubic phase is allowed to form. After 24 hour annealing, the yttria content of the «  $t'$  » phase is reduced to about 5wt%, to the benefits of cubic phase (or a tetragonal phase with a  $c/a$  ratio close to 1) with ca. 11wt%  $\text{Y}_2\text{O}_3$ , which is the lower limit for the existence of this phase at  $1200^\circ\text{C}$ . After further annealing during 96 hours, the yttria content of the «  $t'$  » phase still decreases, to about 4wt%, but it remains constant for the cubic phase. This means that in this second step, the yttria transferred from the «  $t'$  » to the «  $c$  » phase has been consumed only to allow the increase of the cubic phase volume fraction within the sample, as is observed on Figure 10. The return to thermodynamic equilibrium, by development of the cubic phase, is somewhat faster than that observed by Lelait [30] for plasma-sprayed  $\text{ZrO}_2 - 8\text{wt}\% \text{Y}_2\text{O}_3$ .

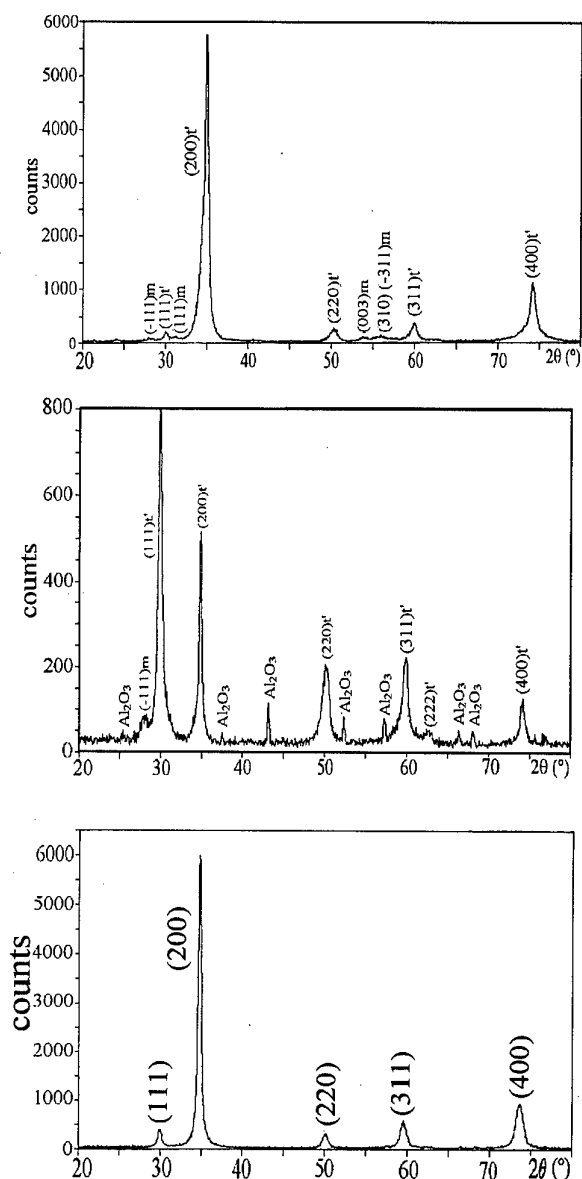


Figure 9 - XRD diagrams of as-deposited PECVD  $\text{ZrO}_2 - x\text{Y}_2\text{O}_3$ , with  $x = 7\text{wt}\%$  (top),  $11\text{wt}\%$  (middle) and  $16\text{wt}\%$  (bottom).  $\text{Al}_2\text{O}_3$  peaks are due to spalled areas (edges) on an alumina substrate.

coatings, which appears after about 250 hours at  $1200^\circ\text{C}$ . This different behaviour of the PECVD sample may be explained by the high porosity level of the coating deposited at low temperature ( $T_s = 400^\circ\text{C}$ ): the high amount of internal surfaces thus generated may favour, comparatively to volume diffusion, the surface diffusion of  $\text{Y}^{3+}$  cations, which are responsible for the evolution of the « t' » metastable system towards thermodynamic equilibrium.

#### 4. CONCLUSION

Plasma-assisted chemical vapor deposition has been successfully used to deposit thick (20 - 150  $\mu\text{m}$ ) zirconia- (5-20wt%) yttria coatings on metallic and alumina

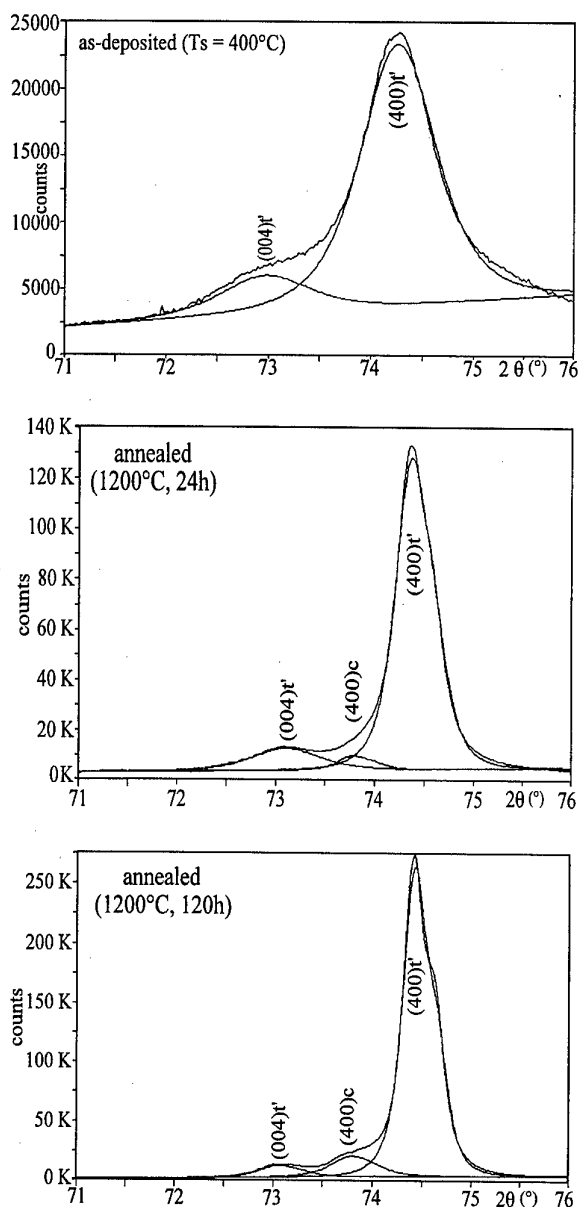


Figure 10 - {400} region of XRD diagrams for a  $\text{ZrO}_2 - 7\text{wt}\%$   $\text{Y}_2\text{O}_3$  coating. Experimental diagrams and calculated contributions of the « t' » and « c » phases : as-deposited (top), annealed at  $1200^\circ\text{C}$  in air for 24 hours (middle) and 120 hours (bottom).

substrates, with high rates (up to  $150 \mu\text{m}/\text{h}$ ) at temperatures ranging from  $400$  to  $750^\circ\text{C}$ .  $\text{ZrCl}_4$  and  $\text{Y}(\text{thd})_3$  were used as source materials; vaporization, handling and storage procedures have been established for both precursors.

Morphology, impurity content and crystallographic structure of the coatings were investigated. At all deposition temperatures, the coatings exhibited columnar morphology and {100} crystallographic texture. At low substrate temperature ( $400^\circ\text{C}$ ), the pore volume fraction was high (ca. 50%) and the coatings incorporated some carbon and chlorine impurities, but at higher temperature ( $750^\circ\text{C}$ ), the pore volume fraction reduced to about 25% and little carbon and no chlorine were detected. It thus



appears that medium to high temperatures are unavoidable to synthesize suitable coatings for thermal barrier applications.

Metastable tetragonal «t'» phase was the major constituent of coatings with 7 and 11wt% yttria, while 16wt%-yttria coatings exhibited only the cubic phase, in accordance to the phase diagram. Annealing for 24 and 120 hours of  $\text{ZrO}_2$  - 7wt%  $\text{Y}_2\text{O}_3$  coating deposited at 400°C showed that cubic phase with an yttria content of about 11wt% is allowed to grow, at the expense of the «t'» phase whose yttria content diminishes to 5wt% and 4wt%. This relatively fast evolution towards thermodynamic equilibrium may be related to the high porosity level.

Work is in progress to further investigate the applicability of PECVD to coat complex-shaped substrates and to study the relationships between deposition parameter and coating properties.

## ACKNOWLEDGEMENTS

This study has benefited from a partial financial support from the Délégation Générale de l'Armement (DSP and SPAÉ). Thorough XRD investigations performed by C. Diot and T. Ochin, as well as fruitful discussions, have been greatly appreciated.

## REFERENCES

- [1] Stecura S., « Optimization of  $\text{NiCrAl/ZrO}_2\text{-Y}_2\text{O}_3$  thermal barrier systems », NASA TM 86905 (1985).
- [2] Maleto M.I., Solovjeva L.I., Turesvskaya E.P., Vorolotov K.A., Yanovskaya M.I., « Alkoxy-derived  $\text{Y}_2\text{O}_3$ -stabilized  $\text{ZrO}_2$  thin films », *Thin Solid Films* 249, 1-5 (1994).
- [3] Yamane H., Hirai T., « Yttria stabilized zirconia transparent films prepared by chemical vapour deposition », *J. Crystal Growth* 94, 880-884 (1989).
- [4] Kim J.S., Marzouk H.A., Reucroft P.J., « Deposition and structural characterization of  $\text{ZrO}_2$  and yttria-stabilized  $\text{ZrO}_2$  films by chemical vapour deposition », *Thin Solid Films* 254, 33-38 (1995).
- [5] Cao C.B., Wang J.T., Yu W.J., Peng D.K., Meng G.Y., « Research on YSZ thin films prepared by plasma-CVD process », *Thin Solid Films* 249, 163-167 (1994).
- [6] Brinkman H.W., Meijerink J., de Vries K.J., Burggraaf A.J., « Kinetics and morphology of electrochemical vapour deposited thin zirconia/yttria layers on porous substrates », *J. Eur. Ceram. Soc.* 16, 587-600 (1996).
- [7] Carter W.B., Godfrey S., « Combustion vapor deposited partially stabilized zirconia coatings », in « Elevated temperature coatings : Science and technology I », Dahotre N.B., Hampikian J.N., Stiglich J.J. Eds., The Minerals, Metals & Materials Society, 103-111 (1995).
- [8] Andritschky M., Rebouta L., Teixeira V., « Corrosion and adherence of stabilized  $\text{ZrO}_2$  coatings at high temperatures », *Surf. Coat. Technol.* 68/69, 81-85 (1994).
- [9] Kreutz E.W., Lemmer O., Wesner D.A., Alunovic M., Erkens G., Leyendecker T., Voss A., « Electron and laser radiation as sources of zirconia film deposition », *Surf. Coat. Technol.* 74/75, 1005-1011 (1995).
- [10] Movchan B.A., « EBPVD technology in the gas turbine industry : present and future », *JOM*, 40-45 (nov. 1996).
- [11] Grünling H.W., Mannsmann W., « Plasma sprayed thermal barrier coatings for industrial gas turbines : morphology, processing and properties », *J. Phys. IV, Colloque C7 suppl. J. Phys. III*, 3, 903-912 (1993).
- [12] Mévrel R., « Barrières thermiques pour aubages de moteurs aéronautiques. Etat de l'art et perspectives », *La Recherche Aérospatiale* 5-6, 381-392 (1996).
- [13] Meier S.M., Gupta D.K., « The evolution of thermal barrier coatings in gas turbine engine applications », *ASME J. Eng. Gas Turbines Power* 116, 250-257 (1994).
- [14] Osyka A.S., Rybnikov A.I., Leontiev S.A., Nikitin N.V., Malashenko I.S., « Experience with metal/ceramic coating in stationary gas turbines », *Surf. Coat. Technol.* 76/77, 86-94 (1995).
- [15] Parker D.W., « Improving thermal efficiency with ceramic thermal barrier coatings », *Proceed. of the Internat. Symp. on Developments and Applications of Ceramics and New Metal Alloys*, Quebec City, Canada, aug. 29 - sept. 2, 1993, 603-613.
- [16] Minh N.Q., « Ceramic fuel cells », *J. Am. Ceram. Soc.* 76(3), 563-588 (1993).
- [17] « Thermal Barrier Coating Workshop '95 » (Cleveland, Ohio, USA, mar. 27-29, 1995), NASA-CP-3312 (1995).
- [18] « Thermal Barrier Coating Workshop 1997 » (Cincinnati, USA, may 19-11, 1997).
- [19] DeMasi-Marcin J.T., Gupka D.K., « Protective coatings in the gas turbine engine », *Surf. Coat. Technol.* 68/69, 1-9 (1994).
- [20] Rossnagel S.M., Cuomo J.J., Westwood W.D., Eds., « Handbook of plasma processing technology », Noyes Publications, ISBN-0-8155-1220-1 (1990).
- [21] Seiberras G., « Réalisation et caractérisation de revêtements de zircone obtenus par dépôt chimique en phase vapeur assisté par un plasma micro-onde », Thèse de Doctorat, Université Paris 11-Orsay, mar. 24<sup>th</sup>, 1994.
- [22] Bertrand G., Mévrel R., « Zirconia coatings realized by microwave plasma-enhanced chemical vapor deposition », *Thin Solid Films* 292, 241-246 (1997).
- [23] Gavillet J., Belmonte T., Hertz D., Michel H., « Low temperature zirconia thin film synthesis by a chemical vapour deposition process involving  $\text{ZrCl}_4$  and  $\text{O}_2\text{-H}_2$ -Ar microwave post-discharges. Comparison with a conventional CVD hydrolysis process », *Thin Solid Films* 301, 35-44 (1997).
- [24] Chevillard S., « Etude d'un procédé de dépôt chimique en phase vapeur assisté par un plasma micro-

onde pour la réalisation de revêtements de zircone yttrée », Thèse de Doctorat, Université Paris 11-Orsay, feb. 11<sup>th</sup>, 1997.

[25] Chevillard S., Vidal-Sétif M.H., Drawin S., « Ytria partially stabilised zirconia coatings by microwave plasma enhanced CVD (MPECVD) », 10<sup>th</sup> Intern. Colloq. on Plasma Processes, Antibes (France), jun. 11-15, 1995, Suppl. Revue « Le Vide : science, technique et applications » 275, 431-434 (1995).

[26] Yahya S.M., « Fundamentals of compressible flows », Halsted Press (John Wiley & Sons, 1982).

[27] Fluxexpert code, DT2I, Chemin des Prèles, 38240 Meylan ZIRST (France).

[28] Scott M.G., « Phase relationship in the zirconia-ytria system », J. Mater. Sci. 10, 1527-1535 (1975).

[29] Yang Y.G., Johnson R.A., Wadlay H.N.G., « A Monte Carlo simulation of physical vapor deposition of nickel », Acta Mater. 45(4), 1455-1468 (1997).

[30] Lelait L., « Etude microstructurale fine de revêtements céramiques de type barrière thermique ; incidence sur la résistance thermomécanique de ces revêtements » Thèse de Doctorat, Université Paris 11-Orsay, 1994.

## THERMAL SPRAYED NANOSTRUCTURED THERMAL BARRIER COATINGS

L. T. Kabacoff  
Materials Division  
Office of Naval Research  
800 N. Quincy Street  
Arlington, VA 22217-5660

### Summary

Nanostructured ceramics exhibit a number of enhanced mechanical and thermal properties which may make them attractive as thermal barrier coatings. The phonon contribution to thermal conductivity is greatly reduced at room temperature, but becomes significant at operating temperatures only for grain sizes below 20 nm. Improvements in mechanical properties, such as fracture toughness and resistance to spalling, can be achieved at larger grain size, in the range of 30 - 70 nm. Suitable coatings, consisting of a composite of zirconia with a second immiscible phase, such as alumina, can be fabricated by thermal spray. However, development of techniques to produce the required microstructure are at an early stage and may require advances in the state of the art for thermal spray technology.

### Introduction

Nanostructured materials have traditionally been defined as any material having some physical length scale smaller than 100 nm. This could be a particle size, layer thickness, fiber diameter, or grain size (0-, 1-, 2-, and 3-dimension respectively). The choice of 100 nm is somewhat arbitrary, but is based on the fact that the characteristic length of many interesting mechanical, optical, and magnetic phenomena are of this order. Thus, as the layer thickness or grain size become very small, the associated properties begin to diverge radically from "conventional" values. Another reason why nanostructured materials exhibit unusual

properties is that, as the physical scale becomes very small, a larger proportion of atoms are found at surfaces or interfaces. For example, in a 3-D nanostructured material with a grain size of 10 nm, the proportion of atoms at grain boundaries approaches 50% (depending on the width of the grain boundary). This has a profound effect, not only on mechanical properties, but also diffusion, ionic conductivity and permeability.

Nanostructured coatings and structures can be fabricated by a number of processing methods. Nanoscale multilayers are generally formed by a sputtering or evaporative process performed in controlled atmosphere. Polycrystalline nanostructured materials are formed by consolidation of either very small particles or larger particles containing very small grains. The consolidation process involves the application of thermal energy and the challenge is to carry out the consolidation without engendering excessive grain growth. Last year, the Office of Naval Research launched a new program with the goal of producing nanostructured coatings for a variety of applications using thermal spray processing. These include resistance to wear, erosion, and cavitation. The feasibility of fabricating nanostructured thermal barrier coatings for gas turbine engines is also being considered. Thermal spray is attractive for several reasons. It is a very fast process, making it relatively easy to control grain growth. It is also an inexpensive process which is already in wide spread use. Implementation will not require any major capital investment or extensive

operator training. The program will concentrate on several materials including alloys, composites and ceramics. Development of TBC's will mostly deal with composites containing zirconia.

The changes in mechanical properties and thermal conductivity which can be obtained in an ultrafine materials can, potentially, be exploited to produce thermal barrier coatings which are, in some way, superior to a coating of the same material, but with conventional microstructure. Whether or not such coatings are possible depends on resolving several issues:

- 1) What grain size must be achieved to obtain significant improvement in thermal resistivity and mechanical properties such as toughness and resistance to cracking and spallation.
- 2) Can a suitable nanostructured material be synthesized at reasonable cost and in adequate quantity?
- 3) Can the synthesized material be processed into a coating which retains the nanostructure?
- 4) Can a nanostructured coating be fabricated with sufficient thermal stability to withstand typical service temperatures experienced in a gas turbine engine?

As will be discussed below, research to date indicates that it *may* be possible to produce nanostructured thermal barrier coatings for gas turbine engines which exhibit significantly enhanced properties and which are relatively inexpensive.

#### Properties of Nanostructured Ceramics

The properties of a nanostructured material can differ radically from a coarser

material of the same composition.

Understanding of these properties is very incomplete, especially those of nanostructured ceramics. This is partly due to the fact that until recently, it has been very difficult to fabricate good quality test specimens reproducibly. Some properties important to consideration of TBC's have been well documented. For example, it has been widely observed that nanoscale ceramic particles have greatly suppressed melting temperatures and also sinter remarkably well at relatively low temperature (Ref 1). This is due to the very large surface area leading to a very large surface tension (producing a high effective pressure) and extreme reactivity. The high surface energy also leads to the stabilization of phases favored by the higher pressure. For example, the ambient stable phase of zirconia particles smaller than a critical size is rutile. Coarsening produces a transformation to anatase. The critical size is temperature and purity dependent, about 30 nm at room temperature. This is illustrated in Figure 1. A consequence of this stabilization is that the use of yttria must be reexamined. Normal compositions of YSZ are greatly over

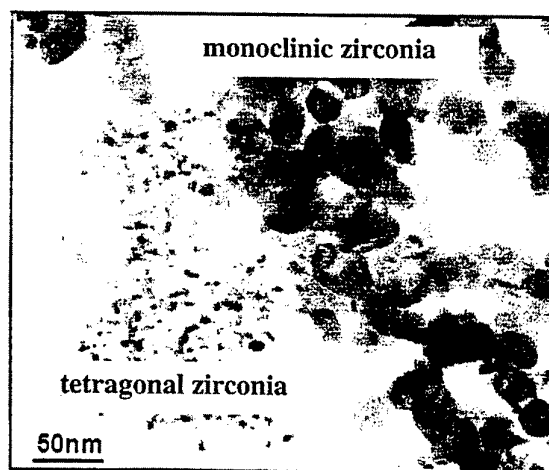


Figure 1. Zirconia nanoparticles above (anatase) and below (rutile) critical size. (Courtesy of C. Berndt)

stabilized and exhibit no transformation toughening. The toughening mechanism reappears if the percentage of yttria is reduced to below 2 percent (Ref 2). Another important feature of nanostructured ceramics is reduced thermal conductivity (Ref 3). This effect results from the grain boundaries being closer together than the typical distance between point defects in a conventional ceramic. Thus, the grain boundary contribution to phonon scattering becomes anomalously high. The calculated phonon contribution to thermal conductivity is illustrated for zirconia (figure 2) and YAG (figure 3). In both cases, the thermal conductivity at room temperature is

dramatically reduced as the grain size goes below 100 nm, the traditional definition of a nanostructured material. However, the drop in thermal conductivity at operating temperatures within gas turbine engines becomes significant only when the grain size goes below about 20 nm. Several unpublished studies have demonstrated that this is indeed the case. Not shown in the calculations is the photon contribution to thermal conductivity. This is of major importance since nanostructured zirconia is quite transparent to infrared. Therefore, a nanostructured TBC' would have to include micron size inclusions, either pores or a suitable second phase.

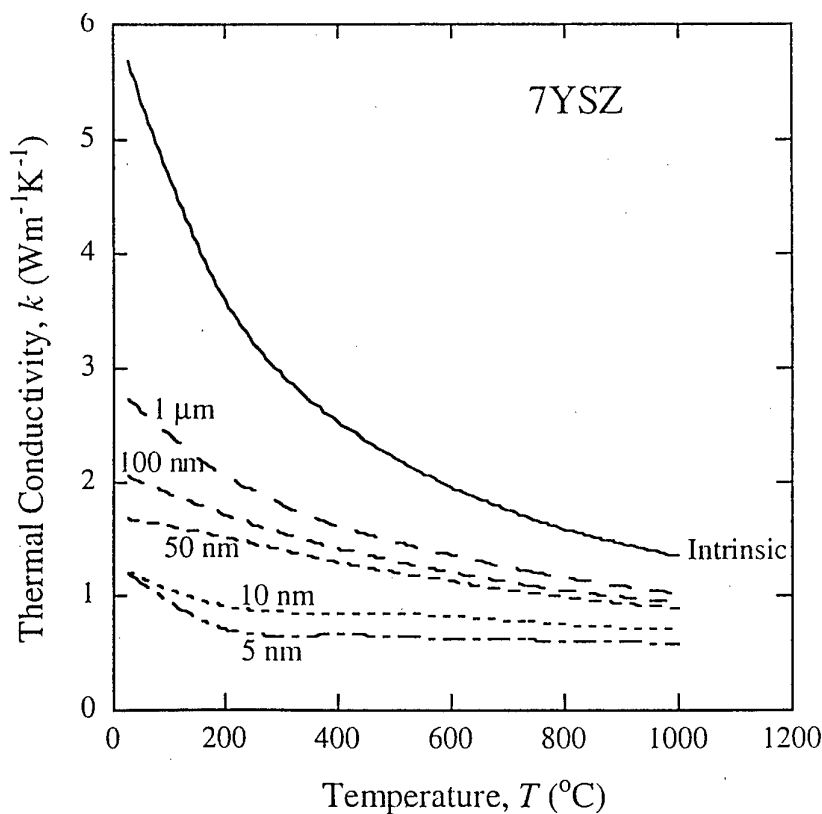


Figure 2. Thermal conductivity of 7YSZ versus grain size and temperature (Ref. 3)

It was previously observed that it is difficult to consolidate nanostructured powder without excessive grain growth. This is illustrated in figure 4, which shows final grain size as a function of sintering temperature (Ref 4). Two things are evident. Grain growth becomes significant as temperatures approach 800 C. Also, porosity is not effective in inhibiting grain growth, as can be seen by the fact that sintering of green bodies with differing porosity result in the same final grain size. This implies that grain growth in service would be a problem. Clearly, a monolithic nanoceramic cannot be used as a TBC in a gas turbine engine. The material must be a

composite, moreover one containing immiscible phases. Some research has been done on a composite of zirconia and alumina. Coatings were fabricated by atmospheric plasma spray using several different sources of nanostructured starting materials. It was found that the percentage of alumina needed to stabilize the structure depended considerably on the morphology of the thermal spray feedstock and, therefore, the morphology of the coating. In the best coatings, 30 % alumina stabilized the grain size and, therefore, tetragonal phase up to 1100 C (Ref 5). A very fine grain size (below 20 nm) could not be achieved because there was complete melting

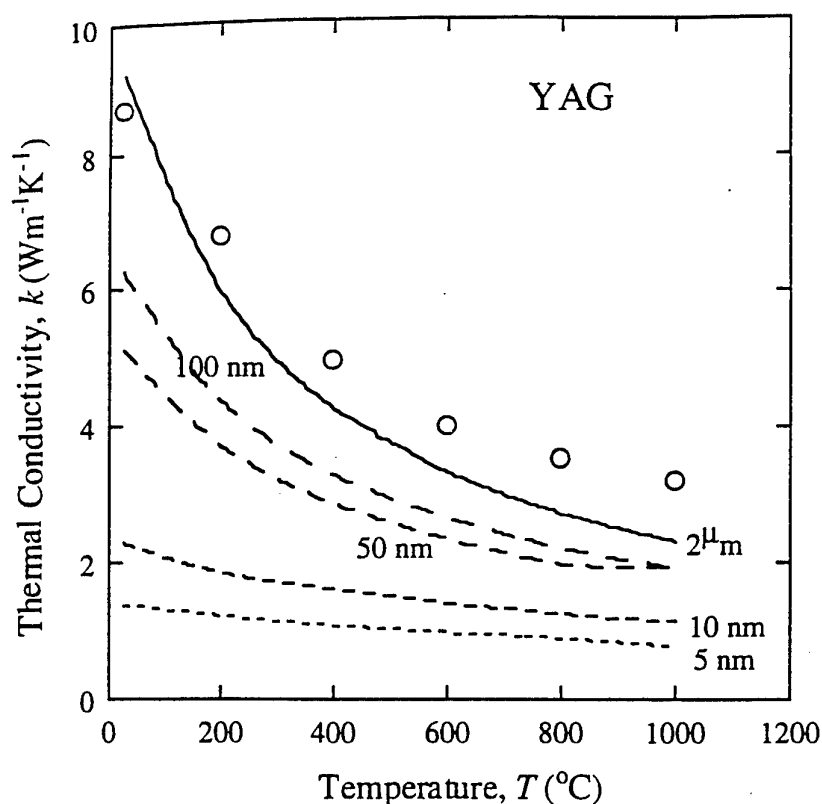


Figure 3. Thermal conductivity of YAG versus grain size and temperature (Ref. 3)

of the sprayed powder during processing. The grain size was limited by the quench rate and the phase separation of zirconia and alumina during solidification. The critical size for stabilization of rutile was larger in the composite than that found in individual pure particles. Typical grain size in these studies was 30 to 50 nm.

The mechanical properties of nanostructured ceramics depend critically on composition and microstructure. Almost all of the studies have been performed on "fully dense" material (in reality, unintentionally porous). Very little work has been done on intentionally porous materials, as one would prefer to have in a

TBC. In spite of the lack of a large body of definitive data, two facts emerge. Nanostructured ceramics deform superplastically at moderate temperature (Ref 6). This temperature is typically less than half the melting temperature and can be even lower for very small grain size. It has also been observed that intrinsic stress can be relieved at low temperature, perhaps even room temperature. Room temperature relaxation has definitely been observed in nanostructured cermets (Ref 7). It was also observed in nanostructured titania by Gleiter (Ref 8). Gleiter attributed this to very high room temperature diffusion (more than six orders of magnitude higher than that found in microscale

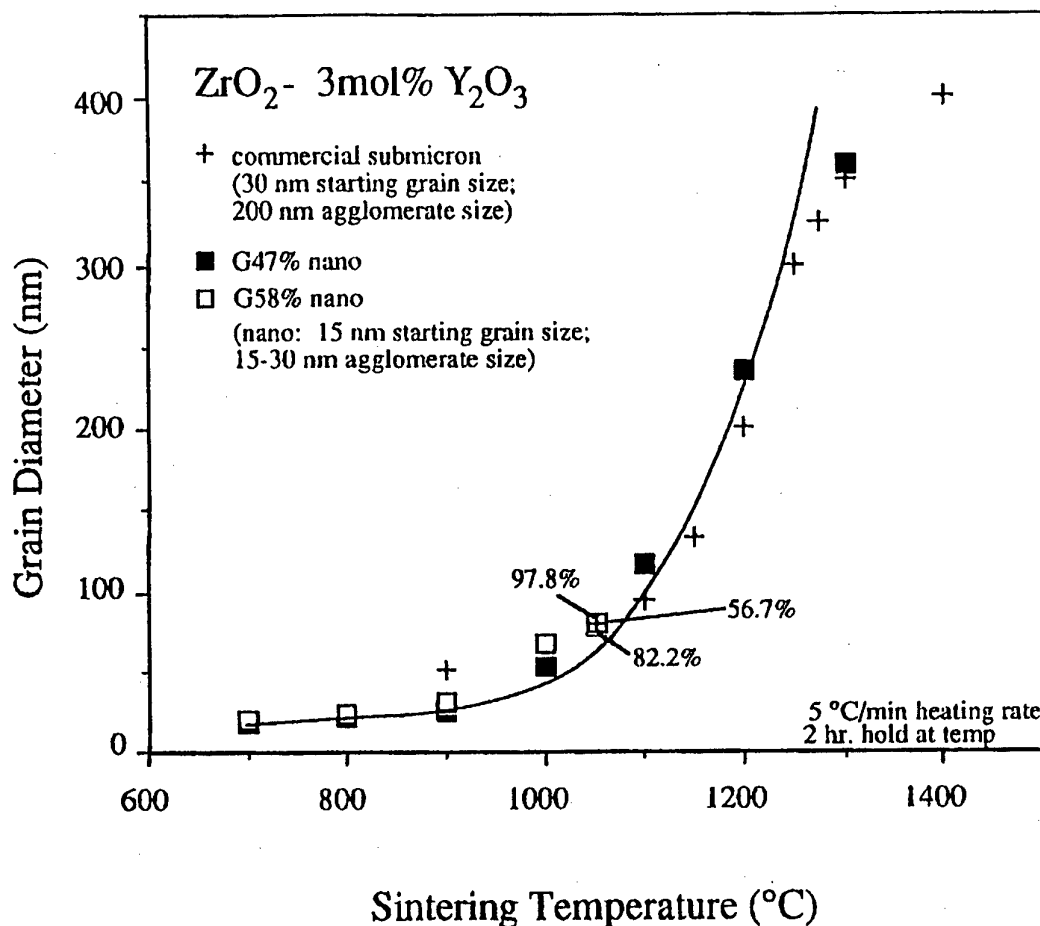


Figure 4. Grain size versus temperature for sintered nanoscale 3YSZ powder.

materials). It is clear that these coatings should not be used in situations where creep resistance is required. Another property affected by the ultrafine microstructure is fracture toughness. In the case of thermally sprayed nanostructured zirconia, the biggest effect may depend on the way the coating is formed. If the feedstock consists of agglomerated small particles, such as colloidal material, and no melting (or only partial melting) occurs, then the coating will lack the splat boundaries present in conventional coatings. These splat boundaries are a major factor in the failure of conventional thermal sprayed coatings. It is possible to form coatings without melting because of the very high sinterability of the small particles. Moreover, use of such small particles is necessary if one wants to achieve a grain size small enough to effect thermal conductivity. If melting does occur, the coating will still be nanostructured provided the sprayed material is a composite of immiscible phases. In this case, the thermal conductivity will not be greatly reduced, but the mechanical properties will still be enhanced. Several companies are pursuing both strategies, but the information is considered proprietary at this time.

### Discussion and Conclusions

The first requirement for successful fabrication of nanostructured TBC's is to obtain suitable material for thermal spray. The synthesis of suitable sprayable material has not been difficult. Nanoscale ceramic powder can be synthesized by gas condensation, by sol gel and colloidal processes, by various flame and plasma processes, and mechanical attrition. Several techniques have also been developed for reprocessing raw powder into a suitable form for thermal spray. These reprocessing techniques are proprietary and cannot be disclosed at this time. At present, commercial manufacturing of large quantities of nanoscale

ceramic powder does not exist. Several companies have the capability to provide production capacity, but will need to see an adequate market before doing so. Research quantities are easily obtained from numerous sources.

Development of techniques for fabricating coatings by thermal spray are at a very early stage. It was noted above that improvement of thermal resistivity will require an extremely small grain size, of the order of 10 - 20 nm, while improvement of mechanical properties can be achieved by reducing grain size only to about 30 - 70 nm. The difficulty in retaining an ultrafine microstructure in the coating during processing and subsequent exposure to elevated temperature increases dramatically with reduced grain size. One reason for this is that the driving force for grain coarsening is highly grain size dependent. Another reason is that, while it is possible to produce a 30 - 70 nm grain structure through melting and rapid solidification, a 10 - 20 nm grain structure can only be achieved by avoiding melting, relying instead on rapid sintering of very fine particles. This may, in fact, be quite feasible, but it has yet to be demonstrated. Clearly, improving mechanical properties will be much easier than reducing thermal conductivity. In both cases, control of coating microstructure will require very tight control of the thermal history of the sprayed particles. This, in turn, will require excellent control of both the size and morphology of sprayed particles, and spray conditions. It may, in fact, require real time process control at a scale not currently available. Thus, it may be necessary to extend the state of the art in thermal spray. This is much more likely to be true for improvement in thermal conductivity than for improvement of mechanical properties. Finally, a great deal of research still needs to be done in order to determine exactly what composition and microstructure to attempt to achieve. This will



include a thorough study of creep and stress relief in the coatings.

In conclusion, the use of nanostructured TBC's with enhanced properties relative to existing materials is possible. It will require a great deal of effort both in research on nanostructured ceramic composites and in development of thermal spray techniques capable of achieving desired microstructures. The kind of effort required to reduce thermal conductivity will be quite different from that required to improve mechanical properties, with very different attendant risks. Ongoing work under the ONR program should clarify most of these issues during the next year.

### References

1. Birringer, R., "Nanocrystalline Materials", *Mat. Sci. And Eng.*, *A117*, 1989, pp 33-43.
2. Mayo, M. J., To be published.
3. Klemens, K. G., "Theory of Thermal Conductivity of Nanophase Ceramics", in "Chemistry and Physics of Nanostructured and Related Non-equilibrium Materials", TMS Proceedings, 1997, p. 97.
4. Mayo, M. J., "Processing of Nanocrystalline Ceramics from Ultrafine Particles", *International Materials Review*, *21*, 1996, pp 85-115.
5. Provenzano, V. And Ying, J., To be Published.
6. Mayo, M. J., "High and Low Temperature Superplasticity in Nanocrystalline Materials", *Nanostructured Materials*, *9*, 1997, pp 717-726.
7. Mayo, W. Private Communication.
8. Karch, J., Birringer, R. And Gleiter, H., "Ceramics Ductile at Low Temperature", *Nature*, *330*, 1987, pp 556-558.

## Modelling the Thermal Conductivity of Thermal Barrier Coatings

J.-M. Dorvaux, O. Lavigne, R. Mévrel, M. Poulain, Y. Renollet, C. Rio

ONERA - Materials Science Department

29, av. de la Division Leclerc

92322 Châtillon Cédex

France

### ABSTRACT

The thermal conductivity of ceramic coatings is a function of the thermal conductivity of the individual constituents (nature of phases, presence of point and planar defects, etc.) and of the morphology of the coating (pores, cracks). This latter aspect is particularly important for TBCs as it explains why their thermal conductivity is significantly lower than the corresponding values for dense materials.

This paper presents a model developed to calculate the thermal conductivity of porous and microcracked ceramic coatings based on a finite difference method applied on digitised images of yttria partially stabilised zirconia (YPSZ) coatings deposited by plasma spraying. The influence of the different types of morphological features on the thermal conductivity is discussed.

### 1. INTRODUCTION

Thermal barrier coatings are constituted of a ceramic external layer, most generally composed of partially stabilised zirconia ( $\text{ZrO}_2$ -6 to 8wt%  $\text{Y}_2\text{O}_3$ ) deposited on top of an oxidation resistant metallic layer (MCrAlY alloy or modified aluminide). Their main function is to thermally isolate the superalloy components, blades or vanes, which they protect from the hot gases circulating in the turbine. Typically, the use of a 250  $\mu\text{m}$  thick ceramic layer can provide about 200°C temperature reduction on the metallic part, thus prolonging its lifetime, reducing thermal transients, etc. [1].

Up to now, most of the efforts dedicated to thermal barrier coatings have been focused on the obtention of performant reliable systems and a predominantly empirical approach has permitted their introduction in service even on highly stressed components such as first stage blades [2].

Only recently, as witnessed for instance by the dedication of a full session during a recent TBC workshop [3] and on-going research programmes [4], significant attention has been increasingly directed towards characterising, understanding and lowering thermal conductivity, an altogether essential property for these systems.

Zirconia-based thermal barrier coatings exhibit already low thermal conductivities (typically between 1 and 2 W/m.K). These low values of thermal conductivity arise both from the intrinsic value of dense partially (and fully) stabilised zirconia materials and from the heterogeneous microstructure of the coatings deposited by plasma spraying or EBPVD (electron beam physical vapour deposition).

The introduction of a stabiliser, required to avoid the detrimental effect of monoclinic to tetragonal phase transformation at typical service temperature, is accompanied by the incorporation of a substantial amount of vacancies. Thus, in the case of yttria stabilised zirconia, the substitution of two tetravalent zirconium ions by trivalent yttrium ions is accompanied by the incorporation of one oxygen vacancy. For PSZ containing 8wt%

$\text{Y}_2\text{O}_3$ , this corresponds to a vacancy content of the order of 4.4 mol.%, providing an efficient source of scattering for phonon propagation. This also explains why the thermal conductivity of these materials is a decreasing function of the yttrium content (at least for relatively low stabiliser contents [5, 6]). Another way of decreasing the intrinsic thermal conductivity of ceramic layers would be to substitute zirconium ions with heavier metallic ions [7, 8], an approach followed by Maloney et al. [9] with a work on  $\text{CeO}_2$ - $\text{Y}_2\text{O}_3$  system, at the expense though of an increase in density.

Another efficient way to decrease the thermal conductivity of a material is to introduce microstructural defects such as pores, voids, microcracks which constitute obstacles against the through-thickness heat transfer propagation. Fortunately, the presence of such defects, produced during fabrication, seems to be indispensable for the thermomechanical resistance of these systems. It is doubtful however that their distribution in existing coatings is optimised regarding the thermal properties and, in order to design more performant TBCs, it now appears necessary to be able to characterise and understand the relationship between thermal conductivity and microstructural features constituting these heterogeneous materials.

It must be reckoned that guidelines that can be derived from the literature, in particular from models relating morphology (porosity) and thermal conductivity of solid materials are of limited usage in the case of thermal barrier coatings due to the complexity of the microstructures.

A variety of models have been developed to estimate the thermal conductivity of multiphased solids, in particular porous materials. Most of them assume the material constituted of a dispersion of a more or less concentrated and randomly distributed second phases. While early models proposed by Maxwell [10], Eucken [11], Russel [12] and Bruggeman [13] for example, consider only spherical particles, improved versions elaborated by Murabayashi [14], Schulz [15], Koh and Fortini [16], Cunningham [17] and McLachlan [18] consider ellipsoids characterised by shape and orientation factors.

As a general rule, the thermal conductivity  $\lambda$  of a porous solid derived with these models can be expressed as :

$$\lambda/\lambda_0 = f(\epsilon, n_i)$$

where  $\lambda_0$  is the thermal conductivity of the pore-free solid,  $\epsilon$  is the volume fraction of the pores and  $n_i$  are adjustable parameters, to be determined empirically, related to the shape and/or orientation of pores.

To evaluate the validity of these models, several authors have examined the analytical results given by some of these models in light of experimental values on different systems [19, 20, 21, for example]. Examining experimental data on alumina, graphite, uranium dioxide, sandstone, silica brick and limestone, and with

porosity up to 75%, Rhee [19] found a satisfactory correlation with the equation proposed by Aizanov and Domashnev [22]. For El-Fekey et al. [20] who evaluated the Maxwell, Loeb and Murabayashi models on thoria compacts with porosities up to 46%, the Murabayashi model [14] yields the best result among the three. More recently, Jackson et al. [21] found that McLachlan's equation [18] comes closest to modelling the experimentally measured thermal conductivity of  $\text{AlN-Ln}_2\text{O}_3$  systems.

Remarking that the experiments considered may not be suited to determine the quality of theoretical calculations, due to various experimental inaccuracies and simplifications, Bakker et al [23] have computed the influence of pores of different shapes (cylinders, spheres, ellipsoids) with the FEM technique. The comparison with the equations describing the effect of inclusions on the overall thermal conductivity shows that the analytical equation of Schulz [15] gives a good description of such materials.

A full review of all the models is beyond the scope of this article. However, the puzzling diversity of conclusions derived by these authors point out to the fact that all these models with simple algebraic expressions assume that the porosity can be experimentally assessed with a very limited number of parameters (the pore volume fraction  $\epsilon$  and adjustable parameters), which singularly restricts their predictive capacity.

To overcome these shortcomings, several authors have developed more sophisticated theoretical approaches as well as finite element calculations to estimate the effective thermal conductivity of multiphase materials.

Tzou [24] estimated the thermal conductivity starting from a general field theory (supposing uniformly distributed internal cavities), deriving tractable analytical expressions for simple pore geometries, i.e. insulated spherical cavities and penny-shaped cracks.

In a more sophisticated approach, Furmanski [25] developed an effective macroscopic description for heat conduction in heterogeneous materials using an averaging technique and Green's function method and applied it to describe a model composite with randomly oriented parallelepiped inclusions distributed in an epoxy matrix.

The expressions obtained with these approaches become readily complex and apparently they have been used up to now only in the case of uniform distributions involving rather simple geometrical shapes for the pores (ellipsoid, cubes). For materials having complex pore microstructures, such as those met in plasma sprayed coatings, and in order to be closer to the real structure (interconnected porous structure), however, numerical schemes appear to be the most promising approaches.

With the objective of extending the rather simple analytical approaches (and poorly predictive) proposed by McPherson [26] and by Moreau et al. [27] on the thermal conductivity of plasma sprayed coatings (and later improved by Bjornekleit et al.[28]), Hollis [29] developed a numerical scheme in which the actual pore structures of vacuum (VPS) and air (APS) plasma sprayed tungsten coatings are used as the basis of finite-element models to calculate the effect of pores on the thermal conductivity of plasma sprayed coatings. If, for VPS coatings, whose pore distribution and shapes are relatively simple, this approach gives a reasonable agreement between calculated and experimental values (respectively 70% and 60% of the bulk value), for APS coatings, instead, a large discrepancy exists between calculated

and measured values. This is attributed to the complex pore structure, which cannot be properly taken into account by the limited areas on the cross sectional micrographs serving as input information into the calculation.

In a study on the thermal conductivity of  $\text{UO}_2$  pellets, Bakker [30] used a finite element method to compute the conductivity of a matrix containing a dispersed phase (pores). Starting from a photograph of a cross section, the microstructure of the material is described as a triangular mesh used as input data. Arbitrary temperatures are imposed on the upper and lower boundaries of the corresponding area (other boundaries are taken adiabatic) and the FEM program computes the conductivity from the thermal flux profile. As explained later, it remains doubtful whether this type approach can be extended to large areas, keeping memory storage reasonable.

In the work presented here, the objective was to develop and evaluate an alternative approach, based on a finite-difference calculation for computing the thermal conductivity of thermal barrier coating, using as input data digitised images of the real material. With this method, the morphology of the ceramic coating, as complex as it can be, is properly taken into account.

## 2. CHARACTERISATION OF TBCs POROUS STRUCTURE

In order to provide data to the thermal conductivity calculation software, reliable procedures have been developed to quantify the real TBCs porous structure. The success of the modelling strongly depends on the accuracy and reliability of the results of these procedures. The complete microscopic characterisation of the TBC morphology involves numerous steps as sample preparation, image acquisition, image analysis and validation with macroscopic porosity determination.

### Sample preparation

A correct and reproducible metallographic preparation of plasma sprayed  $\text{ZrO}_2$  coatings is not straightforward but is essential for obtaining a representation of the real porous structure. Porosity determination by quantitative image analysis and numerical calculation of the thermal conductivity will give reliable results provided that no error is introduced at the sample preparation stage.

### Materials

All investigations are performed on a 1 mm thick free standing TBC plasma sprayed by SNECMA, initially on a HastelloyX substrate without any bondcoat. The powder is a commercial 8 weight% yttria partially stabilised zirconia spray dried powder (HCST Amperit 827.423).

### Sample preparation

The following procedure has been set up. The free standing coating is vacuum impregnated (Struers/Epovac,  $P \sim 100$  mbar) with a superfluid epoxy dye (Struers/Epofix 301) before sectioning. Sample slices are then cut off with a precision saw (Struers/Accutom-2) using a thin diamond wheel and the lowest rotation and sample forward speeds to avoid any damage. The slices are then manually polished according to the following steps : 1200 then 4000 SiC papers for grinding, polishing using a 3  $\mu\text{m}$  diamond spray first on a hard cloth (Struers/Pan W, blue lubricant) then on a smoother cloth (Struers/DP-Mol, pink lubricant), final polishing with a  $\frac{1}{4}$   $\mu\text{m}$  diamond paste. Polishing quality and absence of pull-outs are checked with light microscopy after each step. For scanning electron microscopy observations a  $\sim 20$  nm thick conducting carbon layer is vacuum sputtered within a Balzers MED010 unit.

### Image acquisition

Cross sections of TBC prepared as previously described have been observed in a digital scanning electron microscope (Zeiss/DSM960). Backscattered electron mode is chosen preferentially to secondary electron mode due to the higher contrast between zirconia matrix and porosity (pores and cracks). The adopted acquisition conditions are the following : 15 kV acceleration voltage, 9 mm working distance, « low » electron current. Brightness and contrast are adjusted in order to obtain a reproducible grey level histogram (Fig. 1). Two magnification levels ( $180 \times 180 \mu\text{m}^2$ ;  $45 \times 45 \mu\text{m}^2$ ) and two image resolutions (512x512 or 1024x1024 pixels) have been used for characterising the TBCs morphology. Their influence will be discussed later on (see § 4).

Signal to noise ratio is increased by pixel averaging so that a 1024x1024 pixels image acquisition takes about 400 seconds. Image acquisition is fully automated owing to computer assisted stage displacement. This allows a statistical characterisation of the samples.

### Image analysis

Image analysis procedures have been developed with two objectives :

- provide binary images of TBC cross sections which will be used directly as input data for the thermal conductivity calculation software,
- quantify the porous structure in such a way as to be able to determine the contribution of each morphological feature to the thermal conductivity of a thermal barrier coating.

This will be the starting point for modelling thermal conductivity as a function of the morphology.

#### Thresholding

The transformation of SEM grey level images into binary images is the key step on which depends the reliability of the subsequent results. The threshold level is manually fixed on images with optimised and reproducible grey level histogram (Fig. 1).

This last one contains two peaks : a very sharp and intensive peak at the 0 level (black level) corresponding to the majority of the globular pores and a wider one centred at middle grey levels which includes cracks and zirconia matrix.

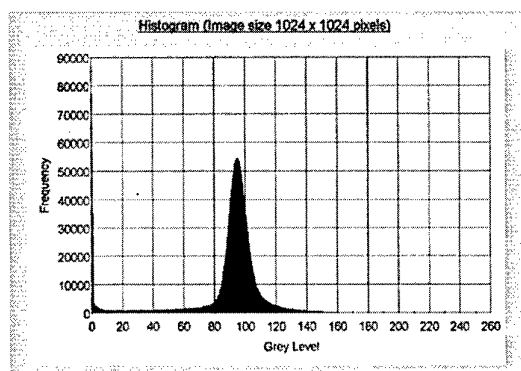


Figure 1: Grey level histogram.

The adopted threshold level which accounts for the whole porosity (pores and cracks) corresponds to the beginning of the lightening of isolated pixels in the solid phase (Fig. 2). This ensures its reproducibility.

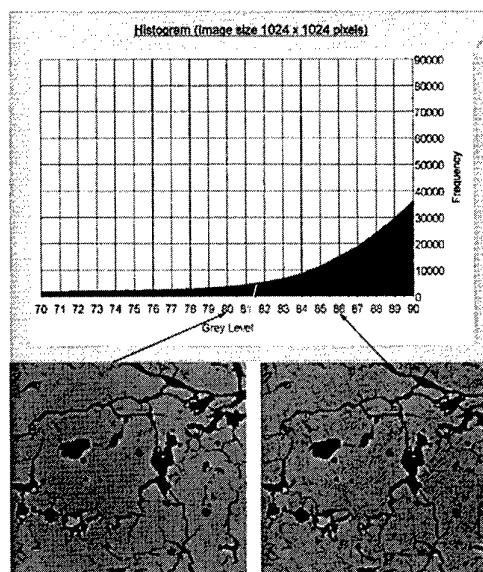


Figure 2: Thresholding.

#### Porosity separation

This procedure is based on opening and reconstruction image analysis operations. It creates three new images from the initial thresholded image : one containing the dispersed globular pores, one with the crack network and one with the globular pores and the cracks directly connected to them.

This fully automated procedure will be widely used to determine the contribution of each morphological feature to the conductivity (see § 4). A still more precise description can be achieved using the following procedure.

#### Porosity reconstruction

From an initial parent binary image it is possible to derive a series of images (about 300 or more according to the morphology complexity) with evolving porosity. This is done by applying a sequence of erosion image analysis operations to the parent image which leads to a final image containing only « ultimate erodeds ». These pixels exactly correspond to the globular pore centroids. Starting from this new image, a step by step reconstruction of the porous features creates the derived images. The operation is ended when the initial total porosity is completely reconstructed (Fig. 5).

An application of this procedure in relation with the thermal conductivity computation will be shown in the last section.

#### Image assembling

This algorithm is developed to provide large size images of the samples which are more representative for the conductivity calculation. This is done by an automatic search of maximal overlap between two binary images from contiguous and slightly overlapping fields.

#### Analysis of globular pores

Each individual globular pore is characterised by a set of parameters (area, perimeter, Feret's diameters, number of neighbours,...). In this way different pore distributions (in number, surface,...) can be obtained (Fig. 3).

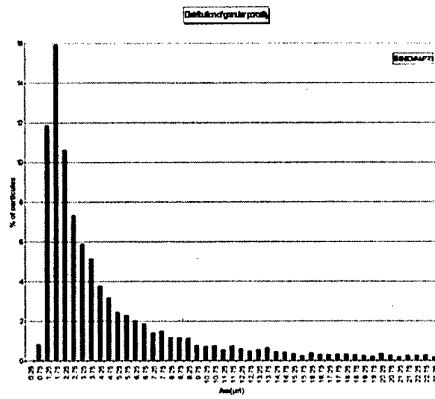


Figure 3: Globular pore distribution (% of particles versus area)

#### Analysis of the crack network

This procedure is based on the «skeletonization» (image analysis terminology) of the crack network, followed by a decomposition in juxtaposed segments of minimal fixed length. A distribution of these segments with regards to their orientation is then available (Fig. 4).

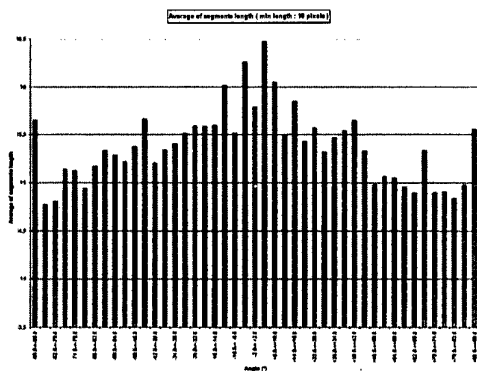


Figure 4: Segment orientation (average of segment length versus angle)

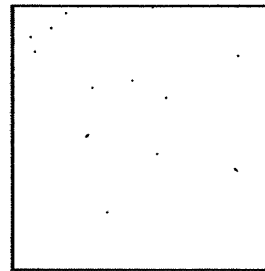
#### Porosity determination

The total porosity of a TBC can be estimated from binary images of cross sections using image analysis provided that the number of analysed fields is statistically relevant. A total of 105 images ( $180 \times 180 \mu\text{m}^2$ ;  $1024 \times 1024$  pixels) corresponding to two transverse perpendicular cross sections have been considered. The mean porosity value obtained for this image set is 15% with a 2% standard deviation.

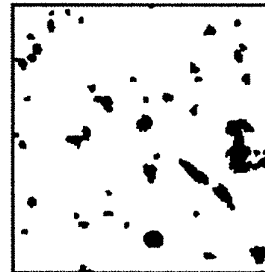
Furthermore the volumetric total porosity of the whole free standing coating ( $60 \times 45 \times 1 \text{ mm}^3$ ) has been determined to  $12 \pm 1\%$  from water immersion experiments and X-ray diffraction theoretical density data. Closed porosity is less than 1%.

The relatively good agreement between image analysis results and volumetric porosity shows that the sample preparation procedure as well as the thresholding one do not introduce too many artefacts. The higher value obtained by image analysis is attributed to some remaining pull-outs and mostly to the fact that backscattered electron detection slightly enlarges the narrowest cracks.

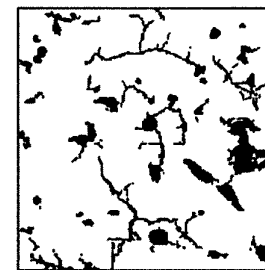
Start: centroids from globs



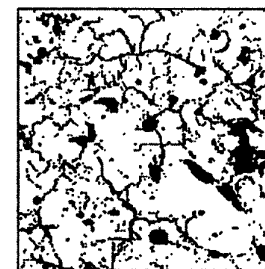
Reconstruction to globs



Reconstruction to globs and linked cracks



Reconstruction to total porosity



### 3. NUMERICAL COMPUTATION OF THE THERMAL CONDUCTIVITY

It has been shown that the morphology of a zirconia plasma sprayed coating is relatively complex in so far as it involves dispersion of pores with various sizes and shapes and connected crack network. As we are concerned with the influence of morphology on thermal conductivity and we want all the morphological information obtained with SEM to be taken into account, the modelling method must face this structure complexity without oversimplification.

Analytical or empirical models mentioned in the introduction only deal with simplified geometrical shape dispersions and are not well suited for connected porosity. The variety of pore structure families does not allow an efficient use of such models, which are generally restricted to one simple type of shapes and cannot handle connectivity effects with a fair accuracy.

Computations on very complex geometry are tractable with some numerical methods. The finite-element method is well known for its possibilities in this field. Recent works [29,30] demonstrate these capabilities by computing the thermal and electrical conductivities of porous metals or metallic oxides.

The finite-element method, among others, uses a grid representation of the geometry. The mesh properties of this grid are however submitted to some constraints. Then its application to very complex shapes may lead to some difficulties. As each shape to be modelled must be decomposed in simple geometric elements (triangles or quadrilaterals), the resulting amount of nodes and meshes may become tremendous when the geometry presents very small details. For example the minimal shape that we may encounter is a single square of one pixel size. If we want to decompose it in triangular or quadrilateral meshes, this single pixel produces, at least, four nodes. Continuity constraints on the neighbouring meshes may impose some grid refinements on the vicinity of this isolated pixel, even if the closest shapes are very large. As a consequence the resulting mesh density in the area close to this square may become very high. For thin cracks (their minimal thickness is one pixel) this may lead to more dense mesh distribution and untractable continuity constraints. Therefore, as the solution methods are generally global (e.g. they are often reduced to a minimisation problem), the associated algebraic system may reach an unpracticable size. So the finite element method seems to be difficult to apply in our field of study if no restriction on the geometry is acceptable.

On the other hand, the standard finite-difference method seems to undergo equivalent restrictions as it needs some grid representation, and therefore, some specific processing on the internal boundaries (e.g. boundaries between porosity and matrix).

However, this can be overcome if :

- the grid can be constructed directly from the input data image,
- the discretisation does not need specific processing on internal boundaries,
- the resulting set of algebraic equation remains practicable.

#### Specific implementation of the finite difference method

The grid construction may be reduced to a very simple process if we use a regular uniform mesh grid where nodes are simply defined by the pixels (square pixels) of the input image. With such a grid no geometric internal boundary information is associated with meshes. These information are related to the

properties of each node (e.g. the local thermal conductivity) and are stored as coefficients of the partial derivative equation to be solved. The schematic representation of our problem is shown on figure 6 :

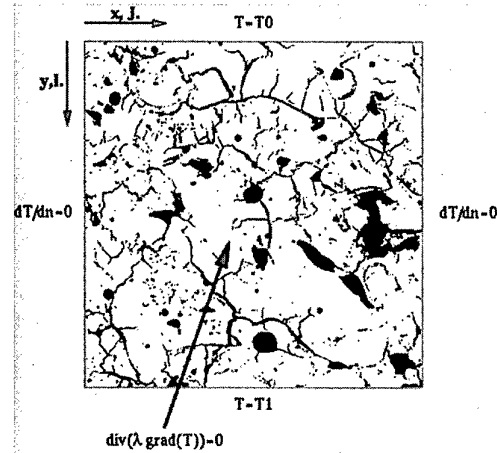


Figure 6: Problem definition.

Then we have to build the finite-difference equation to be solved for each node. This is done by means of the well known five points scheme, that is :

$$\begin{aligned} (A(i,j) + B(i,j) + C(i,j) + D(i,j))T(i,j) \\ = \\ A(i,j)T(i,j-1) + B(i,j)T(i-1,j) \\ + C(i,j)T(i,j+1) + D(i,j)T(i+1,j) \end{aligned}$$

If we do not want to treat the discontinuities of these A,B,C,D coefficients with specific equations occurring when the local conductivity exhibits a step, an implicit way has to be found. For example the well known [31] five weighted conductivities scheme widely used in variable (but continuous) properties problems where the coefficients are defined by :

$$\begin{aligned} A(i,j) &= 1/2(\lambda(i,j-1) + \lambda(i,j)) ; \\ B(i,j) &= 1/2(\lambda(i-1,j) + \lambda(i,j)) ; \\ C(i,j) &= 1/2(\lambda(i,j+1) + \lambda(i,j)) ; \\ D(i,j) &= 1/2(\lambda(i+1,j) + \lambda(i,j)) . \end{aligned}$$

and which is of second order (for continuous properties) is not applicable in our case because it smoothes the discontinuities. Indeed, one can easily see that for small sized (e.g. one or two pixel thickness) objects this scheme leads to erroneous values as no node is assigned its real conductivity.

More suited schemes can be constructed using asymmetrical distributions of conductivity. For example the Upper Left scheme we commonly use is defined by :

$$\begin{aligned} A(i,j) &= \lambda(i,j-1) ; \\ B(i,j) &= \lambda(i-1,j) ; \\ C(i,j) &= \lambda(i,j) ; \\ D(i,j) &= \lambda(i,j) . \end{aligned}$$

Four first order distinct schemes can be constructed on this basis (the four corner implementations). It can be shown that they lead to a space transformation in the neighbourhood of discontinuities as they operate a small translation along bisectrix of  $i,j$  axes. For random geometries they are not strictly equivalent as they produce small variations (about  $10^{-4}$  or less)

of the resulting computed conductivities, but as we will see below (Fig. 9) this is not the most critical source of uncertainties in the present problem.

For the main boundaries (e.g. the boundaries where Dirichlet or Neumann conditions are applied) we use the standard method, that is the image method based on the same scheme for Neumann condition (the Dirichlet condition does not need any computation as  $T$  is imposed).

When the temperature is known for each node, the average or equivalent thermal conductivity of the whole domain is computed from :

$$\lambda_m = \frac{e}{l} \frac{\int_0^l \lambda \frac{\partial T}{\partial y} dx}{T_1 - T_0}$$

where  $e$  is the height and  $l$  the width of the domain, the integration being done on one of the horizontal boundaries. The space step being constant, that integration can be performed with standard quadrature formulas.

### The solver

The proposed scheme leads to a set of  $N_x \cdot 2 \cdot N_y$  linear equations to be solved. As we are concerned with large values of  $N_x$  and  $N_y$  (computation with  $N_x \sim 4200$  and  $N_y \sim 5100$  has been performed), the solver has to be as efficient as possible.

The first difficulty is to have the most compact form of the problem in order to reduce memory occupation. This can be done efficiently by reducing the coefficient storage.

With the definition of A,B,C,D we have seen before, it can easily be shown that, for a simple diphasic problem, we have to store only  $2^3 + 2^2 + 2^3$  different configurations. So the storage for A,B,C,D can be drastically reduced provided that we can store some case index for each node.

As this case number is in the range of tens, an array of bytes is convenient. So the minimal storage required is :

- one  $N_x \cdot N_y$  double precision array for  $T$ ,
- one  $N_x \cdot N_y$  byte array for case markers,
- $4 \cdot 20$  double precision scalars for coefficients,
- one  $N_x \cdot N_y$  byte array for input data.

This is about 10 Moctets for a  $1024 \times 1024$  problem and up to 210 Moctets for a  $4200 \times 5100$  problem. So if the solver does not need intermediate storage, we expect that such problems can be solved on common 256Mo RAM computers. The solution method may be chosen with respect to this criterion. The two common approaches for this kind of solver are iterative matrix methods and iterative by points methods.

The first kind is well represented by the conjugate gradient method [32] which, as other matrix methods, does not satisfy our criterion. It needs, at least, two or three times the minimal storage defined above. So the maximal dimensions of the problems we could solve with such methods would be reduced by a factor of  $\sqrt{2}$  or  $\sqrt{3}$ . Alternatively, we would need some supercomputer. Therefore, matrix methods are very efficient on computers with high vectorisation capabilities (as Cray for example), but seems to be less attractive on scalar or superscalar computers (such as common workstations) [33].

The second kind is commonly known as the Gauss or Gauss-Seidel method [32].

They can be implemented without extra storage so our criterion is satisfied. Provided that we are able to find some well suited (Fig. 7) convergence acceleration parameter (over-relaxed Gauss-Seidel method), they can outperform matrix methods when applied on scalar or superscalar computer [33], but they are notably less efficient when deep vectorisation is allowed.

So we have implemented an over-relaxed Gauss-Seidel solver which allows the solution of problems with sizes up to about  $6000 \times 6000$  on our 512Mo RAM workstation. With the commonly used SEM magnification this theoretically allows the computation of TBC conductivity for thick samples ( $1.2 \times 1.2 \text{ mm}^2$ ), or extended areas of relatively thin coatings (for example  $0.20 \times 36 \text{ mm}^2$ ).

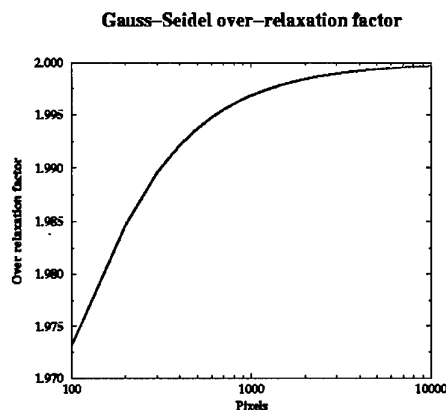


Figure 7: Convergence acceleration parameter.

For huge problems, the main limitation is the duration of computation. The following table shows computation duration in seconds for a standard  $1024 \times 1024$  problem with  $10^{-4}$  precision criterion (e.g. the convergence criterion on heat flux in relative form), for three different superscalar computers :

HP9000/780	DEC Alpha 500	Pentium Pro
260	405	1164

The computation was achieved with 3000 iterations using a convergence acceleration parameter of 1.997. The maximal residual error on heat flux (relative value) was about  $9.4 \cdot 10^{-5}$ .

One can consider this case as the simplest one because the input data image was of medium complexity. For higher complexity input the maximal computation time may be twice the indicated time. For the  $4200 \times 5100$  problem we have solved only on the HP workstation, the computation time was about 10 hours in the most difficult case. Notice that the complexity (which can be evaluated as some function of the number of porous objects) increases roughly as the area of the domain. Despite that, the relation between the size of the domain and the computation time which is a power function of the maximal dimension of the domain exhibits an exponent close to 3, which is the theoretical value for the over-relaxed Gauss-Seidel method.

The initial value for  $T$  may also strongly influence the speed of convergence. Our standard initialisation is the temperature distribution for the homogeneous medium. A possibly more efficient initial distribution may be constructed from the Richardson's extrapolation concept [34]. Let  $T_{1/2}$  be the solution of the problem for the domain reduced by a factor 2 in each dimension (e.g. we compute only one node out of two). This

solution may be achieved within a time  $t_c/8$ , where  $t_c$  is the computation time for the whole problem.

The values of  $T$  are then determined on alternate nodes using bilinear interpolation. The global cost of these two operations remains close to  $t_c/8$ . As we do not need an "exact" solution for  $T_{1/2}$ , we can reduce the precision criterion in order to reduce this time. So the initial data construction has a cost less than  $t_c/10$  for example. Our major expectation is that such an initialisation would be very close to the whole solution  $T$ . Then the amount of computation needed to obtain  $T$  would be substantially reduced.

Experiments have shown that the effective global computation time may be reduced by a factor of about 2 for low complexity input (globular porosity for example). For higher complexity input the time reduction is often imperceptible as small details (cracks for example), which are partially lost in the  $T \rightarrow T_{1/2}$  input transformation, have a major contribution to the whole solution. So this is not a very efficient method for the reduction of computation duration because of its lack of generality.

#### Computation output

The computation program outputs some convergence information and the computed equivalent thermal conductivity. Therefore, the resulting array of temperatures is saved in a compacted binary file. This file can be read by another program for visualisation purpose. The temperature, its gradient, and the heat flux can be visualised by means of isovalue representation as shown on figure 8.

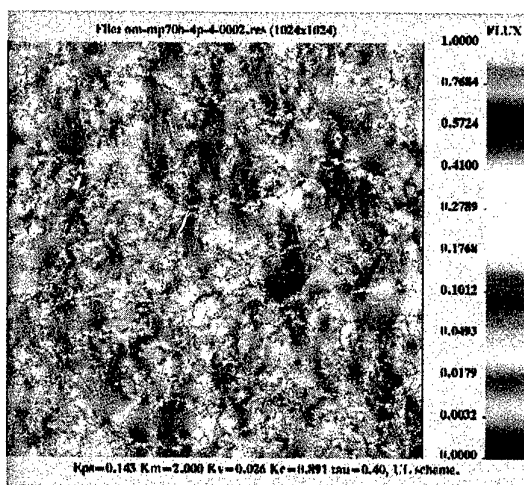


Figure 8: Heat flux representation.

Such representations performed on images with separated porosity give a qualitative useful description of the effect of each morphological feature on the heat transfer through a TBC.

#### 4. APPLICATIONS

Before applying these tools to various TBCs, three major points have to be considered.

##### The resolution problem

The first one concerns the optimal choice for input image resolution. As figure 9 shows, the computed conductivity strongly depends on the input image dimensions.

Images of the same physical field with various resolutions (e.g. 256x256, 512x512, 1024x1024, 2048x2048 pixels) lead to four inputs which have been used for conductivity computation. An

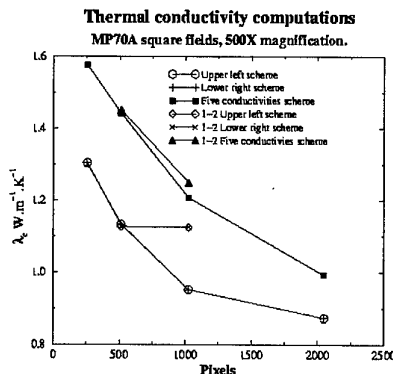


Figure 9: Thermal conductivity versus resolution.

extra 1024x1024 image (referenced 1-2) is obtained from the 512x512 one by a pixel duplication technique. The computed conductivity is a decreasing function of the resolution whereas the total porosity is nearly a constant. As results for the 512x512 and the 1-2 cases are quasi identical we can assert this is not a discretisation effect. The main justification we found is the loss of small morphological details (loss of crack continuity for example) which results from the resolution decrease but does not strongly affect the total porosity. The computed conductivity seems to be related to the resolution by :

$$\lambda_c = \lambda_{inf} + \frac{\alpha}{N}$$

where  $\lambda_{inf}$  is the value we would obtain for an ideal resolution and  $N$  is the resolution expressed as the number of pixels on one side of the image. Thus we are able to find a resolution independent value of the thermal conductivity for each field if we have two different resolution input images. This is an easy thing to do as a 512x512 input image can be constructed from a 1024x1024 one by pixel destruction. So all the following results are presented with three values (the 1024 resolution, the 512 resolution computed values and the ideal resolution extrapolated value) for the computed conductivities.

##### The matrix thermal conductivity problem

The second problem concerns the conductivity data of the different phases. For the computations, the needed data are the morphology and the thermal conductivity of each phase.

For the porous one, we can use the thermal conductivity of air which is well known. The major problem is for the zirconia matrix thermal conductivity. At present only bibliographical values are available. They fall between 2 and 3  $W.m^{-1}.K^{-1}$  [5], so the related uncertainties on computed thermal conductivities are large. Some in-situ evaluations of the matrix conductivity are in progress by means of microscopic thermal diffusivity measurements on real TBCs. They may lead to more realistic values of matrix properties in a near future. In the meantime, we have used an arbitrary value of 2  $W.m^{-1}.K^{-1}$  for all computations.

##### The 2D to 3D effects

The third point is related to restriction on actual geometry. All the data and results we are able to obtain with these methods are



two-dimensional. Three-dimensional effects can heavily change the conductivity if inclusions have geometrical properties which cannot be evaluated with two-dimensional sections. As Bakker [29] mentioned, the three-dimensional problem is unreachable with current computers. Therefore the construction of the relevant three-dimensional input data sets would be unpracticable with the resolution we use. So the present work is limited to the two-dimensional approach. Fractographies performed on plasma sprayed TBCs suggest that the cracks, which are responsible of the main conductivity reduction, have depth/width ratios far exceeding one and a two-dimensional section is an acceptable representation for such geometries. But this is not the case for globular porosity.

Owing to these various uncertainties the computation results have to be considered indicative rather than exact.

### Results

These tools were first applied to a free standing TBC plasma sprayed by SNECMA. Extensive analysis and computations were done on such coating in order to :

- test and validate the different procedures,
- study the influence of different classes of porosity on thermal conductivity.

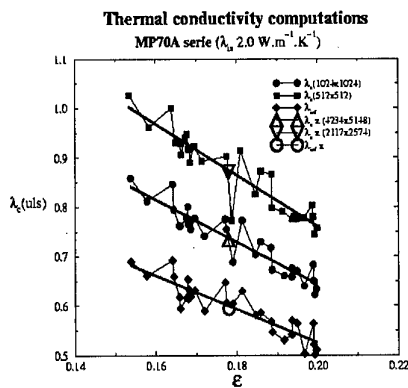


Figure 10: Plasma sprayed TBC computed thermal conductivity versus porosity.

A set of 35 adjacent (1024x1024 pixels) fields was obtained with the SEM. The thermal conductivity has been computed on each field and is represented versus porosity on figure 10

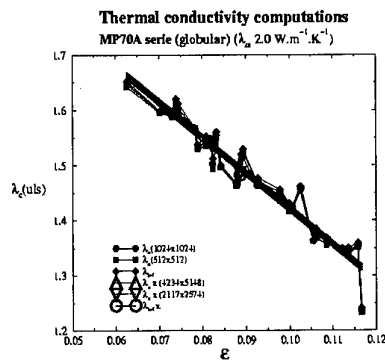


Figure 11: Globular porosity contribution.

(medium line). The lower line corresponds to ideal resolution images and is derived from calculations with 1024x1024 and 512x512 resolutions as explained above. The open symbols

correspond to the thermal conductivity computed from the global 4234x5148 image resulting from the assembly of the 35 fields according to §2.

The first important result is that the average values of the 35 fields computed conductivities are very close to those obtained for the global field as it can be seen on figure 10.

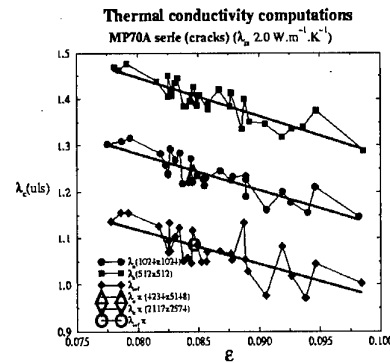


Figure 12: Crack contribution.

Therefore the decomposition in small (180x180 μm<sup>2</sup>) domains with somewhat arbitrary boundary conditions leads to a correct estimation of the equivalent conductivity of a larger element of TBC.

The second important result comes from computations done for each class of porosity (Fig. 11 and 12).

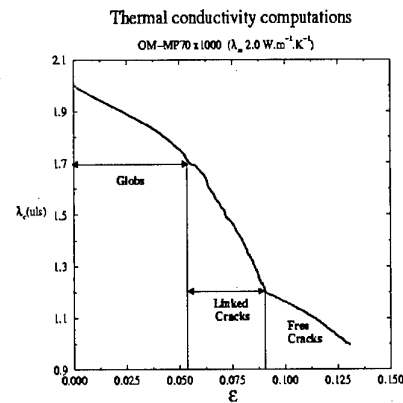


Figure 13: Influence of porosity class.

For almost identical porosity content, fields containing only the crack network present a thermal conductivity 10 to 30% smaller than that of fields with only globular pores. Analysis of computed conductivities reinforce the intuition that the major conductivity reduction results from the cracks which are mostly oriented in a direction perpendicular to the heat flow (see Fig. 4) in plasma sprayed TBCs.

This can be demonstrated even more clearly using porosity reconstruction (see §2) as computation input (Fig. 13). The rate of variation of the thermal conductivity with the porosity (e.g.  $\partial\lambda_e/\partial\epsilon$ ) strongly depends on the morphological class.

As the crack family has the highest rate of variation this class of porosity is the most efficient in reducing thermal conductivity in the case of plasma sprayed TBCs.

## 5. CONCLUSION

A software has been developed for the computation of the thermal conductivity of porous coatings (plasma sprayed TBCs) from binary images of real material cross sections. This approach based on a finite difference method takes directly into account the actual complex morphology of the ceramic which is mostly original with regard to existing models. This numerical model is able to determine the contribution of each morphological feature to the thermal conductivity and therefore compare different microstructures or coating architectures. In a near future it will be associated to a morphology generator for building a predictive tool. This one will be used in particular by engine manufacturers as guideline for modifying coating spraying conditions in order to obtain specific morphologies leading to optimised coating thermal properties.

It is important to note that this approach, developed on TBCs is most general and can be applied to a variety of multiphase media (refractories, composites, etc.).

**Acknowledgements :** Part of the work reported has been carried out within a Brite Euram project [4] and the support of the European Commission is gratefully acknowledged. Special thanks are due to SNECMA who provided the plasma sprayed coatings.

## References

1. Sheffler K.D., Gupta D.K., « Current status and future trends in turbine application of thermal barrier coatings », *J. Eng. Gas Turbines Power* (Trans. ASME), 110, 1988, pp. 605-609.
2. Bose S., DeMasi-Marcin J., « Thermal barrier coating experience in the gas turbine engine at Pratt & Whitney », in NASA CP 3312, 1995, pp. 63-78.
3. Thermal Barrier Coating Workshop. (Cincinnati, 19-21 may 1997)
4. High Insulation Thermal Barrier Systems. Brite Euram Project BE96-3226 (1996).
5. Youngblood G.E., Rice R.W., Ingel R.P., « Thermal diffusivity of partially and fully stabilised (yttria) zirconia single crystals », *J. Am. Ceram. Soc.* 71(4), 1988, pp. 255-260.
6. Hasselman D.P.H., Johnson L.F., Bentsen L.D., Syed R., Lee H.L., Swain M.V., « Thermal diffusivity and conductivity of dense polycrystalline  $ZrO_2$  ceramics : a survey », *Am. Ceram. Soc. Bull.* 66(5), 1987, pp. 799-806.
7. Kingery W.D., Bowen H.K., Uhlmann D.R., in « Introduction to ceramics ». J. Wiley (NY, 1976).
8. Madarasz F.L., Klemens P.G., « Reduction of lattice thermal conductivity by point defects at intermediate temperatures », *Internat. J. Thermophysics.* 8(2), 1987, pp. 257-262.
9. Maloney M.J., Achter H.S., Barkalow B.K., « Development of low thermal conductivity thermal barrier coatings ». Communication presented in Thermal Barrier Coating Workshop (Cincinnati, may 1997).
10. Maxwell J.C., « Treatise on Electricity and Magnetism ». Oxford University Press.
11. Eucken A., « Thermal conductivity of ceramic refractory materials : calculation from thermal conductivity of constituents », *VDI-Forschungsh.* 353 (3-4), 1932, pp. 1-16.
12. Russel H.W., *J. Am. Ceram. Soc.* 18, 1939, p1.
13. Bruggeman D.A.G., « Berechnung Verschiedener Physikalischer Konstanten von Heterogenen Substanzen », *Ann. Phys.* 24(7), 1935, pp. 636-679.
14. Murabayashi M. et al., « Effect of porosity on the thermal conductivity of  $ThO_2$  », *J. Nucl. Sci. Tech.* 6, 1969, p. 47
15. Schulz B., in *High Temperature-High Pressure* 13, 1981, pp 649-653.
16. Koh J.C., Fortini A., « Thermal conductivity and electrical resistivity of porous material », NASA report NAS3-12012, CR 1200854 (1971)
17. Cunningham M.E., Peddicord K.L., « Heat conduction in spheres packed in an infinite regular cubical array », *Internat. J. Heat and Mass Transfer* 24, 1991, pp1081-1088.
18. McLachlan D.S., Blaszkiewicz M., Newnham R.E., « Electrical resistance of composites », *J. Am. Ceram. Soc.* 73(8), 1990, pp 2187-21203.
19. Rhee S.K., « Porosity-thermal conductivity correlations for ceramic materials », *Mat. Sci. Eng.* 20, 1975, pp 89-93.
20. El-Fekey S.A., El-Mamoon Yehia M., El-Hakim M.N., « Mathematical analysis of the dependence of thermal conductivity on porosity », *Powder Met. Internat.* 10(2), 1978, pp 90-91.
21. Jackson T.B., Virkar A.V., More K.L., Dinwiddie R.B., Cutler R.A., « High thermal conductivity aluminium nitride ceramics : the effect of thermodynamics, kinetic, and microstructural factors », *J. Amer. Ceram. Soc.* 80(6), 1997, pp 1421-1435.
22. Aizanov M.I., Domashnev I.A., in *Poroshkovaya Met.* 8, 1968, p 51.
23. Bakker K., Kwast H., Cordfunke E.H.P., « The contribution of thermal radiation to the thermal conductivity of porous  $UO_2$  », *J. Nucl. materials* 223, 1995, pp 135-142.
24. Da Yu Tzou, « A universal model for the overall thermal conductivity of porous media », *J. Composite Materials* 25, 1991, pp1064-1084.
25. Furmanski P., « Effective macroscopic description for heat conduction in heterogeneous materials », *Int. J. Heat Mass Transfer* 35(11), 1992, pp 3047-3058.
26. McPherson R., « A model for the thermal conductivity of plasma-sprayed ceramic coatings », *Thin Solid Films* 112, 1984, pp 89-95.
27. C. Moreau, S. Boire-Lavigne, R.G. Saint-Jacques, « The relationship between the microstructure and thermal diffusivity of plasma-sprayed tungsten coatings », in *Proc. of the 7th National Thermal Spray Conference* 20-24 June 1994, Boston (MA). Edited by C.C. Berndt and S. Sampath (ASM, 1994), pp 621-626.
28. Bjornekleit A., Haukeland L., Wigren J., Kristiansen H., « Effective medium theory and the thermal conductivity of plasma-sprayed ceramic coatings », *J. Mat. Science* 29, 1994, pp 4043-4050.

29. Hollis K.J., « Pore phase mapping and finite-element modelling of plasma sprayed tungsten coatings », in *Advances in Thermal Spray Science and Technology. Proc. 8th National Thermal Spray Conference*, 11-15 sept. 1995, Houston, Texas Edit. C.C. Berndt, S. Sampath (ASM), pp 403-408
30. Bakker K., « Using the finite element method to compute the influence of complex porosity and inclusion structures on the thermal and electrical conductivity », *Int. J. heat Mass Transfer* 40(15), 1997, pp 3503-3511.
31. Nogotov E.F., « Application of Numerical Heat Transfer », *Series in Thermal and Fluids Engineering*, McGraw-Hill Book Company, 1978.
32. Peyret R., Taylor D., « Computational Methods for Fluid Flow », Springer-Verlag, 1986.
33. Orignac E., « Compared efficiencies of the conjugate gradient and the SOR methods applied to the solution of a three-dimensional laplacian », Private communication, ONERA 1997.
34. Anderson D.A., Tannehill J.C., Pletcher R.H., « Computational Fluid Mechanics and Heat Transfer », Hemisphere Publishing Corporation, 1984.

# MICROSTRUCTURE AND THERMAL CONDUCTIVITY OF LAYERED THERMAL BARRIER COATINGS PROCESSED BY PLASMA SPRAY AND PHYSICAL VAPOR DEPOSITION TECHNIQUES

K. S. Ravichandran, K. An, R. E. Dutton\* and S. L. Semiatin\*

Department of Metallurgical Engineering  
412 WBB, University of Utah, Salt Lake City, UT 84112, USA

\*Materials Directorate, WL/MLLM, Wright Laboratory  
Wright Patterson Air Force Base, OH 45433, USA

## SUMMARY

Thermal conductivity is an important design parameter for thermal barrier coatings. Accurate thermal conductivity data is therefore required to ensure proper design and reliability of gas turbine blades. In the present research, thermal conductivities of  $\text{Al}_2\text{O}_3$  and 8wt.%  $\text{Y}_2\text{O}_3$  stabilized  $\text{ZrO}_2$  (8YSZ) coatings, including monolithic and multilayer configurations, made by air plasma spray (PS) and electron beam physical vapor deposition (EB-PVD) techniques, were determined from the measurements of thermal diffusivity and specific heat as a function of temperature. Thermal diffusivity was determined by the laser flash technique. Specific heat was determined by a Differential Scanning Calorimeter (DSC). Detailed analyses of the results indicate that in the case of PS coatings, the thermal conductivity is sensitive to coating density (porosity), interfaces between splats as well as the interface between the coating and the substrate. In the case of EB-PVD coatings, it is shown that the multilayer conductivity is simply a series representation of monolithic coatings, provided comparisons are made under same microstructural condition. Further, analyses of sensitivity of the laser flash technique to variations in the coating and the substrate parameters, for the coatings evaluated in this study, were also performed. The results are discussed in the context of coating characteristics, reference conductivity data for dense materials and the sensitivity of the measurement method to coating parameters.

## 1. INTRODUCTION

High temperature materials are often protected by the use of thermal barrier coatings (TBCs) [1-4]. These coatings are applied by plasma spray (PS) or electron beam physical vapor deposition (EB-PVD) techniques with an

intermediate NiCoCrAlY alloy bond coating to improve adherence and to reduce oxidation. The principal TBC material is Zirconia ( $\text{ZrO}_2$ ) partially stabilized with about 6 to 8 wt.%  $\text{Y}_2\text{O}_3$  (hereafter referred to as "YSZ"; for example, 8YSZ is used to refer to  $\text{ZrO}_2$  stabilized with 8wt.%  $\text{Y}_2\text{O}_3$ ). Hereafter, the composition of  $\text{Y}_2\text{O}_3$  is quoted in wt.%, unless otherwise indicated) owing to its reasonable toughness (due to transformation toughening), low density, low thermal conductivity, high melting point, and good thermal shock resistance.

Although YSZ has low thermal conductivity, yet further reductions in thermal conductivity are caused by porosity and thermal resistance at imperfect interfaces in the coating. However, there has been limited work [5-9] performed to generate an understanding of the coating aspects that influence the heat transfer characteristics. Additionally, the conductivity data reported in the literature exhibit significant variations due to differences in processing parameters and microstructural characteristics. Among the microstructural variables that are known to have an effect on thermal conductivity, only the effects of the type and the amount of stabilizer in  $\text{ZrO}_2$  has been studied in a systematic fashion [5, 7, 8]. Further, microstructural differences between bulk  $\text{Al}_2\text{O}_3$  and YSZ and the coatings often exacerbates the difficulty in the assessment of coating thermal conductivity.

The primary objective of this study was to understand the issues involved in the assessment of thermal conductivity of  $\text{Al}_2\text{O}_3$  and YSZ made by PS and EB-PVD techniques. For this purpose, thermal conductivity of coatings were studied from room temperature to 1000°C. The results are analyzed in terms of: (i) coating porosity, (ii) thermal resistance at the interfaces, (iii) the discrepancy among the thermal conductivity data of monolithic materials and (iv) the coating microstructure relative to that of the dense materials. The

reliability of the conductivity data is assessed in terms of the sensitivity of the laser flash technique to the uncertainties in the coating and the substrate parameters.

## 2. EXPERIMENTAL PROCEDURE

Plasma-sprayed coatings were obtained by spraying 8YSZ and  $\text{Al}_2\text{O}_3$  onto 3 mm thick Rene 95 superalloy substrates measuring 62.5 mm X 12.5 mm. Prior to deposition, the substrate surfaces were grit blasted to improve coating adherence. Powders of 8YSZ (Metco 204NS; average particle size: 10  $\mu\text{m}$ ) and  $\text{Al}_2\text{O}_3$  (Plasmalloy Al-1010; average particle size: 5  $\mu\text{m}$ ) were used. A Plasma Technik Spray system with a single spray nozzle and dual powder feeder was employed. Both monolithic and multilayer coatings involving alternating layers of  $\text{Al}_2\text{O}_3$  and 8YSZ were prepared. The coatings exhibited residual porosity. Porosity levels were determined using measurements of coating mass and volume as well as by image analysis and point counting techniques on optical micrographs. To determine if residual porosity could be closed by sintering, heat treatment of the coatings was performed at 1300°C for 50 hrs in a furnace under flowing argon. For this purpose, 10 mm<sup>2</sup> size samples, cut using a diamond wafering blade, were employed. The coatings detached from the substrate as units after the heat treatment. The surfaces of the detached coatings that corresponded to the coating-substrate interfaces were metallographically polished to remove the metal oxide layers formed during the heat treatment. EB-PVD coatings were made by electron beam evaporation of high purity  $\text{Al}_2\text{O}_3$  and 8YSZ sputtering targets on to CMSX-4 single crystal superalloy substrates. The substrate temperature was about 300-500°C during the deposition process. Both monolithic and multilayer coatings involving alternating layers of  $\text{Al}_2\text{O}_3$  and 8YSZ were prepared by this technique.

Thermal diffusivity measurements were made using the laser flash technique [10]. The laser flash technique involves heating one side of the sample with a laser pulse of short duration and measuring the temperature rise on the other side with an infrared detector. The thermal diffusivity is determined from the time required to reach one-half of the peak temperature and a transient heat conduction analysis of a two-layer body. From this analysis, the thermal diffusivity of a single layer coating on a substrate can be independently determined. Measurements were made on the coatings with substrate in the as-

sprayed condition and on the detached coatings in the heat-treated condition. Measurements were made from room temperature to a temperature of 1000°C. For the high temperature measurements, the samples were heated in a vacuum chamber in 100°C steps; a thermal diffusivity measurement was made at each step. Specific heat measurements of  $\text{Al}_2\text{O}_3$  and 8YSZ were also made using a standard Perkin-Elmer Model DSC-2 Differential Scanning Calorimeter with sapphire as the reference material. Powders, scrapped from the as-sprayed coatings were used for this purpose. The standard and the sample were subjected to the same heat flux as a blank and the differential powers required to heat the sample and standard at the same rate were determined. From the masses of the sapphire standard and the sample, the differential power, and the known specific heat of sapphire, the specific heat of the sample was computed. The thermal conductivities of the coatings were determined using the relationship:

$$k = \alpha C_p \rho \quad \dots(1)$$

in which  $k$  is the thermal conductivity,  $\alpha$  is the thermal diffusivity,  $C_p$  is the specific heat and  $\rho$  is the density of the coating. X-ray diffraction analyses of the coatings were performed using Siemens D5000 unit, with  $\text{CuK}\alpha$  radiation, to identify the phases.

## 3. RESULTS: PLASMA SPRAYED COATINGS

### (a) Monolithic Coatings:

Microstructures of the as-plasma sprayed coatings are shown in Fig. 1(a&b); those after heat treatment are illustrated in Fig. 2(a&b). The coatings exhibited a porous structure, typical of air-plasma-sprayed TBCs. A comparison of Figures 1 and 2 reveals little change in porosity in  $\text{Al}_2\text{O}_3$  and YSZ layers after heat treatment. Therefore, porosity levels in the as-sprayed condition were assumed for the heat treated coatings.

Table I. Data on Monolithic Coatings

Property	$\text{Al}_2\text{O}_3$	8YSZ
Coating thickness (mm)	0.34	0.37
Porosity (%)	19	12
Density of monolithic (g/cc)	3.9	5.74
Expt. coating density (g/cc)	3.17	5.06
Calc. coating density (g/cc)	3.28	5.13

The porosity, density and the thickness of each coating are presented in Table I. As mentioned above, porosity levels were determined by a "mass/volume" (direct) measurement, or by

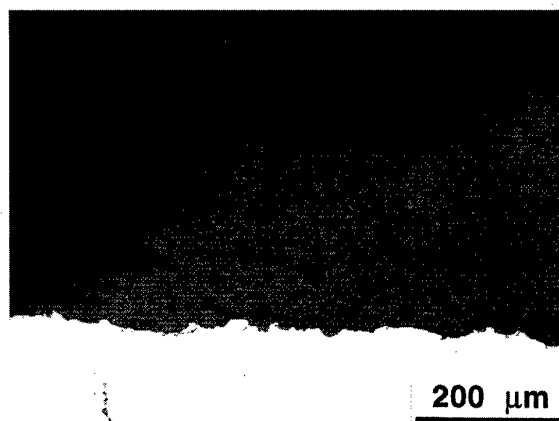


Fig. 1(a) Microstructure of PS  $\text{Al}_2\text{O}_3$  in the as-sprayed condition

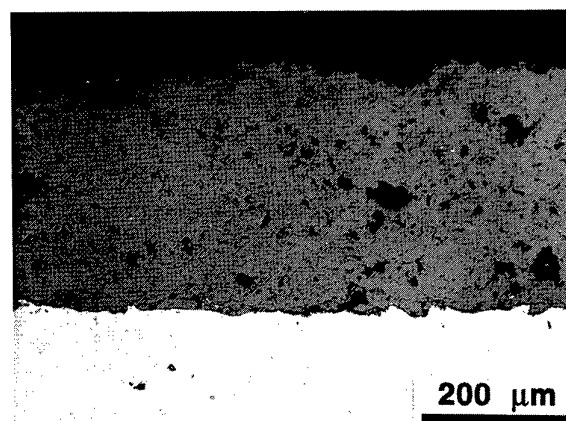


Fig. 1(b) Microstructure of PS 8YSZ coating in the as-sprayed condition

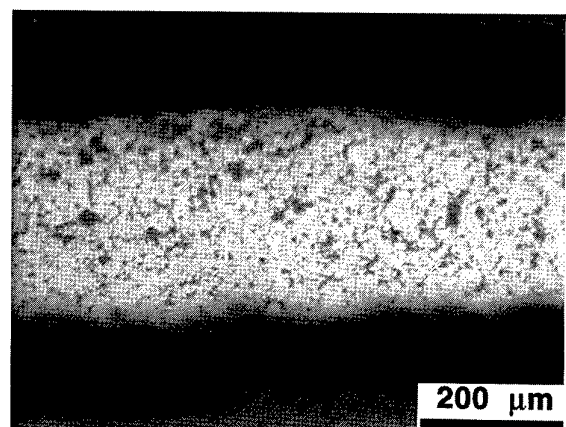


Fig. 2(a) Microstructure of PS  $\text{Al}_2\text{O}_3$  in the heat treated condition

image analysis/point counting techniques on polished cross-sections. The various techniques gave reasonable agreement once polishing

procedures were optimized to minimize particle pull-out. Additionally, the density values determined using the porosity levels in Table I and the theoretical densities were nearly in agreement, suggesting that the density values determined by the "mass/volume" technique are reliable.

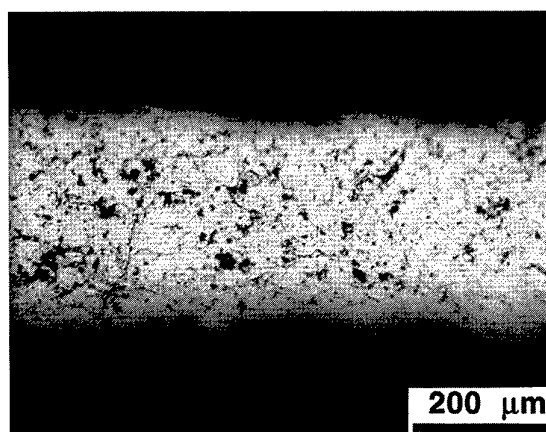


Fig. 2(b) Microstructure of PS 8YSZ in the heat treated condition

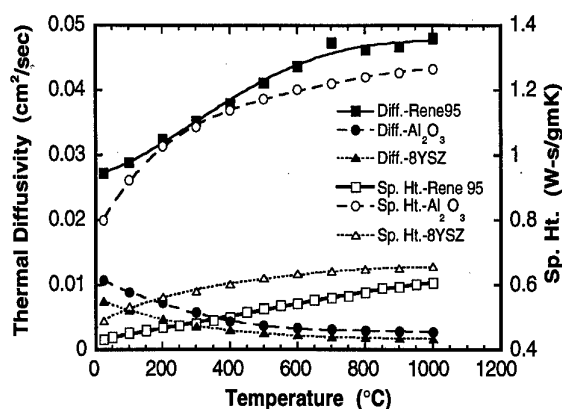


Fig. 3. Thermal diffusivity and specific heat data for Rene 95 substrate,  $\text{Al}_2\text{O}_3$  and 8YSZ

Thermal diffusivity and specific heat data for the Rene 95 substrate,  $\text{Al}_2\text{O}_3$  and 8YSZ are presented in Fig. 3. Thermal conductivities of monolithic  $\text{Al}_2\text{O}_3$  and 8YSZ as-sprayed coatings as a function of temperature, determined through Eqn. (1) using the data in Fig. 3, are presented in Figures 4 and 5, respectively. In these figures, thermal conductivity of as-sprayed coatings are compared with that of the solid materials incorporating the effect of porosity. It is to be noted that the data for solid  $\text{Al}_2\text{O}_3$  could not be obtained during the period of this study, due to difficulties in sintering the spray powder. Therefore, the thermal

conductivity data reported in literature is employed in Fig. 4.

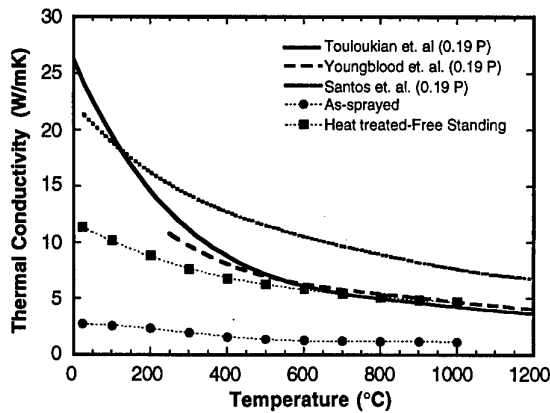


Fig. 4. Thermal conductivity of  $\text{Al}_2\text{O}_3$  coatings compared with the porosity-corrected data for various solid  $\text{Al}_2\text{O}_3$  reported in literature

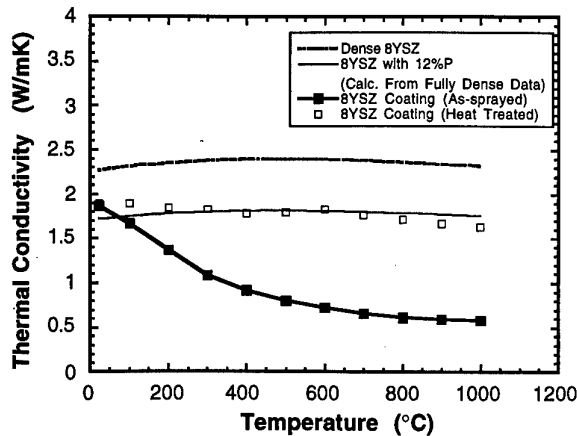


Fig. 5. Thermal conductivity of 8YSZ coatings compared with the porosity-corrected data of solid 8YSZ

The degree of reduction in thermal conductivity due to porosity can be calculated from [11]

$$k_p = k[1 - P^{2/3}] \quad \text{..(2)}$$

in which  $k_p$  and  $k$  are the thermal conductivities of the porous material (with a porosity of volume fraction  $P$ ) and the fully dense material, respectively. During the present work, Eqn. (2) was found to accurately describe the reduction in room-temperature thermal conductivity due to the presence of pores in solid  $\text{Al}_2\text{O}_3$  and  $\text{ZrO}_2$  ceramics, when evaluated [11] against the data on sintered monolithic materials reported in literature [12-15]. Therefore, Eqn. (2) was used to incorporate the effects of porosity on thermal conductivity in Figures 4 and 5.

## (b) Multilayer Coatings

Microstructures of multilayer coatings: AZ4 and AZ8 are shown in Figs. 6 (a&b) in the as-sprayed condition and in Figs. 7 (a&b) after heat treatment. A refers to  $\text{Al}_2\text{O}_3$  and Z refers to 8YSZ, with the numbers indicating the number of layers of each material. For example, AZ4 contains 4 layers of  $\text{Al}_2\text{O}_3$  and 4 layers of 8YSZ, arranged alternately. Table II illustrates the total coating thickness, individual layer size and the experimentally measured and calculated porosity levels, for various multilayer coatings made by the PS technique.



Fig. 6(a) Microstructure of PS AZ4 coating in the as-sprayed condition

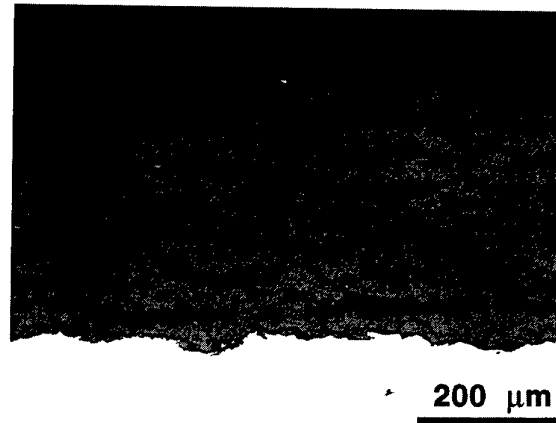


Fig. 6(b) Microstructure of PS AZ8 coating in the as-sprayed condition

Thermal conductivity data as a function of temperature for multilayer coatings in the as-sprayed and sprayed-and-heat treated conditions are presented in Figures 8 and 9, respectively. The conductivity data for fully dense materials are also included. In addition, estimates of conductivity of bilayer coatings (assuming  $\text{Al}_2\text{O}_3$  and 8YSZ in series) using either the porosity-corrected data for fully dense  $\text{Al}_2\text{O}_3$  and 8YSZ or

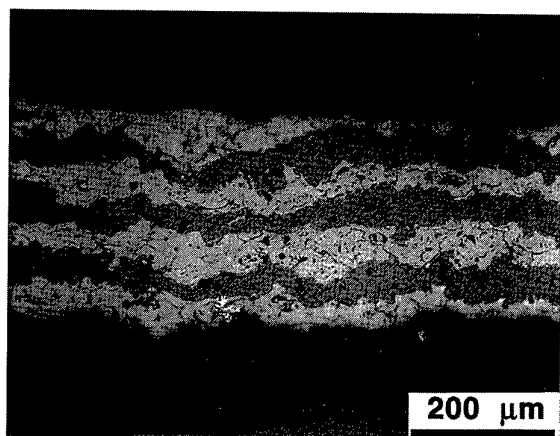


Fig. 7(a) Microstructure of PS AZ4 coating in the heat treated condition

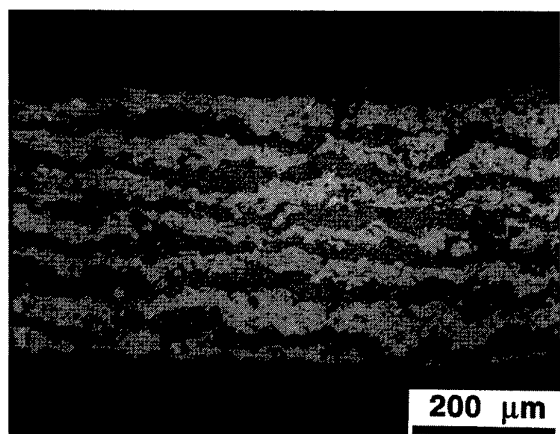


Fig. 7(b) Microstructure of PS AZ8 coating in the heat treated condition

Table II. Data on Multilayer Coatings

Property	AZ1	AZ2	AZ4	AZ8
Thickness (mm)	0.36	0.36	0.35	0.35
Each layer size (mm)	0.18	0.09	0.044	0.022
Porosity (%)	15.5	17	12.7	13.7
Density of solid (g/cc)	4.82	4.82	4.82	4.82
Coating density* (g/cc)	4.07	4.0	4.21	4.16
Coating density <sup>+</sup> (g/cc)	4.17	4.12	4.28	4.24

\*Experimentally determined

<sup>+</sup>Calculated from porosity and solid density

the experimentally measured data for monolithic  $\text{Al}_2\text{O}_3$  and 8YSZ coatings, are presented. These calculations were performed using Equation (3) in the following form:

$$k_c = \frac{k_a k_z}{(k_a t_z + k_z t_a)} \quad \dots(3)$$

in which  $k_c$  is the composite thermal conductivity with the layers in series

arrangement, and  $t_a$  and  $t_z$  are the thickness fractions of  $\text{Al}_2\text{O}_3$  and 8YSZ layers, respectively. Because the thickness fractions of  $\text{Al}_2\text{O}_3$  and YSZ are nearly the same and equal in all of the multilayer coatings, these calculations provide a baseline for comparison with the measured thermal conductivities of the multilayer coatings.

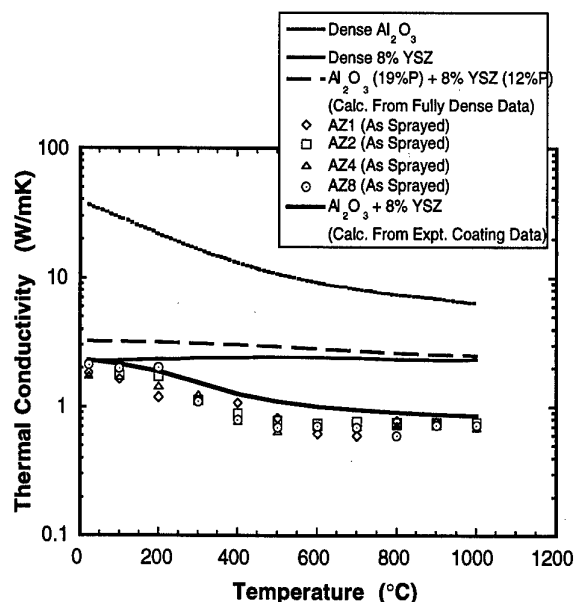


Fig. 8. Comparison of experimental conductivity data of as-sprayed multilayers with the data for monolithic dense materials as well as calculated data for a bilayer coating

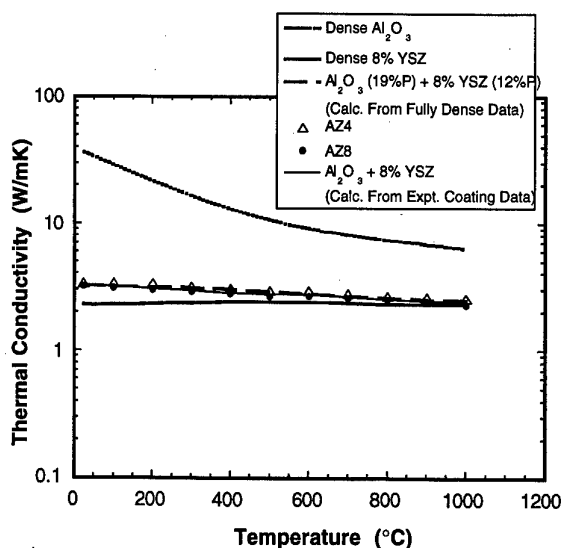


Fig. 9. Comparison of experimental conductivity data of heat treated multilayer coatings with the data for monolithic dense materials as well as calculated data for a bilayer coating



#### 4. DISCUSSION: PLASMA SPRAYED COATINGS

##### (a) **Monolithic Coatings:**

The conductivity levels in the as-sprayed condition are substantially lower than the porosity-incorporated data of solid materials, for both  $\text{Al}_2\text{O}_3$  and 8YSZ coatings (Figs. 4 & 5). However, the data of  $\text{Al}_2\text{O}_3$  and 8YSZ free-standing heat treated coatings agreed well with the porosity-incorporated data of solid materials. For  $\text{Al}_2\text{O}_3$ , the agreement is good with the data of Youngblood et. al. [16]. The rationale behind this choice is discussed in the next section.

The heat treated coatings differed from the as-sprayed in two respects: (i) a high degree of elimination of interfaces between the splats in the coating due to sintering and (ii) the elimination of the coating/substrate interface, since the coatings detached after heat treatment. Therefore, the increase in conductivity is perceived to be due to the elimination of both of these interfaces in the heat treated condition.

Since dense specimens of  $\text{Al}_2\text{O}_3$ , for reference conductivity measurements, could not be made from the plasma spray powders, conductivity data reported in literature for  $\text{Al}_2\text{O}_3$  were used in assessing the conductivities of present coatings. In this context, one of the primary issues is the accuracy of reference data and the equivalency of the microstructure of the reference material to that of the coating. For example, the literature thermal conductivity data (Fig. 4) for solid  $\text{Al}_2\text{O}_3$  differed significantly, possibly due to variations in microstructure. The data of Youngblood et. al. [16] was generated using AD 995  $\text{Al}_2\text{O}_3$  powder (Coors Ceramics, Inc., Golden, CO.) sintered to >99% theoretical density. The details regarding purity, phases and microstructure were not available. The data of Touloukian et. al. [17] is for  $\text{Al}_2\text{O}_3$  having >98% theoretical density, but the details on purity and phases were not available. The data of Santos et. al. [18] was generated using 99.8% pure  $\text{Al}_2\text{O}_3$  (A-16SG powder from ALCOA) and correcting the measured conductivity data for residual porosity. Because of the different sources of these powders, considerable variability in the thermal conductivity data of dense  $\text{Al}_2\text{O}_3$  is seen (Fig. 4). Further, since the details on purity, phases and microstructure are not known, a comparison of them with the  $\text{Al}_2\text{O}_3$  coating is difficult. The X-ray diffraction pattern of the  $\text{Al}_2\text{O}_3$  coating is shown in Fig. 10. The figure indicates that both  $\alpha$ - $\text{Al}_2\text{O}_3$  and  $\gamma$ - $\text{Al}_2\text{O}_3$  phases are present in significant

quantities. In addition, small intensity maxima, characteristic of an amorphous phase, such as  $\text{SiO}_2$ , are also present. Amorphous  $\text{SiO}_2$  is known [19] to be present as grain boundary phase in sintered  $\text{Al}_2\text{O}_3$ . Due to its low thermal conductivity relative to  $\text{Al}_2\text{O}_3$ , a significant change in conductivity, due to small changes in  $\text{SiO}_2$  content can be expected. Figure 4 indicates that the conductivity data of Youngblood et. al. [16] agreed better with that of the heat treated material. The lack of agreement with the data of other reference materials, even after correcting for porosity, could be due to the microstructural differences between the coating and these materials. Further study is needed to clarify the role of purity, phases and microstructure on the thermal conductivity of  $\text{Al}_2\text{O}_3$ .

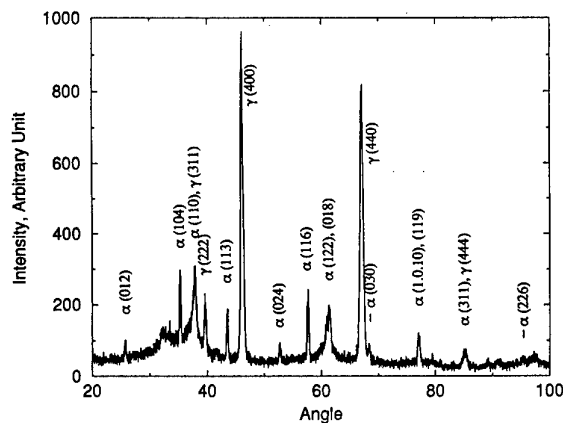


Fig. 10. X-ray diffraction pattern for as-sprayed  $\text{Al}_2\text{O}_3$  coating.

##### (b) **Multilayer Coatings:**

Figure 8 reveals that the thermal conductivities calculated from Equation (3), using the data for dense materials and accounting for porosity, are significantly higher than the experimental measurements for the multilayers. On the other hand, the estimates from Equation (3) using the experimental conductivity data for the monolithic  $\text{Al}_2\text{O}_3$  and 8YSZ coatings are in reasonable agreement with the multilayer data. The latter agreement may be surmised to be due to the effect of thermal resistance due to splat interfaces and cracks, which is already included in the conductivities of the monolithic coatings. The conductivities of all of the multilayer coatings fall in a narrow band, suggesting that the contribution from the interlayer interfaces in reducing the overall thermal conductivity of the coating is relatively small. It should be noted that all the coatings had the same overall thickness with varying number of layers and corresponding layer thicknesses. Therefore, the

total number of splat interfaces in each coating can be expected to be nearly the same. It appears that due to this similarity, the thermal conductivity levels of multilayer coatings differed little and thus can be predicted with reasonable accuracy from the experimental data of monolithic coatings.

While the measured conductivity data for all the as-sprayed multilayer coatings showed a significant decrease with temperature, the data after heat treatment (Figure 9) were largely independent of temperature. Several microstructural factors should be considered in understanding thermal conductivity changes after heat treatment. Porosity and thermal resistance at interfaces can significantly influence the thermal conductivity in solids [4, 5, 10, 11, 15]. Since porosity levels changed only a little, the effect on thermal conductivity due to this change can be considered negligible. On the other hand, interfaces between the splats in thermal sprayed coatings have been suggested to reduce the thermal conductivity due to the

interface thermal resistance [5, 11]. This effect due to internal interfaces can be appreciated from the data shown in Fig. 9. The predictions for a bilayer, calculated from the porosity-corrected data of fully dense materials as well as from the experimental data for heat-treated monolithic coatings using Equation (3), agree well with the experimental data for multilayer coatings. This suggests that heat treatment may have eliminated the effects due to the imperfect splat interfaces in the coatings and that the primary microstructural factor that influences thermal conductivity in this condition is the porosity within the layers. However, since the coatings detached after heat treatment, it was not possible to determine the relative contribution of the coating-substrate interface versus that of the splat interfaces.

## 5. RESULTS: EB-PVD COATINGS

Details of EB-PVD coatings, including total coating thickness, individual layer thickness and density are presented in Table III.

**Table III. Description of Coatings, Layer Thickness and Density Values for EB-PVD Coatings with CMSX Single Crystal Substrates.**

ID	Coating Type	Calc. Density* (gm/cc)	Meas. Density (gm/cc)	Subst. Thick. (mm)	Total Coating Thick. (mm)	Thick. of 8YSZ layer (mm)	Thick. of Al <sub>2</sub> O <sub>3</sub> layer (mm)
PVD2	Substrate+ bond coat**	8.567	8.52	0.915***			
PVD4	PVD2 + 1 layer 8YSZ	5.74	5.41	0.865	0.111	0.111	
PVD5	PVD2 + 1 layer each of Al <sub>2</sub> O <sub>3</sub> and 8YSZ	4.75	4.69	0.749	0.094	0.049	0.045
PVD6	PVD2 + 4 layer each of Al <sub>2</sub> O <sub>3</sub> and 8YSZ	4.65	4.71	0.609	0.116	0.015	0.014
PVD7	PVD2 + $\approx$ 350 alt. Al <sub>2</sub> O <sub>3</sub> and 8YSZ layers	5.11	4.64	0.614	0.117	0.00065	0.00035
PVD8	PVD2 + $\approx$ 1000 alt. Al <sub>2</sub> O <sub>3</sub> and 8YSZ layers	5.08	4.83	0.485	0.139	0.00064	0.00034

\* Calculated from theoretical density of Al<sub>2</sub>O<sub>3</sub> and 8YSZ, using layer thicknesses.

\*\* Substrate+bond coat was treated as a single material in thermal conductivity measurements and calculations.

\*\*\* Refers to the total thickness of bond coat + substrate.

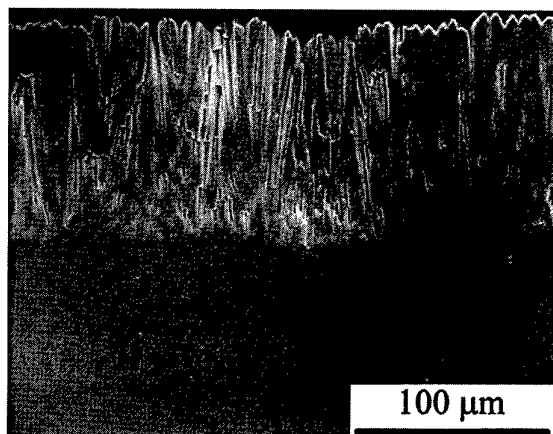


Fig. 11. Microstructure of single layer EB-PVD 8YSZ coating

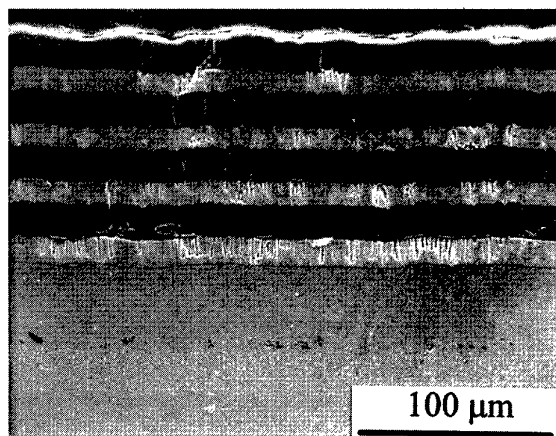
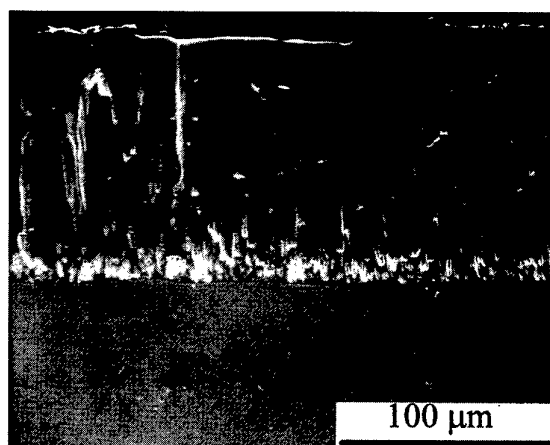


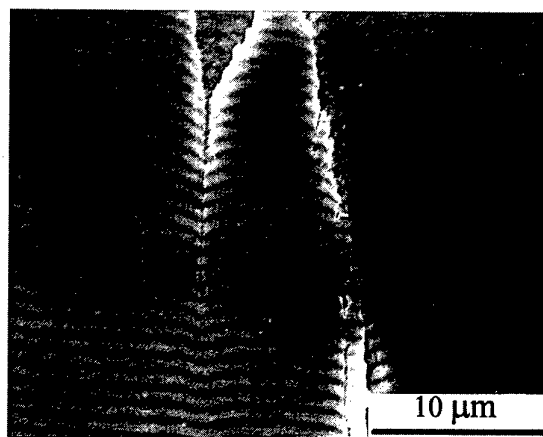
Fig. 12. Microstructure of multilayer coating with 4 alternating layers of each of 8YSZ and  $\text{Al}_2\text{O}_3$

Microstructures of EB-PVD coatings are presented in Figs. 11 through 13. Figures 11 and 12 illustrate the microstructures of the single layer 8YSZ (PVD4) and 8 layer coating involving 4 alternate layers of each of 8YSZ and  $\text{Al}_2\text{O}_3$ , respectively. Figures 12 (a&b) illustrate the microstructure of the multilayer coating with about 350 total alternating layers of 8YSZ and  $\text{Al}_2\text{O}_3$ . The microstructure of single layer 8YSZ coating is an array of fairly closely packed columns that run perpendicular to the interface of coating and substrate. As the total number of layers was increased, the tendency to exhibit the columnar structure decreased. The measured thermal conductivity data as a function of temperature for all the coatings studied are presented in Fig. 14. The solid 8YSZ data is for the original bulk material that was used to deposit the coating.  $\text{Al}_2\text{O}_3$  could not be sintered to obtain a dense material. Therefore, the data for solid  $\text{Al}_2\text{O}_3$  was taken from literature. This data

is the same (Santos et. al. [18]) as the data reported in Fig. 4. Additionally, single layer  $\text{Al}_2\text{O}_3$  coating with the same thickness as the other coatings, could not be deposited without cracking and spallation. The data calculated on the basis of series heat transfer model (Eqn. 3) using the thickness fractions of layers in each type of coating, is also presented. It can be seen that the multilayers have higher conductivity than that of 8YSZ, but lower than the data of bulk  $\text{Al}_2\text{O}_3$ , as expected. It appears that as the columnar nature of the layers decreased, the thermal conductivity also decreased. This is clearly evident by comparing the data of 2 layer coating and the 8 layer coating.



(a)



(b)

Fig. 13 (a&b). Microstructures of multilayer coating with 350 total alternating layers of 8YSZ and  $\text{Al}_2\text{O}_3$

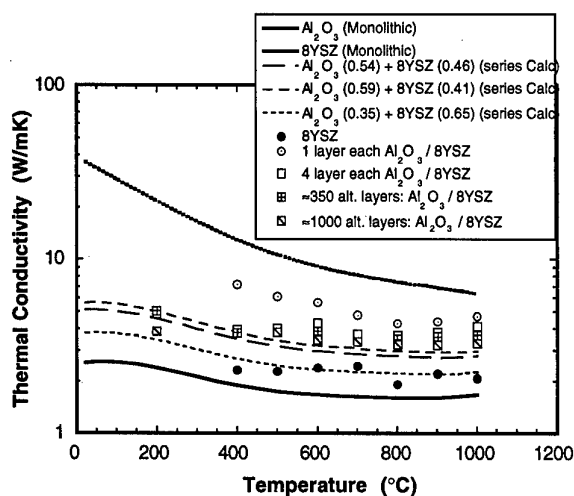


Fig. 14. A comparison of the experimental thermal conductivities of EB-PVD coatings with the data for solid materials and the calculated data for multilayer coatings

## 6. DISCUSSION: EB-PVD COATINGS

First of all, the thermal conductivity data of 8YSZ coating is higher than the bulk 8YSZ data by a factor of 1.5. In order to understand this discrepancy, some microstructural factors are to be considered. The solid 8YSZ and the coating deposited using it, were found to be not under the same microstructural condition. Whereas the solid consisted of a mixture of monoclinic and tetragonal phases (Fig. 15), the coating consisted almost entirely of tetragonal phase (Fig. 16). The type of phase present in the YSZ microstructure is known [20] to affect the thermal conductivity and therefore, this factor should be considered in the comparison of the monolithic material and the coating.

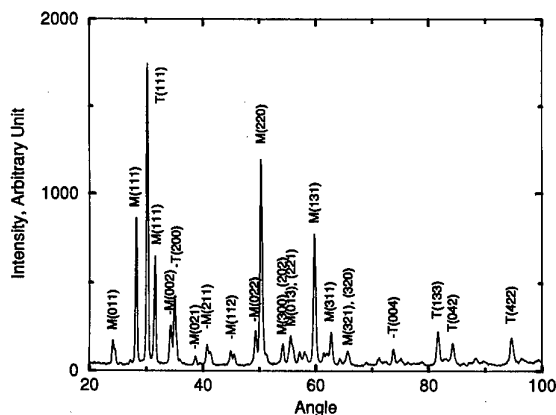


Fig. 15. X-ray diffraction pattern for solid 8YSZ material

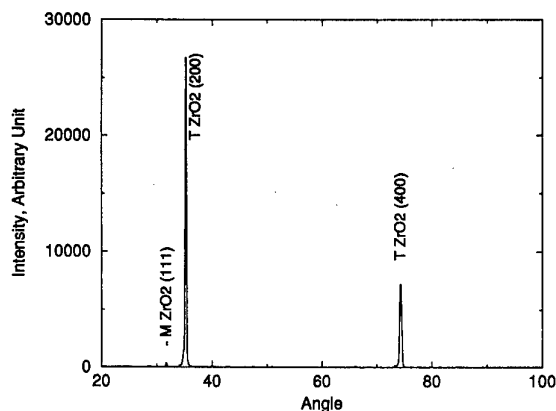


Fig. 16. X-ray diffraction pattern for the 8YSZ coating

First, it is of interest to see how the relative proportion of phases in YSZ, influenced by  $Y_2O_3$  level, would influence the conductivity of YSZ. In Fig. 17, the conductivity data of various dense YSZ specimens reported in literature [16,20,21], as well as that of solid 8YSZ evaluated in the present study, are compared. The data differed significantly among them, owing to the variation in the amount of  $Y_2O_3$  stabilizer. For example, increasing  $Y_2O_3$  from 5.3wt.% to 9wt.%, a significant decrease in the conductivity level can be seen, over the entire temperature range. However, at 11wt.%  $Y_2O_3$ , the conductivity appears to increase, relative to that of 8-9wt.%  $Y_2O_3$  stabilized  $ZrO_2$  specimens. This trend is consistent with the variation in thermal diffusivity as a function of  $Y_2O_3$  content, as observed by Youngblood et. al. [16].

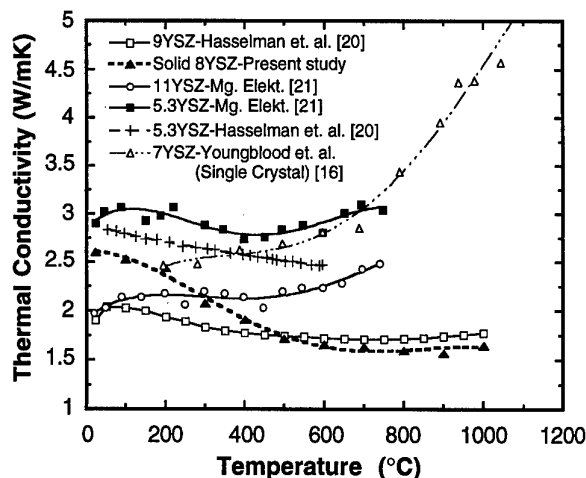


Fig. 17. Thermal conductivity data for YSZ with various amount of stabilizer content, compiled from literature

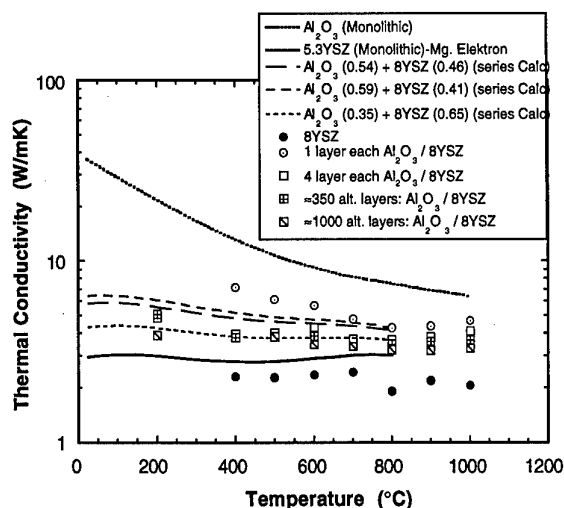


Fig. 18. A comparison of the experimental thermal conductivities of EB-PVD coatings with the revised data

The study of Hasselman et. al [20] indicates that in the range of  $Y_2O_3$  content varying from 4.5 to 5.5 wt.%,  $Y_2O_3$ , YSZ almost entirely consists of tetragonal phase. Above 5.5 wt.%  $Y_2O_3$ , a mixture of tetragonal and monoclinic phases was seen. The proportion of monoclinic phase was determined to be 25% in the 8.6YSZ specimen. This is consistent with the X-ray data of 8YSZ dense material (Fig. 15) evaluated in the present study. Therefore, the present 8YSZ coating and the 8YSZ dense material are not truly comparable due to the differences in the amount of tetragonal and monoclinic phases. The relative proportions of phases can affect the thermal conductivity of coatings due to: (i) the second phase-effect on thermal conductivity in composites [19], (ii) phonon scattering at the interphase interfaces [22] and (iii) a change in defect structure with composition [23]. In Fig. 18, the thermal conductivity comparisons employed in Fig. 14 have been revised using the solid 5.3wt% YSZ conductivity data, since, this material entirely consisted of tetragonal phase. As can be seen, the agreement between the conductivities of solid 8YSZ and 8YSZ coating as well as between the experimental data and the calculated data for multilayer coatings has improved. It is to be noted that the variations between the conductivity levels of multilayer coatings appear to be due to differences in the relative layer thicknesses of 8YSZ and  $Al_2O_3$  layers.

## 7. ANALYSIS OF SENSITIVITY OF THERMAL CONDUCTIVITY MEASUREMENT

Thermal diffusivities of the coatings with the substrate, investigated in this study, were determined using a two-layer calculation procedure which is discussed in detail elsewhere [10]. The input parameters which enter this calculation are the thicknesses, densities and the specific heat values of the coating and the substrate, the thermal diffusivity of substrate and the measured half-times. The sensitivity of each of these parameters also depends on the relative values between these parameters, i.e. the relative layer thicknesses, the relative magnitudes of diffusivities, etc. The situation is further complicated by the fact that the calculation of the diffusivity (or conductivity) of the coating is an iterative procedure. The effect of uncertainties in the input parameters for the PS and EB-PVD 8YSZ coatings, on their calculated thermal conductivity values, was determined by introducing positive and negative errors in the parameters. The changes in the coating conductivity values are plotted as a function of positive and negative changes in different input parameters, in Figs. 19 and 20 for 8YSZ coatings, deposited by PS and EB-PVD techniques, respectively.

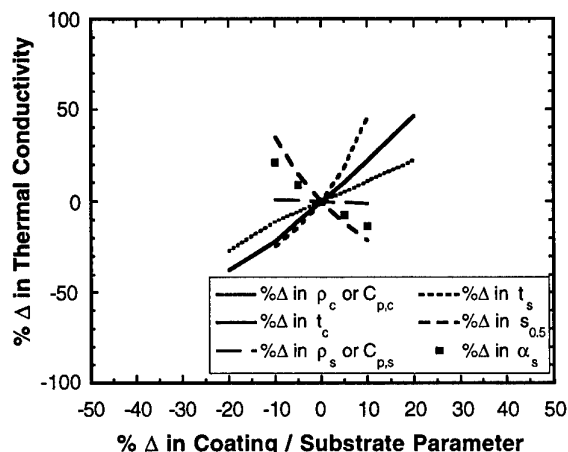


Fig. 19. Sensitivity of thermal conductivity of PS 8YSZ coating to the changes in coating/substrate parameters

For the PS 8YSZ coating, in the order of decreasing sensitivity, the coating conductivity is sensitive to: substrate thickness ( $t_s$ ), half-time ( $S_{0.5}$ ), substrate diffusivity ( $\alpha_s$ ), coating thickness ( $t_c$ ), coating density ( $\rho_c$ ) or specific heat ( $C_{p,c}$ ) and substrate density ( $\rho_s$ ) or specific heat ( $C_{p,s}$ ). For example, for PS 8YSZ coating (Fig. 19), a -10/+10 change in the parameter caused changes in the coating conductivity as: -24/+46 for substrate thickness, +35/-20 for half-time, +22/-13 for substrate diffusivity, -21/+21 for coating

thickness,  $-11/+11$  for coating density or specific heat and  $+1/-1$  for substrate density or specific heat.

For the present PS coatings, the accuracy of the conductivity data principally depends on the parameters that cause the most variability in the present coatings. Since substrate thickness could be measured to the accuracy of 0.1 mm, the uncertainty in substrate thickness (0.03%) is too small to cause any change in coating conductivity. The half-times are recorded using digital oscilloscopes, so the uncertainty in their measurement can be considered to be better than 1%. The substrate diffusivity was independently measured using the free-standing sample and hence the measurements can be considered accurate within  $\pm 1\%$ . The density of the substrate were determined within  $\pm 1\%$  using the Archimedes principle. The specific heat values of the coating and the substrate can also be determined to a level of  $\pm 1\%$  or better. This leaves the coating thickness and the density as the most sensitive parameters involved in the present study. The coatings thicknesses were of the order of 400  $\mu\text{m}$ , with the coating surface roughness of the order of 40-50  $\mu\text{m}$ , indicating that the variability in coating thickness is about 10%. Additionally, the measurements of density of plasma sprayed coatings could be in error to some degree, due to the penetration of liquid medium through the open pores. Therefore, the present thermal conductivity data for PS coatings can be expected to be subject to these uncertainties.

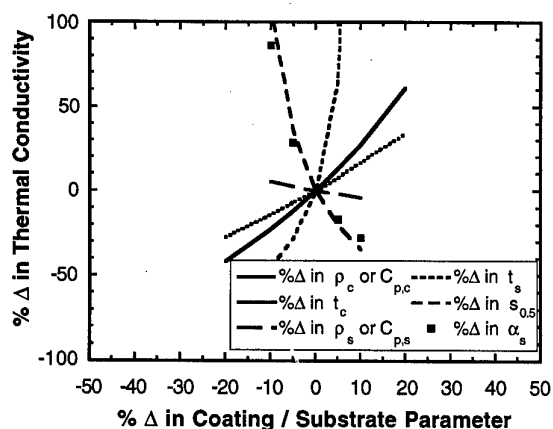


Fig. 20. Sensitivity of thermal conductivity of EB-PVD 8YSZ coating to the changes in coating/substrate parameters

For the EB-PVD coating, in the order of decreasing sensitivity, the coating conductivity is sensitive to: substrate thickness, half time,

substrate diffusivity, coating thickness, coating density or specific heat and substrate density or specific heat. For example, a  $-10/+10$  change in the parameter caused changes in the coating conductivity as:  $-44/+∞$  for substrate thickness,  $+105/-35$  for half-time,  $+86/-29$  for substrate diffusivity,  $-22/+27$  for coating thickness,  $-15/+16$  for coating density or specific heat and  $+5/-3$  for substrate density or specific heat (Fig. 20). The order of parameters in sensitivity ranking is similar to that of the PS coatings.

It is to be noted that for the EB-PVD coatings the variability encountered in coating parameters are about the same as that of the PS coatings. However, the EB-PVD coating thickness is a factor of 4 smaller compared to the PS coatings. The substrate thickness was 1 mm. The sample used for thermal conductivity measurement was prepared by mechanically grinding the substrate from its original thickness of 3 mm to 1 mm. After grinding, the average variation in substrate thickness was found to be about  $\pm 0.04$  mm. This would suggest that the uncertainty in substrate thickness is  $\pm 4\%$ . Therefore, the increased sensitivity of conductivity data in the case of EB-PVD coating, relative to PS coatings, seems to arise from the reduced thicknesses of the coating and the substrate.

## 8. CONCLUSIONS

### Plasma Sprayed Coatings:

(1) The reductions in the thermal conductivities of single layer as well as multilayer plasma-sprayed  $\text{Al}_2\text{O}_3$  and 8YSZ coatings are brought about by porosity and thermal resistance at the interfaces in the coating. The thermal resistance appears to arise from the interfaces between the splats as well as the coating/substrate interface. The interlayer interfaces in the multilayer appears to play only a minor role in influencing the coating thermal conductivity.

(2) The thermal conductivity levels of multilayered coatings of  $\text{Al}_2\text{O}_3$  and 8YSZ are comparable to that of the single layer 8YSZ coating. Therefore, primarily the interface thermal resistance and secondarily the porosity appear to be the parameters that can be manipulated to reduce the thermal conductivity of thermal barrier coatings.

(3) The uncertainty in the thermal conductivity values of the  $\text{Al}_2\text{O}_3$  and  $\text{ZrO}_2$  coatings were determined to be primarily due to the uncertainties in the coating thickness and density values.

**EB-PVD Coatings:**

(4) Microstructures of EB-PVD coatings consisted of an array of closely packed columnar grains. The columnarity decreased as the number of layers increased, in the case of multilayer coatings involving  $\text{Al}_2\text{O}_3$  and 8YSZ.

(5) The  $\text{Al}_2\text{O}_3$  and 8YSZ layers consisted of almost entirely  $\gamma\text{-Al}_2\text{O}_3$  and tetragonal phase, respectively, in the coatings. This is in contrast to the observation of a mixture of  $\alpha/\gamma$  phases in bulk  $\text{Al}_2\text{O}_3$  and monoclinic and tetragonal phases in bulk 8YSZ.

(6) An accurate evaluation of thermal conductivity of EB-PVD coating requires accurate reference data on monolithic material having the same microstructural condition as the coating. For  $\text{Al}_2\text{O}_3$ , the relative proportion of  $\alpha/\gamma$  phases, impurity levels and microstructure may influence the reference conductivity data. For YSZ, the nature and the proportion of phases appears to be important (tetragonal, cubic or monoclinic).

(7) Thermal conductivity of multilayer coatings can be predicted from the bulk material data, using the series heat transfer model. This suggests that there is no apparent effect of interface thermal resistance due to the interlayer boundaries.

(8) Thermal conductivity data determined by laser flash technique can be subject to considerable errors due to the variability in coating parameters that are used as input in the calculations. The errors increase as the coating and the substrate thicknesses become small.

**ACKNOWLEDGMENT**

The research at the University of Utah was supported by a contract (F33615-92-C-5900) from Wright Laboratory, Wright Patterson AFB, OH, through UES Inc., Dayton, OH. The authors thank Dr. S. Sampath, State University of New York, Stony Brook, NY, and Mr. K. Murphy, Operhall Research Center, Howmet Corporation for preparation of coatings and discussions.

**REFERENCES**

1. Miller, R. A., *Surf. Coat. and Tech.*, 30, 1-11 (1987)
2. Lammermann, H. and Kienel, G., *Adv. Mater. Processes*, 140, 18-23 (1991)
3. Herman, H., Berndt, C. C. and Wang, H., *Ceramic Films and Coatings*, J. B. Wachtman and R. A. Haber, eds., 131-183, Noyes Publications, N. J. (1986)
4. Brink, R. C., *Trans. ASME: J. Eng. for Gas Turbines and Power*, 111, 570-577 (1989)
5. Pawlowski, L. and Fauchais, P., *Int. Metall. Rev.*, 31, 271-289 (1992)
6. Pawlowski, L., Lombard, D. and Fauchais, P., *J. Vac. Sci. Technol.*, 3, 2494-2500 (1985)
7. Brandon, J. R. and Taylor, R., *Surf. Coat and Tech.*, 39/40, 143-151 (1989)
8. Morrell, P. and Taylor, R., in *Advanced Ceramics*, Vol. 24, Science and Technology of Zirconia, 927-943, The American Ceramic Society, Westerville, OH (1988)
9. Rudajeva, A., *Thin Solid Films*, 223, 248-252 (1993)
10. Taylor, R. E. and Maglic, K. D., *Compendium of Thermophysical Property Measurement Methods*, K. D. Maglic, ed., 305-336, Plenum Publishing Co., (1984)
11. Ravichandran, K. S., *J. Am. Ceram. Soc.*, Submitted for Publication, (1997).
12. Francl, J. and Kingery, W. D., *J. Am. Ceram. Soc.*, 37, 99-101 (1954)
13. Saegusa, T., Kamata, K., Iida, Y. and Wakao, N., *Heat Transfer-Japanese Research*, 3, 47-52 (1974)
14. Swain, M. V., Johnson, L. F., Syed, R. and Hasselman, D. P. H., *J. Mater. Sci. Lett.*, 5, 799-802 (1986)
15. Pei-feng Hsu and Howell, J. R., *Expt. Heat Trans.*, 5, 293-313 (1992)
16. Youngblood, G. E., Rice, R. W. and Ingel, R. P., *J. Am. Ceram. Soc.*, 71, 255-60 (1988)
17. Touloukian, Y. S., Powell, R. W., Ho, C.Y. and Clemens, P. G., *Thermophysical Properties of Solids*, 2, Y. S. Touloukian and C. Y. Ho, ed., Plenum Press, New York (1970)
18. Santos, W. N. D. and Taylor, R., *High Temp.-High Press.*, 25, 89-98 (1993)
19. Kingery, W. D., *Introduction to Ceramics*, John-Wiley & Sons, New York (1967)
20. Hasselman, D. P. H., Johnson, L. F., Bentsen, L. D., Syed, R., Lee, H. M. and Swain, M. V., *Am. Ceram. Soc. Bull.*, 66, 799-806 (1987)
21. Stevens, R., *Zirconia and Zirconia Ceramics*, p. 30, 2nd Edition, Magnesium Elektron Ltd., (1986).
22. Buykx, W. J. and Swain, M. W., *Advances in Ceramics*, Vol. 12: Science and Technology of Zirconia II, 518-527, N. Claussen, M. Ruhle and A. H. Heuer, eds., American Ceramic Society, Columbus, OH (1984)
23. Gorelev, V. I. and Palguyev, S. F., *Izv. Akad. Nauk. SSSR, Neorg. Mater.*, 13, 181-182 (1977)

## EVALUATION OF THERMAL BARRIER COATINGS FROM BURNER RIG TESTS

J.-P. Immarigeon, V.R. Parameswaran, D. Chow and D.D. Morphy

Institute for Aerospace Research  
National Research Council of Canada  
Ottawa, Ontario, K1A 0R6

P. Gougeon, M. Prystay and C. Moreau

Industrial Materials Institute  
National Research Council of Canada  
Boucherville, Quebec, J4B 6Y4

### SUMMARY

A series of thermal barrier coatings were deposited on superalloy pins by various techniques using different processing parameters, in order to optimize the durability of the coatings for aerospace applications. These coatings were subjected to simulated high temperature engine operating conditions in a high velocity burner rig. The durability of the coatings at different temperatures was assessed at regular intervals from changes in pin weight due to oxidation and/or loss of coating. The thermal characteristics of some of the coatings were also assessed on-line by monitoring the core temperatures of the pins. After thermal cycling, the specimens were subjected to metallographic examination, to study the change in microstructure brought about by the burner rig cyclic tests. The test methodology and the results are discussed.

### 1. INTRODUCTION

Thermal barrier coatings (TBC's), as the name implies, are protective barriers used to isolate turbine components (usually cooled by air flow from the compressor) from the high temperature of the engine, so that the temperature felt by the substrate is considerably lower than that in which the component is operating. Lowering the metal temperature improves the creep life and reduces the thermal stresses induced by transients caused by accelerations and decelerations in the engine. Thermal barrier coatings consist of a metallic bond coat, usually MCrAlY (where M stands for Ni, Co, Fe, or a combination of these) of thickness up to 150  $\mu\text{m}$ , over which a ceramic oxide overlay coating of thickness up to 500  $\mu\text{m}$  is applied. The bond coat layer has higher oxidation and hot corrosion resistance than the superalloy substrate material and it also provides a base for mechanical bonding of the ceramic layer to the metal.

The most widely used ceramic overlay coating is based on zirconia, which has a thermal expansion coefficient close to that of the superalloy substrate. Pure zirconia, however, undergoes phase transformation in the temperature range of gas turbine engine operation. Above 2370°C,  $\text{ZrO}_2$  exists in the cubic form and as it cools down below 2370°C, it transforms to the tetragonal form,

which in turn undergoes solid state transformation to the monoclinic phase below 1170°C. This latter phase change (tetragonal to monoclinic) is accompanied by a volume increase of about 9%, which will cause cracking and lead to spalling of the ceramic zirconia layer from the bond coat. This phase transformation, however, can be suppressed by the addition of stabilizing agents such as  $\text{Y}_2\text{O}_3$ ,  $\text{MgO}$ ,  $\text{CeO}_2$  and  $\text{CaO}$ , which lower the phase transformation temperature. Of these, yttria has been found to be a good stabilizer for the range of turbine operating temperatures and partially stabilized zirconia containing 8%  $\text{Y}_2\text{O}_3$  (called YPSZ), has been found to perform well in aero engines (1). Other ceramic systems based on various oxides (e.g.  $\text{MgO}$ ,  $\text{CeO}$ , and  $\text{CaO}$ ) and oxide mixtures as well as metal silicates (e.g.  $\text{Ca}_2\text{SiO}_4$ ,  $\text{ZrSiO}_4$ ) have also been considered for marine applications where hot corrosion is a concern (2).

TBC's can be applied by one of several methods, including flame spraying, plasma spraying, detonation gun projection, and electron beam physical vapour deposition (EBPVD). Several modifications and innovations have been made in these techniques to suit particular applications and to obtain coatings of high integrity and durability (3-5). Plasma spraying, for example, has been carried out under low pressure (partial vacuum) to produce coatings of higher density. In a recent NASA Tech Brief (October 1996, p 97), it has been reported that a vacuum plasma sprayed zirconia TBC endured five times as many engine stop/start cycles as coatings applied in air (6). Using EBPVD, graded coatings with gradual transition of composition and properties through the thickness have been produced. This will prevent an abrupt transition zone, where the likelihood of failure can be high due to drastic differences in the properties of the metallic and ceramic layers (7). Nano-structured TBC's (containing nanograins or nanolayers) could provide the basis for new generations of TBC's (8).

The microstructures of TBC's vary significantly with deposition technique. Typical microstructures of coatings applied by air plasma spraying (APS), vacuum plasma



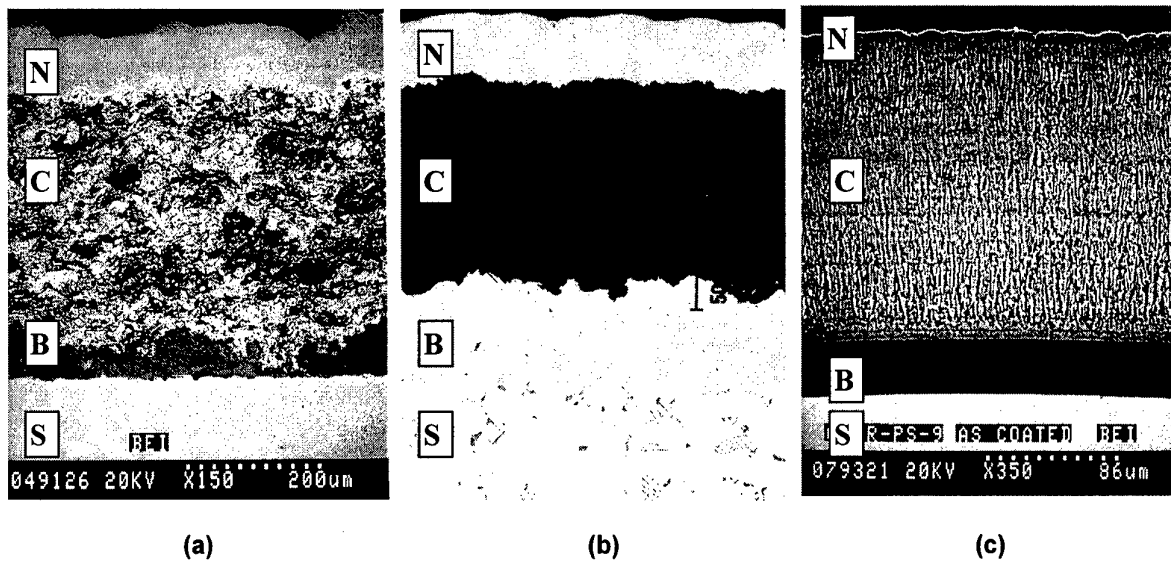


**Figure 1** Representative microstructures of TBC's applied by (a) plasma spraying in air (b) vacuum plasma spraying and (c) EBPVD (S: substrate, B: bond coat, C: ceramic overlay layer, N: electroless Ni film used to protect ceramic for metallography).

spraying (VPS) and electron beam physical vapour deposition (EBPVD) are shown in **Figure 1**. APS coatings (Fig. 1a) usually exhibit a layered structure, with a swirl pattern and a large amount of voids and pores. The pores help to increase the insulating capacity of the oxide. VPS coatings (Fig. 1b) are also layered but are denser than APS coatings and the interface between the bond coat and the ceramic layer is generally more uniform than in air sprayed products. EBPVD coatings (Fig. 1c) have a dense columnar structure, which can accommodate the strains arising from differential thermal expansion between the metallic and ceramic layers.

#### *Failure Modes of Thermal Barrier Coatings*

The life of the overlay ceramic is limited by its susceptibility to thermal fatigue cracking, while the life of the bond coat is limited by its oxidation and corrosion behaviour. Hot corrosion of the ceramic overlay may also be life limiting in marine environments. The combined effects of stress, time at high temperatures and oxidizing environment are complex, causing changes in the microstructure of the coatings as well as the substrates. These changes eventually will lead to failure of the coatings. Transverse and longitudinal cracks form at the surface and inside the ceramic layer, due to thermally induced stresses. Oxidizing gases penetrate through the transverse cracks and oxidize the bond coat. The layer of  $\text{Al}_2\text{O}_3$ , which forms at the interface between the bond coat and the ceramic (and possibly between the bond coat and substrate), thickens during service. In this layer, oxidation products such as  $\text{Cr}_2\text{O}_3$ ,  $\text{NiO}$ ,  $\text{HfO}_2$  and spinels ( $\text{NiO-Cr}_2\text{O}_3\text{-Al}_2\text{O}_3$ ) are formed by loss of  $\beta\text{-NiAl}$  from the bond coat. In the case of EBPVD coatings, cracks form in this layer of oxides, causing the top ceramic coating to spall, whereas plasma sprayed coatings are

known to fail above this oxide layer. The mechanisms of the reactions of the coatings with the environment in the engine and the ultimate coating failure are discussed in detail, elsewhere (8-10).

#### *Evaluating Thermal Barrier Coatings*

The effectiveness of a TBC coating is assessed from its ability to stay in place without spalling. The best way to assess coating durability is from actual engine tests. These, however, are expensive and time consuming. Alternatively, the performance of a coating can be evaluated in a burner rig, where engine operating conditions can be closely simulated. Engine manufacturers have used burner rig tests in the past to evaluate and compare the performance of coatings for screening purposes, prior to actual engine tests. In Canada, military operational groups have also relied on burner rig tests to assess the potential of emerging coatings for use in their engines, under various component retrofit programs. However, there is no standard procedure established for burner rig tests. Manufacturers and users adopt different cycling times and temperatures (heating times from a few minutes up to an hour, at temperatures from  $1000^\circ\text{C}$  to  $1500^\circ\text{C}$ , followed by cooling for a few minutes) tailored to suit their end use.

#### *Objectives of the present study*

At NRC, several studies have been performed using burner rig testing to compare TBC's produced by different techniques and different processing conditions, and to optimize some of the coatings for use in Canadian Forces engines. The objective of this paper is to discuss the testing procedures and methodologies employed in these studies with a view to evaluating the suitability and

practicality of burner rig testing as a laboratory ranking method for TBC's. The influence of key test parameters on modes and rates of damage accumulation is discussed. Ways to ensure that the modes known to be life limiting in engines are reproduced during rig testing are also addressed.

## 2. EXPERIMENTAL MATERIALS AND METHODS

### 2.1 Materials and Test Coupons

The TBC's investigated in this work included experimental coatings produced by EBPVD, APS and VPS, under three development programs, as well as TBC's produced by established techniques by commercial vendors. In the first series of tests, the performance of experimental EBPVD TBC's having compositionally and functionally graded interfaces between the metallic bond coat and the ceramic layer, was evaluated. These coatings were applied to nickel base superalloy pins, 0.25" diameter and 4" long, made from IN625 and a proprietary single crystal (7). In the second series of tests, zirconia and calcia based TBC's were plasma sprayed onto IN625 pins, 0.5" diameter and 5.5" long, using different conditions of particle velocities and temperatures, and studied to assess the effects of composition and processing conditions on product performance (11,12). In the third series of tests, the performances of a non-graded EBPVD TBC, TBC's with VPS bond coats and APS ceramic overlays and TBC's with VPS bond coats and VPS overlays, were also studied. These latter coatings were applied to the same pins as those used for the first series of tests.

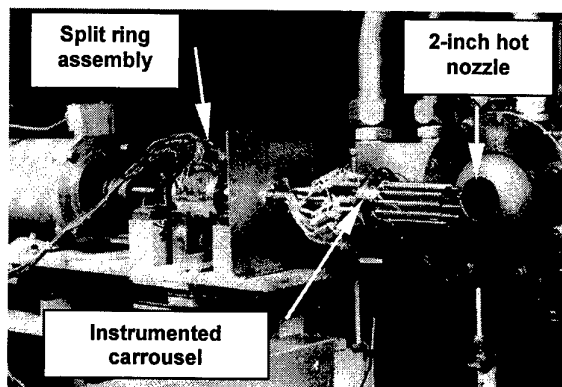


**Figure 2** The IAR burner rig equipped with the 2-inch exhaust nozzle for testing  $\frac{1}{4}$  inch diameter test pins. The slip rig assembly accommodates up to eight thermocouples for instrumentation of test pins

### 2.2 Testing and Evaluation

The coated pins were subjected to thermal cycling in a high velocity/atmospheric burner rig. The design of this rig is based on a dynamic combustor similar to that used in gas turbine engines (13). The mixing and flow in the combustor closely approximate conditions that exist within conventional combustors and the critical features

of combustor chemistry are readily reproduced and controlled. This is particularly important when assessing the effects of gas/coating reactions on the durability of coatings (14,15). Fuel (JP-4), along with compressed air, is introduced through a pressure-atomizing nozzle into the primary section of the combustor, within which combustion occurs in a swirl stabilized recirculation zone. The expanding combustion gases are cooled by dilution within a secondary section, and are exhausted through a nozzle in front of which the test pieces are placed for exposure to high velocity hot gases. By independently adjusting the primary and secondary air flows, along with the fuel flow, it is possible to vary the gas velocity and gas temperature independently of each other. With a standard 2-inch axisymmetric circular exhaust nozzle, gas velocity can be varied from Mach 0.2 to Mach 0.8 and gas temperature from 540°C (1000°F) to 1650°C (3000°F). The latter is controlled by a programmable microprocessor and measured by a thermocouple located near the throat of the exhaust nozzle. Nozzles of different sizes can be used to vary the cross sectional geometry of the hot gas jet to accommodate different test piece geometries. In the present studies, the standard 2-inch diameter nozzle was used when testing the  $\frac{1}{4}$ " diameter pins and a 3-inch oversized nozzle was used for the  $\frac{1}{2}$ " diameter pins. In both cases, the pins were positioned 1.5" away from the exhaust nozzle.

The rig in the standard 2-inch nozzle configuration is shown in **Figure 2**, with a set of uncoated  $\frac{1}{4}$  inch diameter pins positioned in front of the exhaust nozzle. The test pins are mounted on a rotating carousel, used to translate the pins back and forth between the hot gases and a jet of room temperature air from a 2-inch diameter pipe located beside the hot nozzle. In this way, the pins can be alternately heated and cooled, simulating thermal cycling in engines. Rotation of the pins, typically at 100 to 200 rpm, is used to promote gas mixing and ensure uniform exposure of the pins to the hot and the cold gases. An electrical slip ring assembly mounted on the drive shaft of the rotating carousel can be used for instrumentation of 8 of the 12 test pins.

The rig in its 3-inch nozzle configuration is shown in **Figure 3**, with a set of coated  $\frac{1}{2}$  inch diameter pins positioned in front of the cooling nozzle. With the oversized carousel required to handle the  $\frac{1}{2}$  inch diameter pins, the larger exhaust nozzle was needed to achieve efficient heating of the pins. However, at equivalent air to fuel mass flow ratios, the gas velocities and the maximum heating rates and temperatures achievable with the 3-inch exhaust nozzle are not as large as those produced with the 2-inch nozzle, which has a bearing on the modes and rates of damage accumulation in coatings, as discussed below.

In the present studies, the temperatures at various locations at the surface and in the interior of the pins were monitored by thermocouples mounted flush with the surface and inside an axial blind hole. The changes in pin

surface temperature distribution, as a function of gas temperature and gas velocity and the changes in metal temperature at the core of the pins, as a function of number of thermal cycles, were established in this manner. For surface temperature measurements, holes drilled radially and along the axes of the pins were used as feedthroughs for the thermocouple leads, to avoid disturbing the heat transfer boundary layer around the pins. Several pins with one thermocouple each, and with thermocouple beads regularly spaced along the axes of the pins, were used for these measurements. A schematic cross section of the instrumented  $\frac{1}{2}$  inch diameter pins, where all the bead positions have been combined in a single drawing for simplicity, is shown in Figure 4. The surface temperature measurements were performed on bare pins.

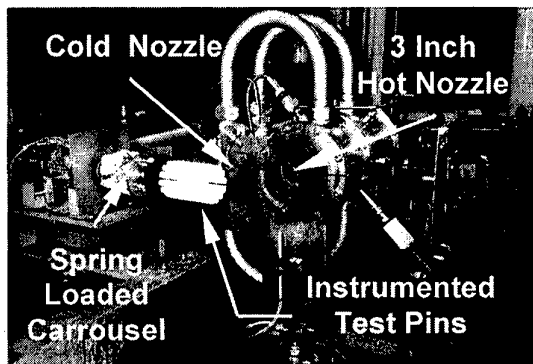


**Figure 3** The IAR burner rig equipped with the 3-inch exhaust nozzle for testing  $\frac{1}{2}$  inch diameter test pins.

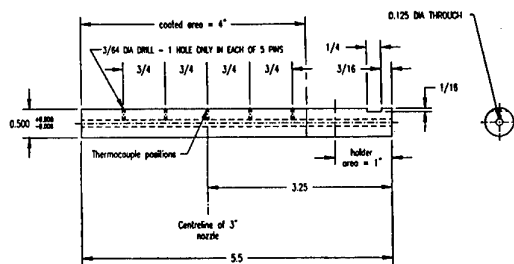


**Figure 4** Schematic cross section of the instrumented  $\frac{1}{2}$  inch pins showing locations of surface thermocouples positioned at regular intervals along the pin length.

Internal temperatures were only measured in the case of the  $\frac{1}{2}$  inch diameter pins. The intent was to track the degradation in thermal protection efficiency of their TBC's as a function of number of thermal cycles, or test time, through measurements of drifts in heating and cooling rates during thermal cycling. To measure the internal metal temperatures, thermocouples (one per pin) were mounted with their beads pushed against the bottom of a blind hole drilled along the axes of the pins, using a spring-loaded mechanism. A schematic of the instrumented  $\frac{1}{2}$  inch diameter pin is shown in Figure 5,

while a close-up view of the spring loaded mechanism is shown in Figure 6, with the test pins removed from the carrousel, but with the thermocouples still in place. The spring-loaded device ensured that the thermocouple beads were kept in contact with the bottom ends of the holes, irrespective of the degree of thermal expansion and contraction experienced by the pins during thermal cycling. The position of the bottom of the hole was chosen to correspond to the position within the hot gas jet known to experience the highest temperature, in order to record the maximum metal core temperatures.

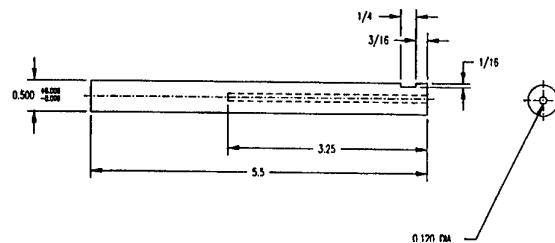


**Figure 5** Schematic cross section of the instrumented  $\frac{1}{2}$  inch pins showing the axial blind hole within which thermocouples were held in positive contact with the bottom end of the holes to measure metal core temperatures of the pins reliably.

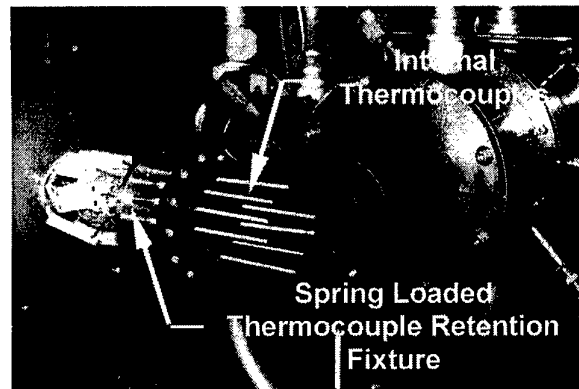


**Figure 6** Close up view of the instrumented carrousel showing the spring loaded thermocouple retention fixture which ensured the thermocouple beads were kept in contact with the test pins (not shown) during thermal cycling.

Burner rig tests involved up to 2150 cycles of 4 minutes of heating in the high velocity hot gas jet followed by 2 minutes of forced air cooling. In some cases, the gas temperature was increased in a stepwise manner, from a minimum of 1300°C to a maximum of 1500°C, to increase the severity of the tests and ensure that failure of the coatings occurred before the end of the tests. The surface conditions of the pins and their weight to the nearest 0.5 mg were recorded before testing and after every 50 to 150 cycles. The weight changes provided a measure of the spalling resistance of the various TBC's to

the combined effects of thermal loads and hot gas erosion. Changes in the heating and cooling rates of the pins during thermal cycling were also extracted on-line from internal temperature measurements. Finally, the microstructures of the TBC's were compared before and after testing, and the extent of thermally induced microstructural changes, including phase transformation as revealed by x-ray diffraction, was assessed.

### 3. RESULTS AND DISCUSSION

#### 3.1 Effects of Pin Size and Testing Conditions on Pin Temperatures

The variation of pin temperature during thermal cycling depends on the heat transferred between the pin and the hot and cold gas jets. This heat transfer is discussed in detail and modelled elsewhere, for the case of an airfoil-like test coupon (16). Considerable heat losses arise from radiation from the surface of the pins and by conduction towards their free ends and into the carousel body. Consequently, the maximum temperatures reached by the pins are considerably lower than the maximum temperature of the impinging hot gases. A record of core temperatures over a complete thermal cycle (4 minutes of heating in Mach 0.22 1500°C gas, followed by 2 minutes of air cooling), for 12 coated ½ inch diameter pins, is shown in Figure 7. Pin temperatures are seen to rise rapidly at first until, after about two minutes, they stabilize. The maximum steady state temperature reached by the pins at the end of the heating cycle depends to some degree on the TBC and, on average, is about 350°C lower than the gas temperature.

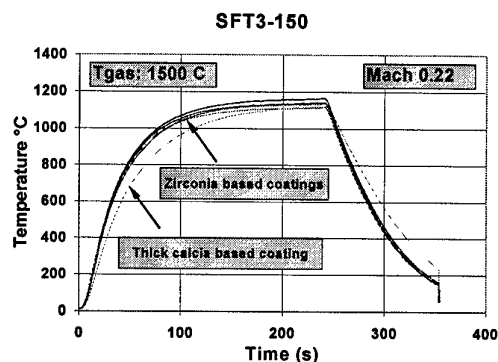


**Figure 7** Typical thermal cycles experienced by ½ inch diameter pins as revealed by thermocouples inside axial blind holes in pins (see Figure 5).

The temperatures of a series of instrumented ½ inch diameter pins, as recorded by surface and internal thermocouples over parts of the heating portion of a thermal cycle, are shown in Figure 8. These data were obtained from 5 uncoated pins (T1 to T5), each equipped with a surface thermocouple, and 2 coated (Tc-Ca8 and Tc-Ca11) and one bare pin (Tc-bare), each equipped with one internal thermocouple. The core temperatures of the coated pins rise more slowly than those of the bare pins, due to the thermal insulating effect of the TBC's.

However, the coated pins reach higher steady state core temperatures than do the bare pins, as the rates of heat loss from the free ends of the coated pins are reduced relative to bare pins. Also, the internal temperatures of both bare and coated pins are higher than their surface temperatures. This difference increases with gas temperature and is higher in coated pins, as shown in Table 1.

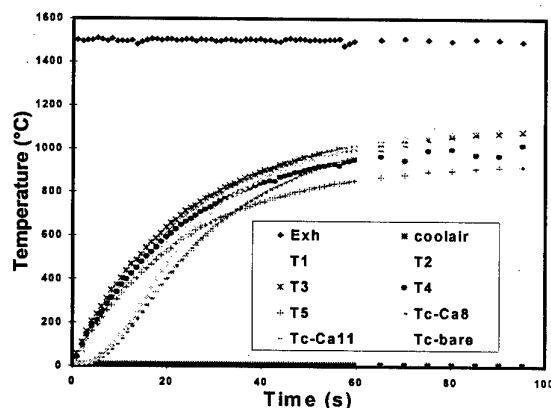


**Figure 8** Surface and internal temperature histories revealed by instrumented test pins over parts of the heating portion of a thermal cycle involving 4 minutes of heating in Mach 0.22, 1500°C gas.

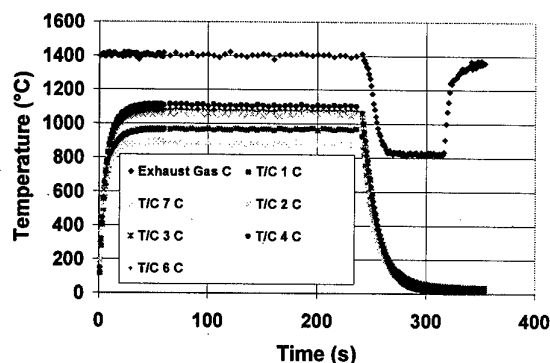
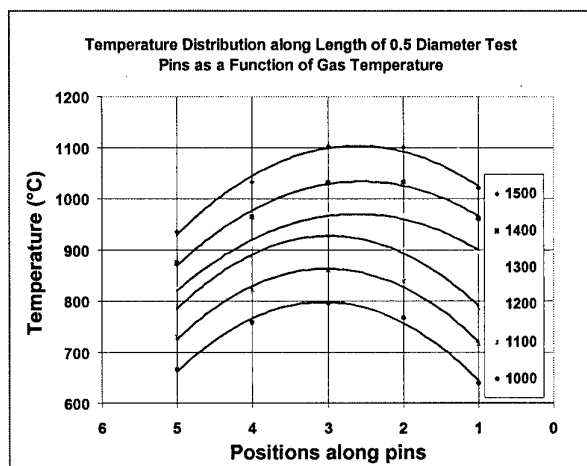
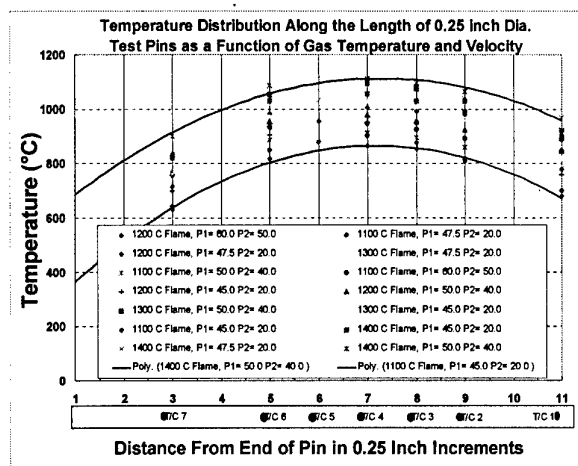


**Figure 9** Surface temperature histories revealed by instrumented ¼ inch diameter pins over parts of the heating portion of a thermal cycle involving 4 minutes of heating in Mach 0.45 1400°C gas.

The heating and cooling rates for ¼ inch diameter pins during thermal cycling, and the maximum metal temperatures reached under steady state, were significantly higher than those observed on the ½ inch diameter pins, when tested at equivalent gas temperatures and mass flow rates of hot gas. For instance, at a gas temperature of 1400°C, with primary and secondary airflows adjusted to give a gas velocity of Mach 0.45, less than 20 seconds were needed for ¼ inch pins to reach their maximum steady state temperatures, as shown in



(a)



(b)

**Figure 10** Profiles of steady state pin (bare) surface temperatures for (a) ½ inch diameter pins, and (b) ¼ inch diameter pins, measured at different gas temperatures and gas velocities.

T <sub>gas</sub> °C	Mach #	T <sub>surface</sub> (max)	T <sub>core</sub> (bare)	T <sub>core</sub> (coated)	ΔT (bare)	ΔT (coated)
1300	0.2	989	996	999	7	10
1400	0.22	1031	1048	1067	17	36
1500	0.22	1097	1122	1146	25	49

**Table 1** Comparison of surface temperatures, axial temperatures and differences between the two for bare and coated ½ inch pins exposed to different gas temperatures and velocities.

**Figure 9.** This compares with more than 80 seconds for ½ inch pins, tested at a higher gas temperature of 1500°C, and the same primary and secondary air flows, **Figure 7**. When both types of pins were heated in a 1400°C gas jet, the maximum steady state temperature of ¼ inch diameter pins was of the order of 1100°C, whereas it was only 1040°C for ½ inch pins. This is shown in **Figure 10** which compares the surface temperatures of ¼ inch and ½ inch diameter bare pins measured at different axial positions along their lengths, over a broad range of gas temperatures and velocities (i.e. under different ratios of primary and secondary gas pressures). The differences in temperature at equivalent mass flow rates of hot gas can be ascribed to the higher velocities that were achieved with the smaller exhaust nozzle used with ¼ inch pins, typically Mach 0.45 for ¼ inch pins vs. Mach 0.22 for ½ inch pins. The temperature gradients along the length of both types of pin were, however, qualitatively similar.

These temperature gradients simulate those present on actual engine parts and can be adjusted to meet specific test requirements by varying pin length or pin position within the hot gas jet. At any given gas temperature and velocity, minimizing the length of the free end of a pin extending outside the gas jet, will increase maximum pin

temperature, owing to decreased heat losses from the free end. Conversely, increasing the pin length will result in steeper longitudinal thermal gradients. These gradients can be used to advantage, and their shape optimized, to study the combined effects of thermal fatigue, gas erosion and hot corrosion of ceramic overlays and bond coats. With corrosive contaminants (sulfur in fuel plus atomized sea-salt solution in combustor air) added to the hot gas jet, those regions of the pins exposed to surface temperatures between 700°C to 900°C may suffer fluxing of the ceramic oxide overlays leading to breakdown of the TBC system. The contaminants may also penetrate along thermally induced cracks and attack the bond coat. These forms of hot corrosion could affect the regions of coated components where temperature drop below 900°C, in engines operating in marine environment. The burner rig test is an ideal tool to study the susceptibility of different TBC systems to this form of attack, and its interactions with other forms of thermally driven damage, should be investigated.

For durability assessment of coatings, it may be preferable to use ¼ inch rather than ½ inch diameter pins, because in addition to being more severely thermally shocked, the ¼ inch pins will accumulate more time at maximum temperature. Thus, over the same number of thermal cycles the bond coat on a ¼ inch pin will be oxidized more than on a ½ inch diameter pin. Accumulation of oxidation damage, can be life limiting in many applications (8-10) and is more easily simulated with ¼ inch diameter pins.

### 3.2 Damage Accumulation

The first sign of damage incurred by the TBC's during thermal cycling was in the form of a network of cracks developed over regions of both the ¼ and ½ inch pins

exposed to the hot gases. The cracked surface of an EBPVD coating on a 1/4 inch pin, after some thermal cycling had been applied, is shown in **Figure 11**.

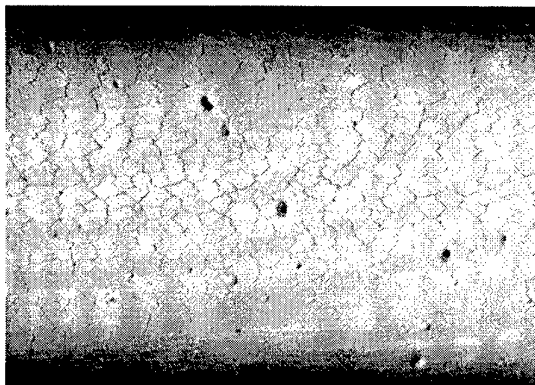


**Figure 11** Network of surface cracks formed on EBPVD TBC's soon after initiation of thermal cycling in burner rig.

The cracks in this instance penetrate right down to the bond coat, as revealed in **Figure 12**. A thin oxide layer has formed at the ceramic bond coat interface, where delamination occurred. Networks of cracks were also observed in plasma sprayed coatings. The density of cracks and their morphology depended on processing conditions and the degree of cracking was usually more severe in thicker coatings. Cracks were present even in as-deposited APS coatings, when the ceramic layer was thick (300-400  $\mu\text{m}$ ).

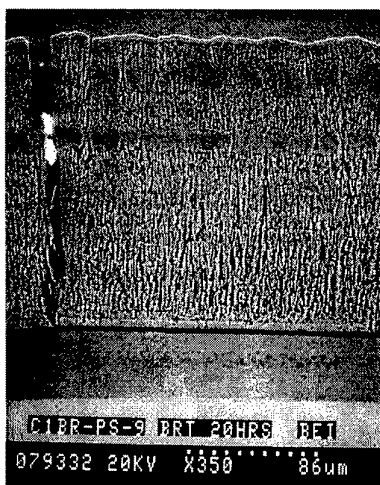


**Figure 12** Metallographic cross-section through EBPVD TBC showing transverse crack through coating penetrating all the way down to the bond coat.

Ablation from the surface of the TBC's due to erosive action of the high velocity hot gases was also observed on all the coatings examined. In the latter stages of the tests, most of the TBC's experienced spalling, or delamination, of their ceramic topcoats. The number of cycles to

spalling initiation varied with the deposition method, and even more significantly, with processing conditions for each of the deposition methods. Some coatings from all four forms of TBC's investigated (EBPVD, APS, VPS/APS and VPS) were found to survive temperatures up to 1500°C for several hundred cycles, without spalling. A series of APS TBC's, after rig testing are shown in **Figure 13**. The 1.2 mm thick calcia based coating, (pin (a) in **Figure 13**), shows no evidence of spalling, whereas the zirconia based TBC's (all about 300  $\mu\text{m}$  thick, pins (b) to (f),) exhibit varying degrees of delamination.

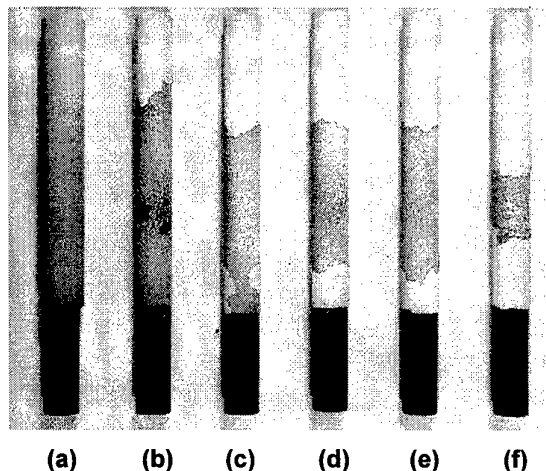


**Figure 13** Conditions of a series of APS coated 1/2 inch pins at the end of burner rig testing, involving 2150 cycles at temperatures up to 1500°C; (a) 1.2 mm thick calcia-based TBC; (b) to (f) zirconia-based TBC's applied under different processing conditions.

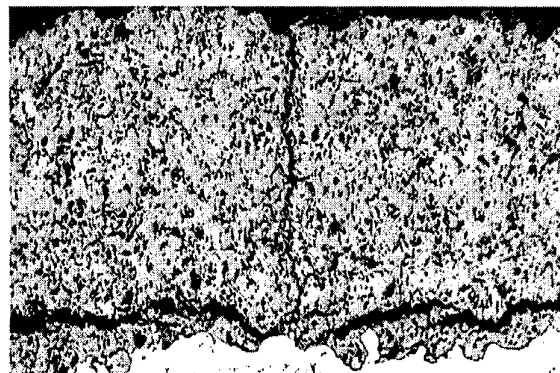


**Figure 14** Micrographs illustrating onset of failure mechanism in zirconia based APS TBC, by cracking above the interface with the bond coat.

A thin layer of ceramic coat remained attached to the surface of the hottest sections of the zirconia pins. This is due to spalling occurring in these APS coatings by propagation and linking of cracks, about 30  $\mu\text{m}$  above the

surface of the bond coat, as shown in **Figure 14**. The vertical cracks may relieve the stresses at the interface, thereby reducing the driving force for delamination. One of the pins, (b) in **Figure 13**, shows evidence of bond coat oxidation, where the ceramic topcoat has been entirely eroded away by the hot gases. These observations are generally consistent with expected modes of failure for APS coatings (8-10).

### 3.3 Damage Monitoring and Quantification

#### Weight Change Measurements

Changes in the weight of some coated  $\frac{1}{2}$  inch pins, measured over 1150 thermal cycles, are presented in **Figure 15**. The weight losses observed for all the TBC's are due to gas-induced ablation and spalling of the topcoats, during the test. The thick APS calcia-based coating appeared to have incurred the least damage in this test, while the performance of APS zirconia-based coatings varied greatly with processing conditions. The relationships between processing conditions, microstructures and properties of APS coatings are being investigated at NRC and the results will be published elsewhere (11,12).

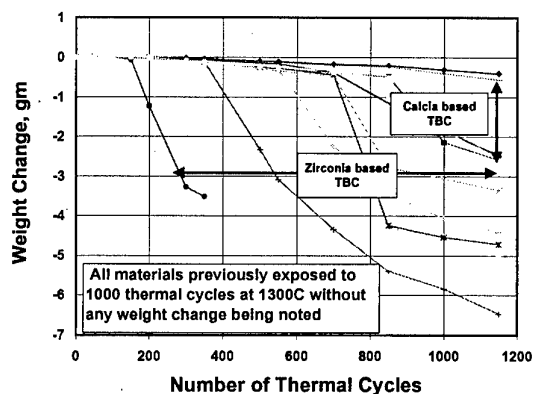


**Figure 15** Changes in mass of a series of APS coated  $\frac{1}{2}$  inch pins as a function of number of thermal cycles over a test 100 cycles at 1350°C followed by 1050 cycles at 1500°C.

Changes in the weight of some coated  $\frac{1}{4}$  inch pins processed by EBPVD, VPS (bond)/APS (ceramic) and VPS are presented in **Figure 16**. All coatings experienced weight gains at the onset of testing. This is from oxidation of the bond coats and, possibly absorption of oxygen by the substoichiometric zirconia of the VPS coatings. Because the  $\frac{1}{4}$  inch pins spent more time at the maximum gas temperature, as compared to  $\frac{1}{2}$  inch pins, (see **Figures 7 and 9** for comparison), there was more time available for their metallic bond coats to oxidize, in the course of the test. This was followed by weight loss from ablation and spalling of the ceramic topcoats, until the temperature was raised from 1200°C to 1300°C and higher, beyond which the weights increased again. These

trends are due to the rate of bond coat oxidation increasing with temperature.

The data shown in **Figure 16** also reveal that processing conditions during deposition can be adjusted to achieve improved performance with VPS coatings. The optimized VPS coating showed minimum weight changes for more than 1000 cycles at gas temperatures up to 1400°C, indicative of good resistance to ablation and spalling. However, it spalled off rapidly after the temperature was raised to 1500°C, as did the APS coatings.

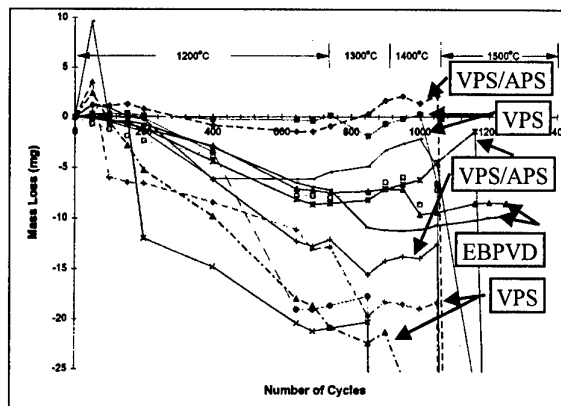


**Figure 16** Changes in the mass of a series of EBPVD, APS and VPS coatings applied to  $\frac{1}{4}$  inch pins as a function of number of rig thermal cycles. The thermal cycling schedule is shown in the figure

Only the EBPVD coating survived the entire duration of the thermal cycling at 1500°C, because of the higher strain tolerance of its columnar microstructure. The apparent shortcoming of APS coatings should be viewed with caution, however, because the test conditions were not entirely representative of service conditions. The stresses within the coatings, caused by the difference in thermal expansion between the coatings and substrates were much larger in pins than those expected to prevail in actual service parts, which are cooled by internal air flow. The internal metal temperatures of the uncooled pins were actually greater than the surface temperatures, by up to 50°C at the centre of the pins under steady state conditions, as seen from **Table 1**. Under these conditions, the ceramic/metallic bond coat interface would be subjected to very large shear stresses conducive to accelerated spalling, as observed experimentally. Thus the coatings on pins may have faced conditions that were too severe, possibly representing an extreme limiting case for plasma sprayed coatings. Using internally cooled pins and ensuring that adequate time is spent at maximum temperature during thermal cycling, to promote bond coat oxidation as experienced in service, would provide a more realistic testing environment and possibly different TBC ranking. Work is underway at IAR to address this issue.

### Heating Rates Measurements

The maximum heating rates experienced by coated  $\frac{1}{2}$  pins, as measured by thermocouples located inside the pin's axial blind holes, are plotted in Figure 17 as a function of the number of thermal cycles. Each data point in Figure 17 corresponds to the maximum slope of the rising portions of the temperature/time curves obtained for each of the thermal cycles, examples of which are shown in Figures 7 and 8. There are several features in Figure 17 that warrant comment. Firstly, the discontinuities in the data arise from interruptions in the test sequence required to weigh the pins, following blocks of 5, 50 or 150 thermal cycles. The initial sharp drop in heating rates at the onset of each block is due to the pins being at room temperature at the onset of the first cycle in a block, and at greater than room temperature for subsequent cycles, because the pins do not cool down fully to room temperature at the end of a cycle (see Figure 7).

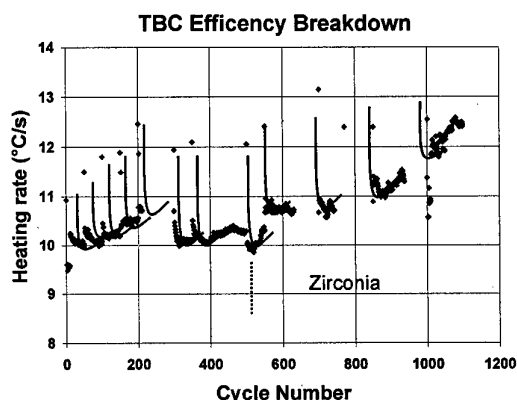


**Figure 17** Changes in heating rates of a  $\frac{1}{2}$  pin coated with zirconia as function of number of thermal cycles applied to the pin, showing change in heat transfer characteristics of coated system.

As the temperature at the start of a cycle increases, the apparent heating rate inside the pin decreases. It takes several cycles for heating rates to become stable because of the complex heat transfer transients affecting the pins and their supporting carousel. Secondly, the general upward trend in the data, observed within each block and from block to block across the plot, may be viewed as an indication of the breakdown in thermal protection efficiency of the TBC system. As the coating ablates, or spalls off the test pin, the internal heating rates increase, as expected, because heat is transferred more quickly into the pins. Thirdly, there appears to be a threshold number of applied thermal cycles beyond which the increase in heating rate accelerates sharply. This threshold is of the order of 500 cycles, and corresponds to the point beyond which significant weight loss was recorded for this coating, as shown in Figure 15. Thus, monitoring the internal temperatures of coated pins could be used as an alternative method for the quantification of damage accumulation in TBC's. However, further work is needed to develop this technique. The type K thermocouples that

were used in the present experiments tended to oxidize and fail by thermal fatigue. Type S thermocouples should perform better in this application and ought to be tested. Also, the measurements should be made on pins that are internally cooled to better simulate the thermal gradients and levels of thermally induced stresses experienced by TBC's applied to internally cooled components.

### CONCLUSIONS

This work has shown that the modes and rates of degradation of TBC's during burner rig testing of coated solid round pins are influenced by many test parameters, besides being influenced by differences in deposition method and processing conditions.

Pins,  $\frac{1}{4}$  inch in diameter, heat up and cool down much faster than  $\frac{1}{2}$  inch pins. They also reach a higher temperature and spend more time at maximum temperature over the duration of a thermal cycle. Thus, coatings applied to  $\frac{1}{4}$  inch pins will be subjected to higher transient and steady state stresses, and their bond coat will oxidize more in the course of a test, as compared to  $\frac{1}{2}$  inch pins.

Over the steady state portion of a thermal cycle, the internal temperature of a solid pin is higher than its surface temperature. This difference is larger in a TBC coated pin than in a bare pin. High internal temperatures in coated pins cause high shear stresses near the interface between the ceramic and metallic layers of the TBC, owing to differential thermal expansion between the two media, thereby promoting delamination near this interface. Because of their highly strain tolerant columnar microstructure, EBPVD coatings generally fared better than thermally sprayed coatings under such testing conditions. Using internally cooled pins, to better simulate service conditions, would reduce the magnitude of these stresses and provide a more realistic laboratory ranking of TBC coatings.

The performance of each type of TBC examined, is a strong function of processing conditions. Analysis of damage modes arising from thermal cycling in a rig confirms that plasma sprayed coatings spall by cracking of the ceramic overlay, above the interface with the bond coat, and in the case of EBPVD coatings, by cracking within the oxide layer that builds up at the surface of the bond coat. The failure modes differ because of differences in the degree of strain tolerance of the two types of coatings.

### ACKNOWLEDGEMENTS

This work was performed at IAR and IMI under projects involving collaboration with a number of companies (Cametoid Advanced Technologies Inc., Pyrogenesis Inc., Orenda Aerospace Corporation, SURFTEC Industrial Consortium), with financial support from the Chief Research and Development of the Department of National Defense. Special thanks are due to Mr. Ray Dainty of IAR, for his support in SEM analysis.



## REFERENCES

1. R.A. Miller, "Thermal Barrier Coatings for Aircraft Engines", Proc. Thermal Barrier Coating Workshop, NASA Lewis Research Center, Cleveland, Ohio, March 1995, NASA Conf. Pub. 3312, 1995, pp17-34.
2. P.E. Hodge, S. Stecura, M.A. Gedwill, I. Zaplatynski and S.R. Levine, "Thermal Barrier Coatings", J. Materials for Energy Systems, Vol. 1, 1980, pp. 47-58.
3. H. Herman and C.C. Berndt, "Plasma Spray Processing of TBC's", Proc. Thermal Barrier Coating Workshop, NASA Lewis Research Center, Cleveland, Ohio, March 1995, NASA Conf. Pub. 3312, 1995, pp. 127-134.
4. D.V. Rigney, R. Viguie and D.J. Wortman, "PVD Thermal Barrier Coating Applications and Process Developments for Aircraft Engines", Proc. Thermal Barrier Coating Workshop, NASA Lewis Research Center, Cleveland, Ohio, March 1995, NASA Conf. Pub. 3312, 1995, pp. 135-149.
5. S. Durham, S. Manning Maier, D.K. Gupta and K.D. Scheffler, "Ceramic Thermal Barrier Coatings", in Advances in High Temperature Structural Materials and Protective Coatings, Eds. A.K. Koul et al, Pub. NRC, Canada, Ottawa, 1994, pp.226-236
6. Anonymous, "Vacuum plasma spray coating protects turbine blades", a note in Advanced Materials and Processes, March 1997, p. 12.
7. F. Jamarani, M. Korotkin, R.V. Lang, M.F. Ouelette, K.L. Yan, R.W. Bertram and V.R. Parameswaran, "Compositionally Graded TBC for High Temperature Aero Gas Turbine Components", Surface and Coatings Technology, 54/55, 1992, pp. 58-63.
8. M. Gell, "Application Opportunities for Nanostructured Materials and Coatings", Materials Science and Engineering, Vol. A204, 1995, pp. 246-251.
9. J. H. Wood and E.H. Goldman. "Protective Coatings" in *Superalloys-II*, Eds. C.T. Sims et al, Pub. John Wiley and Sons, 1987, pp. 359-384.
10. W.J. Brindley and R.A. Miller, "Thermal Barrier Coatings Evaluation Needs", Pres. at Conf. on *NDE of Modern Ceramics*, Columbus, OH, 9-12 July 1990, Am. Cer. Soc. & Am. Soc. for NDT, 1990, pp70-76 (NASA Report, NASA-TM-103708, 1990).
11. M. Prystay, P. Gougeon, C. Moreau, J-P. Immarigeon and V.R. Parameswaran, "Microstructure and Burner Rig Evaluation of Calcia Silica Thermal Barrier Coatings", Proceedings ITSC 98, Nice, France, May 1998.
12. P. Gougeon, M. Prystay, C. Moreau, J-P. Immarigeon and V.R. Parameswaran, "Influence of Plasma Spraying Conditions on In-Flight Characteristics of Zirconia Hollow Sphere Particles and Properties of Resulting TBC's", Proceedings ITSC 98, Nice, France, May 1998.
13. R.R. Dills and F.S. Follansbee, Corrosion, NACE, 1977, 33(11), 385.
14. A.K. Gupta, T. Terada, P.C. Patnaik and J-P. Immarigeon, "Evaluation of High Temperature Protective Coatings for Gas Turbine Engines Under Simulated Service Conditions", Proc. AGARD-NATO Conf. on High Temperature Surface Interactions, Ottawa, May 1989, AGARD-CP-461, 1989, pp. 14-1/14-31.
15. A.K. Gupta, J-P. Immarigeon and P. C. Patnaik, "A Review of Factors Controlling the Gas Turbine Hot Section Environment and their Influence on Hot Salt Corrosion Test Methods", High Temp. Technology, Vol. 7, No. 4, November 1989, pp. 173-186.
16. S. Gendron, N.J. Marchand, C. Korn, J-P. Immarigeon and J.J. Kacprzyzyski, "An Experimental Investigation of Convective Heat Transfer at the Leading Edge of a Turbine Airfoil", Int. Gas Turbine and Aeroengine Congress and Exposition, Cologne, Germany, June 1992, Publication ASME 92-GT-248, 1992

# Graded Design of EB-PVD Thermal Barrier Coating Systems

U. Schulz, T. Krell, U. Leushake, M. Peters

DLR - German Aerospace Research Establishment, Institute of Materials Research,  
D-51147 Cologne, Germany.

## Summary

The most durable TBCs (Thermal Barrier Coatings) are yttria partially stabilized zirconia coatings which are applied by EB-PVD (Electron Beam Physical Vapor Deposition) on metallic bond coats. The EB-PVD process offers the advantage of a superior strain and thermoshock tolerant behavior of the coatings due to their columnar microstructure. The interface between ceramic and metal is the weakest link in this system. Spallation occurs in that area which is mainly attributed to oxidation of the bondcoat and to thermomechanical stresses of this two-layered coating.

The concept of graded materials is one approach to lower both stresses and also oxidation of the bondcoat. This concept is presented in detail with special emphasis on chemically graded alumina-zirconia TBCs. Microstructures and phases of alumina, alumina-zirconia, and of graded coatings deposited by EB-PVD are evaluated. Mainly alumina undergoes phase transformation in the mixed and graded layers from the amorphous state to the desired  $\alpha$ -Al<sub>2</sub>O<sub>3</sub>. Finite element modeling was performed to study the influence of coating thickness and composition on heat flux and stress distribution.

## 1. Introduction

Thermal barrier coatings (TBCs) are increasingly used in gas turbines for aircraft engines and for power generation. They must withstand for a long time heavy thermal cyclic loads under oxidizing conditions. The application range for TBCs in gas turbines includes insulation of the combustion chamber and protection of turbine blades and vanes. Major advantages and key factors that rule the lifetime of TBC systems have been described elsewhere /1, 2/.

Development of gas turbines clearly aims for increased gas turbine inlet temperatures (TIT) passing well beyond 1600°C. Future TBC applications as integral design elements of highly loaded engine parts need a higher temperature capability of the TBC, a better bonding of the ceramic on the metal and also a lower oxidation rate of the bond coat. Thermomechanical stresses caused by this high TIT can only be maintained by usage of uneconomically extensive cooling techniques or by the introduction of electron-beam physical vapor deposited TBCs /3/. The latest generation of TBCs offers significantly extended lifetimes compared to plasma-sprayed TBCs, smooth aerodynamically attractive surfaces and only minor cooling hole closure. The superiority

of EB-PVD TBCs is due to their columnar microstructure. Their processing, microstructure, and lifetime in service is often described in literature /1, 4, 5, 6, 7, 8/. But there is still a lack of detailed understanding of failure mechanisms and damage accumulation on a microscopic scale that can be combined with stress modeling, thus enabling a phenomenological based safe life prediction under the wide variety of application conditions.

State-of-the-art TBCs for turbine blades consist of an oxidation protective bond coat (BC) (typically aluminides or MCrAlY, M=Ni, Co), and a thermally insulating yttria partially stabilized zirconia (YPSZ) top layer. This multilayer system is not thermally stable under long time exposure at elevated temperatures. A thermally grown oxide scale (TGO) is formed by oxidation at the BC/zirconia interface. This scale consists mainly of alumina formed by selective oxidation of aluminum from the bond coat but it can vary from this ideal constitution particularly in the early stages of oxidation /9, 10/. The TGO and the interfaces to BC and TBC are the crucial locations of the TBC system that determine in most cases the lifetime. In addition, interdiffusion between the bond coat and substrate leads to microstructural changes in the BC. Another phenomena is the reduction of thermal shock resistance of the zirconia layer due to sintering. Having these phenomena in mind, several potential areas for the application of the Functionally Graded Materials (FGM) concept for a TBC system can be suggested.

## 2. Graded Thermal Barrier Coating Systems

Graded materials are characterized by a one or more dimensional continuous or stepwise change of material properties. The change is designed to achieve optimum materials behavior for a given loading situation. FGMs differ from bulk materials and composites by their macro- and microscopic inhomogeneity. To lower residual stresses, coatings can be optimized for the case of fabrication and/or application conditions. Both cases may demand different approaches. The design of graded materials is mainly optimized by numerical or analytical calculations. By applying the FGM concept, changes in the magnitude or location of the critical local stresses can be achieved, although not all stress components are reduced in every case. To improve performance it is often only necessary to modify the stresses which cause failure.

For TBCs a continuously graded layer between bond coat and zirconia would lower the stresses at the interface substantially. Those systems have been described very early for plasma spraying /11/ and for EB-PVD too /12/, but more recently investigations have indicated that they are limited in their potential application. Graded bondcoat-zirconia layers showed improved performance under pure thermal cycling conditions but they suffer from rapid oxidation of BC particles in the zirconia due to their high surface area under oxidizing conditions. This results in a dramatic performance reduction compared to multilayered TBCs /13, 14, 15, 16/. A possible application field for this kind of graded metal-ceramic coating would be limited to non-oxidizing conditions or short time exposure, e.g. reentry. But for turbine engines these graded coatings are not useful.

In 1995 a joint research program on functionally graded materials, funded by the Deutsche Forschungsgemeinschaft (DFG), was started in Germany. Part of this program is the investigation of graded TBCs. It is intended to combine the thermal insulation potential of zirconia with the low oxygen diffusivity of alumina or similar materials. Some results in literature indicate that the introduction of an alumina interlayer between bondcoat and ceramic offers a potential solution to some major problems of TBCs by incorporating a layer with reduced oxygen diffusivity, thereby reducing the TGO growth rate and prolonging cyclic lifetime /17, 18, 19/. These alumina layers have been fabricated by CVD and sputtering techniques. Furthermore, adhesion of EB-PVD PYSZ TBCs is known to be favored on  $\alpha$ -alumina compared to adhesion on MCrAlY /10/.

The large mismatch in coefficient of thermal expansion (CTE) between discrete layers within a multicomponent TBC system results in residual stresses that can cause coating failure. Obviously, fully dense alumina layers

can not be maintained under thermocyclic loading due to the CTE mismatch. The advantage of a continuously graded coating compared to a single alumina interlayer is the avoidance of a sharp discontinuity in properties and the associated stress concentrations. Starting with alumina on top of the bondcoat a continuous increase of the PYSZ content is envisaged to benefit from the FGM concept. In addition, by controlled oxide/TBC interface formation, better adhesion and reduced thermal stresses may be realized. Among the large variety of alumina polymorphs,  $\alpha$ - $\text{Al}_2\text{O}_3$  is the most desirable phase because of its low oxygen diffusivity and high thermal stability at the application temperature range. Therefore, one target is to get  $\alpha$ -alumina. All ceramic layers within the graded TBC are produced by PVD techniques, preferentially by high rate EB-PVD.

Another possibility to apply the FGM concept to TBCs would be a graded layer between metallic bondcoat and an alumina interlayer. This approach would harden the bond coat outer region and therefore lower the creep rate of MCrAlY. Furthermore, improved adhesion of the alumina is expected but some processing problems will occur too.

Fig. 1 shows the state-of-the art two-layer coating compared to the new proposed graded ceramic design. First results of the work carried out on this graded TBC system have been published previously /20, 21, 22/.

## 2.1 Processing of graded TBCs

In order to combine the advantages of columnar and graded structures several issues must be incorporated. The vaporization during EB-PVD depends on the vapor pressure of each compound which makes it difficult to simultaneously vaporize materials with large differences in vapor pressure (e.g.  $\text{ZrO}_2$  and  $\text{CeO}_2$ ). Using a single source coater only certain chemical gradients can be produced, although some types of gradients have been successfully produced, e.g. density graded PYSZ and chemically graded bondcoats /23, 24/. Another attempt is the use of a special mixture of aluminum, alumina, and zirconia as a starting composition in form of pressed tablets on top of YPSZ ingots to get a graded structure /25/. Controlled chemically graded coatings can be fabricated by vaporizing from multiple sources utilizing one or more electron guns.

To develop the graded TBC system described above several problems had to be solved in advance:

- evaporation material must be in a condition that allows continuous evaporation
- influence of evaporation conditions on microstructure of single alumina layers must be evaluated
- dual source evaporation of alumina and zirconia to get mixtures of both species must be established.

Finally, grading from alumina to YPSZ was carried out.

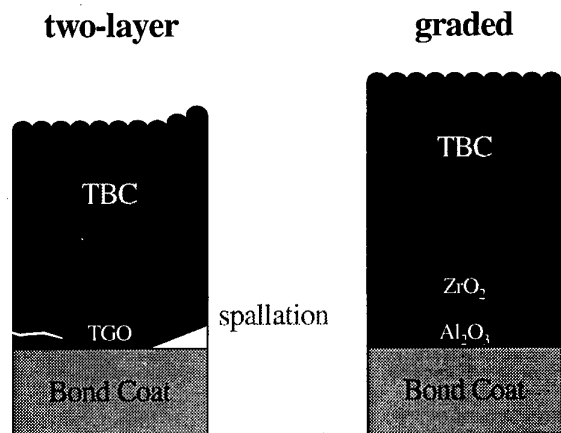


Fig. 1: Comparison of conventional and graded design of TBCs

## 2.2 Experimental procedure

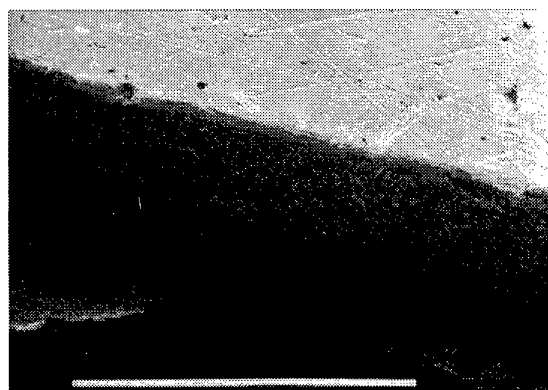
In the present study, a single gun dual source jumping electron beam coater was used (for details see /5/). It consists of chambers for loading, preheating and deposition and facilities for specimens rotation and manipulation. Ingots of 50 mm and 63 mm diameter were fed into the crucibles from bottom during evaporation in order to ensure continuous deposition. By adjusting electron beam parameters different deposition rates can be achieved for each source via independent adjustment of melting pool temperatures. Alumina films were deposited by reactive magnetron sputtering and also by reactive EB-PVD.

X-ray diffraction (XRD) was carried out with  $\text{Cu K}_\alpha$  radiation. If not noticed explicit otherwise patterns are given corrected for background and  $\text{K}_\alpha 2$ . Concentration was measured quantitatively by energy dispersive X-ray spectroscopy on polished cross sections.

## 3. Results and discussion

### 3.1. Alumina ingots

Semi-industrial or industrial size coaters use a continuous feeding system for ceramic rod source materials (ingots). They must exhibit a high thermal shock resistance to withstand the high thermal gradients associated with EB-PVD processing. Therefore, ingots generally have a relative density of about 60%. The current processing method for YPSZ ingots involves powder and material specific sintering and calcination and cannot easily be transferred to other powders or materials. An alternative method was developed that involves the use of bimodal powder mixtures and a sinterless powder metallurgical processing /21, 22, 26/. This processing route can be applied to a large variety of different powders and materials for ceramic rod fabrication, achieving suitable vaporization behavior and high thermal shock resistance at low cost.



1 mm

Fig. 2: Cross section of a thick alumina coating obtained by EB-PVD at low pressure

### 3.2. Alumina coatings

Phase content and morphology of alumina coatings, produced by PVD methods, were investigated as a function of process parameters. Chamber pressure during alumina evaporation was varied by an optional additional oxygen gas flow and by adjustment of the pumping rate in order to achieve in some experiments reactive conditions.

In the case of lower chamber pressures, extremely high ceramic deposition rates up to 60  $\mu\text{m}/\text{min}$  occurred. In Fig. 2 an example is given for a coating deposited under such conditions. It can be concluded that higher deposition rates and the associated lower chamber pressures result in relatively dense, less columnar microstructures, probably as a result of changed adatom mobility /22/.

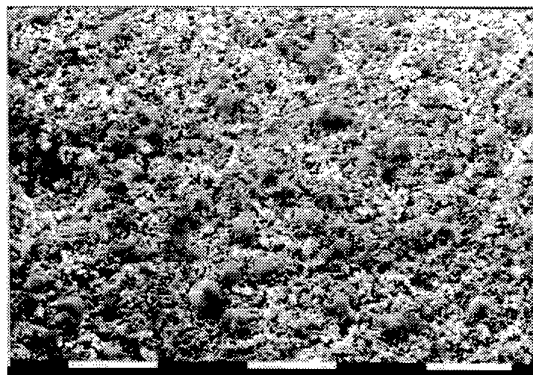
On the other hand, a 5 to 8  $\mu\text{m}$  thin alumina layer deposited by EB-PVD under reactive conditions exhibits a columnar microstructure. After annealing a tendency to sintering was observed /20/.

Thin alumina layers produced by reactive magnetron sputtering showed a rough surface which reproduces the surface of the underlying metal as it is characteristic for PVD. In Fig. 3 an example is given where the bond coat morphology is still visible because peening was omitted.

Obviously, the morphology of alumina films produced by PVD strongly depends on deposition parameters and for sputtering on the substrate surface too. Deposition rate, chamber pressure and atmosphere, film thickness, and substrate temperature are the most important parameters that rule the morphology of alumina.

In the temperature range of deposition alumina undergoes phase transformations, so that not only microstructure of the coatings but also phase formation depends on the substrate temperature. It was intended to get the most stable alpha phase of alumina.

Alumina deposition was carried out in the temperature range between 750 and 1150°C. In Fig. 4 the influence



10  $\mu\text{m}$

Fig. 3: Surface of sputtered alumina layer on top of NiCoCrAlY bondcoat

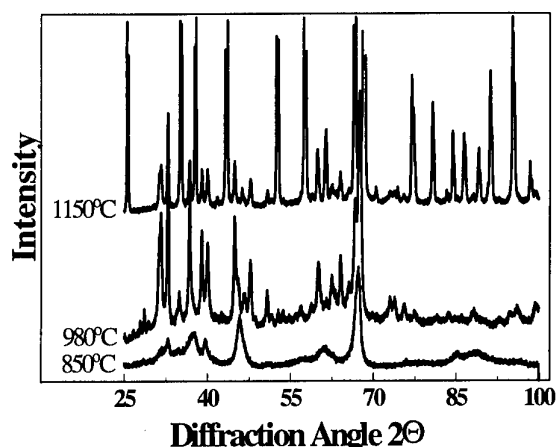


Fig. 4: XRD of EB-PVD alumina films for various deposition temperatures (not corrected)

of deposition temperature on phase formation of alumina is shown.

XRD peaks were broadened for alumina films deposited at low temperatures. This can be attributed to the presence of areas within the coating that were not fully crystallized. Coatings deposited at the highest temperature showed the presence of only the stable  $\alpha$ - $\text{Al}_2\text{O}_3$  phase. Additionally it was found that chamber pressure and deposition rate had only little influence on phase formation of alumina which is contrary to results found for the morphology.

Phase transformation was also studied after annealing in the temperature range between 1000°C and 1200°C for 1 to 9 hrs. Annealing at 1000°C had little effect on any of the coatings; only a sharpening of diffraction peaks was observed. For all coatings, transformation to  $\alpha$ - $\text{Al}_2\text{O}_3$  started upon annealing at 1100°C. Short term (1 h) annealing at 1100°C resulted in partial transformation to  $\alpha$ - $\text{Al}_2\text{O}_3$ . The higher the deposition temperature was, the lower was the tendency for phase transformation. This can be explained by the fact that the driving force for transformation (i.e. difference between coating and annealing temperature) is lower. After annealing at 1200°C for 9hrs all coatings consisted mainly of  $\alpha$ - $\text{Al}_2\text{O}_3$  with only small amounts of other phases [21, 22].

Alumina layers deposited by reactive magnetron sputtering were amorphous but they showed a rapid phase transformation behavior. Observations are in good agreement with literature data on alumina layers obtained by sputtering [27, 28] and by reactive aluminium evaporation [29].

As a consequence, alpha alumina coatings can be achieved either by in-situ deposition at elevated temperatures or by post coating annealing. Since the phase transformation driving force is proportional to the temperature difference between the coating temperature and

the annealing temperature, coatings deposited at lower temperature show faster phase transformation.

### 3.3. Mixed alumina-zirconia layers

Due to the continuous change of composition and properties within a graded alumina - PYSZ coating a direct analyses of phases is difficult. Therefore, mixtures of alumina and PYSZ were investigated. They represent individual layers of the graded ceramic.

Co-evaporation of alumina and PYSZ was carried out using the jumping-beam technique. First, vaporization parameters such as scanning pattern, e-beam focus, dwell time and vapor cloud geometry were determined for each material separately. The several mixtures of alumina/PYSZ with various amounts of the oxides were produced by dual source evaporation.

In Fig. 5 chemical composition is plotted as a function of sample position above the ingots. Experiments clearly show that dual source evaporation of two ceramics with widely differing vapor pressures and melting points is possible using the jumping-beam technique. A mixing of both ceramic vapor clouds takes place and both species condense on the substrates thereby forming mixed layers. While the portion of  $\text{Al}_2\text{O}_3$  decreases more rapidly with decreasing distance to the  $\text{ZrO}_2$ -ingot, the portion of  $\text{ZrO}_2$  rises slower and shows a flatter gradient. The zirconia content is predominant in all coatings. The reason for that is the difference of vapor pressures and evaporation behavior between  $\text{ZrO}_2$  and  $\text{Al}_2\text{O}_3$  that leads to a different geometry of the vapor clouds. Furthermore it can be assumed that the re-evaporation rate of alumina is higher than that of zirconia because of its lower melting and boiling point.

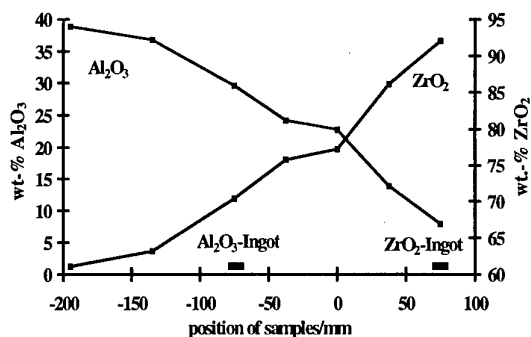


Fig. 5: Composition of mixed alumina-PYSZ layers as a function of position in the chamber

The morphology of these coatings is exemplified in Fig. 6. All coatings have a columnar microstructure, but contrary to pure PYSZ TBCs the alumina-zirconia coatings show a much more closely packed structure.

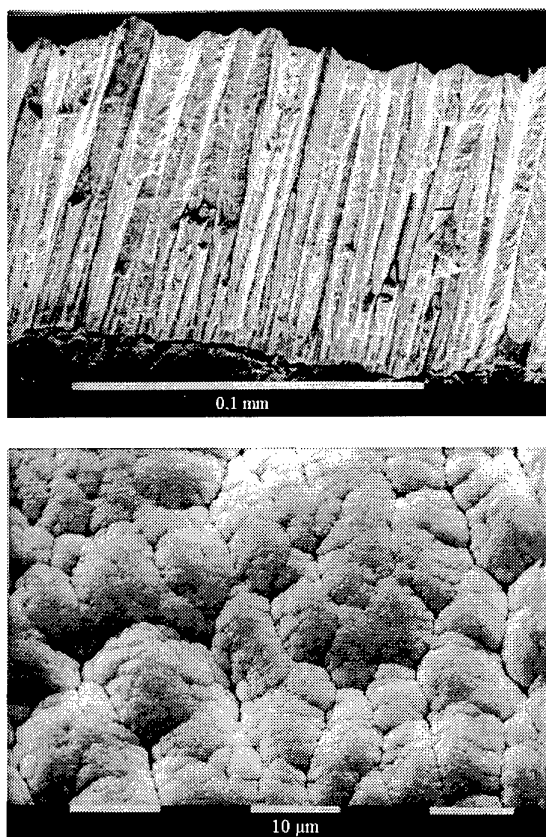


Fig. 6: SEM of mixed alumina-PYSZ layers, fractograph (above) and surface (below)

Moreover, surfaces of the columns are no flat faces with characteristic shapes as it was found for yttria and ceria stabilized zirconias /30/, but they are round shaped with cauliflower type appearance. Furthermore they possess less opened inter-columnar porosity. Even small amounts of alumina can cause these microstructural changes. Since microstructure was nearly the same for all mixtures, one can conclude that not the amount of alumina but the presence itself is sufficient for the change in morphology.

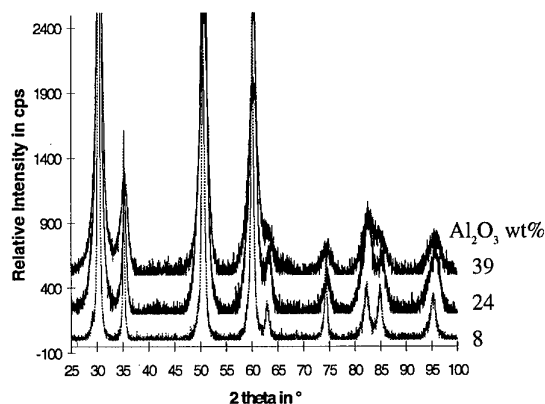


Fig. 7: XRD of EB-PVD mixed coatings from alumina and PYSZ

Results of XRD are shown in Fig. 7.

Phase analyses only reveals strongly broadened PYSZ-peaks which are getting sharper with increasing content of zirconia. No alumina peaks were found in the as coated condition. This suggests that alumina only exists as an amorphous phase, but it is not clear where this phase is located beside the zirconia crystals. Additional investigations by transmission electron microscopy are under way in order to clarify this question.

Because of the broadened peaks zirconia must be very fine grained which is contrary to pure PYSZ TBCs where each column is nearly single crystalline. A first calculation of the grain size based on zirconia peak half-width gave evidence for 5-15  $\mu\text{m}$  grains, depending on the alumina content. Thermal conductivity and other properties of this fine-grained two-phase structure may significantly differ from values that were calculated using simple rules of mixture. Since lattice parameters of PYSZ are only slightly changed by the addition of alumina one can conclude that only small amounts of alumina were incorporated into the tetragonal lattice of the  $t'$  phase of PYSZ.

### 3.4. Graded alumina-PYSZ thermal barrier coatings

By continuously changing the evaporation rates of alumina and zirconia a change in composition over the coating thickness was achieved. Due to the different deposition conditions which are necessary to maintain suitable evaporation of alumina, zirconia and various mixtures thereof, an increase of the substrate temperature occurs with increasing zirconia content in the vapor cloud.

Initially a pure and thin alumina layer was put on top of a NiCoCrAlY bondcoat, followed by compositional graded mixed alumina - PYSZ layers. At the top side pure PYSZ was deposited. A cross-section of such a graded coating is shown in Fig. 8. The backscattered electron imaging (right part of picture) indicates a steep gradient in chemical composition between alumina and zirconia. In contrast, change of microstructure from bottom (alumina) to top (zirconia) appears not continuous.

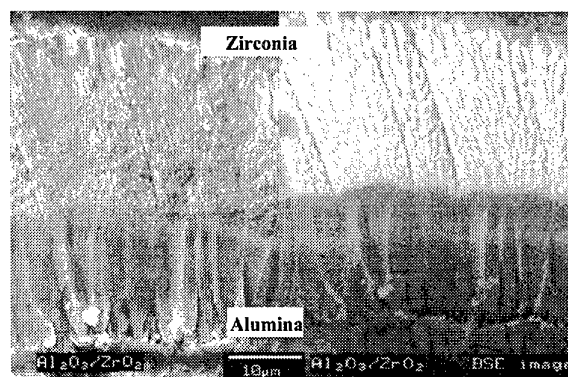


Fig. 8: Cross section of a graded alumina-PYSZ TBC

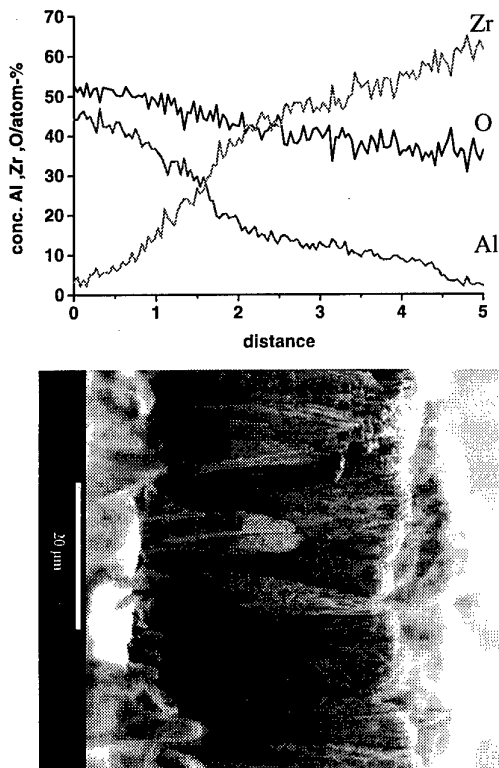


Fig. 9: Graded alumina-PYSZ coating, composition (above) and fractograph (below)

Fig. 9 evidences a continuous chemical gradient. For better visibility the graded layer is shown as a fractured cross section.

Although there is still a step in the gray-scale of the SEM picture the concentration profile shows only a slightly steeper change of concentration in this area.

Experiments have revealed that two-source evaporation can produce a distinct graded layer although only one electron-beam gun has been used. Application of jumping beam technology on ceramics requires a fast

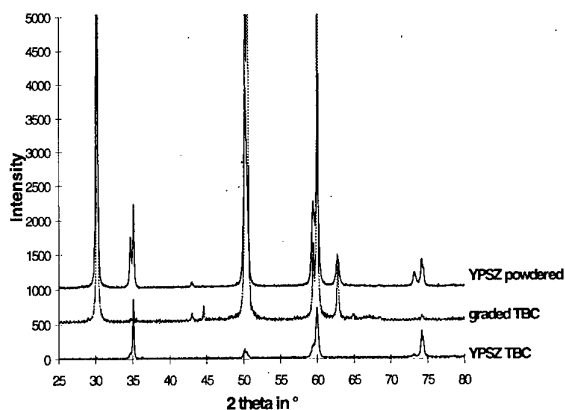


Fig. 10: XRD of different EB-PVD TBCs

beam deflection system with capability of beam scanning frequencies up to 1 kHz. It was found that adjusting the beam pattern and beam focus to the different ceramics was the key point for a reproducible evaporation behavior and also to omit spitting mainly from the alumina ingot. This task is complicated because zirconia needs approximately two to three times more energy for evaporation but beam power cannot be changed quickly during the jumping procedure.

To illustrate the problems of microstructure investigation of graded layers XRD patterns of a graded, a standard PYSZ TBC, and a powdered PYSZ TBC are compared in Fig. 10.

The absence of any alumina peaks in the graded layer must be noticed which is similar to observations on mixtures. The thin PYSZ layer on top of the graded zone additionally complicates the investigation of the FGM because of the low x-ray penetration depth in zirconia. The highly textured growth of both EB-PVD coatings can be seen but some differences in the preferred orientation can be already determined from simple diffraction patterns. While PYSZ TBCs grow primarily with {100} planes parallel to the surface /5, 31/ the graded layers possess mainly strong {220} and {113} peaks. Taking into account the results of mixed layers (Fig. 7) it is obvious that alumina additions to PYSZ lower the tendency to preferred growth of some crystallographic orientations. The fine grain size within graded layers instead of single crystalline columns in case of pure PYSZ may further contribute to the observed texture differences.

In a final step the fully ceramic graded thermal barrier coating system was produced. One important aspect to consider is the change in overall thermal conductivity of the graded layer due to the higher thermal conductivity of alumina compared to zirconia. This also depends on the compositional gradient itself, and it has to be compensated by an additional zirconia layer. Numerical and analytical computations can help to calculate the appropriate thermal fluxes and thicknesses of the individual layers. This topic will be discussed in chapter 4.

A standard PYSZ-TBC of approximately 200 μm thickness was applied on top of the graded layer in order to maintain the desired thermal conductivity of the whole system. The TBC is shown in Fig. 11.

The zirconia layer on top exhibits the desirable columnar microstructure typical for EB-PVD coatings. The graded region, however, is characterized by a coarser microstructure within the columns and a smaller column diameter. Here, spacings between columns seem to be smaller and the FGM looks more compact compared to the opened columnar PYSZ region. The temperature increase during evaporation mentioned above may have further supported occurrence of this morphology. Columns go through from the graded zone to the PYSZ top layer which is necessary for a good bonding. Micro-

structural features are in good agreement with observations on mixed layers described in chapter 3.3.

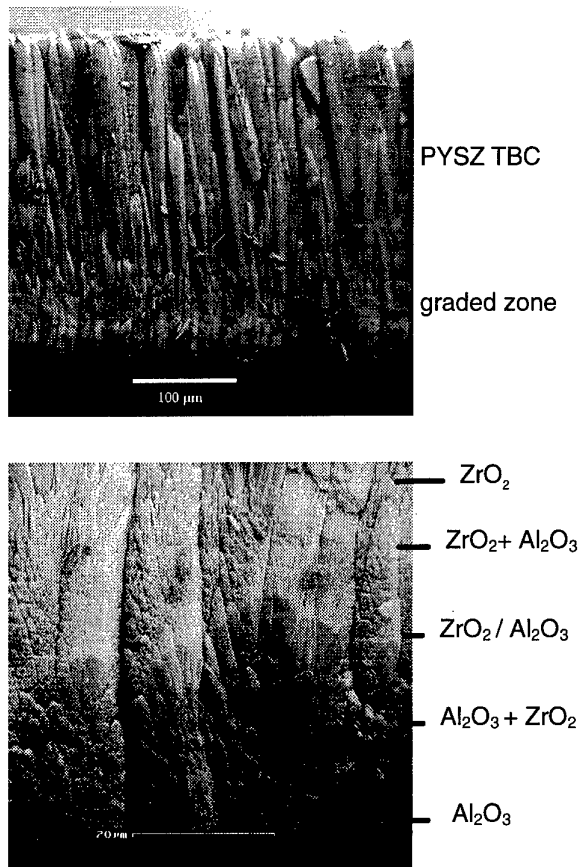


Fig. 11: Morphology of a ceramic graded EB-PVD TBC system

#### 4. Finite Element Modeling for graded TBCs

Finite Element Method (FEM) and analytical calculations provide a useful tool for an understanding of complex thermal and stress fields. The reliability of the calculations depends strongly on the used material properties and boundary conditions. Assumptions like pure linear elastic behavior or certain boundary conditions may have a substantial effect on the results. In most cases the microstructure is modeled on a macroscopic scale, since the real columnar microstructure of EB-PVD or the splashy one of plasma sprayed coatings is too complex for a microscopic model. Calculations are based on knowledge of material properties. For bulk materials, most properties are known or can be measured. For coatings, however, data availability is limited. This may cause some uncertainties about the accuracy of stress calculations and finite element modeling. The properties of composites are often estimated by different rule of mixtures according to their microstructure. The designing process of FGMs should include the calculation of thermal fields and their stresses and also residual stresses during fabrication. For a complete

calculation of the stress state effects like creep, plastic deformation, oxidation, and sintering have to be taken into account. It must contain also stresses after fabrication, in the transient stages, in the temperature field during service and after cooling down to room temperature. All these aspects described above have to be taken into account in order to draw the right conclusions from calculations.

In the following one special aspect of the design of graded TBCs will be explained in detail.

The designing process is based on a parametric variation of a chosen grading function, which describes the change in chemical composition along the coating thickness. Widely used is a simple power law function:

$$c(x) = \left( \frac{d}{h} \right)^p = x^p \quad (1)$$

where  $c$  is the concentration,  $d$  the distance to the interface or surface,  $h$  the coating thickness,  $x$  the normalized height and  $p$  the profile parameter. By variation of the profile parameter  $p$  different chemical profiles are defined and according to the local composition and microstructure the local material properties can be set. A widely used approach is that the grading function also directly describes the variation of material properties.

Variation of the profile parameter  $p$  leads to different stress situations and the minimization of the critical stress component responsible for failure can be defined as an optimum. Variation of the grading function also affects the FGMs overall thermal conductivity and therefore the thermal field. In case of a constant coating thickness and of boundary conditions that are given by fixed surface temperatures the heat flux depends on the profile parameter. If the boundary conditions are set different the maximum temperature of the metal may exceed a certain value. These variations complicate the comparison of calculated stress fields and the design process has to be extended to take this effect into account. The variation of coating thickness itself and the corrected thermal boundary conditions affect the stress distribution in the graded system.

Thermal conductivity of alumina is substantially higher than that of zirconia and therefore the thickness of the graded coating has to be increased. The increase can be calculated by defining an effective thermal resistivity  $R$ :

$$R^* = \int_0^1 \frac{1}{\lambda(x)} dx \quad (2)$$

with  $x$  the normalized height,  $\lambda(x)$  the local thermal conductivity. In combination with different rules of mixtures for the thermal conductivity of composites and the grading function (1) the effective thermal resistivity  $R^*$  can be calculated either analytically or numerically.

Fig. 12 shows the effect of the profile parameter  $p$  on the effective thermal resistivity. These curves can be used to estimate coating thicknesses of same heat flux. To meet



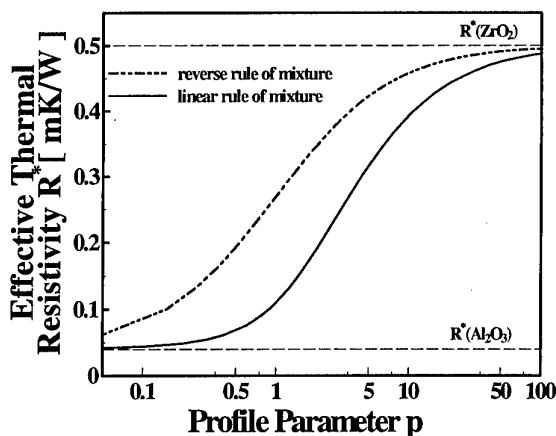
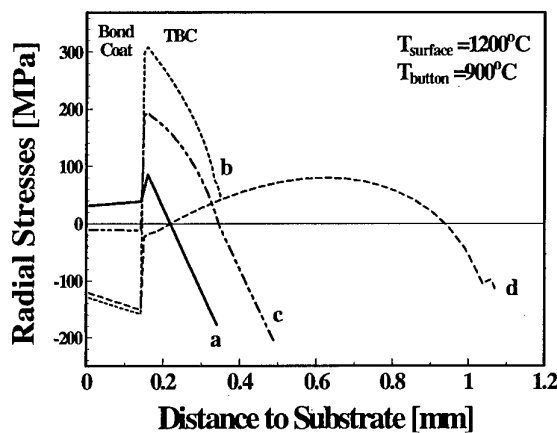


Fig. 12: Effective thermal resistivity for different rules of mixtures and profile parameters

this requirement, thickness has to be increased by a factor of 4.6 in case of a linear graded layer compared to pure PYSZ. Increase of coating thickness is limited to a certain level for aero engines. Therefore application of an additional zirconia layer on top of the graded layer is preferred to get same heat fluxes.

For a loading situation similar to a turbine blade stresses of different coating systems have been calculated (Fig. 13). In a biaxial stress state the radial stresses of an infinite plate have been calculated assuming linear elastic behavior /32. The model involves a 1mm thick superalloy substrate that possesses a NiCoCrAlY bondcoat of 150  $\mu\text{m}$  and the TBC on top. All material properties were assumed to follow the linear rule of mixture and to be not temperature dependent which causes only little



curve	ZrO <sub>2</sub> $\mu\text{m}$	FGM $\mu\text{m}$	heat flux $\text{MW/m}^2$
a	200	0	2
b	0	200	4.2
c	150	200	2
d	0	920	2

Fig. 13: Effect of corrected coating thickness on stress distribution

deviations because of small temperature gradients.

Compared to a non-graded TBC of 200  $\mu\text{m}$  ZrO<sub>2</sub> (curve a) the heat flux of a linear graded coating with the same thickness (curve b) is more than twice as high. In this case the graded layer shows higher interfacial tensile stress, which should decrease performance. Based on (1) and (2) the overall thickness of the graded layer was increased to same heat flux conditions (curve d), resulting in the lowest compressive interface stresses in the ceramic but in a dramatic higher thickness too. Alternatively, a 150  $\mu\text{m}$  thick zirconia layer was applied on top of a 200  $\mu\text{m}$  thick graded layer (curve c), resulting in the same heat flux as the conventional system. Stresses in the bondcoat are much lower than for all other systems, but interfacial stresses are higher compared to a and d. From these examples one can see that the grading profile significantly influences the stress situation. For optimization, knowledge of critical stresses that are responsible for failure is essential. In case of coating thickness of same heat flux the FGM concept offers a potential for improvement of coating performance.

## 5. Conclusions

The potential of chemically graded thermal barrier coatings to improve lifetime and reliability of turbine blades was evaluated. It has been demonstrated, that graded ceramic coatings can be produced by dual source EB-PVD and jumping beam technology. Various mixtures of alumina-PYSZ as well as pure alumina and graded coatings have been produced and analyzed.

1. Morphology and phases of PVD alumina films depend on deposition parameters, mainly on deposition rate, chamber pressure and atmosphere, film thickness, and substrate temperature. Alpha alumina can be obtained either by high substrate temperatures or by post coat annealing.
2. Morphology of alumina-zirconia mixtures is more compact than that of pure YPSZ TBC but it depends to a less extend on the amount of alumina. Zirconia is very fine grained in an amorphous alumina matrix.
3. By defining an effective thermal resistivity coating thickness can be adapted to constant heat flux conditions. With a graded transition zone and with a modified coating thickness a variation of the stress field can be achieved.

Optimization of coating conditions and the design of the graded zone with respect to chemical composition profile, phases, microstructure, morphology, and optimized lifetime remains to be carried out in future research.

## ACKNOWLEDGEMENTS

The authors gratefully acknowledge technical support by J. Brien, C. Kröder, H. Mangers and H. Schurmann.. The work was partially funded by the Deutsche Forschungsgemeinschaft.

## References

- 1 Kaysser et al. AGARD this issue
- 2 M. Peters, K. Fritscher, G. Staniek, W.A. Kaysser, U. Schulz: Design and properties of thermal barrier coatings for advanced turbine engines. *Materialwissenschaft und Werkstofftechnik* 28(1997) 357-362
- 3 J.T. DeMasi-Marcin and D.K. Gupta, "Protective Coatings in the Gas Turbine Engine", *Surface and Coatings Technology* 68/69 (1994)1-9
- 4 S.M. Meier, D.M. Nissley, K.D. Sheffler, T.A. Cruse: "Thermal barrier coating life prediction model development", *ASME J. Eng. Gas Turbine Power* 114(1992) 258-263
- 5 U. Schulz, K. Fritscher, C. Leyens, M. Peters, W.A. Kaysser: Thermocyclic Behavior of Differently Stabilized and Structured EB-PVD Thermal Barrier Coatings. *Materialwissenschaft und Werkstofftechnik* 28(1997) 370-376
- 6 Schulz, U.; Fritscher, K.; Rätzer-Scheibe, H.-J.; Peters, M.; Kaysser, W.A.: Thermocyclic Behaviour of Microstructurally Modified EB-PVD Thermal Barrier Coatings. 4th International Symposium on High Temperature Corrosion and Protection of Materials. Les Embiez 20-24.5.1996
- 7 Sohn, Y.H.; Biederman, R.R.; Sisson Jr, R.D.: Microstructural development in physical vapour-deposited partially stabilized zirconia thermal barrier coatings. *Thin Solid Films* 250(1994)1-7
- 8 Maricocchi, A.; Bartz, A.; Wortman, D.J.: PVD TBC experience on GE Aircraft engines. *Proc. TBC workshop Cleveland 1995*, ed. W.J. Brindley, NASA Conf. Publication 3312 (1995) 79-89
- 9 Schmücker, M.; Fritscher, K.; Schulz, U.: Haftmechanismen in ausgewählten EB-PVD Wärmedämmschichtsystemen. *Fortschrittsberichte der DKG, Werkstoffe, Verfahren, Anwendung* 10(1995)4, 379-384
- 10 Fritscher, K.; Schmücker, M.; Leyens, C.; Schulz, U.: TEM Investigation on the Adhesion of EB-PVD Thermal Barrier Coatings. 4th International Symposium on High Temperature Corrosion and Protection of Materials. Les Embiez 20-24.5.1996
- 11 Goward, G.W.; Grey, D.A.; Krutenat, R.C.: US Patent No. 4 248 940
- 12 Jamarani, F.; Korotkin, M.; Lang, R.V.; Ouelette, M.F.; Yan, K.L.; Bertram, R.W.; Parameswaram, V.R.: Compositionally graded thermal barrier coatings for high temperature aero gas turbine components. *Surface and Coatings Technology* 54/55(1992) 58-63
- 13 Ulion, N.E.; Ruckle, D.L.: Columnar grain ceramic thermal barrier coatings on polished substrates. *European Patent EP 0044329B1*
- 14 Alaya, M.; Grathwohl, G.; Musil, J.: A comparison of thermal cycling behaviour of graded and duplex  $ZrO_2$ -thermal barrier coatings. *Proc. FGM'94*, eds. B. Ilschner et al. Lausanne (1994) 405-411
- 15 Lee, W.Y.; Stinton, D.P.; Berndt, C.C.; Erdogan, F.; Lee, Y-D.; Mutasim, Z.: Concept of functionally graded materials for advanced thermal barrier coating application. *J. Am. Ceram. Soc.* 97 (1996) 12, 3003-3012
- 16 Vincenzini, P.: Zirconia thermal barrier coatings for engine applications. *Industrial Ceramics* 10(1990)3, 113-126
- 17 Schmitt-Thomas, Kh.G.; Dietl, U.: Surface and coatings technology, 68/69 (1994) 113-115
- 18 Sun, J.H., Chang, E.; Wu, B.C.; Tsai, C.H.: The properties and performance of  $(ZrO_2-8wt\%Y_2O_3)/(chemically\ vapour-deposited\ Al_2O_3)/(Ni-22wt\%Cr-10wt\%Al-1wt\%Y)$  thermal barrier coatings. *Surface and Coatings Technology* 58(1993) 93-99
- 19 Strangman, T.E; Solfest, P.A.: Ceramic thermal barrier coating with alumina interlayer. *US Patent 5 015 502* (14.5.1991)
- 20 T. Krell, U. Schulz, M. Peters, W.A. Kaysser: Influence of various process parameters on morphology and phase content of EB-PVD thermal barrier coatings. *Poc. EUROMAT 97*, eds. L.A.J.L. Sarton and H.B. Zeedijk, Netherlands Soc. for Materials Science, Vol. 3(1997) 3/29-3/32
- 21 U. Leushake, U. Schulz, T. Krell, M. Peters, W.A. Kaysser:  $Al_2O_3$  -  $ZrO_2$  Graded Thermal Barrier Coatings by EB-PVD - Concept, Microstructure and Phase Stability. *Proc. 4th Int. Symp. on FGM'96*.
- 22 U. Leushake, T. Krell, U. Schulz, M. Peters, W.A. Kaysser: Microstructure and Phase Stability of EB-PVD Alumina and Alumina/Zirconia for Thermal Barrier Coating Application. *ICMCTF '97, Surface and Coatings Technology* (in press)
- 23 Fritscher, K.; Schulz, U.: Burner-rig performance of density-graded EB-PVD processed thermal barrier coatings. in "Ceramic Coatings" ed. K.Kokini, New York, ASME MD-Vol.44 (1993) 1-8.

---

24 Schulz, U.; Fritscher, K.; Peters, M.; Kaysser, W.A.: Processing and behavior of chemically graded EB-PVD MCrAlY bond coats. Proc. FGM 94, eds. B. Ilschner, N. Cherradi, Presses polytechniques et universitaires romandes (1995), Lausanne, 441-446

25 Movchan, B.A.: EB-PVD technology in the gas turbine industry: present and future. JOM 11(1996) 40-45

26 U. Leushake, W. Luxem, C.-J. Kröder, W.-D. Zimmermann: German patent application #A19623587.1, European patent application No. 97108972.7-2111

27 J. A. Thornton, J. Chin: Structure and Heat Treatment Characteristics of Sputter-Deposited Alumina, Ceramic Bulletin, 56 5 (1977) 504-508

28 R. F. Bunshah, R. J. Schramm: Alumina Deposition by Activated Reactive Evaporation, Thin Solid Films, 40 (1977) 211-216

29 A. L. Dragoo, J. J. Diamond: Transitions in Vapor-Deposited Alumina from 300-1200°C, Journal of The American Ceramic Society, 50, 11 (1967) 568-574

30 Schulz, U.; Fritscher, K.; Peters, M.: EB-PVD  $Y_2O_3$  and  $CeO_2/Y_2O_3$  Stabilized Zirconia Thermal Barrier Coatings - Crystal Habit and Phase Composition. Surface and Coatings Technology 82 (1996) 259-269

31 Schulz, U.; Oettel, H.; Bunk, W.: Texture of EB-PVD thermal barrier coatings under variable deposition conditions. Zeitschrift für Metallkunde 87(1996)6, 488-492

32 M. Finot, S. Suresh, Multitherm, MIT

## BOND COAT CONSIDERATIONS FOR THERMAL BARRIER COATINGS

A.M. Freborg<sup>1</sup>, B. L. Ferguson<sup>1</sup>,  
W.J. Brindley<sup>2</sup> and G. J. Petrus<sup>1</sup>

<sup>1</sup>Deformation Control Technology, Inc.  
Cleveland, Ohio USA

<sup>2</sup>NASA Lewis Research Center  
MS 24-1, 21000 Brookpark Road  
Cleveland, Ohio 44135, USA

### Abstract

Bond coat oxidation has been clearly established as a factor contributing to the failure of a TBC. However, the mechanism by which oxidation effects TBC failure has not been determined. Similarly, other bond coat properties have been cited as influencing TBC residual stresses, but neither the magnitude of the effects nor the exact mechanisms by which these properties act, and interact, have been elucidated. A finite element model was developed to evaluate residual stresses induced by thermal cycling of a typical plasma sprayed TBC system. It was found that bond coat properties of oxidation, creep, coefficient of thermal expansion (CTE) and roughness, as well as top coat creep, all strongly influence ceramic layer stresses. Roughness and CTE were found to have the strong effects in a parametric study, acting primarily as stress multipliers for other active mechanisms. A detailed examination of the time dependent properties of creep and oxidation indicates that these factors account for evolution of the residual stresses with thermal cycling. It is the combination of these effects over the lifetime of the coating that drives the generation of stresses required to initiate and propagate delamination cracks.

### Introduction

It is universally acknowledged that bond coats for plasma sprayed TBCs have a strong effect on the thermal fatigue life of the ceramic layer, but the specific mechanisms by which the bond coat influences TBC life have not been established [1, 2, 3, 4]. As an example, bond coat oxidation has been clearly linked to spallation of the ceramic top coat but the mechanism by which oxidation causes failure of the top coat has not been clearly identified [1, 4, 5]. Similarly, bond coat coefficient of thermal expansion (CTE), roughness and creep properties have been proposed to influence TBC failure, but the magnitude of the effects and the physical mechanisms by which these effects act, and interact, have not been established [1, 2, 6].

Part of the difficulty in determining which mechanisms and interactions are involved is due to the difficulty in

isolating variables in a real material system so that unambiguous results can be obtained. An alternative is to perform modeling studies to determine trends in the effects of various factors as well as determine the mechanisms that precipitate failure. There have been only a few models that have focused in this important area for TBCs. These models have examined the TBC residual stresses resulting from single cooling cycles from a stress free state [6, 7] and residual stresses during thermal cycling [8], but have all been incomplete in that some known factors were not included. The purpose of the current work was to develop a more inclusive finite element model to characterize the effects of TBC system properties, and particularly bond coat properties, on the residual stresses in TBCs. This was accomplished by adding cyclic oxidation and multiple thermal cycle capability to the previous Petrus model [8], which had already incorporated the effects of creep, CTE and roughness on TBC stresses during a single thermal cycle. As will be shown, the results of this inclusive model indicate that creep processes dominate the generation of ceramic layer stress early in the life of a TBC, oxidation dominates stress generation later in life, but that there is interaction between all the effects throughout coating life that cannot be ignored.

### 2. Methodology

This study used NIKE 2-D stress models [9] to describe a burner rig test of a 2.54 cm (1.0 in.) diameter solid Waspaloy rod coated with 0.013 cm (0.005 in.) of NiCrAlY bond coat, which was in turn coated with a "top coat" of 0.025 cm (0.010 in.) ZrO<sub>2</sub>-8wt.% Y<sub>2</sub>O<sub>3</sub> (Figure 1(a)). It was assumed that the coating was stress free after deposition and cooling to room temperature a reasonable assumption in view of the low in-plane compressive stresses (approximately 3 MPa) measured on TBCs fabricated with appropriate temperature control [10]. The model geometry was a thin axisymmetric slice of the substrate coating system, as was used previously (Figure 1(a)) [8], with a condition of generalized plane strain. Unlike the Petrus model [8], the current model used refined elements for the bond coat and top coat at the interface region to allow for growth and analysis of an oxide layer. The

geometry of the bond coat/ceramic interface was modeled as a sine wave to simulate circumferential surface roughness conditions typical for a plasma sprayed TBC (Figure 1(b).) [6, 7, 8].

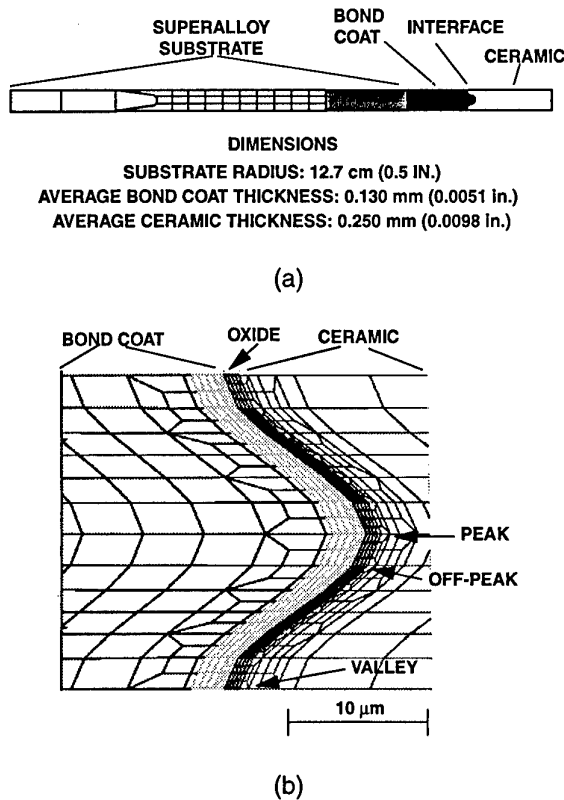


Figure 1. Finite element mesh geometry for TBC oxidation model showing (a) overall geometry of axisymmetric slice and (b) detail view of the interface region.

The thermal cycle profile for the model was based on the actual burner rig profile (Figure 2) [8]. The model included the temperature gradients that naturally occur during heating and cooling. It should be noted that the temperature gradient was approximately zero at the hold temperature since the modeled specimens were not internally cooled.

Creep behavior was defined using a temperature dependent power-law creep model, with creep behavior as defined in the literature [2, 11, 12]. Further properties information required for the model included the temperature dependent properties of bulk modulus, shear modulus and coefficient of thermal expansion, and were derived from the literature [2, 11, 12, 13].

The two levels for oxidation were defined as a low of

no oxidation and a high equal to the oxidation rate found empirically for the alumina former NiCoCrAlY [11]. The oxide scale was assumed to be of uniform

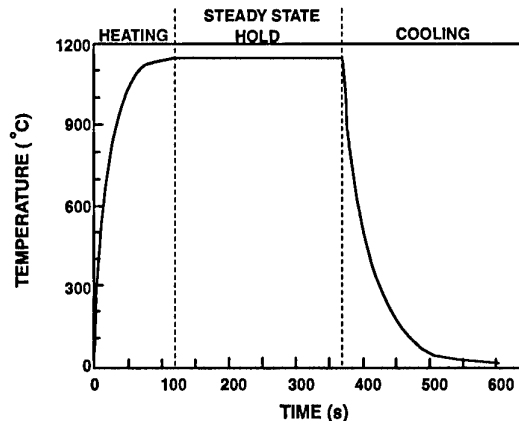


Figure 2. Measured burner rig test thermal profile used in the FEM model.

thickness across the entire interface and was further assumed to be composed entirely of alumina. The properties used for the CTE and modulus of the scale were those for a sintered 95% dense alumina [13]. The scale was assumed to behave elastically under all conditions.

The procedure for incorporating a growing oxide on the bond coat used the element "birth" and "death" capabilities of NIKE. Bond coat oxidation was thus modeled through the replacement of bond coat elements with the same size of oxide elements at set time intervals. The first oxide birth was in the elements located at the ceramic metal interface. Subsequent growth occurred through oxide elements birthed at the scale/ metal interface at the start of the high temperature hold portion of the cycle. The oxide elements were allowed to "grow" during steady state to the full volume dictated by the growth rate equation by assigning an artificially high CTE to the oxide and imposing a small temperature increase during steady state, similar to the method used by Chang et al. [6]. In this way the stress due to oxide growth, relaxation of growth stresses and thermal cycling was incorporated in the model. Since the oxide elements were birthed at the oxide/bond coat interface, the model simulates the inward growth of an oxide scale.

Five factors were intentionally varied, in addition to the main factor of oxidation. The five factors were bond coat roughness, bond coat CTE, bond coat creep, top coat creep and the number of thermal cycles. Information on stress as a function of location is also a part of the output of the model. After a few brief

comments on the effects of roughness and CTE, the remainder of the paper will concentrate on the effects of oxidation and creep of the constituents.

The output of the model included stress as a function of time, location and direction. It was found that the radial stresses in the ceramic (perpendicular to the interface) provided an adequate indication of the stresses most likely to promote delamination cracking. Therefore, radial stresses will be presented as a function of time and location to depict the active stress generating mechanisms in a TBC system and to try to define the likely failure scenario. It was also found (see Figures 8 and 9, discussed later) that the highest tensile radial stresses were located at the bond coat peak, off-peak and valley regions. Therefore, the large volume of data generated during FEM modeling will be narrowed to these locations in order to facilitate comparison of the various cases presented.

### 3. Results and Discussion

The first point to note in the discussion is that the intent of the model at this stage of development is to examine mechanisms that generate residual stresses (or strains) in TBCs. A reasonable assumption is that high residual stresses are a cause of ceramic failure. Thus, knowing how the residual stresses are generated provides insight on how the coating fails. The intent of a "final" model is to relate the stress generating mechanisms to failure of the TBC. Thus, the important points to follow in this paper are the trends in residual stress development with the selected factors, not the absolute values of the stresses. With this in mind, it is informative to compare the calculated stresses to those measured in real systems. Coating stress measurements are of the stress in the plane of the coating, not the stresses normal to the plane. For zirconia, these stresses are quite low for the as-deposited coating, between 0 and 5 MPa. After one cycle, the in-plane stresses typically jump to 20 to 30 MPa, and jump to 25 to 35 MPa after 10 one hour cycles to 1100°C [10]. In the current study, the average compressive residual stresses in the plane of the coating have been calculated to be as high as 200 MPa after 4 cycles if coating cracking is not allowed, in obvious disagreement with the measured values. However, when the coating is allowed to crack in the model, the average coating stresses after 4 cycles drop to approximately 20 MPa. This comparison indicates: the calculated stress is sensitive to the fracture stress of the coating, the model is capable of predicting realistic stresses when fracture is included, it is best to use the stresses reported in the current paper as an indication of the likelihood of coating fracture rather than an indication of the true stresses in a system.

The effects of roughness and bond coat CTE will first be discussed to demonstrate general effects that are important to the detailed analysis of the effects of oxidation and creep that are presented later.

#### Roughness

Interfacial roughness has been the subject of study for TBCs [6, 8] and is a well known consideration for stresses in thin oxide films [14]. The case that is usually treated is for cooling of a two layer system that is assumed stress free at some high temperature, generally the maximum temperature of a thermal cycle. Petrus et al. [8] started with the assumption of a stress free condition at room temperature and then modeled one entire thermal cycle for a plasma sprayed TBC. They demonstrated that the assumption of a stress free

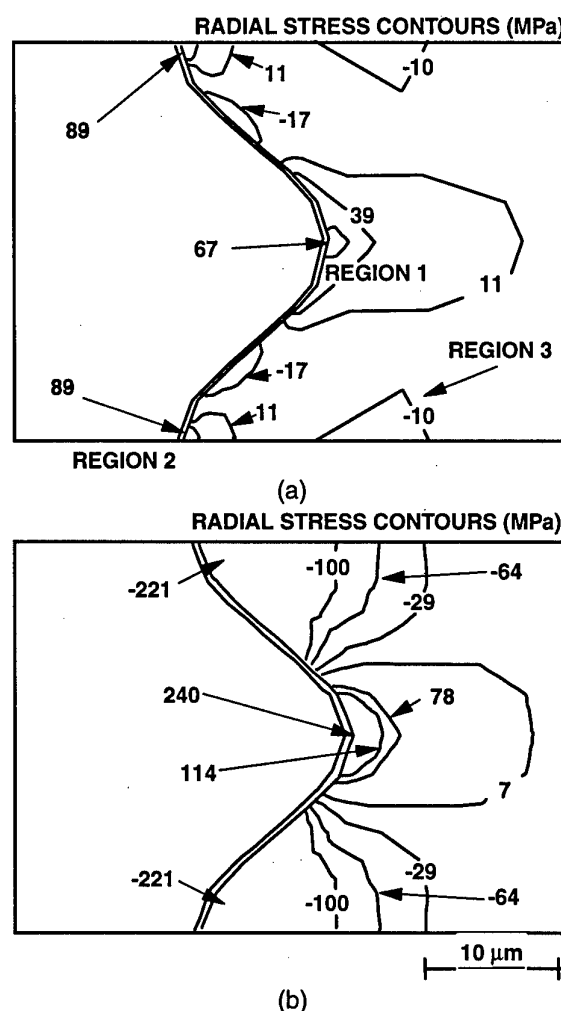


Figure 3. Contour plots of the radial stresses at a rough interface for (a) a low CTE bond coat and (b) a high CTE bond coat.

condition at high temperature is valid for a TBC if the bond coat and / or top coat relax sufficiently during a high temperature hold. When this holds true, Petrus et al. achieve qualitatively similar results as previous studies: a rough interface causes an increase in delamination stresses (tensile stresses normal to the interface) at the peaks of the metallic asperities while increasing compression normal to the surface in the valleys between asperities, as compared to a smooth surface. This finding was reexamined for the current study using four thermal cycles, instead of one, and including oxidation. It was found that, even when oxidation is considered, a smooth surface had stresses normal to the interface ranging from 5 MPa at the interface to 0.5 MPa at the surface. A rough surface, however, exhibited tensile delamination stresses as high as 67 MPa at bond coat peaks, and normal compressive stresses as high as 17 MPa in the valleys (Figure 3(a)). Tensile stresses were also developed in the valleys due to oxidation, as will be discussed later. Several points of interest arise from this finding: 1) roughness tends to cause a substantial increase in stresses in the near interface region as compared to a smooth interface, and 2) the stress is periodic and should tend to limit cracking to the bond coat peak regions. This result is qualitatively the same as for previous models that considered only cooling and only one thermal cycle. A third point is noted that the properties of the bond coat have nearly no influence on TBC stresses for the case of a smooth interface. However, bond coat properties become extremely important when the interface is rough [7, 8]. Note that roughness profiles, and hence the effect of roughness on stress, are extremely complex and at an early stage of investigation.

### Bond Coat CTE

For the case of a smooth interface, it has been demonstrated that the properties of the bond coat are relatively unimportant. Rather, the substrate dominates stress generation in the coating. The strength of an effect in the presence of a rough bond coat is exemplified by the effect of bond coat CTE. Figure 3 shows the radial ceramic layer stresses for low CTE (Figure 3(a)) and high CTE (Figure 3(b)) bond coats and the standard conditions of oxidation and creep of the top coat and bond coat. The tensile stresses at the bond coat peak increase from 67 to 240 MPa with the increase in CTE from  $14 \times 10^{-6} \text{ }^{\circ}\text{C}^{-1}$  to  $20 \times 10^{-6} \text{ }^{\circ}\text{C}^{-1}$ . Also, the valley stresses for the high CTE case are compressive, up to -221 MPa, while the valley stresses for the low CTE case tend to be mildly tensile. The factor of approximately three change in stress level at the peak scales well to the approximately factor of three change in CTE mismatch between the ceramic and the

bond coat for these conditions. This large effect emphasizes the importance of roughness to the stresses in the near interface region.

While it is tempting to suggest that a high CTE bond coat favors cracking at bond coat peaks and should therefore shorten TBC life, a high bond coat CTE also favors crack arrest over the valleys at this small number of cycles. As will be shown later, oxidation at larger numbers of cycles may have a dramatic effect on this situation. The combined effect of CTE and higher oxidation at large numbers of cycles has not yet been investigated, but it is known that CTE interacts with some of the other parameters studied [15].

The remainder of the discussion will focus on the generation of stresses due to the operation of oxidation and creep. The effects of the various mechanisms are best understood when presented separately, starting with the simple, all elastic case.

### Elastic Case

In the case where all the constituents are elastic and there is no oxidation, the radial stress profiles for the three locations are the same for all four cycles (Figure 4 (a)). At the bond coat peak, the ceramic is driven into compression on heating and returns to zero stress on cooling. The stress in the off-peak location also cycles between a compressive stress and zero stress. However, the stress in the valley cycles between a zero cool-down stress and a tensile stress of approximately 70 MPa during steady state heating. The change in sign of stress from the peak to the valley is a result of the change in sign of the radius of curvature [14].

Oxidation is introduced incrementally in the model, with the first increment of oxidation starting with the start of the hold time in the third cycle. Oxidation changes the stresses significantly from the case of no-oxidation (compare cycles 1 and 2 to cycles 3 and 4 in Figure 4(b)). Oxidation pushes the peak radial stress toward slightly greater compression for all portions of the cycle and reduces the amplitude of the stress per cycle. Concurrently, the off peak cool-down stress becomes tensile while the off-peak steady state stress remains constant. This results in an increase in the cyclic stress amplitude for the off-peak location, where an increase in the stress amplitude may have an effect on the fatigue life of this material [16]. The most dramatic effect is on the stress in the valley. The valley stress increases rapidly with growth of the oxide. The linear, nearly vertical increase in stress reflects the linear growth rate imposed on the oxide. This rapid increase in stress is exaggerated due to the fact that all

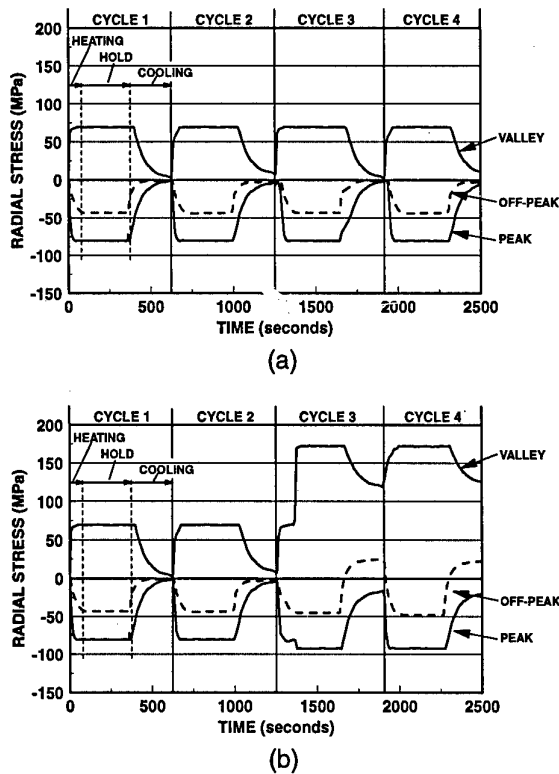


Figure 4. Ceramic layer radial stresses at the peak, off-peak and valley locations for the case of (a) no oxidation and (b) oxidation starting at cycle 3.

of the oxide growth for the first three cycles is made to occur during a short time in the third cycle in the model. As is shown later, this exaggerated increase in stress is unimportant when creep is allowed to occur. The valley cool-down stress increased from zero to 120 MPa and the steady state stress increased from roughly 50 to 170 MPa, causing a substantial oxidation induced increase in the mean tensile stress. Figure 4(b) provides an indication of the stress levels that are expected if stresses due to oxide growth are not relieved. The change in stress amplitude for all locations is a result of the change in the system properties with the addition of a very thin oxide layer with a drastically different modulus and CTE than the coating materials.

This simple case illustrates a trend found throughout the results: oxidation tends to cause radial cool down stresses at the bond coat peak to become more negative, and off-peak and valley stresses to become more positive. Oxidation also causes a decrease in the peak and valley cyclic stress amplitudes and a concurrent increase in the off-peak stress amplitude.

The overall view in Figure 4(b) is that oxidation can

have a significant effect on stress when no other mechanisms are active. Interestingly, the four cycle stress history in Figure 4 b would result in a system that could not support the commonly observed peak-to-peak cracking. This is due to the fact that the radial stresses are zero or compressive over the bond coat peaks for all 4 cycles. A real system, however, includes plasticity and creep (or, identically, stress relaxation) behavior that can modify these stresses substantially.

### Creep Effects

Before examining the interactions of top coat and bond coat creep with oxidation, it is informative to revisit the effect of these mechanisms on stresses in the absence of oxidation [8] and to examine how these stresses evolve with thermal cycling. Figures 5 and 6 show the peak,

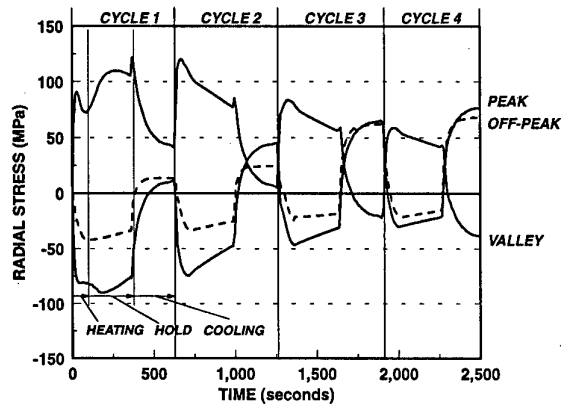


Figure 5. Variation in ceramic radial stress with position and time for the case of a creep in the ceramic and an elastic bond coat.

off-peak and valley stresses for systems with creeping top coat-elastic bond coat and creeping bond coat-elastic top coat, respectively. While the stress always returns to zero in the all-elastic case (without oxidation), creep of the top coat (Figure 5) causes a deviation from a zero cool-down stress at all locations. At the peak, the cool down stress progressively increases from the zero stress of the all-elastic case to roughly 70 MPa during the course of four thermal cycles. This gradually increasing cool-down stress is a result of partial relaxation of the top coat compressive stresses at the peak during each steady state hold (Figure 5). As with any relaxation process, the relaxation rate decreases with time (apparent as a decreasing slope during the hold time) and the cool-down stress tends toward a steady state value. However, relaxation is not complete by the end of the fourth cycle. The stresses at the off-peak and valley



locations also change as a function of time. The off-peak stresses become progressively more positive with cycling. The valley cool-down stress is actually more positive than the elastic case for the first cycle, but then becomes progressively more negative, eventually reversing sign by the fourth cycle.

The stress amplitude for each cool-down portion of the cycle remains constant with increasing cycling for each location, but the mean stress changes. The reason that the stress amplitude remains constant is that there has been no change in materials properties of the system during this process and relaxation is relatively inactive during the transients. The change in mean stress is due to the relaxation of stress during the steady state hold.

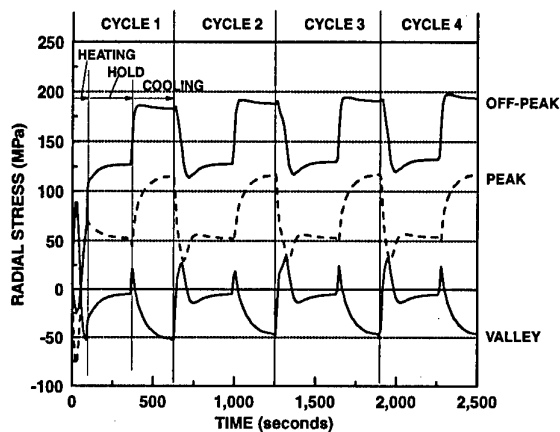


Figure 6. Variation in ceramic radial stress with position and time for the case of creep in the bond coat and an elastic top coat.

Bond coat creep has a similar effect to that of top coat creep, but the rate of the change is much higher simply because the bond coat creeps more readily (Figure 6) [2]. The magnitude of the change is also greater within the first four cycles. This is due to the fact that relaxation at steady state hold runs to completion for each hold cycle, including the first, resulting in stabilization of the thermal fatigue cycle after the very first cycle. Therefore, stress profiles for all three locations remain constant for the second through fourth cycles. This does not mean that bond coat creep stops after the first cycle. The evidence of continuing bond coat creep is apparent as a slight decrease in the stress during hold for all 4 cycles. Other work has also shown that bond coat creep is active for some materials during cool down on every cycle [2]. As with top coat creep, bond coat creep causes the peak and off-peak stresses to become more positive and the valley stress to become more negative.

### Combined Effects

The combination of the effects of top coat creep, bond coat creep and oxidation are compared in Figures 7(a) - (c) as the radial cool-down stresses for the peak, off-peak and valley locations. First, note that the stresses

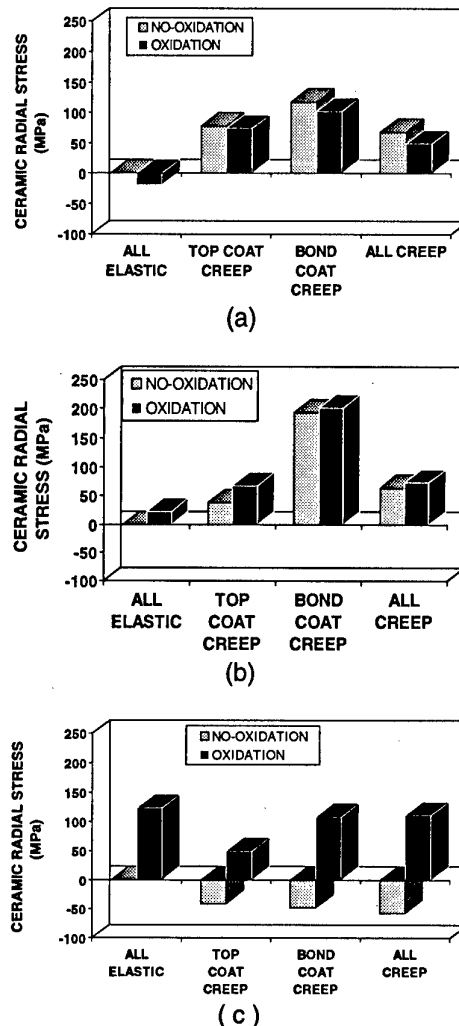


Figure 7. Ceramic radial cool-down stress variation for the cases of all-elastic, creeping top coat (elastic bond coat), creeping bond coat (elastic top coat) and "all creep" (combined top and bond coat creep) in oxidizing and non-oxidizing conditions for (a) the peak, (b) off-peak and (c) valley locations.

resulting from the combination of top coat creep and bond coat creep cannot be expressed by simple addition of stresses due to the mechanisms acting separately.

The peak stress is lower, the off-peak stress is intermediate and the valley stress is higher than would

be expected of either mechanism separately. This result illustrates the difficulty in looking at only one mechanism to characterize the stresses in a system that has more than one mechanism operating. The various creep cases do, however, remain consistent in the sign of the stress at each location.

Comparing oxidized to non-oxidized stresses shows there is interaction among mechanisms at the valley location but that oxidation and creep are roughly additive for the other locations. In the valley, oxidation reverses the stress from moderately negative in all three creep cases to highly positive. An interesting point is that the magnitude of the stress change is for the creeping bond coat and combined creep case is nearly double that for the ceramic creep case.

The results appear to indicate that the stresses at the peak and off-peak locations are tensile whether oxidation occurs or not. Thus, even if no oxidation occurs, the stress state at these locations is favorable to delamination cracking. The stress in the valley region without oxidation is compressive, clearly not conducive to cracking in this region, in agreement with previous considerations of wavy interfaces [14]. However, addition of oxidation changes the sign of the stress to become highly tensile, and conducive to delamination cracking, as noted by previous authors [6, 7]. It should be remembered, however, that the stresses reported in Figures 7(a)-(c) are from single elements quite close to

Figure 3(a)), shows that the area of the peak, off-peak and especially the valley tensile stress regions are small and not connected. Also, a compressive region exists between the peaks (note Region 3 in Figure 8) that would prevent planar cracking from peak top to peak top, as is usually observed in failed coatings. Similarly, the high tensile stress regions are not in the same plane, so that cracks moving from one region to another would have to follow a path well off of parallel to the interface. Since cracks typically appear planar and parallel to the interface, this configuration does not agree with observations.

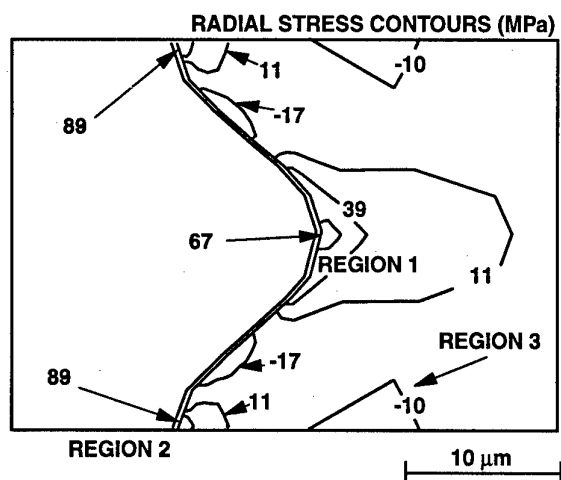


Figure 8. Contour plot of the radial stress in the ceramic after cool-down following 4 thermal cycles for the case of combined oxidation and creep.

the interface. Examination of a contour plot for the general creep case with oxidation, Figure 8 (same as

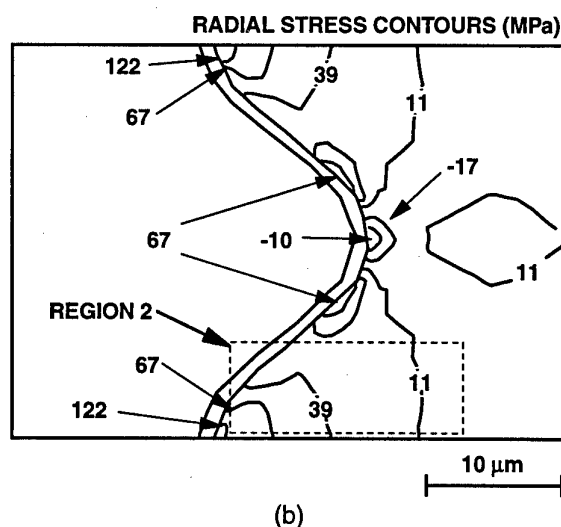
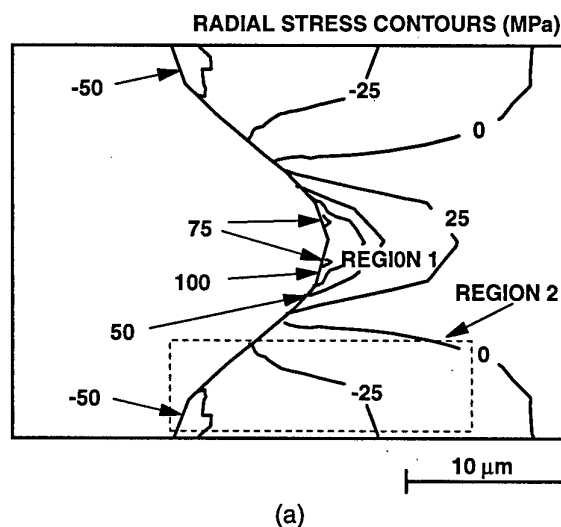


Figure 9. Contour plots of the radial ceramic stress at cool-down following 51 cycles for the case of combined creep and (a) without oxidation and (b) with oxidation.

This difficulty was resolved by running an additional combined creep case, with and without oxidation, to a greater number of thermal cycles. Figure 9 compares contour plots of the radial stresses after 51 thermal cycles for non-oxidizing and oxidizing cases. For 51 cycles without oxidation, a compressive stress region extends from the valley well into the ceramic layer (Region 2 in Figure 9 (a)). These compressive stresses would limit cracking to the region above the bond coat peaks. With oxidation, it is evident in both the 4 and 51-cycle cases (Figures 8 and 9(b), respectively) that the tensile stress at the peak has become compressive. In the 51 cycle case the tensile off-peak region has grown in area and become more tensile. Additionally, the compressive radial stress regions over the valley after 4 cycles with oxidation (Region 3 in Figure 8), and after 51 cycles without oxidation (Region 2 in Figure 9(a)), have completely disappeared after 51 cycles with oxidation (Figure 9b, Region 2). Thus, the stresses at 51 cycles with oxidation is much more favorable to crack growth over the valleys than is the four cycle case. However, the stresses at 51 cycles are unfavorable for crack growth at the peak of the bond coat. The histograms in Figure 10 provide a direct comparison of the stresses at each position for each case.

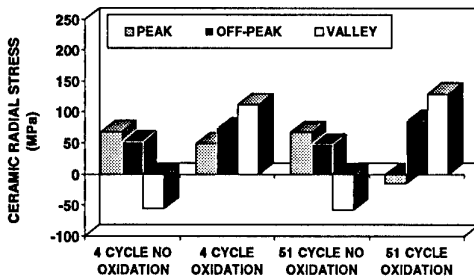


Figure 10. Radial stress in the ceramic at the end of cool-down as a function of location, number of thermal cycles and oxidation.

An overall view of the cracking process begins to emerge from these results. At small numbers of thermal cycles, the relatively rapid processes of ceramic and bond coat creep make cracking favorable at the peak and off-peak locations. However, cracking over the valley locations, except right at the interface, is still difficult due to compressive stresses and/or low tensile stresses. As the relatively slow process of oxidation proceeds, cracking over the peaks becomes less favorable while cracking at the off-peak and valley locations becomes easier. As oxidation proceeds even further, the regions above the valleys grow further until the tensile regions of neighboring valleys converge to

form a uniform tensile region a short distance from the bond coat. Cracking in this large, general tensile region then becomes possible. Thus, it appears that early cracking should occur at bond coat peak regions, aided by ceramic and bond coat creep, and continued cracking is driven by the changes in stress over the valleys driven by oxidation.

### Summary and Conclusions

The failure mechanisms of thermal barrier coatings have been examined through a FEM model of residual stress generation due to oxidation, top coat creep and bond coat creep. The results indicate that top coat and bond coat creep act to generate tensile stresses at bond coat peak and off-peak locations, while generating compressive stresses in the valley regions. The primary effect of creep on the cool down stress appears to be limited to short times at temperature. Oxidation acts opposite to creep, causing increasing tensile stresses in the valleys while pushing the peak regions into compression. Continuing oxidation results in an increase in the size of the tensile region associated with the valley, growing to the point that the tensile stresses in the valley extend beyond the peak regions. Continued oxidation also causes a slight increase in the maximum tensile stresses at the off-peak and valley locations.

The combination of oxidation, top coat creep and bond coat creep yields a stress distribution in time and in location along the interface that is not achievable by any one mechanism acting alone. The picture of the failure mechanism resulting from this evolution of residual stresses is as follows: 1) Early cracking at bond coat peaks, driven by tensile peak stresses generated due to creep processes. 2) Cracks generated early in life do not propagate due to creep generated compressive stress regions over the valleys. 3) At higher numbers of cycles, and therefore higher oxide thicknesses, stresses over the valleys become increasingly tensile and the size of the tensile region increases. 4) The tensile region over the valley is then capable of sustaining crack growth, resulting in linking of the near-peak cracks generated during early cycling. This description of failure is supported by the qualitative observations of cracking progression.

This progression of cracking is clearly a result of the combined action of creep, oxidation and thermal cycling. An accurate description of the entire process requires a model including these factors. However, failure of a TBC is very complex and is clearly not completely described by a simple model. Other factors, such as: sintering; phase changes in the oxide, bond

coat and ceramic layer; ceramic layer cracking; and compositional changes are also thought to be important aspects that should be included for a complete description of the failure mechanism.

## References

1. R.A. Miller and C.E. Lowell, Thin Solid Films, 95 (1982) 265.
2. W.J. Brindley, J. Thermal Spray Tech., 6 [1] (1997) 85.
3. D.J. Wortman, E.C. Duderstadt and W.A. Nelson, ASME Paper 89-GT-134, ASME, New York (1989).
4. R.A. Miller, J. Amer. Cer. Soc., 67 (1984) 517.
5. J.T. DeMasi-Marcin, K.D. Sheffler and S. Bose, ASME Paper 89-GT-132, ASME, New York (1989).
6. G.C. Chang, W.A. Phucharoen and R.A. Miller, Surf. Coat. Tech., 30 (1987) 13.
7. W.A. Phucharoen, Ph.D Dissertation, Cleveland State Univ., Cleveland, OH (1990).
8. G.J. Petrus and B.L. Ferguson, J. Thermal Spray Tech., 6 [1] (1997) 29.
9. B. Engelmann and J.O. Hallquist, *NIKE2D, A Nonlinear, Implicit, Two-Dimensional Finite Element Code for Solid Mechanics - User Manual*, UCRL-MA-105413, Lawrence Livermore National Laboratories, Livermore, CA, 1983.
10. R.T.R. McGrann, J.A.S. Graves, E.F. Rybicki, J.R. Shadley and W.J. Brindley, Proc. of the 9<sup>th</sup> National Thermal Spray Conference, Cincinnati, Ohio, October 7-11, 1996, ASM International, Materials Park, Ohio, 1996, p. 885.
11. J.T. DeMasi, M. Ortiz and K.D. Sheffler, *Thermal Barrier Coating Life Prediction Model Development, Phase I Final Report*, NASA CR-182230, NASA (1989).
12. High Temperature High Strength Nickel Base Alloys, INCO, Saddlebrook, NJ, 1984.
13. D.W. Richerson, *Modern Ceramic Engineering*, Marcel Dekker, Inc. (1992) pp. 166-186.
14. A.G. Evans, G.B. Crumley and R.E. Demaray, Oxid. Met., 20 [5/6] (1983) 193.
15. A.M. Freborg, B.L. Ferguson, G.J. Petrus and W.J. Brindley, *Proc. of the TBC Workshop 1997, Cincinnati, OH, May 19-21, 1997*, NASA Lewis Research Center, Cleveland, OH (1997).
16. C.A. Andersson, *Fracture mechanics of ceramics. Volume 6 - Measurements, Transformations, and High-Temperature Fracture*, Plenum Press, New York, 1983, p. 497.

# THE EFFECT OF TBC UTILIZATION IN THE DESIGN OF ROBUST AIRCRAFT COMBUSTORS

Carlos A. Arana  
Aero Propulsion & Power Directorate  
Air Force Wright Laboratory  
Wright Patterson AFB OH USA

## ABSTRACT

As performance objectives of new and derivative military engines require combustion systems to operate at higher pressures and temperatures, balancing conflicting demands of improved durability, stability, and operability becomes more difficult without technology improvements in combustor liner designs. Since combustor thermo-mechanical fatigue is currently a significant contributor to engine life cycle costs, improved structural durability must be achieved, without compromise of other combustor requirements. This paper addresses the application and verification of liner cooling schemes and their interaction with thermal barrier coatings (TBCs) for the design of robust aircraft turbine engine combustor liners to meet the above mentioned demands. An analytical investigation was conducted to determine the effect of TBCs on the average metal temperature for a full annular, semi-transpiration cooled combustor liner. The perspective is from a customer's viewpoint, a combustor liner designer who is continuously challenged to increase combustor temperature rise capability and operability for new products while maintaining cooling flow levels.

## LIST OF SYMBOLS

$A$	area
$\sigma$	Stefan-Boltzmann constant
$\alpha$	absorptivity
$\rho$	density
$\delta$	thickness
$\mu$	viscosity
$\theta$	cooling effectiveness
$C_p$	specific heat
$D$	combustor diameter
$eff$	effective
$\epsilon$	emissivity
$f_c$	flame chamber
$f/a$	fuel air ratio
$h$	heat transfer coefficient
$k$	thermal conductivity
$L$	luminosity factor

$l_b$	mean beam length of radiation path
$\dot{m}$	mass flow rate
$\eta$	thermal effectiveness
$P$	pressure
$q''$	heat flux
$T$	temperature

## Subscripts

$a$	air
$AN$	annulus
$c$	casing
$g$	gas
$w$	wall
$WH$	flame side
$WC$	cold side
$3$	combustor inlet
$4$	combustor exit

## 1.0 INTRODUCTION

Air dominance is maintained by fielding affordable and durable high performance air platforms capable of delivering payload when and where needed in the field command. Key to successful air platforms is the propulsion system. The major key to higher specific thrust is higher engine operating temperature. Current combustion systems still operate well below the stoichiometric chemical limits of kerosene based fuels. In the future, major increases to these values will be required (Hill, 1997) [1]. It is estimated that overall pressure ratios are expected to grow from a present 20 to over 40, and the turbine entry temperatures from 1800 to 2400°K. As a result of these higher combustion pressure and gas temperatures, the heat flux levels in these engines will also increase making the task of combustor liner durability design extremely challenging. Therefore, a critical technology need for the development of advanced gas turbine engines will be the control of heat transfer. Since thermal barrier coatings are an effective approach to heat transfer control, advanced materials will need to be integrated with robust thermal barrier coatings and innovative cooling techniques to minimize increases in cooling flow requirements. For a combustor

liner system, TBCs act as thermal insulators reducing the amount of heat transmitted to the combustor wall from the products of combustion. The heat flux gets dissipated through radiation back into the hot gas path, conduction across the coating and substrate, and convection through back side cooling air.

## 2.0 THE PROBLEM

Hot section components are significant maintenance items in today's engines. Almost 7 percent of unscheduled removals of F100-200 engines in the F-16 due to core components during 1991 were caused by combustor or turbine problems. In fact, during this period of time, the mean time between failures of the combustor in the -200/F16 system did not meet the Engine Structural Integrity Program requirements (Turner, 1996) [2]. TBCs can alleviate this problem, however, at a cost. Currently the Air Force spends on average \$143.3 per kilogram (\$65/lb) for TBC bond materials. Each combustor consumes around 0.9 - 1.7 kilograms (2-3 lbs) of bond coat. For a typical top coat the cost is about \$28.7 per kilogram (\$13/lb) and each combustor consumes around 1.7 kilograms (3 lbs). Labor time for the application of these TBC systems is approximately 1.84 hours per combustor.

## 3.0 CHALLENGES

In the future, the entire combustor section of a high performance aircraft engine, as shown in figure 1, will be subjected to an increasingly severe thermal environment which will eventually approach stoichiometric conditions.

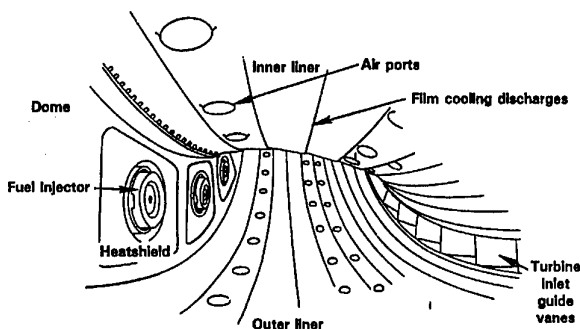


Figure 1. Internal view of a typical annular combustor system

Two major factors will significantly impact the ability to cool the combustor liner:

- **Combustor Inlet Temperature:** As the inlet temperature to the combustor increases, gas temperature also increases and, therefore, the liner temperature increases proportionally requiring more air to maintain a given liner temperature. TBCs can ameliorate this issue by enabling a reduction in the amount of radiant heat flux from the flame to the liner (figure 2).

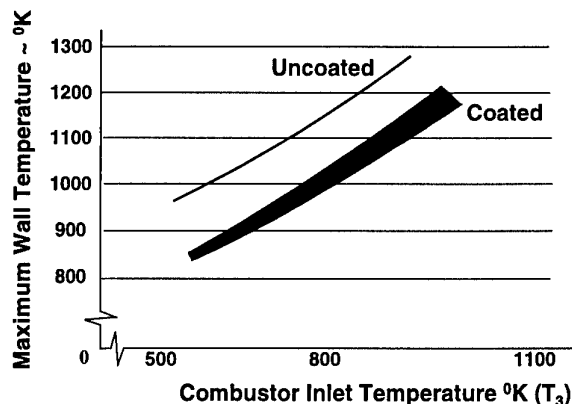


Figure 2. Typical TBC payoff for combustor liners

- **Combustor Temperature Rise:** It is estimated that for the high temperature rise combustors which will be required to operate at an equivalence ratio of 80 percent, over 85% of the entire combustor air flow will be required to be introduced in the primary combustion zone to completely react all of the fuel. As a result, the amount of air remaining for liner cooling and combustor exit temperature control becomes scarce (figure 3). If the cooling air is not reduced, there would be no dilution available to reduce hot streaks. This further complicates the task of maintaining the liner temperature at that allowed for conventional metal materials.

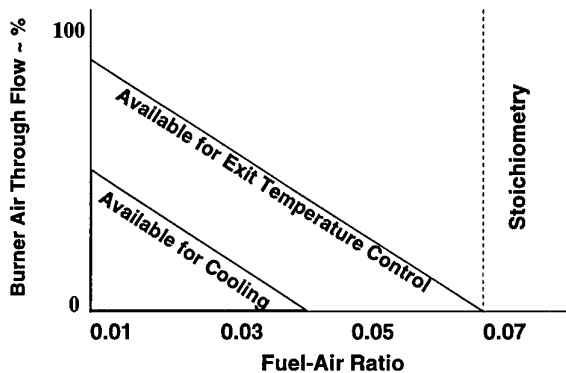


Figure 3. Increased combustor exit temperatures reduce available dilution and cooling air

From the practical combustor design standpoint, the objective is not to use improved cooling methods to lower wall temperatures below the levels achieved with present methods, but rather to achieve the same wall temperatures despite reductions in the amount of coolant flow as shown in figure 4.

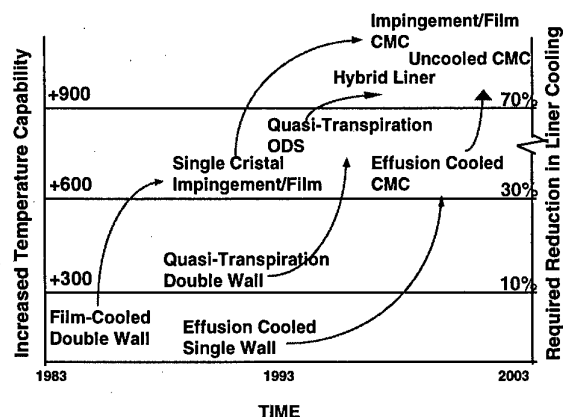


Figure 4. Combustor liner material/cooling progression for the past 15 years.

#### 4.0 GENERAL REQUIREMENTS AND DESIGN CONSIDERATIONS

The primary technical objective of combustor research and development is to provide the technology that will enable the designers attain combustor performance, operability, weight and cost objectives for a particular mission and cycle definition.

As systems become more efficient and probably more complex, the next generation of combustor designs will need to balance conflicting demands such as increased temperature while improving durability, maintainability, and affordability. In order to achieve these demands an integrated product/process must be implemented. This process should enable the production of a robust design capable of operating efficiently in a wide variety of environments dictated by the intended air vehicle. To satisfy the requirements of future cycle parameters, technology improvements are required. Advanced planning allow us to establish combustor performance objectives that will support overall engine system improvements. Some combustor specific performance objectives are:

- 50% weight reduction
- 100% increase in volumetric heat release rate
- +900° F maximum combustor exit temperature
- +400° F combustor inlet temperature
- 300% increase in fuel/air turndown ratio

- 99% efficiency at all operating conditions

Other combustor system design considerations:

- 2000 engine flight hours and 4000 Low Cycle Fatigue TACS - hot parts
- 4000 engine flight hours and 8000 Low Cycle Fatigue TACS - cold parts
- 10 hour of operation at any steady-state flight condition
- 1 hour of operation at simultaneous  $T_3/T_4$  condition
- 350 hour of test cell operation

Other requirements:

- Buckling margin of safety as dictated by combustor geometry (shape and wall thickness) shall exceed 50 percent under maximum pressure and temperature
- 5% creep limit without loss of mechanical alignment, as dictated by structural geometry to mitigate the interaction of thermal and mechanical stresses
- Component high cycle fatigue life greater than  $10^7$  cycles, as determined by both material and structure
- $-3\sigma$  material properties (average for crack propagation)
- 500 0-maximum-0 cycles at maximum power

#### 5.0 COMBUSTOR TBC EVOLUTION

Since the birth of thermal barrier coatings in the early 1960's, combustors and augmentors have benefited from a series of incremental growths in this technology. This has resulted in an increased ability to withstand higher temperatures with a decrease in the severity of oxidation damage, and an improved cracking resistance to severe thermal cycling for longer periods of time (Harris, 1991)[3]. Early combustor coatings consisted of an outer ceramic insulative layer of air plasma deposited, 22 weight percent MgO stabilized  $ZrO_2$ , and an inner metallic bond coat of air plasma deposited Ni-Cr or Ni-Al (Gupta, et al., 1994)[4].

As these temperatures in the combustor have been increased, the durability of this early combustor coating has become inadequate. The maximum use

temperature of the plasma sprayed magnesia-stabilized zirconia coating is on the order of 1255°K since magnesia-stabilized zirconia crystallographically destabilizes above 1227°K.

By replacing the 22 weight percent magnesia with 7 weight percent yttria composition, the spallation life at temperature above 1255°K has been improved substantially (Stecura, 1979)[5]. This improvement is approximately 4 times that of 22 percent magnesia fully stabilized zirconia coating at 1367°K (Gupta et al, 1991)[6].

Since the operating temperature of the combustor was increased to take advantage of the increased temperature capability of the yttria stabilized zirconia, the underlying bond coat oxidation became a problem. By adopting a more oxidation-resistance NiCoCr AlY bond coat composition from the turbine section of the engine, the performance of the combustor has been improved (Gupta et al., 1994)[4]. Figure 5 illustrates the progression of TBC's for hot section applications.

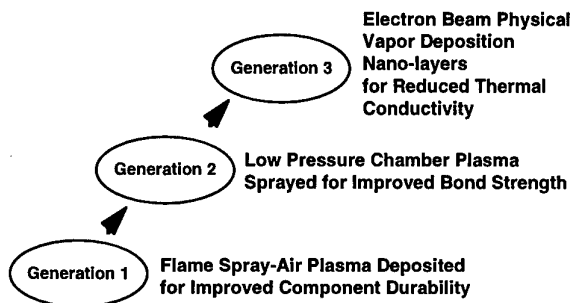


Figure 5. TBC Progression for Hot Section Applications

## 6.0 TBC APPLICATION ADVANTAGES

Let us look at other potential benefits of applying TBC's in the combustor section:

### 6.1 Efficiency and Idle Emissions

As summarized by the results of Mularz et al., 1978 [7], from which figure 6 is reproduced, the application of thermal barrier coating along the inside of the combustor liner allows combustion gases near the wall to be at higher temperatures. This minimizes wall quenching effects of the combustion chemical kinetics and therefore, reducing unwanted exhaust emissions such as carbon monoxide and unburned hydrocarbons. Since the design intent of cooling air is to protect the liner surface, air intro-

duced through the liner walls downstream of the dilution jets may not be effective in the combustion process, therefore, contributing to potential combustor inefficiency.

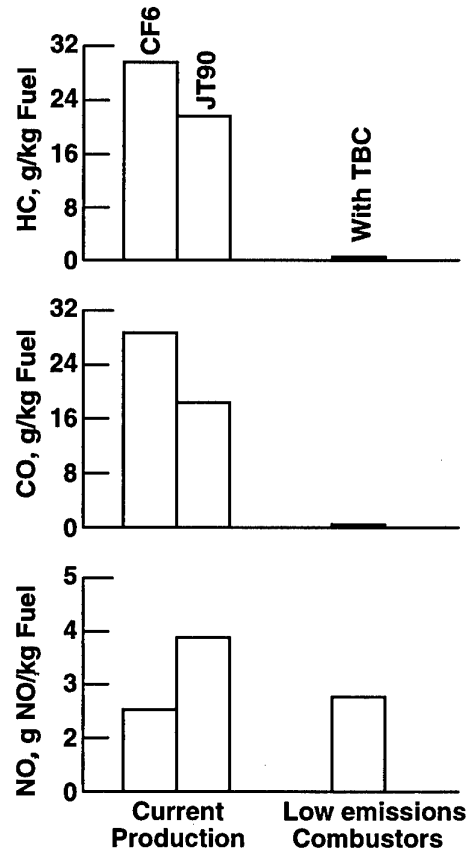


Figure 6. Efficiency Benefits for Idle Engine Operating Condition

### 6.2 Exhaust Smoke Emissions

Exhaust smoke numbers decrease slightly with thermal barrier coatings as reported by Butze, et al., 1976 [8] from which figure 7 is reproduced, for a cruise condition. Soot is the primary source of flame emissivity at high pressures. The intense radiation from the ceramic coating back to the flame results in a decrease in soot concentrations due to reduction of the amount of soot formed initially and through burnup of the soot formed.

### 6.3 Combustor Liner Life

The average cooling temperature that is required in a typical production combustor today is graphically illustrated in figure 8. The gas temperature referred to in this figure represents the maximum combustor exit temperature. The allowable operating temperature for the metal liner is about half



way between the maximum gas temperature and the temperature of the cooling flow ( $T_3$ ). Also shown in this figure is the relationship of the allowable design metal temperature levels to the incipient metal temperatures. As shown, the allowable metal temperature levels are near the incipient melt point of nickel based superalloys. Therefore, any breakdown in the cooling layer would be detrimental.

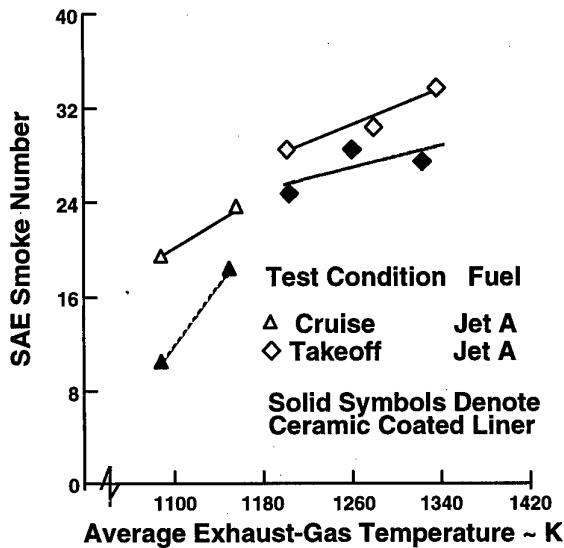


Figure 7. Effect of ceramic coating on SAE smoke number

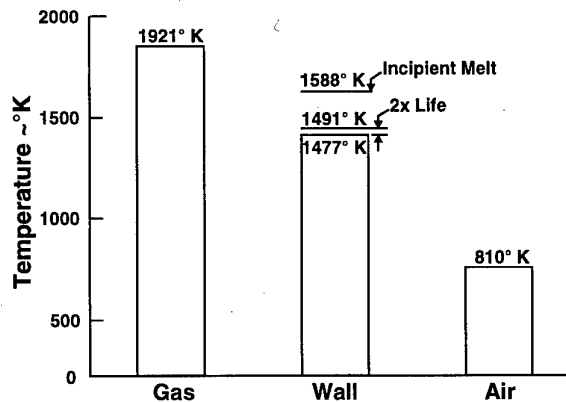


Figure 8. Exhaust, Wall and Air Temperature Comparison

## 7.0 HEAT MODEL

According to experimental results from Butze et al., 1976 [9], as shown in figure 9, the liner metal temperature reductions available through the use of ceramic coatings can be accurately predicted using a one-dimensional heat transfer model. Having that in mind, a one-dimensional heat transfer analysis

was performed in order to estimate the thermal performance of TBCs and compare the capability of TBC improvements against cooling effectiveness improvements and  $T_3$  reductions. The heat transfer model outlined in this section closely follows the development approach as detailed by Lefebvre, et al., 1960 [11].

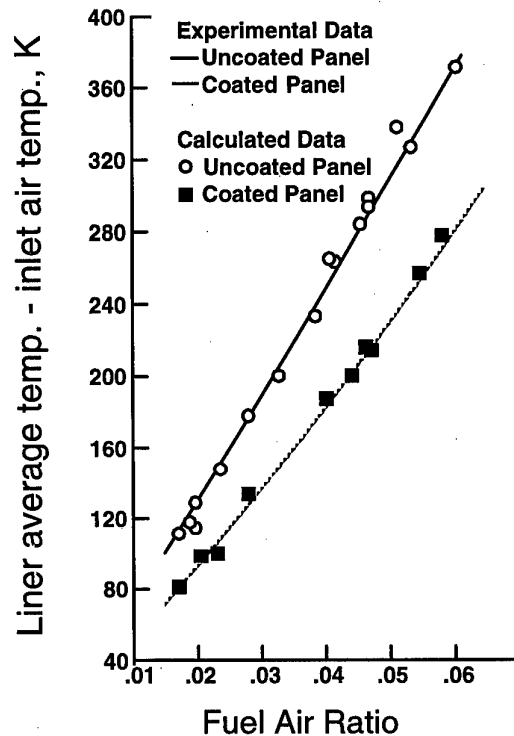


Figure 9. Liner Temperature Prediction vs. Experimental Results

Figure 10 illustrates the schematic of radiant heat flow through a TBC at isothermal conditions. For this analysis the temperature drop through the ceramic was assumed to be linear since yttria-stabilized zirconia thermal conductivity is nearly constant over the temperature range of interest ( $1.5 \pm 0.1$  W/m $\cdot$ K over 1200 to 2260°K). Emittance and transmittance were assumed invariant with temperature. The cycle conditions chosen for the analysis are as follow:

$$P_3 = 3040\text{KPa}, T_3 = 1144^\circ\text{K}, \text{coolant mass flux} = 3.416 \text{ Kg/s-m}^2$$

It was assumed that the gas temperature next to the wall is equal to the average flame temperature, having a value close to stoichiometric. This assumes the possibility of a hot streak occurring next to the wall due to combined effects of a localized low annulus velocity on one side of the wall coinciding with a breakdown in the cooling layer on the other.

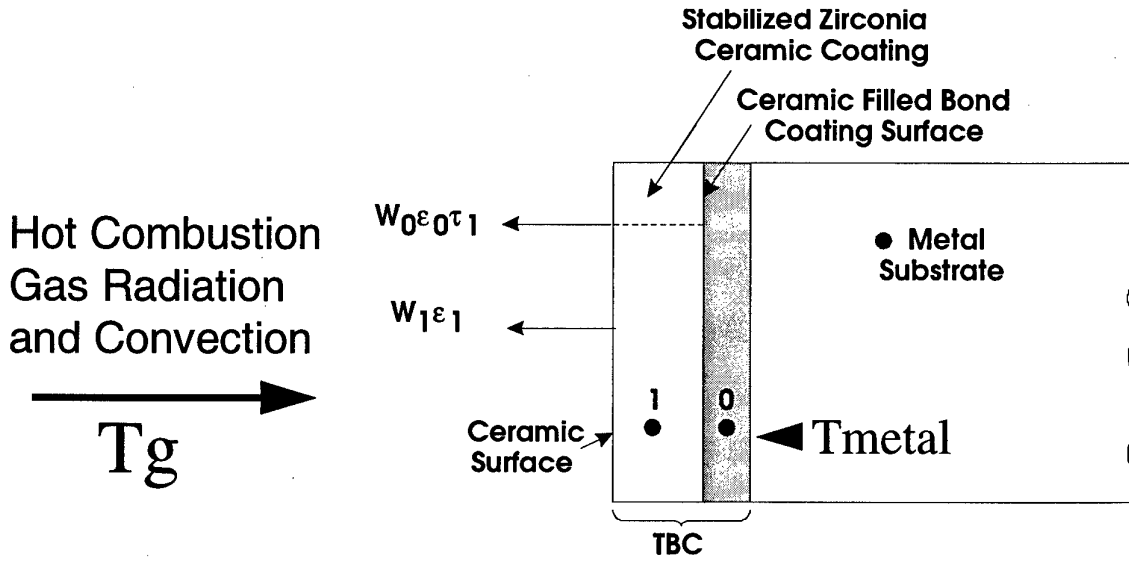


Figure 10. Schematic of radiant heat flow through the TBC at isothermal conditions.

#### 7.1 Internal Radiant Heat Flux

The radiation heat flux was calculated for the case of a TBC-coated liner using the results obtained by Liebert, 1978 [12] where emittance of both the ceramic translucent layer and the material substrate were taken into consideration.

$$q''_{RAD} = \sigma(0.5)\epsilon_g T_g^{1.5} (T_g^{2.5} - T_{WH}^{2.5}) \quad \{1\}$$

The radiation heat flux was calculated for the case of an uncoated liner using reference [11]:

$$q''_{RAD} = \sigma \frac{(1 + \alpha_w)}{2} \epsilon_g T_g^{1.5} (T_g^{2.5} - T_{WH}^{2.5}) \quad \{2\}$$

The flame emissivity,  $\epsilon_g$ , was calculated using reference [11]:

$$\epsilon_g = 1 - \exp(-290 P_g L \sqrt{(f/a)} l_b T_g^{-1.5}) \quad \{3\}$$

where the luminosity factor was calculated using reference [13]:

$$L = 0.0691(C/H - 1.82)^{2.71} \quad \{4\}$$

where C/H is the fuel carbon/hydrogen ratio by weight. For future high pressure ratio engines, the practicality of using this correlation could be somewhat dubious. More experimental data will need to be generated.

#### 7.2 External Radiant Heat Flux

Radiant heat flow from the combustor liner to the casing is given by:

$$q''_{RAD} = \sigma \frac{\epsilon_W \epsilon_C (T_{WC}^4 - T_3^4)}{\epsilon_C + \epsilon_W (1 - \epsilon_C) (A_W / A_C)} \quad \{5\}$$

#### 7.3 Internal Convective Heat Flux

Convective heat flow to the combustor liner from the gases is given by:

$$q''_{CONV} = 0.02 \frac{k_g}{D_{fc}^{0.2}} \left( \frac{\dot{m}}{A_w \mu} \right)_g^{0.8} (T_g - T_{WH}) \quad \{6\}$$

#### 7.4 External Convective Heat Flow

Convective heat flow from the combustor liner to the annulus air is given by:

$$q''_{CONV} = 0.02 \frac{k_a}{D_{AN}^{0.2}} \left( \frac{\dot{m}}{A \mu_a} \right)_{AN}^{0.8} (T_{WA} - T_3) \quad \{7\}$$

#### 7.5 Conduction Heat Flux

The radial heat flux conducted through the liner wall is given by:

$$q''_{COND} = \left( \frac{k}{\delta} \right)_{eff} (T_{WH} - T_{WC}) \quad \{8\}$$

$$\text{where } \left( \frac{k}{\delta} \right)_{eff} = \frac{1}{\left( \frac{\delta}{k} \right)_{TBC} + \left( \frac{\delta}{k} \right)_{Metal}} \quad \{9\}$$

### 7.6 Convective Heat Flux Through Liner

The heat flux picked up by the coolant as it passes through the semi-transpiration cooled wall is expressed by

$$q''_{air} = \dot{m}_{air} C_{p,air} \eta \cdot (T_{WH} - T_3) \quad \{10\}$$

where  $\eta$  is the thermal effectiveness, which is a function of the internal heat transfer coefficient within the liner. This heat flux is absorbed by the coolant and therefore reduces the heat load that must be removed by  $q''_{CONV}$  and  $q''_{RAD}$  on the outside liner.

The following figures summarize the results of the investigation:

- Figure 11 shows the potential reduction in metal wall temperature attainable with a refractory coating for the semi-transpiration cooled liner system. It is obvious that changes in TBC thickness have a pronounced effect on combustor liner temperature as reflected in the figure. It is also evident that with the application of the TBC to the liner, the liner wall metal temperature would be capable of meeting life requirements as mentioned in section 4.

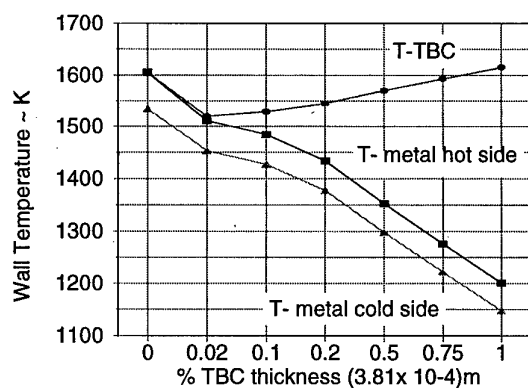


Figure 11. The Effect of TBC Thickness on Liner Wall Temperature

- Figure 12 shows how the heat fluxes vary as the effective conductivity changes. The heat flux due to conduction diminishes as the thickness of the TBC system is increased. For the same case, the outside convective and radiation heat fluxes also decrease as expected. The internal radiation heat flux is maximum for the case of the uncoated liner since a small fraction of the heat gets reflected back to the gases.

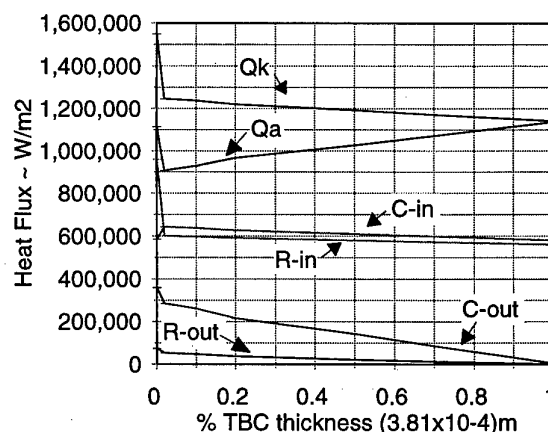


Figure 12. The Effect of TBC Thickness on heat fluxes

- Figure 13 shows the reduction in metal temperatures without TBC as coolant temperature decreases for the same amount of coolant flow rate. Comparing these results with the results from figure 14, it is evident that although the TBC surface temperature is higher, the actual metal temperature (substrate) on the gas side is much lower.

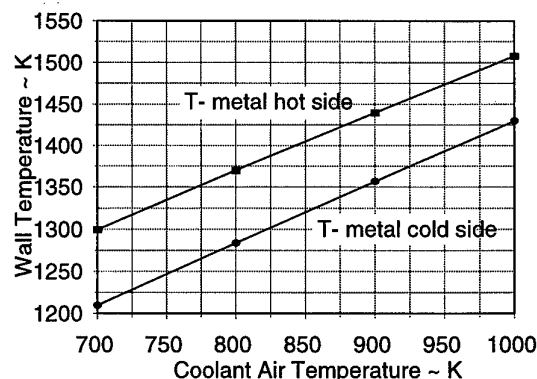


Figure 13. The Effect of Coolant Air Temperature Variation on Liner Wall Temperature (Uncoated)

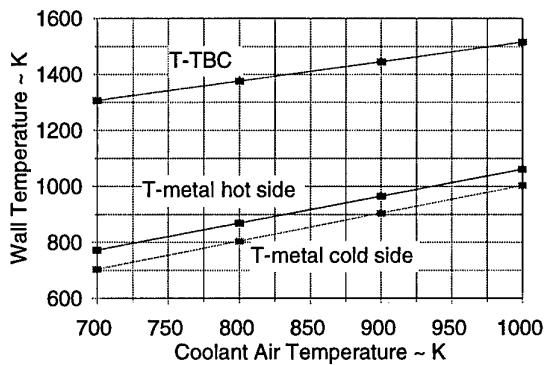


Figure 14. The Effect of Coolant Air Temperature Variation on TBC Liner Wall Temperature

- Figure 15 shows the impact of liner thermal effectiveness variation on wall temperatures. As would be expected, the hot side metal temperature is reduced as the ability of the liner to extract heat becomes greater for the same amount of coolant flow rate

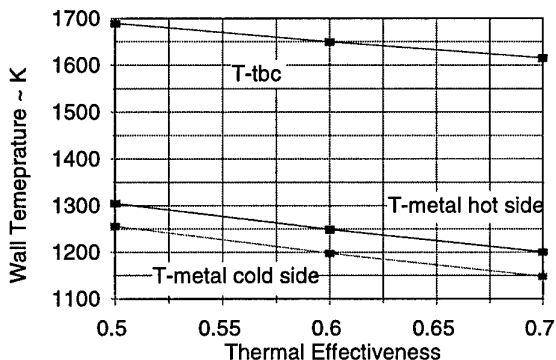


Figure 15. The Effect of Variation of Thermal Effectiveness on TBC Liner Wall Temperature

## 8.0 SUMMARY

The quest for higher thrust-to-weight ratio will entail increasing combustor inlet and exit temperatures. This will impose very stringent requirements for the development of robust aircraft combustors. A large portion of the heat transferred to the liner wall from the hot combusting gases and particles within the combustor will be by radiation. But significant advances can be obtained by incorporating third generation TBC into the next production of combustor liners. To maximize the potential, there needs to be a focused effort. The thermal effect of the TBC ceramic layer must become an integral element of the combustor liner design sys-

tem. TBC reliability must be equal or greater than the substrate since the integrity of the coating becomes prime reliable as loss of the coating can result in rapid deterioration of the liner. Also, the ability to apply TBCs to components with complex geometries should be improved. As combustor inlet air temperature approaches the maximum allowable wall temperature, there simply will not be enough cooling potential left to cool the wall adequately. This leaves the possibility of no metal wall structure, no matter how effective, will maintain reasonable metal temperatures at those conditions.

An analytical investigation was conducted to determine, through qualitative trends rather than quantitative values, the effect of a ceramic coating on the average metal temperatures of a full annular, semi-transpiration cooled combustor liner. This investigation was conducted at a pressure of 3040 KPa, inlet air temperatures of 1144°K and an overall fuel air ratio of 0.67. The insulating effects as well as increased reflectivity of the ceramic coating were responsible for the reduction in heat transfer through the liner walls.

To solve the heat flux equations a non linear algorithm was used. For that purpose a Newton-Raphson non-linear solver was developed to solve the equations in an iterative manner. It should be mentioned that the energy balance equations represent a gross approximation to the heat transfer process taking place between the liner structure and its surroundings. A more rigorous formulation for the heat transfer process may be developed if specific details are required.

It appeared that the reduction in metal temperature at any given coating thickness is considerably greater than any improvements achieved solely by cooling configuration changes.

It was noted that a relationship between liner cooling effectiveness and effective conductivity exists. That relationship was considered in the analysis, however, with some limitations. In other words as cooling effectiveness changes there corresponds a change of effective conductivity.

## 9.0 REFERENCES

- Hill, R.J., "The Future of Gas Turbine Engines", in "Propulsion and Energy Issues for the 21st Century", AGARD CP 824, March 1997, Chapter 2.

2. Turner D., "Enhanced Performance Extended Life Combustor", WL-TR-2136, November 1996
3. Harris, D., "Composite Thermal Barrier Coatings", Fourth National Spray Conference, CF, May 1991.
4. Gupta D.K., Meier, S.M., "The Evolution of Thermal Barrier Coatings in Gas Turbine Engine Applications", Transaction of ASME, Vol. 116, January 1994.
5. Stecura, S., "Effect of Compositional Changes on the Performance of a Thermal Barrier Coating System", NASA TM-78976, 1979
6. Gupta D.K., Meier, S.M., "Ceramic Thermal Barrier Coatings for Commercial Gas Turbine Engines", JOM, March 1991
7. Mularz, E.J., Cleason C.C., and Dodds, W.J., "Combustor Concepts for Aircraft Gas Turbine Low Power Emissions Reduction", AIAA/SAE No. 78-999, 14th Joint Propulsion Conference, 1978
8. Butze, H.F., Liebert, C.H., "Effect of Ceramic Coating of JT8D Combustor Liner on Maximum Liner Temperatures and Other Combustor Performance Parameters", NASA TM X-73581, December 1976
9. Claus, R.W., Wear, J.D., Liebert, C.H., "Ceramic Coating Effect on Liner Metal Temperatures of Film-Cooled Annular Combustor", NASA Technical Paper No. 1323, 1979
10. Wassel, A.B., "The Design and Development of High Performance Combustors", Lecture Series 93, Von Karman Institute of Fluid Dynamics, Brussels, 1997.
11. Lefebvre, A.H., Herbert, M.V., "Heat Transfer Processes in Gas Turbine Combustion Chambers", Proc. Inst. Mech. Eng., 1960, Vol. 174, No.12, pp 463-473.
12. Liebert, C.H., "Emittance and Absorptance of NASA Ceramic Thermal Barrier Coating System", NASA Technical Paper 1190, April 1978.
13. Odgers, J., Kretschmer, D., "A Simple Method for the Prediction of Wall Temperatures in a Gas Turbine", ASME Paper No.78-GT-90, April 1978.

## Advantages/Disadvantages of Various TBC Systems as perceived by the Engine Manufacturer

P.Morrell and D.S.Rickerby

Rolls-Royce plc

PO Box 31

Derby DE24 8BJ

United Kingdom

### SUMMARY

This paper discusses the relative advantages and disadvantages of Thermal Barrier Coatings systems (TBC's) produced by thermal spraying and electron-beam PVD processing technology from a design point of view. This paper reviews the structure/property relationships for electron-beam physical vapour deposition (EB-PVD) TBC's in contrast to those of plasma sprayed TBC's, particularly with respect to thermal conductivity, erosion resistance and mechanical behaviour. Examples are used to show how, through the development of customised bondcoat systems, the performance of TBC systems can be considerably enhanced, an important incremental step towards the ultimate goal of "designed-in TBC's".

### INTRODUCTION

To improve fuel efficiency and performance the operating temperatures of the turbine section of the aero-engine have been increased significantly over the past twenty years. This temperature rise has been met by the use of materials with increasing temperature capability, the introduction of advanced manufacturing technology producing cast blades with improved cooling effectiveness, and the introduction of directionally solidified and single crystal turbine blade technology

(Figure 1), [Ref.1]. Thermal barrier coatings (TBC's) offer the potential of allowing an increase in operating temperature of 70 to 150°C without any increase in metal operating temperatures or the ability to reduce the mass flow of coolant whilst maintaining the operating temperature of the turbine. Both possibilities are very attractive to the turbine blade designer. In the first case the equivalent of 2-3 generations of turbine alloy development can be achieved with the application of the coating, in the second case improvements in specific fuel consumption of 0.25% can be realised. This saving may not appear significant, but can result in an annual saving of the order of £6M for an airline operating a fleet of 747 or 777 aircraft.

### USE OF ZIRCONIA-BASED TBC'S

By virtue of a low thermal conductivity, TBC's reduce the heat flux into a component allowing a high thermal gradient to be sustained across the thickness of the ceramic (Figure 2). In addition, TBC systems are designed to match as close as is practical the expansion characteristics of the nickel-based component to ensure that the thermal mismatch stresses are minimised. During the early 1970's, due to their relatively high coefficients of thermal expansion and low thermal conductivities [Ref. 2], zirconia partially stabilised with magnesia (20% MgSZ), calcia (20% CaSZ) or yttria (8wt. % PYSZ) were

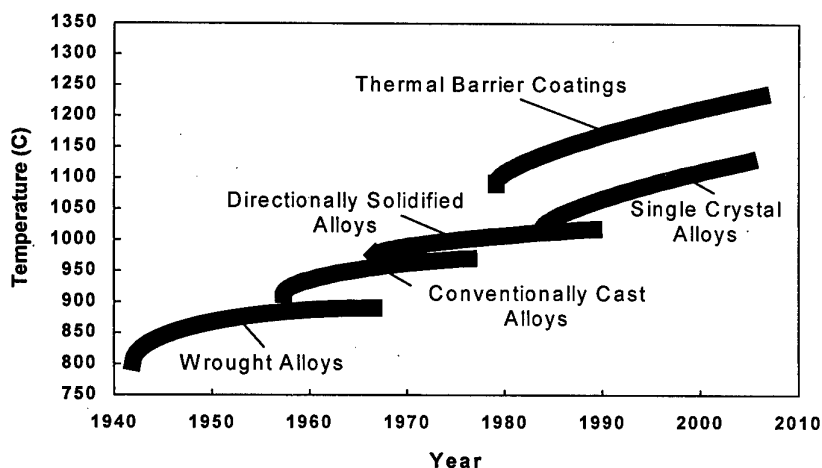


Figure 1 Increase in operational temperature of turbine components made possible by alloy, manufacturing technology and thermal barrier development.

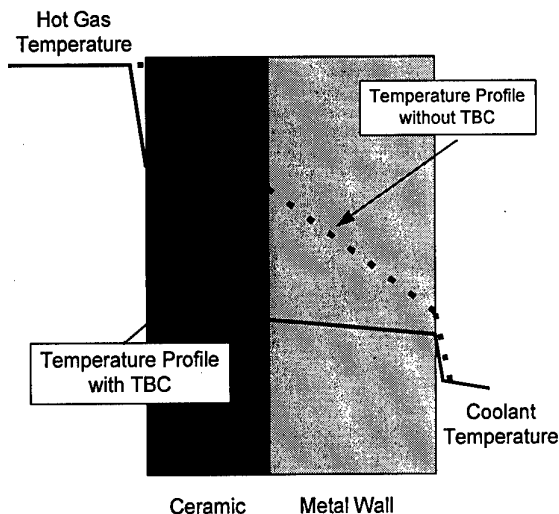


Figure 2 Schematic of the principle of the thermal barrier coating

used for plasma sprayed thermal barrier applications. Early TBC's were manufactured from magnesia or calcia stabilised zirconia, which performed well in service at operating temperatures below c.a. 1000°C. Above this temperature significant diffusion of the magnesium or calcium ions occurs and precipitates of MgO or CaO are formed [Ref. 3] which results in an increase in thermal conductivity (Figure 3) and the monoclinic content of the coating. This rise in the monoclinic content leads to mechanical instability of the coating as a result of the microcracking associated with the martensitic monoclinic/tetragonal phase change on thermal cycling.

This limitation of low operating temperature allied to phase instability was overcome by the introduction of 8% PYSZ in the late 1970's, a material which is relatively stable for elongated periods at temperatures up to 1500°C with no precipitation of  $Y_2O_3$  from solution; (Figure 4) [Refs. 4,5]. PYSZ TBC's have performed well in service, significantly increasing the life of components. For example, the application of 8% PYSZ TBC to combustion can walls reduces the thermal stresses in the can and can result in component lives in excess of 20,000 hours (Figure 5).

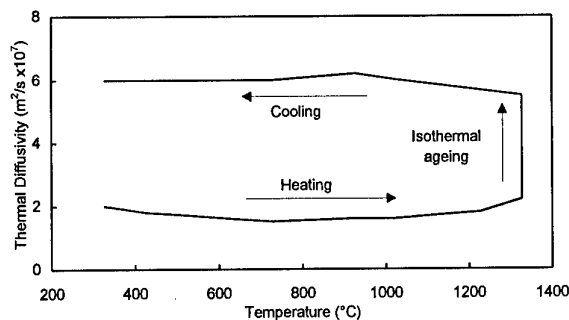


Figure 3 Thermal diffusivity of CaSZ TBC showing thermal instability due to precipitation of CaO out of solution.

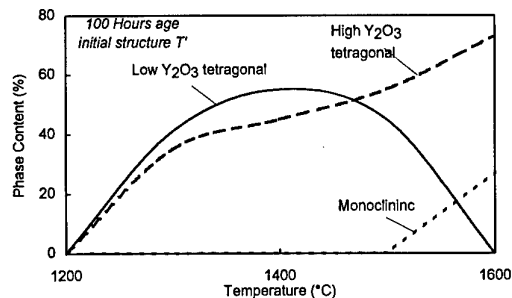


Figure 4 Relative phase compositions of aged 8% PYSZ TBC's. Note the initial coatings were all T' face-centred tetragonal phase.

### PLASMA SPRAYED VERSUS PVD TBC'S

Although plasma sprayed TBC's have performed well in service on annular surfaces in the engine, their microstructures do not lend themselves to producing coatings with the necessary strain compliance, erosion resistance or surface finish required for successful application on blade or nozzle guide vane aerofoils. As a result their introduction into the high-pressure turbine has been limited. An example of the structure of a plasma sprayed coating is shown in Figure 6, where the individual platelets formed from the droplets impinging on the surface during the spraying process can clearly be seen. In contrast, more recently electron-beam physical vapour deposition (EB-PVD) has been used to deposit TBC's which, because of their columnar microstructure, exhibit very high levels of strain compliance (Figure 7). The columnar microstructure which forms is due to the atomistic processes, nucleation and growth of the coating from the vapour phase. In addition to their good compliance, EB-PVD TBC systems also offer other benefits over plasma sprayed TBC's in terms of improved adhesion, surface finish and erosion resistance which has led to their application onto turbine aerofoils. The effects of these properties on both coating and engine

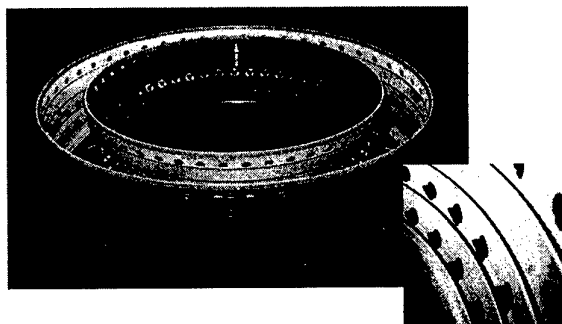


Figure 5 An example of a combustion can with plasma sprayed TBC on the inner can walls.

performance are discussed in the following sections.

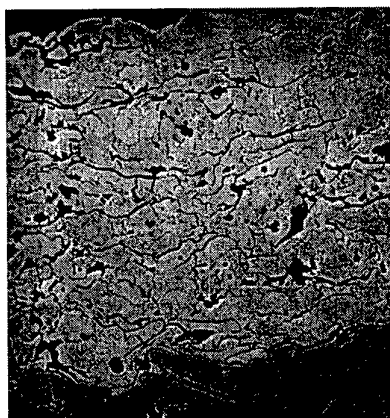


Figure 6 Photomicrograph of a plasma sprayed TBC coating. The network of microcracks (platelet boundaries) are clearly visible together with the porosity associated with these coatings.

### Surface finish

For aerofoil applications, the coefficient of friction ( $C_f$ ) of the surface of the blade is directly related to roughness [Ref. 4] and in turn the  $C_f$  value influences the heat transfer coefficient and efficiency of the turbine [Refs. 6,7,8]. The primary loss coefficient is plotted in Figure 9 for Reynolds numbers between  $0.5-1.5 \times 10^6$  which covers the range for high-pressure turbine aerofoils. As can be seen in Figure 8, the as deposited plasma sprayed TBC will have a significant effect on the performance of the turbine. The plasma sprayed TBC has a typical surface roughness of c.a  $10 \mu\text{m}$  Ra (Figure 9) and a peak to valley height of  $80-100 \mu\text{m}$  which results in an increase in the primary loss coefficient in the turbine of the order of 2% (from 1.5% to 3.5%) [Ref. 7]. In contrast the EB-PVD TBC surface finish is close to that of the metal surface, typically  $1.0 \mu\text{m}$  Ra (Figure 10) with a peak to valley height of  $10 \mu\text{m}$ . These coatings exhibit a primary loss coefficient of the order of 1.5%, and do not appear to increase the loss coefficient over that observed for the uncoated metal surface.

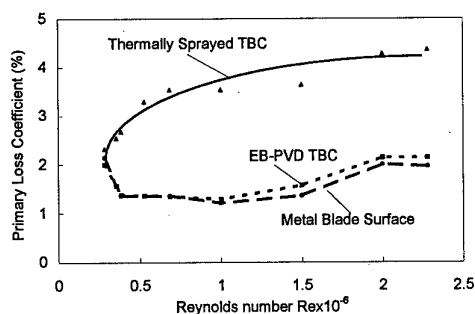


Figure 8 Primary loss coefficient for a high pressure turbine aerofoil showing the effects of different surface roughness of TBC.

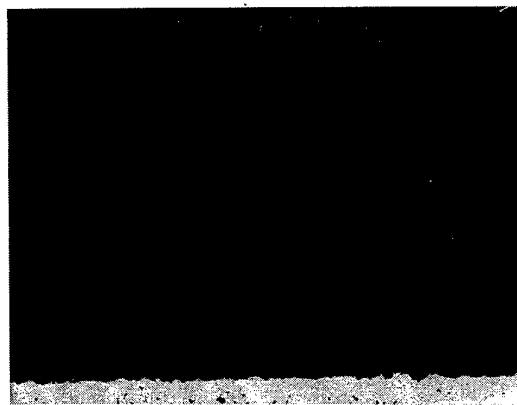


Figure 7 Photomicrograph of EB-PVD TBC showing the columnar microstructure.

Polishing of the thermally sprayed TBC results in a surface finish of  $2-3 \mu\text{m}$ , however as will be discussed later, erosion of the coating in service will increase the surface roughness of the TBC back to values approaching  $10 \mu\text{m}$ . As a result the designer will favour EB-PVD TBC systems for use on high pressure turbine blade and nozzle guide vane aerofoils for the aerogas turbine engine.

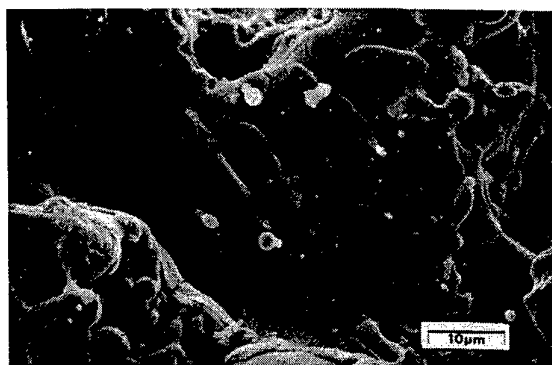


Figure 9 Scanning electron micrograph of the surface of a plasma sprayed TBC showing the high surface roughness and undulating nature of the surface.

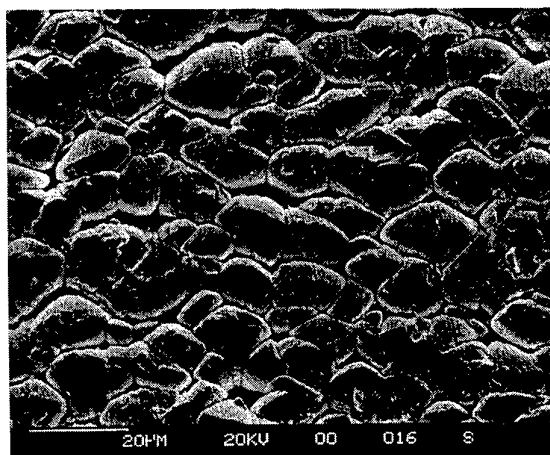


Figure 10 Scanning electron micrograph of the surface of an EB-PVD coating showing the pyramidal end form of the columns and low surface roughness.



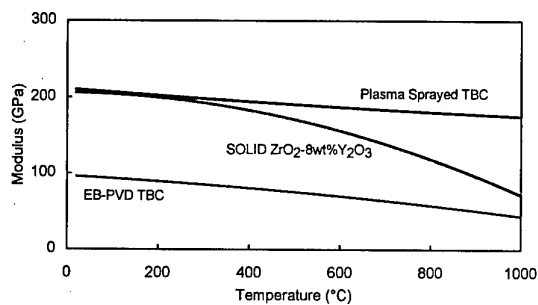


Figure 11 Young's moduli of solid sintered 8% PYSZ, plasma sprayed and EB-PVD 8% PYSZ TBC systems measured by dynamic techniques.

For TBC applications in large turbine components (particularly in the power generation industry) the relative roughness of the plasma sprayed TBC compared to the blade chord dimensions becomes more favourable and the effects of increase friction coefficient become less important. Similarly, the local gas velocities in the combustion zones are lower which can lead to low coefficient of friction losses and use of plasma sprayed TBC systems in such circumstances are not so detrimental to performance.

#### Strain Compliance

Several papers have been published detailing the modulus of TBC systems measured by various techniques including compressive and tensile tests [Ref. 9], dynamic vibration and ultrasonic velocity measurements tests [Refs. 10,11] and the values generated vary depending on the techniques used. More specifically the values vary dependent on the displacements the test method imposes during measurement.

In this paper the moduli of bulk sintered 8% PYSZ material and EB-PVD 8% PYSZ TBC were measured by a laser ultrasonic method [Ref. 11] and compared to those values measured by a resonant technique for plasma sprayed 8% PYSZ [Ref. 9]. In both methods the calculation of modulus is based on the measurement of a compression surface and shear elastic waves in the coating material. Figure 11 summarizes the Young's moduli of solid sintered 8% PYSZ, plasma sprayed and EB-PVD 8% PYSZ TBC's. The modulus of the plasma sprayed TBC systems is similar to that of the sintered material, with a room temperature value of 200 GPa reducing to 160 GPa at 1000°C. The EB-PVD TBC in comparison exhibits a Young's modulus approximately half of that of the bulk material, ranging from 100 GPa at room temperature down to 40 GPa at 1100°C. Care has to be taken to remember that this is the modulus of the coating when the columns of the PVD coating are in contact and they are capable of transferring a compressive elastic wave through the structure. When

measurements are made with the laser ultrasonic method at high temperatures the signal is very highly attenuated by the coating indicating that the column boundaries are playing a significant role. It is expected that when the coating is in tension and the column boundaries open up, the composite tensile modulus of the EB-PVD coating and column boundaries will reduce significantly more than the compressive values.

The relatively high modulus associated with the plasma sprayed TBC can lead to high thermal strains in the coating, especially around tight radii of curvature which are found around the leading edges of high-pressure turbine aerofoils. As an example Figure 12 compares the microstructures of a plasma and an EB-PVD TBC which have undergone thermal cyclic testing. In the case of the plasma sprayed coating, there has been significant cracking within the ceramic leading to gross failure of the TBC system, whereas the EB-PVD system has suffered little mechanical damage within the ceramic layer.

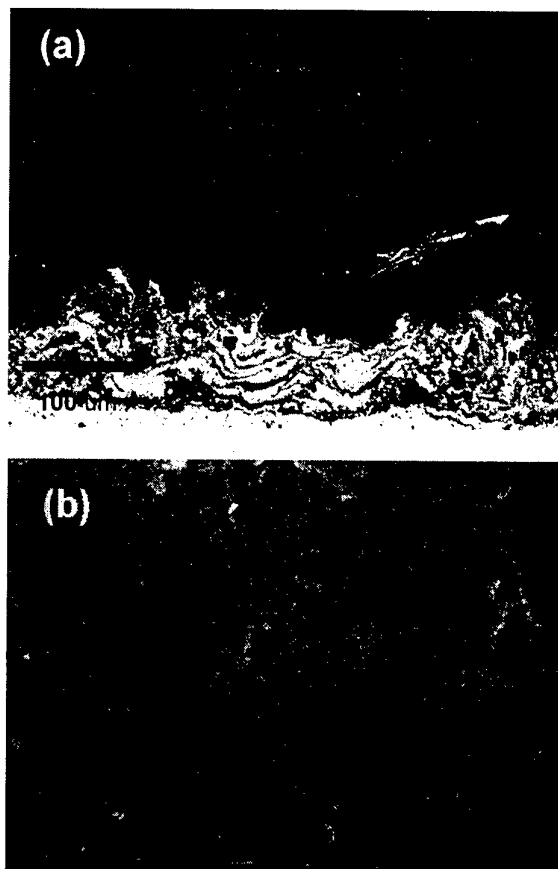


Figure 12 Photomicrographs of (a) plasma sprayed and (b) EB-PVD, TBC's showing the thermal strain damage in the plasma sprayed TBC following burner rig testing.

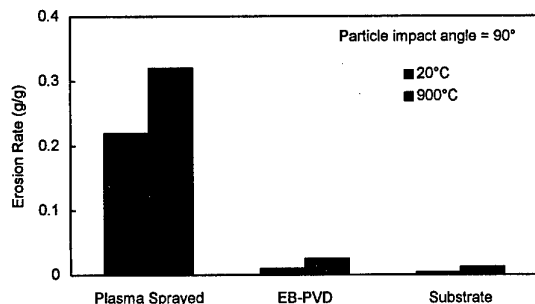


Figure 13 Erosion resistance of plasma sprayed and EB-PVD TBC's, compared to that of a metallic substrate.

Again, like surface finish, the EB-PVD TBC systems are more attractive to the designer where the coating is subjected to high thermal and mechanical loads during engine operation. The conditions encountered around the aerofoil surface in the high-pressure turbine represent such an environment and it is not surprising that EB-PVD is the principal choice in this region.

#### Erosion resistance

The erosion resistance of TBC coatings has been measured using high-temperature erosion facilities. Early studies [Ref. 12] showed that the erosion resistance of EB-PVD TBC's was approximately 8-10 times that of the plasma sprayed TBC system. Further erosion studies at temperatures up to 910°C [Ref. 11,13] using  $\text{Al}_2\text{O}_3$  erodant at velocities up to 230 m/s, showed that the erosion resistance of EB-PVD at both 20 and 910°C were approximately 7 times that of plasma sprayed TBC's at 90° impingement (Figure 13). Erosion tests at room temperature also showed that the angle of incidence of the particle also had a notable effect on the erosion rate. For the plasma sprayed TBC systems the erosion rate decrease with the angle of incidence with the rate at 30° impingement being one third of that at 90° (Figure 14) [Ref. 13].

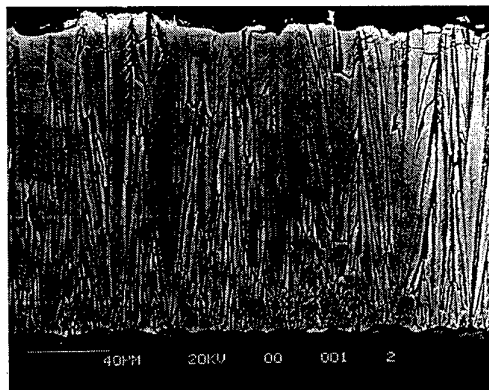


Figure 15 Generation of cracks in the near surface region of the EB-PVD TBC systems during erosion testing. The reasons for this erosion behaviour and the

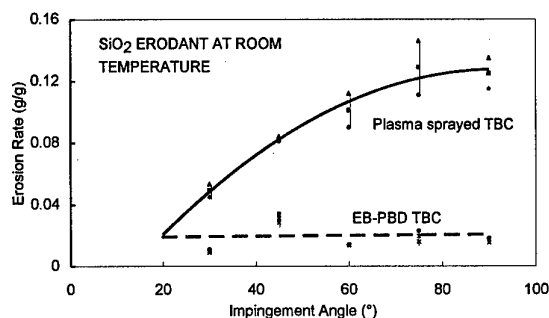


Figure 14 Room temperature erosion rate of plasma and EB-PVD TBC systems as a function of impingement angle.

mechanisms of erosion are well understood [Ref. 13]. At low and intermediate temperatures, the erosion of plasma sprayed TBC systems involves the removal of coating material in the form of the mechanically bonded platelets. This requires relatively low amounts of energy as the coating already contains a high number of microcracks, and particle boundaries, therefore the erodant has to do little work on the systems to generate small amounts of new crack surface to remove the platelet. As relatively large masses are removed with little mass of erodant, the mass erosion rate is high. In contrast, the erosion of EB-PVD TBC's requires the generation of a new crack surface across individual columns which needs a relatively high amount of energy compared with the plasma sprayed coating (Figure 15). When this fracture has occurred, the amount of material which is released is relatively small in comparison to the platelets in a plasma sprayed deposit and, as a consequence, the erosion rate is low. In addition, because the cracking damage in the EB-PVD TBC due to small erodant particles is limited to the near surface regions, the surface finish of the coating is not adversely affected by the erosion process. This is not the case for plasma sprayed TBC's which have been polished, where erosion of the coating causes the surface finish to revert quite quickly to the as deposited values, leading to significant performance penalties as discussed earlier (Figure 16) [Ref. 12].

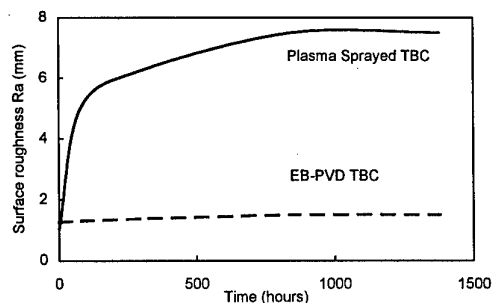


Figure 16 Effects of erosion on the surface finish of EB-PVD and plasma sprayed TBC's.

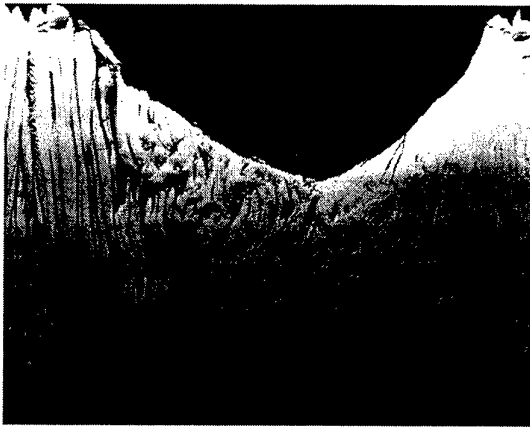


Figure 17 Example of large particle damage at high temperature showing the degree of plasticity shown by the 8% PYSZ coating.

At high temperatures there is certainly evidence within EB-PVD TBC's that significant plasticity can occur especially when large particles, foreign object damage (FOD), impinge onto the surface (Figure 17). This FOD mechanism of coating damage has been seen in development engines where the impact damage matches that produced in the high-temperature erosion rig used for laboratory assessment.

In summary, for low angle impingement, such as exists on the annular surfaces of the combustion can and nozzle guide vane platforms, or where gas velocities (and subsequently particle velocities) are low, plasma sprayed TBC systems can perform as adequately as PVD. However where the gas velocities are high and the impingement angle moves closer to 90°, EB-PVD TBC systems offer significant advantages over plasma sprayed TBC's.

### Coating adhesion

Traditionally the adhesion of plasma sprayed coatings has been assessed by the use of bend testing, lap shear testing and pull-off testing amongst other techniques [Ref. 14]. For plasma sprayed TBC's of 0.25 mm thickness, as deposited adhesion strengths are in the range 20-40 MPa with the strength decreasing as the coating thickness increases. As deposited EB-PVD TBC systems exhibit adhesive strengths higher than the glue and generally no useful data is generated from pull-off testing these systems. To aid in the development of improved bondcoat systems, a method of assessment of adhesion had to be developed which could differentiate between the various forms of aluminide and MCrAlY EB-PVD TBC systems. This requirement led to the development of the transverse scratch adhesion test [Ref. 15].

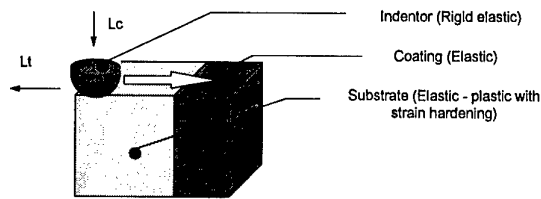


Figure 18 Schematic of the transverse scratch-adhesion test

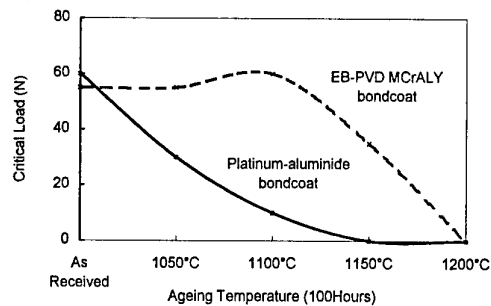


Figure 19 Scratch test adhesion values for EB-PVD TBC's systems on directionally solidified MarM002 alloy.

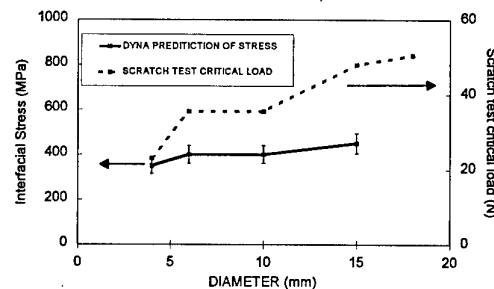


Figure 20 The effect of radius of curvature on scratch test value and the resolved interfacial strength.

Briefly this test involves indenting the substrate of a coated sample which is metallographically prepared in a mount, and moving the indenter from the substrate through the interface region and the coating to the mount material (Figure 18). This process is repeated several times at various indentation loads, the crack length at the interface of the bondcoat and ceramic layers being plotted as a function of load and extrapolated to a no-cracking critical load. This load is then used directly to rank coating systems or can be converted via finite element modelling to an interface strength in MPa [Ref. 15]. Figure 19 shows the scratch-test data for two EB-PVD TBC systems, one with a EB-PVD MCrAlY bondcoat the other with a platinum-aluminide bondcoat. As can be seen from the figure the test has enabled differences in the ageing performance of the interface region to be studied, even at adhesive strengths far in excess of those measurable by the pull-off test (typically equivalent to 5N load on the scratch test). The modelled adhesive strength for the as deposited coating systems was 400 MPa (Figure 20).

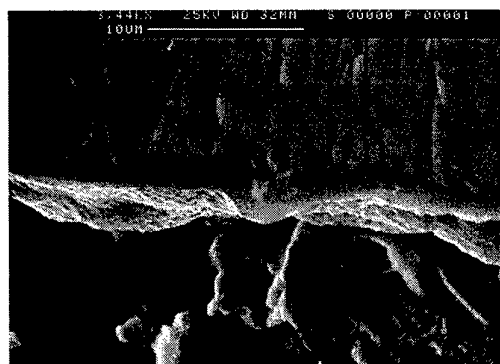


Figure 21 Transport of Hf through grain boundaries in the platinum-aluminide (top) to form  $\text{HfO}_2$  pegs (bottom) at the interface with the  $\text{Al}_2\text{O}_3$  thermally grown oxide scale.

### Thermal Conductivity

Where as the EB-PVD TBC system offers significant benefits over plasma sprayed TBC's for aerofoil application in the areas of compliance, surface finish, erosion and adhesion, the thermal conductivity of EB-PVD TBC's are higher than their plasma sprayed counterparts. A typical plasma sprayed TBC will have a thermal conductivity of 0.7-0.9 W/m.K [Ref. 4] whilst a 0.25 mm thick PVD coating exhibits a thermal conductivity of 1.6 W/m.K [Ref. 16]. Again, these property differences are related to the microstructure of the systems, in the case of the plasma sprayed TBC the platelet boundaries (air gaps) offer a significant resistance to heat flow whilst the EB-PVD TBC column boundaries lay parallel to the principal heat flux direction and have little effect on the conductivity [Ref 17]. Further more, due to the structure of the EB-PVD coating, the thermal conductivity varies as a function of the thickness of the coating. This variation is related to the high thermal resistance of the coating near the interface region where the coating has a high density of column boundaries due to the nucleation and competitive growth nature of the PVD process [Ref. 17]

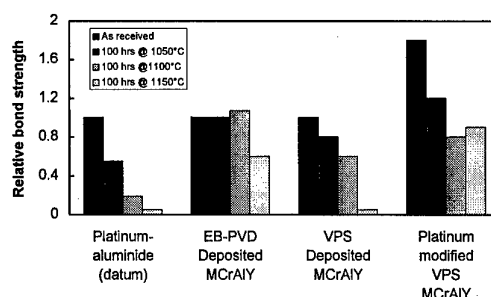


Figure 22 Relative bond strengths of PVD TBC systems on MarM002 substrates (datum = platinum -aluminide bondcoat)

### BONDCOAT DEVELOPMENT

The first bondcoat systems for EB-PVD TBC's were based on the environmental protection coatings that were in use, for example MCrAlY coatings produced by EB-PVD. During the early development phase of bondcoat technology, it became apparent that the substrate played an important role in the adhesion of the ceramic, especially with regard to the diffusion of alloying elements from the substrate through the bondcoat to the near interface region with the oxide [Ref. 18]. This led to a development programme where the rules for the design of a bondcoat were formulated from a detailed understanding of the mechanisms of interface degradation and ceramic spallation. For example, in the case of a platinum-aluminide bondcoat applied to MarM002 the degradation mode was identified as:

- Short circuit diffusion of matrix elements along prior  $\beta$ -phase ((NiPt)Al) grain boundaries forming hafnia pegs.
- With continued exposure growth of these hafnia pegs occurs, these being surrounded by a shell of  $\alpha$ -alumina, and finally,
- Void formation and coalescence which causes a plane of weakness at the thermally grown oxide (TGO) bondcoat interface which results in ceramic spallation (see Figure 21) [Ref. 18].

The progressive reduction in the adhesive strength of the platinum-aluminide EB-PVD TBC systems being previously shown in Figure 19.

Further research showed that even within the MCrAlY family of bondcoats of the same composition, significant variation in the adhesive strengths of the ceramic could result from differences in the processing techniques (Figure 22) [Ref. 19]. The differences in the adhesion behaviour of the EB-PVD and vacuum plasma sprayed (VPS) MCrAlY bondcoats are due to the role of yttrium and the cleanliness of the bondcoat manufacturing processes. In the case of the EB-PVD bondcoat, the yttrium is available as Y in an uncombined form (yttrium nickel intermetallic) which is mobile and can be taken up

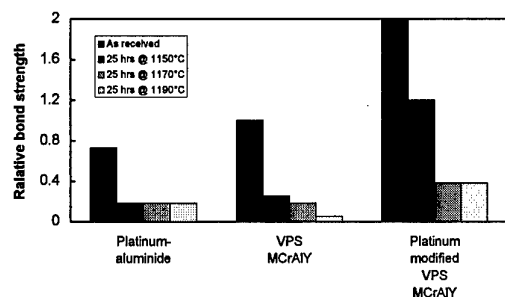


Figure 23 Relative bond strengths of PVD TBC systems on CMSX-4 substrates (datum = platinum-aluminide bondcoat on MarM002)

by the growing oxide. In the case of the VPS coating, the yttrium is present as  $Y_2O_3$  and although dispersed throughout the coating, cannot migrate and is not available to be incorporated into the coating or to tie-up tramp elements coming through from the substrate.

When single crystal substrates were evaluated the cyclic lives were lower than the same coating systems on MarM002 and showed lower adhesion values (Figure 23) [Ref. 19]. One important contributing factor to these differences in TBC adhesion relates to the lower carbon levels in the single crystal alloys. Carbon, present in directionally solidified and conventionally cast alloys as a grain boundary strengthener, combines with alloying elements like titanium and tantalum to form grain boundary precipitates. With the low levels of carbon in single crystal alloys there is little to combine with the titanium and other alloying additions to stop them diffusing through to the interface with the thermally grown oxide. Such elements disrupt the growth of  $\alpha$ -alumina and markedly reduce TBC adherence.

To counteract this problem with single crystal alloys a bondcoat system was developed to stop the diffusion of these damaging elements from the substrate [Ref. 20]. This comprises of an MCrAlY bondcoat with a thin layer of platinum diffused into it prior to the deposition of the ceramic layer. This layer is effective in blocking the diffusion of the damaging elements from the substrate and as a result has increased not only the adhesion but also has improved significantly the temperature capability of the system (Figures 22 and 23).

#### CONCLUDING REMARKS

This paper has reviewed the advantages and disadvantages of both plasma sprayed and EB-PVD TBC systems and their applications in the modern gas turbine engine. Although in terms of erosion resistance and strain compliance the EB-PVD TBC systems has significant advantages over plasma sprayed TBC's, in many applications in the gas turbine engine, such as the

combustion can and nozzle guide vane platforms, plasma sprayed TBC performs adequately. These applications for plasma sprayed TBC's will continue and because of their relatively low cost compared to EB-PVD TBC's, their application to these types of components in the future seems to be assured.

Where EB-PVD technology undoubtedly wins over plasma sprayed TBC's is on the aerofoils of the modern aero-gas turbine, where a good surface finish is paramount and excellent strain compliance and adhesion are required. In these areas EB-PVD offers significant benefits over plasma spraying which more than justifies the higher manufacturing costs.

#### REFERENCES

1. Driver D., Hall D.W. and Meetham G.W., in "The development of the gas turbine engine", Applied Science Publishers (London), 1981.
2. Morrell P. and Taylor R., "Thermal diffusivity of thermal barrier coatings of  $ZrO_2$  with  $Y_2O_3$ ", High Temperatures-High Pressures, 17, (1985) 79
3. Brandt R. "Thermal diffusivity measurements on plasma sprayed calcia stabilised zirconia", High-Temps. High-Press., 13 (1979).
4. Morrell P. and Taylor R. "Thermal diffusivity and phase structure of zirconia-based thermal barrier coatings", in "Advances in Ceramics" Volume 24: Science and Technology of Zirconia III, (1988), The American Ceramics Society.
5. Brandon J.R., Taylor R. and Morrell P. "Microstructure, composition property relationships in plasma-sprayed thermal barrier coatings", Surface and Coatings Technology, 50 (1992) 141.
6. Moody L.F., Trans. ASME, 77, 1265 (1943).
7. Watt R.M., Allen J.L., Bains, N.C. Simons J.P., and George M., "A study of the effects of TBC surface roughness on the boundary layer characteristics of gas turbine aerofoils", ASME87-GT-202 (1987).
8. Ferreira G., Coney M.H. and Harrogate I., "Observations regarding the influence of surface finish on the performance of a TBC prepared by plasma arc", presented at ISABE Conference, Nottingham 1990.
9. Sheffler K.D., Nissley D.M. and Cruise T.A., "Thermal barrier coating life prediction model development", Trans. ASME, 114, 258, (1992).
10. Hillery R.V., Pilsner B.H., McKnight R.L., Cook T.S. and Hartle M.S., "Thermal barrier coating life prediction model development - Final Report", NASA CR 180807, (1988).
11. Morrell P. and Nicholls J.R., "The development of environmentally tolerant PVD thermal barrier coatings - Final Synthesis Report", BRITE/EuRAM programme BREU-0141, Commission of the

- European Communities (1995).
12. Toriz F.C., Thakker A.B. and Gupta S.K., "Thermal barrier coatings for jet engines", *Surface and Coatings Technology*, 39/40 (1989) 161.
  13. Deakin M.J., Nicholls J.R. and Rickerby D.S., "Erosion of thermal barrier coatings", In *High-Temperature Surface Engineering Conference*, 23-25 September Edinburgh (1997).
  14. Chalker P.R., Bull S.J. and Rickerby D.S., *Materials Science and Engineering A* 140 (1991) 583.
  15. Johnstone A., Rickerby D.S. and Morrell P., "Scratch adhesion testing of TBC systems", In *High-Temperature Surface Engineering Conference*, 23-25 September Edinburgh (1997).
  16. Lawson K.L., Nicholls J.R. and Rickerby D.S., "Thermal conductivity and ceramic microstructure", In *High-Temperature Surface Engineering Conference*, 23-25 September Edinburgh (1997).
  17. Nichols J.R., Rickerby D.S. and Lawson K.L., "Advanced processing for reduced thermal conductivity", Paper 6 at 85th Meeting of Structures and Materials Panel, Aalborg, Denmark 15/16 October 1997.
  18. Tawancy H.M., Sridhar N., Abbas N.M. and Rickerby D.S., "Comparative thermal stability characteristics and isothermal oxidation behaviour of an aluminised and platinum-aluminised Ni-based superalloy", *Scripta Met. et Materiala.*, **33**, 1431 (1995).
  19. Bell S.R., Wing R.G. and Woods J.L., "Electron beam physical vapour deposition (EBPVD) thermal barrier coatings for industrial gas turbine engines", Presented at AMSE Turbo '96 Congress, Birmingham (1996).
  20. "Thermal barrier coatings for a super alloy -article and method of application", European Patent EP0718419A2, (1995).

**RESEARCH and TECHNOLOGY ORGANIZATION**  
**85<sup>th</sup> MEETING of the STUCTURES and MATERIALS PANEL**  
**WORKSHOP 3 « THERMAL BARRIER COATINGS »**  
**AALBORG (DENMARK) - 15-16 OCTOBER 1997**

☆☆☆☆☆☆

**REPORT on the FINAL DISCUSSION**  
**Thursday, october 16<sup>th</sup> 1997**  
**15h10 - 16h25**

**Chairman : Alain LASALMONIE (SNECMA)**  
**Recorder : Stefan DRAWIN (ONERA)**

**Table of contents**

**1. « THIN » TBC (AIRFOIL APPLICATIONS)**

**1.1 THERMAL CONDUCTIVITY**

*1.1.1 Effect of microstructure*

*1.1.2 Effect of composition*

*1.1.3 Modelling*

*1.1.4 Measurements*

**1.2 PROCESSING OF TBCs**

*1.2.1 Plasma spraying (PS)*

*1.2.2 EBPVD*

*1.2.3 Layered structures*

*1.2.4 Plasma assisted CVD*

**1.3 LIFETIME OF TBCs**

*1.3.1 Role of bond coat, TGO and oxidation*

*1.3.2 Testing methodology*

*1.3.3 Modelling*

*1.3.4 Graded structures*

**1.4 OTHER PROPERTIES**

*1.4.1 Erosion*

*1.4.2 TBC repair*

**2. « THICK » TBC (COMBUSTOR APPLICATIONS)**

**2.1 TBC ON FREE-STANDING COMPONENTS**

**2.2 TBC FOR COMBUSTORS**

A. Lasalmonie (SNECMA) opened the round table by rapidly summarizing the themes presented throughout the workshop (see table of contents above).

## 1. « THIN » TBC (AIRFOIL APPLICATIONS)

### 1.1 Thermal conductivity

#### 1.1.1 Effect of microstructure

A. Lasalmonie (SNECMA) - Effects of grain size and shape, (macro-)defects (pores and cracks) and layering were presented in papers N°1, 6, 8, 9, 14, 20. The needs are more quantitative measurements and studies on the stability of the microstructure (vs. time and temperature).

U. Schulz (DLR) - The quantitative values needed are values for thermal conductivity after aging, not on as-deposited TBCs.

W. Brindley (NASA) - Yes, but informations on initial (as-deposited) and final microstructure, as well as on intermediate states, are needed too, to get an idea of the important parameters that govern microstructure evolution during aging.

#### 1.1.2 Effect of composition

A. Lasalmonie (SNECMA) - Is 8YSZ (8 wt%-yttria partially stabilized zirconia), the composition that is the most studied and the most used industrially, really the most appropriate composition, since higher yttria contents seem to exhibit lower thermal conductivities? The role of dopant and the use of other oxides has also to be studied (needs for basic research).

P. Morrell (ROLLS-ROYCE) - Yes, as shown by Y. Jaslier in paper N°1, and in other studies, thermal conductivity decreases with increasing yttria content, but if the yttria content is higher than *ca.* 20 wt%, ordering phenomena appear and thermal conductivity increases.

The 8YSZ composition has been developed and optimized by Chromalloy by durability tests on *plasma-sprayed* coatings. This composition has, from then on, be « conservatively » adopted by the aeroengine industry.

W. Brindley (NASA) - Temescal 20YSZ EBPVD coatings exhibited nasty erosion problems.

A. Lasalmonie (SNECMA) - It is time now to investigate other compositions.

V.R. Parameswaran (NRC) - Magnesia stabilized zirconia has been tested, but gave bad results. Using ceria (at high content : 25%), good results were obtained up to 1600°C, but ceria was (partially) reduced to Ce<sub>2</sub>O<sub>3</sub> by chromium and aluminum from the substrate.

P. Costa (ONERA) - If ceria and other rare earth oxides are to be studied, the oxides of the elements at the end of the series should give the best thermodynamic stability.

### 1.1.3 Modelling

A. Lasalmonie (SNECMA) - Modelling is important for optimizing the structure and the properties of TBCs. The trends need to be quantified and experimental validation are required.

To study by numerical simulation the influence of the morphology on thermal conductivity to produce guidelines for coating manufacturers is an interesting idea (see paper N°13). Can existing image analysis techniques, such as those developed *e.g.* for grain boundary studies on metallic alloys, be applied to TBCs?

R. Mévrel (ONERA) - The approaches seem to be different.

### 1.1.4 Measurements

A. Lasalmonie (SNECMA) - The thermal conductivity measurement techniques on TBCs, especially at high temperatures, should become more reliable and could be assessed by a Round Robin on standard specimens.

P. Morrell (ROLLS-ROYCE) - Such a Round Robin was performed five years ago in the United Kingdom.

Y. Jaslier (SNECMA) - SNECMA already performed an intercomparison campaign (two laboratories in France, one in the United-Kingdom, one in the United States).

W. Brindley (NASA) - The contributions of the radiative and conductive components of the thermal conductivity should be assessed.

Zimmermann (?XXX) - Experiences have been performed on uncoated polished substrates and 100 µm zirconia-coated substrates and showed that radiation should not be neglected.

## 1.2 Processing of TBCs

### 1.2.1 Plasma spraying (PS)

A. Lasalmonie (SNECMA) - The presented communications (papers N°3 and 4) have shown good improvements in the process control, a better understanding of the influence of deposition parameters and modelling of the coating formation.

Can better structures and properties be achieved by including columnar inner structure to PS splats, as those shown by P. Fauchais (paper N°3)?

Y. Jaslier (SNECMA) - The columns shown by P. Fauchais are generated by a solidification front starting from the cold substrate and proceeding towards the liquid part of the splat, whereas for the columnar structure in EBPVD coatings you have solidification (condensation) from the gas phase to the solid substrate : the properties may not be the same.

XXX (?) - A recent study by Boeing showed that LPPS TBCs exhibit a fivefold longer lifetime than APS coatings.

W. Brindley (NASA) - It has to be noticed that a great variability exists in the properties of PS TBCs from



one coating manufacturer to the other. So, great care should be taken when comparisons are made!

There is place for both processes (PS and EBPVD) in aeroengines and other parameters than durability have to be taken into account.

XXX (??) - Have other studies on reproducibility of PS coatings been performed (*cf* paper N°4)?

A. Lasalmonie (SNECMA) - Equipments are now available and installed, for a good control of the reproducibility.

C. Moreau (NRCC) - A good control for a better reproducibility can be achieved by controlling the particle velocity and temperature and the substrate temperature. The latter depends of the type of thermal contact between splats.

XXX (??) - How much variability can be tolerated?

C. Moreau (NRCC) - For variations of 100°C for the substrate temperature, different coating micro-structures were observed.

P. Morrell (ROLLS-ROYCE) - From the point of view of the manufacturer, the shape of the component to be coated is of prior importance. The now available processes are a compromise of what the engineers want and what they can get.

### 1.2.2 EBPVD

A. Lasalmonie (SNECMA) - Different coating structures and properties can be obtained by EBPVD. If we refer to the presentation by G. Marijnissen (INTERTURBINE, paper N°10), this is a process that has to be further controlled : the influence of a lot of parameters has to be studied.

V.R. Parameswaran (NRC) - Grading should have a good influence on the properties of the EBPVD coatings.

### 1.2.3 Layered structures

A. Lasalmonie (SNECMA) - Interesting results have been presented (*cf* paper N°6), but no thermal stability and lifetime values are available for these TBCs. Furthermore, are these structures industrially feasible?

J.R. Nicholls (CRANFIELD Univ.) - These are still too new systems : they have only been tested at 1100°C for 50 hours.

A. Lasalmonie (SNECMA) - The layer thickness appears to be a fundamental parameter.

J.R. Nicholls (CRANFIELD Univ.) - Yes, the layers should have a thickness comprised between  $\lambda/4$  and  $\lambda$  ( $\lambda$  : wavelength of the incident radiation) to efficiently reduce the radiative contribution to the thermal conductivity. Note that the layers deposited by K.S. Ravichandran (UTAH Univ., paper N°14) were either too thick (15 - 49  $\mu\text{m}$ ) or too thin (0.06 - 0.15  $\mu\text{m}$ ) to induce a noticeable reduction of the thermal conductivity.

### 1.2.4 Plasma assisted CVD

A. Lasalmonie (SNECMA) - This new deposition technique seems to present good potentials ; its application to coat real parts has not still to be demonstrated and the costs have to be evaluated.

V.R. Parameswaran (NRC) - The use of chlorides ( $\text{ZrCl}_4$ ) may lead to environmental issues.

XXX (DLR) - The ability to coat complex-shaped parts remains questionable.

S. Drawin (ONERA) - The problems with chlorides can be solved even for industrial plants ; other zirconium precursors are currently studied. A larger deposition reactor will be built next year, that will be able to coat larger parts, as well coupons as blade and vanes.

J.R. Nicholls (CRANFIELD Univ.) - The use of a plasma will make it possible to deposit layered systems, similarly to what has been achieved in our laboratory.

## 1.3 Lifetime of TBCs

### 1.3.1 Role of bond coat, TGO and oxidation

A. Lasalmonie (SNECMA) - Differences in the coating properties are observed when different bond coats are used : how can they be explained? The role of the bond coat surface preparation (roughness) has to be assessed. Various failure modes are encountered in or at the TGO (Thermal Grown Oxide) : the failure mechanisms have to be understood more precisely.

M.R. Winstone (DERA) - Are the failure mechanisms the same for TBCs having experienced 1000 one-minute cycles and 1000 one-hour cycles? TBC manufacturers have large databases on the possible failure modes ...

W. Brindley (NASA) - Yes, TBCs cycled at maximum temperature for six or sixty minutes present different failure modes. It is thus important to design the right durability tests : maximum temperature, coolant temperature, time at maximum temperature, ...

For highly oxidized TBCs, failure occurs at locations where the experienced temperatures were the highest.

About the surface preparation, the presented paper (N°17) addressed PS coatings with a simplified (sine-wave) roughness. Can the conclusions be generalized to all PS coatings?

### 1.3.2 Testing methodology

A. Lasalmonie (SNECMA) - As shown by paper N°15, burner rig tests may be very difficult to interpret : there is a need to establish a testing methodology for the durability tests.

### 1.3.3 Modelling

A. Lasalmonie (SNECMA) - Thermomechanical modelling of the TBC system should allow a better understanding of the failure mechanisms.

### 1.3.4 Graded structures

A. Lasalmonie (SNECMA) - The feasibility of such structures has been demonstrated, but extensive lifetime tests have still to be performed.

A. Lasalmonie (SNECMA) - Generally, what is missing is the users experience on failure mechanisms, on reliability and aging of the TBCs.

Another issue is the influence of the substrate (directionnally solidified alloys vs. single crystals, sulfur and titanium content and diffusion, ...).

P. Morrell (ROLLS-ROYCE) - Physical phenomena are now understood and coatings have been specifically designed by ROLLS-ROYCE.

J.R. Nicholls (CRANFIELD Univ.) - Different bond coats are needed for different single crystals : in general, now bond coats are designed for specific substrates.

Y. Jaslier (SNECMA) - In the single crystal substrates, the grain boundaries having been removed, sulfur cannot segregate at these locations and has to go somewhere else.

XXX (KLM) - Experience exists, but is not spread worldwide (proprietary data!).

## 1.4 Other properties

### 1.4.1 Erosion

A. Lasalmonie (SNECMA) - Can the erosion behaviour of PS coatings be improved?

C. Moreau (NRCC) - Yes, by using for instance powders with smaller particle size ... but several problems will then occur (feeding of the powder into the plasma torch, moisture sensitivity, cost, ...).

W. Brindley (NASA) - Another way to solve this problem would be to find an erosion-resistant material to spray on the leading edge (and having a lower thermal conductivity than the superalloy substrate).

C. Moreau (NRCC) - Here too, feedback from the users is needed.

P. Morrell (ROLLS-ROYCE) - Currently, TBCs behave well on combustor cans and vane platforms.

W. Brindley (NASA) - The problem is also to get the right informations from the TBC coated parts : this needs periodic inspections, inspections means, and inspection procedures.

P. Morrell (ROLLS-ROYCE) - And how will the metallic substrates be inspected if there is a TBC on it.

### 1.4.2 TBC repair

A. Lasalmonie (SNECMA) - How is the repair of TBCs mastered?

## 2. « THICK » TBC (COMBUSTOR APPLICATIONS)

### 2.1 TBC on free-standing components

XXX (??) - This is user-oriented for specific parts.

### 2.2 TBC for combustors

A. Lasalmonie (SNECMA) - Thick TBCs have to be compared to other solutions (CMC, cooled metals, ...).

## REPORT DOCUMENTATION PAGE

<b>1. Recipient's Reference</b>	<b>2. Originator's Reference</b> AGARD-R-823	<b>3. Further Reference</b> ISBN 92-836-1073-3	<b>4. Security Classification of Document</b> UNCLASSIFIED/ UNLIMITED																		
<b>5. Originator</b> Advisory Group for Aerospace Research & Development North Atlantic Treaty Organization 7 rue Ancelle, 92200 Neuilly-sur-Seine, France																					
<b>6. Title</b> Thermal Barrier Coatings																					
<b>7. Presented at/sponsored by</b> The 85th Meeting of the AGARD Structures and Materials Panel, held in Aalborg, Denmark, 15-16 October 1997.																					
<b>8. Author(s)/Editor(s)</b> Multiple			<b>9. Date</b> April 1998																		
<b>10. Author's/Editor's Address</b> Multiple			<b>11. Pages</b> 188																		
<b>12. Distribution Statement</b> There are no restrictions on the distribution of this document. Information about the availability of this and other RTO unclassified publications is given on the back cover.																					
<b>13. Keywords/Descriptors</b> <table border="0"><tr><td>Protective coatings</td><td>Plasma spraying</td></tr><tr><td>Heat resistant materials</td><td>Coating processes</td></tr><tr><td>Barrier coatings</td><td>Vapor deposition</td></tr><tr><td>Combustion chambers</td><td>Research projects</td></tr><tr><td>Turbine blades</td><td>Electron beams</td></tr><tr><td>Ceramic coatings</td><td>Thermal conductivity</td></tr><tr><td>Temperature gradients</td><td>Bonded coatings</td></tr><tr><td>High temperature</td><td>Reviews</td></tr><tr><td>Aircraft engines</td><td></td></tr></table>				Protective coatings	Plasma spraying	Heat resistant materials	Coating processes	Barrier coatings	Vapor deposition	Combustion chambers	Research projects	Turbine blades	Electron beams	Ceramic coatings	Thermal conductivity	Temperature gradients	Bonded coatings	High temperature	Reviews	Aircraft engines	
Protective coatings	Plasma spraying																				
Heat resistant materials	Coating processes																				
Barrier coatings	Vapor deposition																				
Combustion chambers	Research projects																				
Turbine blades	Electron beams																				
Ceramic coatings	Thermal conductivity																				
Temperature gradients	Bonded coatings																				
High temperature	Reviews																				
Aircraft engines																					
<b>14. Abstract</b> <p>Thermal barrier coatings are an emerging technology which will enable either an increase in turbine inlet temperatures, or a reduction in the duty temperature of the blades and as a result, an extension of their life-cycle.</p> <p>This Workshop presented the state of the art, gave a description of the existing or emerging technologies, summarised our present knowledge of damage mechanisms, including microstructural, mechanical and thermal aspects, and reported on the benefits and drawbacks of the various families as perceived by engine manufacturers and users.</p> <p>A final discussion attempted to identify future R&amp;D requirements.</p>																					

L'AGARD détient un stock limité de certaines de ses publications récentes. Celles-ci pourront éventuellement être obtenus sous forme de copie papier. Pour de plus amples renseignements concernant l'achat de ces ouvrages, adressez-vous à l'AGARD par lettre ou par télécopie à l'adresse indiquée ci-dessus. *Veuillez ne pas téléphoner.*

Des exemplaires supplémentaires peuvent parfois être obtenus auprès des centres de diffusion nationaux indiqués ci-dessous. Si vous souhaitez recevoir toutes les publications de l'AGARD, ou simplement celles qui concernent certains Panels, vous pouvez demander d'être inclus sur la liste d'envoi de l'un de ces centres.

Les publications de l'AGARD sont en vente auprès des agences de vente indiquées ci-dessous, sous forme de photocopie ou de microfiche. Certains originaux peuvent également être obtenus auprès de CASI.

## CENTRES DE DIFFUSION NATIONAUX

## ALLEMAGNE

Fachinformationszentrum Karlsruhe  
D-76344 Eggenstein-Leopoldshafen 2

## BELGIQUE

Coordonnateur AGARD - VSL  
Etat-major de la Force aérienne  
Quartier Reine Elisabeth  
Rue d'Evere, B-1140 Bruxelles

## CANADA

Directeur - Gestion de l'information  
(Recherche et développement) - DRDGI 3  
Ministère de la Défense nationale  
Ottawa, Ontario K1A 0K2

## DANEMARK

Danish Defence Research Establishment  
Ryvangs Allé 1  
P.O. Box 2715  
DK-2100 Copenhagen Ø

## ESPAGNE

INTA (AGARD Publications)  
Carretera de Torrejón a Ajalvir, Pk.4  
28850 Torrejón de Ardoz - Madrid

## ETATS-UNIS

NASA Center for AeroSpace Information (CASI)  
Parkway Center, 7121 Standard Drive  
Hanover, MD 21076

## FRANCE

O.N.E.R.A. (Direction)  
29, Avenue de la Division Leclerc  
92322 Châtillon Cedex

## GRECE

Hellenic Air Force  
Air War College  
Scientific and Technical Library  
Dekelia Air Force Base  
Dekelia, Athens TGA 1010

## ISLANDE

Director of Aviation  
c/o Flugrad  
Reykjavik

## ITALIE

Aeronautica Militare  
Ufficio Stralcio AGARD  
Aeroporto Pratica di Mare  
00040 Pomezia (Roma)

## LUXEMBOURG

Voir Belgique

## NORVEGE

Norwegian Defence Research Establishment  
Attn: Biblioteket  
P.O. Box 25  
N-2007 Kjeller

## PAYS-BAS

Netherlands Delegation to AGARD  
National Aerospace Laboratory NLR  
P.O. Box 90502  
1006 BM Amsterdam

## PORTUGAL

Estado Maior da Força Aérea  
SDFA - Centro de Documentação  
Alfragide  
P-2720 Amadora

## ROYAUME-UNI

Defence Research Information Centre  
Kentigern House  
65 Brown Street  
Glasgow G2 8EX

## TURQUIE

Millî Savunma Başkanlığı (MSB)  
ARGE Dairesi Başkanlığı (MSB)  
06650 Bakanlıklar - Ankara

## AGENCES DE VENTE

## NASA Center for AeroSpace Information (CASI)

Parkway Center, 7121 Standard Drive  
Hanover, MD 21076  
Etats-Unis

## The British Library Document Supply Division

Boston Spa, Wetherby  
West Yorkshire LS23 7BQ  
Royaume-Uni

Les demandes de microfiches ou de photocopies de documents AGARD (y compris les demandes faites auprès du CASI) doivent comporter la dénomination AGARD, ainsi que le numéro de série d'AGARD (par exemple AGARD-AG-315). Des informations analogues, telles que le titre et la date de publication sont souhaitables. Veuillez noter qu'il y a lieu de spécifier AGARD-R-nnn et AGARD-AR-nnn lors de la commande des rapports AGARD et des rapports consultatifs AGARD respectivement. Des références bibliographiques complètes ainsi que des résumés des publications AGARD figurent dans les journaux suivants:

## Scientific and Technical Aerospace Reports (STAR)

STAR peut être consulté en ligne au localisateur de ressources uniformes (URL) suivant:  
<http://www.sti.nasa.gov/Pubs/star/Star.html>  
STAR est édité par CASI dans le cadre du programme NASA d'information scientifique et technique (STI)  
STI Program Office, MS 157A  
NASA Langley Research Center  
Hampton, Virginia 23681-0001  
Etats-Unis

## Government Reports Announcements &amp; Index (GRA&amp;I)

publié par le National Technical Information Service  
Springfield  
Virginia 2216  
Etats-Unis  
(accessible également en mode interactif dans la base de données bibliographiques en ligne du NTIS, et sur CD-ROM)



AGARD holds limited quantities of some of its recent publications, and these may be available for purchase in hard copy form. For more information, write or send a telefax to the address given above. *Please do not telephone.*

Further copies are sometimes available from the National Distribution Centres listed below. If you wish to receive all AGARD publications, or just those relating to one or more specific AGARD Panels, they may be willing to include you (or your organisation) in their distribution.

AGARD publications may be purchased from the Sales Agencies listed below, in photocopy or microfiche form. Original copies of some publications may be available from CASI.

## NATIONAL DISTRIBUTION CENTRES

## BELGIUM

Coordonnateur AGARD - VSL  
Etat-major de la Force aérienne  
Quartier Reine Elisabeth  
Rue d'Evere, B-1140 Bruxelles

## CANADA

Director Research & Development  
Information Management - DRDIM 3  
Dept of National Defence  
Ottawa, Ontario K1A 0K2

## DENMARK

Danish Defence Research Establishment  
Ryvangs Allé 1  
P.O. Box 2715  
DK-2100 Copenhagen Ø

## FRANCE

O.N.E.R.A. (Direction)  
29 Avenue de la Division Leclerc  
92322 Châtillon Cedex

## GERMANY

Fachinformationszentrum Karlsruhe  
D-76344 Eggenstein-Leopoldshafen 2

## GREECE

Hellenic Air Force  
Air War College  
Scientific and Technical Library  
Dekelia Air Force Base  
Dekelia, Athens TGA 1010

## ICELAND

Director of Aviation  
c/o Flugrad  
Reykjavik

## ITALY

Aeronautica Militare  
Ufficio Stralcio AGARD  
Aeroporto Pratica di Mare  
00040 Pomezia (Roma)

## LUXEMBOURG

See Belgium

## NETHERLANDS

Netherlands Delegation to AGARD  
National Aerospace Laboratory, NLR  
P.O. Box 90502  
1006 BM Amsterdam

## NORWAY

Norwegian Defence Research Establishment  
Attn: Biblioteket  
P.O. Box 25  
N-2007 Kjeller

## PORTUGAL

Estado Maior da Força Aérea  
SDFA - Centro de Documentação  
Alfragide  
P-2720 Amadora

## SPAIN

INTA (AGARD Publications)  
Carretera de Torrejón a Ajalvir, Pk.4  
28850 Torrejón de Ardoz - Madrid

## TURKEY

Millî Savunma Başkanlığı (MSB)  
ARGE Dairesi Başkanlığı (MSB)  
06650 Bakanlıklar - Ankara

## UNITED KINGDOM

Defence Research Information Centre  
Kentigern House  
65 Brown Street  
Glasgow G2 8EX

## UNITED STATES

NASA Center for AeroSpace Information (CASI)  
Parkway Center, 7121 Standard Drive  
Hanover, MD 21076

## SALES AGENCIES

## NASA Center for AeroSpace Information (CASI)

Parkway Center, 7121 Standard Drive  
Hanover, MD 21076  
United States

## The British Library Document Supply Centre

Boston Spa, Wetherby  
West Yorkshire LS23 7BQ  
United Kingdom

Requests for microfiches or photocopies of AGARD documents (including requests to CASI) should include the word 'AGARD' and the AGARD serial number (for example AGARD-AG-315). Collateral information such as title and publication date is desirable. Note that AGARD Reports and Advisory Reports should be specified as AGARD-R-nnn and AGARD-AR-nnn, respectively. Full bibliographical references and abstracts of AGARD publications are given in the following journals:

## Scientific and Technical Aerospace Reports (STAR)

STAR is available on-line at the following uniform resource locator:

<http://www.sti.nasa.gov/Pubs/star/Star.html>

STAR is published by CASI for the NASA Scientific and Technical Information (STI) Program  
STI Program Office, MS 157A  
NASA Langley Research Center  
Hampton, Virginia 23681-0001  
United States

## Government Reports Announcements &amp; Index (GRA&amp;I)

published by the National Technical Information Service  
Springfield  
Virginia 22161  
United States  
(also available online in the NTIS Bibliographic Database or on CD-ROM)



Printed by Canada Communication Group Inc.

(A St. Joseph Corporation Company)

45 Sacré-Cœur Blvd., Hull (Québec), Canada K1A 0S7